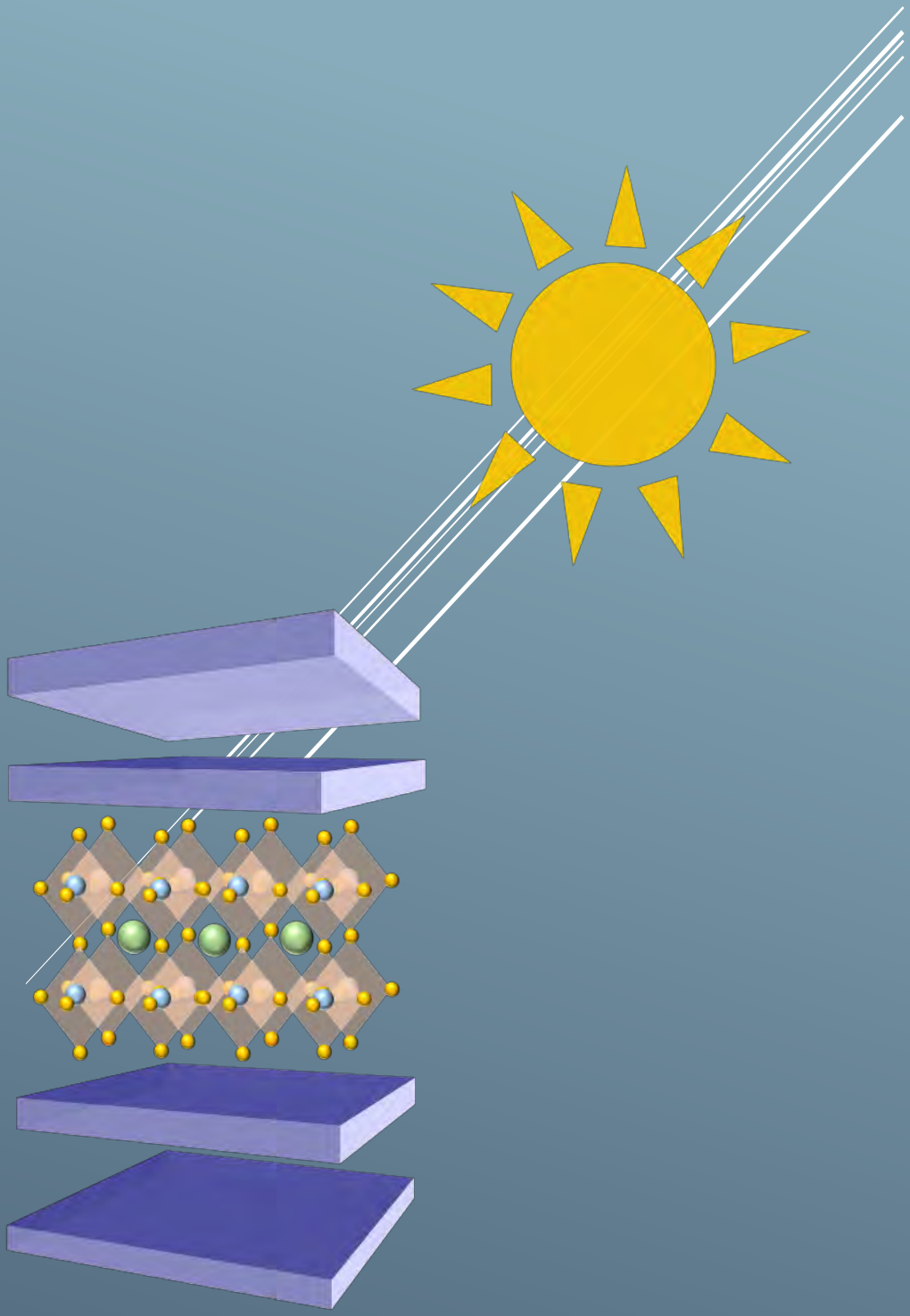

From Selected Lead Halide Perovskite Materials To Solar Cell Devices

Ph.D. Thesis by Rashmi Runjhun

IChF
Institute of Physical Chemistry PAS

EPFL

Ph.D. Thesis

From selected lead halide perovskite materials to solar cell devices

Rashmi Runjhun

Supervisor – Prof. dr. hab. Janusz Lewiński, Instytut Chemii Fizycznej PAN, Poland

Auxiliary Supervisor – Prof. Michael Grätzel, École Polytechnique Fédérale de Lausanne, Switzerland

Warsaw, April 2022

The present thesis was prepared within the International Doctoral Studies in Chemistry at the Institute of Physical Chemistry of the Polish Academy of Sciences Kasprzaka 44/52, 01-224, Warsaw

To my

Grandparents
Indradeo Prasad and Savita Devi

And

Parents
Arbind Kumar Sinha and Renu Sinha

विद्या ददाति विनयम, विनयाद् याति पात्रताम् ।
पात्रत्वात् धनमाप्नोति, धनात् धर्मं ततः सुखम् ॥

कर्मण्येवाधिकारस्ते मा फलेषु कदाचन ।
मा कर्मफलहेतुर्भूर्मा ते सङ्गोऽस्त्वकर्मणि ॥

Acknowledgments

The journey of my Ph.D. has been the most challenging as well as the most rewarding experience in my life. I am grateful that I got an opportunity to work in a very exciting field at two different institutions in two beautiful countries. However, during this time, I faced several challenges, be it with the science or administrative issues, or living in different countries with diverse cultures. Also, the COVID-19 pandemic was a serious challenge. There was even a time when it felt like I would not be able to graduate, and now I am proud to be finishing this thesis. Facing these challenges has made me more confident, persistent, and patient as well as helped me grow both personally and professionally. This journey would not have been possible without the guidance and support of many people.

First of all, I would like to express my sincere gratitude to my supervisor Prof. Janusz Lewiński for his enormous support and supervision throughout my doctoral journey. I thank him for believing in me and allowing me to explore different research areas of the perovskite field. I highly appreciated his enthusiasm and encouragement whenever I got new results. His guidance has helped me polish my skills as a researcher.

My sincere gratitude to my auxiliary supervisor Prof. Michael Grätzel for giving me the opportunity to work in his esteemed lab at EPFL, Switzerland. I also thank him for his valuable input and encouragement.

I would like to thank Dr. Daniel Prochowicz for being an excellent mentor, who introduced me to the solar cell fabrication and characterization techniques at EPFL and guided me in many research projects. I am really grateful for his availability and for quickly solving my research related problems, which saved me a lot of time.

In addition, I thank Dr. Shaik M. Zakeeruddin for his support, guidance, and discussions during my time at EPFL. I express my thanks to my collaborators Dr. Dominik Kubicki, Dr. Pankaj Yadav, and Dr. Jovana Milić for their collaborations and for sharing their knowledge.

I am thankful to my lab mates and friends at IChF PAN, Poland for providing me with a great work environment and making me feel welcomed. I especially thank Natalia Olejnik Feher for helping me settle down in Poland during my initial days in Warsaw and supporting me in many administrative matters, Marcin Saski for training me in the synthesis and characterization of perovskite materials, Wojciech Marynowski for recording the SEM images, for always being kind and helping me out whenever I got into trouble. I thank them for making the lab environment lively through their dad jokes, numerous translations for me, and their efforts to teach me the Polish language. I also thank Jan Nawrocki, Katarzyna Sołtys Brzostek, Anna Cieślak, Piotr Krupiński, Zygmunt Drużyński, Dr. Małgorzata Wolska-Pietkiewicz and Dr. Michał Leszczyński for being great colleagues and their support.

I also thank my colleagues at EPFL for assisting me in my research and making my stay fruitful and enjoyable. I thank Essa A. Alharbi for the productive discussions, collaboration, and creative ideas. I appreciate Dr. Felix Thomas Eickemeyer and Dr. Anurag Krishna for their suggestions and help in various measurement techniques. I also thank Anwar for always helping me with experimental challenges in the thermal evaporator and keeping a cheerful attitude. I thank Hongwei, Masaud and Thomas for helping me in the lab. I especially thank

Elsa John for being a great friend and being there for me during the very difficult time of lockdown at the beginning of the pandemic. I enjoyed our discussions about life, visiting beautiful places, and cooking food together. I also thank my friends Su Htike and Jing Gao.

I am grateful to Prof. Robert Kolos for being an excellent Ph.D. coordinator, giving his input during the Ph.D. seminars and clarifying all our doubts. I also appreciate NaMeS administrative staff, Patrycja Nitoń, Agnieszka Tadrzak, Monika Wydorska, Aleksandra Kapuścińska-Bernatek and Edyta Słojewska for assisting me in handling the administration issues.

I express my gratitude to Ravinthran Ratnasabapathy and Nanthini Ravinthran for providing me accommodation in their house in Switzerland and treating me like a family member. I thank them for their generous care towards me; dropping me to college whenever I was getting late for work, taking me for walks when I was feeling low during the pandemic, teaching me about life, always motivating me to do better, and cooking a lot of delicious foods for me.

I thank my friends in Poland Jyoti, Swaraj, Vicky, Neha, and Alcina for sticking together and making it feel like home here. I thank them for making my stay in Poland more enjoyable and for all the help that I cannot count on. I also thank Nabila and Ayesha for their good company.

I especially thank my college friends Karishma and Ankita for being one of the greatest supports throughout my Ph.D. journey. Even though they stayed in different countries, they always kept in touch, listened to my problems, helped me in every possible way, supported me during my difficult times, and motivated me to keep working towards my goal. I also thank my childhood friends Sulekha and Shikha for always being there for me, believing in me, telling me that I can do anything, and being proud of me.

I cannot put it in words how grateful I am for the immense support my family has always provided me. I especially thank my grandparents Indradeo Prasad and Savita Devi for always loving me unconditionally, caring for me, and continuously supporting me in all my endeavors. They are the reason behind all the success I have achieved in my life so far. They have taught me the value of hard work and never giving up. Thank you for being my greatest strength. I am also forever indebted to my parents, Arbind Kumar Sinha and Renu Sinha for all they have done and sacrificed for making my dreams come true, loving me, supporting me, and being the pillars of my life. I am extremely lucky to have my siblings Sumit and Riya and receive their endless love and encouragement. I thank them for being my strength and always believing and supporting me. I thank my uncles, Ajanavit Prasad, S. Kanhaiya, Ravishankar Savita, and Shashi Ranjan for being the role models in my life. I have always looked up to them since my childhood. I am grateful for their love, support, motivation, and for making me the person I am today. I thank my aunt Rajbinder Kaur for her love and support. I also thank the newest members of my family, my in-laws Vinay Kumar Singh and Madhu Devi for their understanding and encouragement during my studies.

Lastly, I am eternally grateful to my husband Abhijeet for being my biggest cheerleader. Although we stayed thousands of kilometers away from each other, he made sure that I never feel alone on this journey, and stayed together through thick and thin. I particularly thank him for his joyful attitude, humorous jokes, gyan sessions, and extremely useful pieces of advice. He has always inspired me to work hard towards my goals. He has been my family, my friend, my coach, and my audience. Without his love, patience, understanding, continuous support, and encouragement, this thesis wouldn't have been possible.

Statement of originality

I, ***Rashmi Runjhun***, confirm that the research included within the present thesis was conducted by myself or in collaboration with and supported by others, as described in the acknowledgments section. Moreover, the previously published material is listed below.

I attest that I have exercised reasonable care to ensure that the work is original, and does not, to the best of my knowledge, violate any Polish or International law, infringe any third party's copyright or other Intellectual Property Right, or contains any confidential material.

I accept that the Polish Academy of Sciences has the right to use plagiarism detection software to check the electronic version of the thesis. I confirm that my thesis has previously not been submitted for the award of a degree by IPC PAS or any other institute or university.

The copyright of this thesis rests with the author, and no quotation from it or information derived from it may be published without the author's prior written consent.

Place: Warsaw

Date: 11-04-2022 (Signature)

Funding

The presented research was financed by the European Union Horizon 2020 Research and Innovation Programme under the Marie Skłodowska-Curie grant agreement no. 711859 and the Polish Ministry of Science and Higher Education for implementing an international co-financed project in the years 2017–2021.

List of publications

Publications included in the thesis:

1. D. Prochowicz, **R. Runjhun,** M. M. Tavakoli, P. Yadav, M. Saski, Anwar Q. Alanazi, D. J. Kubicki, Z. Kaszkur , S. M. Zakeeruddin, J. Lewiński and M. Grätzel, "Engineering of Perovskite Materials Based on Formamidinium and Cesium Hybridization for High-Efficiency Solar Cells"**,** ***Chem. Mater.,*** 2019, 31, 5, 1620-1627.

2. A. Kalam, **R. Runjhun**, A. Mahapatra, M. M. Tavakoli, S. Trivedi, H. T. Dastjerdi, P. Kumar, J. Lewiński, M. Pandey, D. Prochowicz, P. Yadav, "Interpretation of Resistance, Capacitance, Defect Density and Activation Energy Levels in Single-Crystalline $MAPbI_3$", ***Journal of Physical Chemistry C***, 2020, 124, 3496-3502.

3. A. Mahapatra, **R. Runjhun**, J. Nawrocki, J. Lewiński, A. Kalam, P. Kumar, S. Trivedi, M. Mahdi Tavakoli, D. Prochowicz and P. Yadav, "Elucidation of the Role of Guanidinium Incorporation in Single-Crystalline $MAPbI_3$ Perovskite on Ion Migration and Activation Energy", ***Phys. Chem. Chem. Phys.,*** 2020, 22, 11467-11473.

4. **R Runjhun**[+], E. A. Alharbi[+], Z. Drużyński[+], A. Krishna, M. W. Pietkiewicz, V. Škorjanc, T. P. Baumeler, G. Kakavelakis, F. Eickemeyer, M. Mensi, S. M. Zakeeruddin, M. Grätzel, J. Lewiński, "Zwitterion-Capped-ZnO Quantum Dots and Interfacial Engineering Using Ammonium Halides for High-Efficiency Planar Perovskite Solar Cells", 2022, manuscript submitted.

5. **R Runjhun**, D. J. Kubicki, D. Prochowicz, J. Lewiński, "Solvent Free Mechanosynthesis of 2D Ruddlesden-Popper Perovskites Based on Phenylethylammonium and n-butylammonium Spacer Cations", manuscript under preparation.

[+] Equal contribution

Other publications

1. M. A. Hope, T. Nakamura, P. Ahlawat, A. Mishra, M. Cordova, F. Jahanbakhshi, M. Mladenovic, **R. Runjhun**, L. Merten, A. Hinderhofer, B. I. Carlsen, D. J. Kubicki, R. Gershoni-Poranne, T. Schneeberger, L. C. Carbone, Y. Liu, S. M. Zakeeruddin, J. Lewiński, A. Hagfeldt, F. Schreiber, U. Rothlisberger, M. Grätzel, J. V. Milic, and L. Emsley, "Nanoscale Phase Segregation in Supramolecular π-Templating for Hybrid Perovskite Photovoltaics from NMR Crystallography", ***J. Am. Chem. Soc.,*** 2021, 143, 3, 1529–1538.

2. **R Runjhun**, M. Saski, J. Lewiński, "Tailoring the properties of 2D lead-free MA_2CuX_4 perovskites by ion substitution", manuscript under preparation

Conference presentations

Oral presentation

1. **Rashmi Runjhun**, Marcin Saski and Janusz Lewiński, "Mechanosynthesis of lead free 2-D copper-based perovskites" at 18th International Seminar of Ph.D. students on Organometallics and Coordination Chemistry, Świeradów-Zdrój, Poland, 23-27 September 2018.

Poster presentations

1. **Rashmi Runjhun**, Daniel Prochowicz, Mohammad Mahdi Tavakoli, Pankaj Yadav, Marcin Saski, Anwar Q. Alanazi, Dominik J. Kubicki, Zbigniew Kaszkur, Shaik M. Zakeeruddin, Janusz Lewiński, and Michael Grätzel, "Engineering of Perovskite Materials Based on Formamidinium and Cesium Hybridization for High-Efficiency Solar Cells" at INFORM 19, Valencia, Spain, 5-6 March 2019.

2. **Rashmi Runjhun**, Marcin Saski and Janusz Lewiński , "Tuning of MA_2CuX_4 2-D perovskites by ion substitution" at EMRS Fall Meeting, Warsaw, Poland, 18-21 September 2017.

List of abbreviations

mTOE – Million tonnes of oil equivalent

TWh – Tera watt-hour

UV – Ultraviolet

IR – Infrared

AM – Air mass

PV – Photovoltaics

PCE – Power conversion efficiency

CIGS – Copper Indium Gallium Selenide

CdTe – Cadmium Telluride

DSSC – Dye-sensitized solar cells

PSC – Perovskite solar cells

ITO – Indium tin oxide

FTO – Fluorine doped tin oxide

GaAs – Gallium arsenide

ETL / M – Electron transporting layer/material

HTL / M – Hole transporting layer/material

Spiro-OMeTAD - 2,2',7,7'-tetrakis[N,N-di(4-methoxyphenyl)amino]-9,9'-spirobifluorene

LUMO – Lowest occupied molecular orbital

HOMO – Highest occupied molecular orbital

I-V / J-V – Current-voltage / Current density-voltage

DC – Direct current

$\mathbf{V_{oc}}$ – Open circuit voltage

$\mathbf{I_{sc}}$ / $\mathbf{J_{sc}}$ – Short circuit current/current density

FF – Fill factor

MPP – Maximum power point

$\mathbf{V_{mpp}}$ – Voltage at maximum power point

$\mathbf{I_{mpp}}$ – Current at maximum power point

η – Efficiency

P_{in} – Input power

P_{out} – Output power

IPCE – Incident photon conversion efficiency

EQE – External quantum efficiency

MPPT – Maximum power point tracking

XRD / PXRD – X-ray diffraction / powder X-ray diffraction

NMR – Nuclear magnetic resonance

UV-Vis – Ultraviolet-visible

PL – Photoluminescence

TRPL – Time-resolved photoluminescence

AFM – Atomic force microscopy

SEM – Scanning electron microscopy

UPS – Ultraviolet photoelectron spectroscopy

XPS – X-ray photoelectron spectroscopy

FTIR – Fourier transformed infrared

XRF – X-ray fluorescence

TG-DTA – thermal gravimetric and differential thermal analysis

MA – Methyammonium

FA – Formamidinium

GA/Gua – Guanidinium

EA – Ethylammonium

AA – Acetamidinium

$MAPbI_3$ – Methylammonium lead iodide

$MAPbX_3$ – Methylammonium lead halides

$CsPbX_3$ – Cesium lead halides

$FAPbI_3$ – Formamidinium lead iodide

RP – Ruddlesden-Popper

PEA – 2-phenylethylammonium

FEA – 2-(perfluorophenyl)ethylammonium

QDs – Quantum dots

DMF – Dimethylformamide

DMSO – Dimethyl sulfoxide

NMP – n-methyl-2-Pyrrolidone

GBL – γ-butyrolactone

DMAC – n,n-dimethylacetamide

BA – n-butylammonium

ITC – Inverse temperature crystallization

PTFE – Polytetrafluoroethylene

t – Thickness

ω - Angular velocity

QCM – Quartz crystal microbalance

ADA – 1-adamantylamine

IPA – Isopropyl alcohol

Li-TFSI – Lithium bis(trifluoromethylsulfonyl)imide

DI – Deionized

EAI – Ethylammonium iodide

TCSPC – Time-correlated single-photon counting

MAS – Magic angle spinning

c-GuaI – 2H-pyrimido[1,2-a]pyrimidine-1,3,4,6,7,8-hexahydro-hydroiodide

EIS – Electrochemical impedance spectroscopy

h – hysteresis index

RMS – Root mean square

PCE_{BS} – Power conversion efficiency for backward scan

PCE_{FS} – Power conversion efficiency for forward scan

Abstract

With the increasing energy demands in our society and rising global warming due to the current reliability of fossil fuels, there is an immediate need to develop renewable energy sources. In the last decade, hybrid organic-inorganic metal halide perovskites have attracted widespread attention in the energy research community. They have exceptional optical and electrical characteristics, which make them an excellent class of materials for a broad spectrum of optoelectronic applications. Additionally, the halide perovskites have inexpensive starting materials, which makes them a perfect candidate for being utilized for photoelectric conversion in solar cells. Since the beginning of perovskite solar cell (PSC) research, huge progress has been made resulting in impressive power conversion efficiencies. Nevertheless, various challenges must be solved before bringing this technology to market.

Some of the priority problems in the advancement of PSCs concern (i) the development of environmentally friendly procedures for the synthesis of stable perovskites, (ii) the improvement of existing procedures to produce more efficient perovskite materials and corresponding films for solar cell applications, (iii) an in-depth understanding of the relationship between the composition and the intrinsic electronic properties of perovskite materials, (iv) searching for efficient semiconducting materials suitable for effective electron transport layers, and (v) passivation of interfaces for achieving highly stable and efficient PSCs. Many previous attempts have been made to address these issues, however, further research is still needed. The study presented in this thesis has tackled the abovementioned facets of this very promising and fertile landscape for chemistry, materials science, and society.

One task of the study focused on using an efficient and solvent-free mechanochemical method for synthesizing 2D Ruddlesden-popper layered perovskite materials with the general formula $A_2MA_{n-1}Pb_nI_{3n+1}$. Three distinct potential spacer cations (A-site cation) were investigated: n- butylammonium (BA), 2-phenylethylammonium (PEA), and 2H-pyrimido[1,2-a]pyrimidine-1,3,4,6,7,8-hexahydro-hydroiodide as a cyclic guanidinium (c-Gua), and the resulting materials were characterized using powder X-ray diffraction (XRD) method, UV-Vis absorption spectroscopy, and the solid-state NMR spectroscopy. The studies demonstrated the successful formation of pure phase layered structures in the case of n=1, 2, 3 for BA cation, n=1 for PEA cation, and mixed phases in the case of n=2, 3 for PEA cation. Surprisingly, the c- Gua cations resulted in non-perovskite structures. It was also found that the bandgap of 2D perovskite materials produced with BA and PEA decreased as the value of n increased.

The subsequent task aimed at the preparation of high-quality single crystals of single cation ($MAPbI_3$) and double cation ($Gua_xMA_{1-x}PbI_3$) perovskites and study the effect of a large guanidinium (Gua) cation on the ion transport dynamics in the single crystalline $Gua_xMA_{1-x}PbI_3$ perovskite composition using temperature-dependent electrochemical impedance spectroscopy (EIS). The single crystals were obtained using the inverse temperature crystallization (ITC) technique and their basic characterizations were carried out by XRD, UV-Vis spectroscopy, and the liquid-state NMR spectroscopy. The EIS studies by collaborators revealed that $MAPbI_3$ crystals had a relatively low trap density, and its net impedance spectrum was a result of ionic capacitance and conductivity-related resistance. The incorporation of Gua cation in the 3D perovskite structure induces lattice enlargement, which perturbs the atomic interactions within the perovskite lattice. It was then confirmed by the EIS that the activation energy of iodide migration inside the $Gua_xMA_{1-x}PbI_3$ crystal decreases due to the expansion of lattice upon the incorporation of Gua cation in the 3D perovskite structure, which further increases the hysteresis effect in current-voltage characterization as compared to that of the single-crystalline $MAPbI_3$ counterpart. The results provide the fundamental understanding of hysteresis, which is commonly observed in Gua-based PSCs, and a general protocol for in-depth electrical characterization of perovskite single crystals.

Another part of the research focused on the fabrication and characterization of high-efficiency mesoscopic PSCs based on a 3D double cation perovskite system containing Cs and Formamidinium (FA) as the A-site cations. Thin films of $Cs_{0.2}FA_{0.8}PbI_3$ were deposited using a newly developed one-step solution processing technique, where CsCl was employed as a source of Cs cation instead of the conventionally used CsI. The SEM and AFM images revealed that the resultant 3D $Cs_{0.2}FA_{0.8}PbI_3$ material created a highly homogeneous and smooth perovskite layer with huge grains up to a micrometre in size. These films were later used to fabricate mesoscopic PSCs with an architecture of FTO/c-TiO_2/m-TiO_2/$Cs_{0.2}FA_{0.8}PbI_3$/spiro-OMeTAD/Au. The current density-voltage (J-V) characterization of the devices showed that a high power conversion efficiency (PCE) of 20.6 % was achieved for the champion PSC, with a stabilized PCE of 19.85 %. Further, in order to reduce the defects of the perovskite layer, it was then passivated using two organic salts: 1-adamantylamine (ADA) and guanidinium iodide (GuaI). The passivation from GuaI exhibited a minor improvement in the open-circuit voltage (V_{oc}) of devices, suggesting the suppression of non-radiative charge recombination.

The final part of the thesis elucidated an innovative research work by employing a unique zwitterion (betaine) encapsulated ZnO quantum dot (QD) as the electron transporting layer (ETL) and their further passivation for the fabrication of high-efficiency planar PSC. When a layer of ZnO QDs was used as the ETL in a solar cell with an architecture of FTO/ZnO/$(FAPbI_3)_{0.97}(MAPbBr_3)_{0.03}$/EAI/spiro-OMeTAD/Au, the best device exhibited a PCE of up to 16.7 %. Subsequently, for the optimization of the ZnO/perovskite interface, several ammonium halides (NH_4F, NH_4Cl, and NH_4Br) were used as passivation agents. As a consequence, the ZnO/perovskite band alignment was improved and non-radiative recombinations were minimized. The greatest enhancement was seen in the fill factor (FF) of devices, which dramatically increased from 71.5 % for the reference device to 80.3 % for the NH_4F passivated device. The best performing solar cell with the NH_4F passivation exhibited a champion PCE of 21.9 %, a significant gain in the PCE of 31 % over the reference device. The NH_4F passivated device was also stable for up to 250 hours of continuous illumination under 1 Sun light, keeping 78 % of the initial PCE.

In conclusion, the research outcomes presented in this thesis concerned several aspects of the fertile perovskites chemistry landscape, giving insights into both the development of synthesis methods, as well as, the understanding of inherent structural and optoelectronic properties of the resulting materials. Furthermore, the fabrication of high-performance PSCs in the mesoporous architecture involving double cation perovskite composition as well as in the planar architecture with a novel ZnO QD-based ETL was also elaborately investigated. The results should pave the way for further advancement of this highly promising and valuable field of materials' chemistry.

Abstrakt

Uwzględniając wzrastające społeczne zapotrzebowanie na energię oraz skalę skutków globalnego ocieplenia, istnieje potrzeba wspierania i rozwoju energetyki odnawialnej, w tym m.in. fotowoltaiki. W minionej dekadzie hybrydowe organiczno-nieorganiczne materiały perowskitowe bazujące na halogenkach metali budzą szerokie zainteresowanie w obszarze nowej generacji ogniw fotowoltaicznych. Tego typu materiały posiadają wyjątkowe właściwości zarówno optyczne, jak i elektryczne, co czyni je doskonałą klasą materiałów o szerokim potencjalnym spektrum zastosowań optoelektronicznych. Ponadto substraty stosowane w procesie wytwarzania perowskitów halogenkowych są łatwo dostępne, relatywnie tanie, i w efekcie wspomniane materiały stają się idealnymi kandydatami do wykorzystania w procesie konwersji fotoelektrycznej w nowej generacji ogniwach fotowoltaicznych. Dlatego, od ponad dekady obserwuje się niezwykle dynamiczny rozwój badań nad perowskitowymi ogniwami słonecznymi (ang. perovskite sollar cells, PSCs), czego skutkiem jest m.in. imponująca sprawność ogniw fotowoltaicznych i ich ogromny potencjał komercjalizacyjny. Niemniej jednak, wiele wyzwań musi zostać pokonanych przed ewentualnym wdrożeniem tej technologii do użytku powszechnego.

Obecnie priorytetowe zagadnienia związane z rozwojem perowskitowych ogniw fotowoltaicznych obejmują między innymi (*i*) opracowanie przyjaznych dla środowiska procedur syntezy materiałów perowskitowych, (*ii*) udoskonalenie istniejących już procedur w celu wytwarzania wydajniejszych materiałów perowskitowych i odpowiednich filmów jako komponentów ogniw fotowoltaicznych, (*iii*) pełniejsze zrozumienie korelacji pomiędzy składem chemicznym a właściwościami elektronowymi materiałów perowskitowych, (*iv*) poszukiwanie nowych, efektywnych materiałów półprzewodnikowych do wytwarzania wydajnych warstw transportujących elektrony (ETL) oraz (*v*) pasywacja powierzchni i przestrzeni miedzyfazowych pomiędzy warstwami aktywnymi w celu poprawy stabilności i efektywności ogniw perowskitowych. Problematyka badawcza prezentowanej rozprawy doktorskiej dotyczy wyżej wymienionych interdyscyplinarnych aspektów i łączy badania prowadzone na styku obszarów, takich jak chemia i nauka o materiałach oraz wytwarzanie urządzeń fotowoltaicznych.

Jedno z rozwijanych zagadnień badawczych koncentrowało się na zastosowaniu prostej i wydajnej bezrozpuszczalnikowej metody mechanochemicznej do wytwarzania dwuwymia-rowych materiałów perowskitowych typu Ruddlesden-Popper o wzorze ogólnym $A_2MA_{n-1}Pb_nI_{3n+1}$. Zbadano trzy różne potencjalne kationy rozdzielające A: kation n- butyloamoniowy (BA), 2- fenyloetyloamoniowy (PEA) i 2H-pirymido[1,2-a]pirymidyno-1,3,4,6,7,8-heksahydrojodkowy (cyklicznej guanidyny, c-Gua), a otrzymane materiały scharakteryzowano z zastosowaniem

technik analitycznych takich, jak: proszkowa dyfrakcja rentgenowska (XRD), spektroskopia absorpcyjna UV-Vis oraz spektroskopia magnetycznego rezonansu jądrowego (NMR) w ciele stałym. Badania wykazały pomyślne powstawanie czystych fazowo struktur warstwowych w przypadku n = 1, 2, 3 dla kationu BA, n = 1 dla kationu PEA oraz występowanie faz mieszanych w przypadku n = 2, 3 dla kationu PEA. Natomiast kationy c-Gua prowadziły do powstawania struktur nieperowskitowych. Jednocześnie wykazano, że szerokość przerwy energetycznej dwuwymiarowych materiałów perowskitowych otrzymanych przy użyciu BA oraz PEA zmniejszała się wraz ze wzrostem wartości n.

Kolejne zadanie obejmowało otrzymanie wysokiej jakości monokryształów perowskitów jednokationowych ($MAPbI_3$) oraz dwukationowych ($Gua_xMA_{1-x}PbI_3$), a także badanie wpływu dużego kationu guanidyniowego (Gua) na dynamikę transportu jonów w monokrystalicznej kompozycji perowskitu $Gua_xMA_{1-x}PbI_3$ przy użyciu elektrochemicznej spektroskopii impedancyjnej (EIS). Monokryształy otrzymano techniką odwróconej krystalizacji temperaturowej (ITC), a ich podstawową charakterystykę określono na podstawie danych XRD, spektroskopii UV-Vis oraz spektroskopii NMR w fazie ciekłej. Przeprowadzone przez współpracowników badanie EIS ujawniło, że kryształy $MAPbI_3$ wykazują stosunkowo niską gęstość stanów pułapkowych, a ich widmo impedancyjne wynikało z pojemności jonowej i rezystancji związanej z przewodnością. Wprowadzenie do trójwymiarowej struktury perowskitu rozbudowanego przestrzennie kationu guanidyniowego skutkuje powiększeniem parametrów sieci, co zaburza oddziaływania atomowe w sieci perowskitu. Badanie EIS potwierdziło, że energia aktywacji migracji jodku wewnątrz kryształu $Gua_xMA_{1-x}PbI_3$ zmniejsza się w wyniku rozszerzania sieci po wbudowaniu kationu Gua w strukturę 3D perowskitu, co dodatkowo zwiększa efekt histerezy w porównaniu do monokrystalicznego odpowiednika $MAPbI_3$. Wyniki dostarczają fundamentalnego zrozumienia histerezy prądowej, która jest powszechnie obserwowana w perowskitowych ogniwach fotowoltaicznych opartych na kationie Gua, oraz ogólnego protokołu do dogłębnej charakterystyki pojedynczych kryształów perowskitowych.

Kolejna część badań skupiała się na wytwarzaniu i charakterystyce wysokowydajnych mezoskopowych perowskitowych ogniw fotowoltaicznych (PCS) opartych na układzie dwukationowego perowskitu 3D zawierającego kation Cs i formamidynowy (FA) w pozycji A. Cienkie warstwy $Cs_{0.20}FA_{0.80}PbI_3$ zostały osadzone przy użyciu nowo opracowanej, jednoetapowej metody mokrej, w której jako źródło kationu Cs zastosowano CsCl zamiast powszechnie stosowanego w tym celu CsI. Obrazy SEM i AFM ujawniły, że uzyskany materiał 3D o składzie $Cs_{0.20}FA_{0.80}PbI_3$ tworzy wysoce jednorodną i płaską warstwę perowskitu z dużymi ziarnami o wielkości zbliżonej do mikrometra. Cienkie filmy zostały następnie wykorzystane do otrzymania

mezoskopowych PSC o strukturze FTO/c-TiO_2/$Cs_{0.20}FA_{0.80}PbI_3$/spiro-OmeTAD/Au. Charakterystyka prądowo-napięciowa wykazała wysoką wydajność (PCE) tych ogniw wynoszącą 20.6% dla rekordowego PSC, przy stabilnej wydajności wynoszącej 19.85%. Następnie warstwa perowskitowa została poddana pasywacji przy użyciu dwóch związków organicznych, tj. amantadyny (ADA) i jodku guanidyny (GuaI), w celu zmniejszenia defektów. Pasywacja z GuaI wykazała niewielką poprawę napięcia obwodu otwartego (Voc) urządzeń, sugerując wygaszanie niepromienistej rekombinacji nośników ładunku.

W ostatniej części niniejszej rozprawy przedstawiono innowacyjne badania z wykorzystaniem unikalnych kropek kwantowych ZnO stabilizowanych krótkołańcuchowymi jonami obojnaczymi (tj. betainą) do fabrykacji warstwy transportującej elektrony (ETL) w planarnych PSCs. W przypadku zastosowania kropek kwantowych ZnO jako warstwy ETL w ogniwach fotowoltaicznych o architekturze FTO/ZnO/$(FAPbI_3)_{0.97}(MAPbBr_3)_{0.03}$/EAI/Spiro-MeoTAD/Au otrzymano ogniwo o najlepszej PCE na poziomie 16,7%. Następnie, jako zastosowano halogenki amonu (tj. NH_4F, NH_4Cl i NH_4Br) jako czynniki pasywacyjne na granicy miedzyfazowej ZnO/perowskit. W konsekwencji poprawie uległo dopasowanie poziomów energetycznych dla układu ZnO/perowskit z jednoczesnym zminimalizowaniem rekombinacji bezpromienistych. Największą poprawę zaobserwowano we współczynniku wypełnienia (FF) ogniw, który wzrósł z 71,5% do 80,3% (dla ogniwa pasywowanego z użyciem NH_4F) licząc względem ogniwa referencyjnego. Najlepiej działające ogniwo fotowoltaiczne pasywowane NH_4F wykazało rekordowe PCE na poziomie 21,9%, co oznacza znaczny wzrost PCE o 31% w porównaniu z ogniwem referencyjnym. Ponadto, ogniwo pasywowane NH_4F wykazało stabilność pracy do 250 godzin ciągłego oświetlenia przy oświetleniu równoważnym 1 wartości intensywności promieniowania słonecznego, zachowując 78% początkowej wartości PCE.

Podsumowując, wyniki badań prezentowane w rozprawie doktorkiej dotyczą wielu wątków bogatej chemii perowskitów, dając wgląd zarówno w rozwój metod syntezy jak i wiedzę na temat nieodłącznych właściwości strukturalnych i optoelektronicznych otrzymanych materiałów. Ponadto, zaprezentowano oryginalne badania nad fabrykacją wysokowydajnych ogniw perowskitowych opartych o mezoporowatą architekturę i perowskity dwukationowe, a także wykorzystujących architekturę planarną z zastosowaniem wysoce innowacyjnych kropek kwantowych ZnO jako warstwy przewodzącej elektrony. Otrzymane wyniki przyczyniają się do dalszego rozwoju tego bardzo obiecującego i wartościowego działu chemii materiałowej.

Table of Contents

Chapter 1: Introduction

1.1 Global energy demand and sustainability

With the increase in the world population and technological developments, the global energy demand has raised exponentially in recent years. In 1995, the global energy consumption was 8,588.9 million tonnes of oil equivalent (mTOE), which increased to 13,147.3 mTOE in 2015 [1]. Presently, the three major fossil fuel sources, namely coal, petroleum, and natural gas fulfill about 80% of the energy requirements around the planet. Fig. 1.1 presents the consumption of energy by these sources globally from 1965 to 2019 in terra watt-hour or TWh (1TOE = 1.163 X 10^{-5} TWh) [2]. However, these fossil fuels have presented serious challenges to the environment like water pollution, land degradation, and air pollution. When the fuel is burnt, a huge amount of CO_2 gas is emitted and it traps the heat inside the earth's atmosphere, which results in increasing global warming. Additionally, the burning of fuel also results in the production of harmful pollutants. Due to the significantly increased emission of carbon since the 1970s, visible climate change, as well as environmental degradation, has been observed [3]. Furthermore, fossil fuels will run out eventually as they exist in a limited quantity on earth.

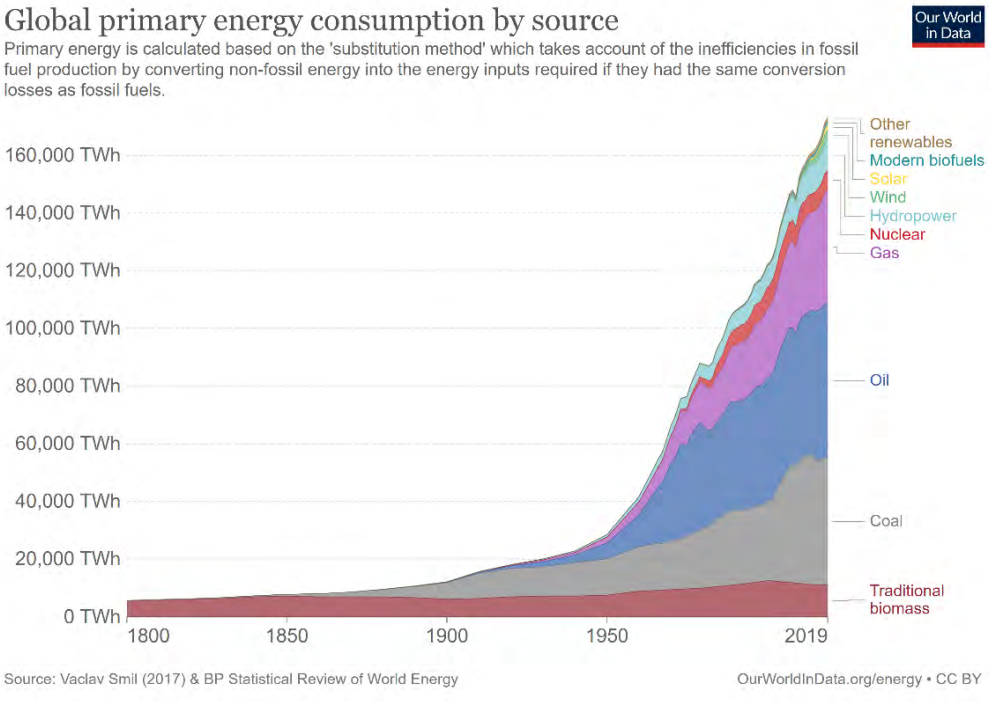

Fig. 1.1: Statistical global energy consumption by different energy sources from 1965 to 2019 [2].

The growth of any nation is essentially dependent on energy resources. Therefore, the energy industry must continue to expand to meet future demands while also keeping up with civilization's growth. It is expected that by 2040, the overall global energy consumption will reach 17,487 mTOE. Relying on fossil fuels to achieve this demand is not a smart idea since it can have disastrous consequences for our climate. As a result, emphasis should be placed on the creation of a sustainable energy supply, which entails lowering the use of fossil fuels, minimizing pollution, and optimizing energy utilization. In this regard, renewable energy technologies hold enormous promise for sustaining current development and meeting future demands. They will also promote the decarbonization of our energy systems. Renewable energy sources such as solar energy, geothermal energy, hydropower, wind energy, tidal energy, and others have demonstrated a strong potential to meet future energy demands. Fig. 1.2 depicts the growing trend in the global proportion of energy generation from renewable sources over the last few decades [4]. Although hydropower has contributed significantly to renewable energy generation thus far, solar energy has also been developing fast since 2010 and is considered to be the most promising.

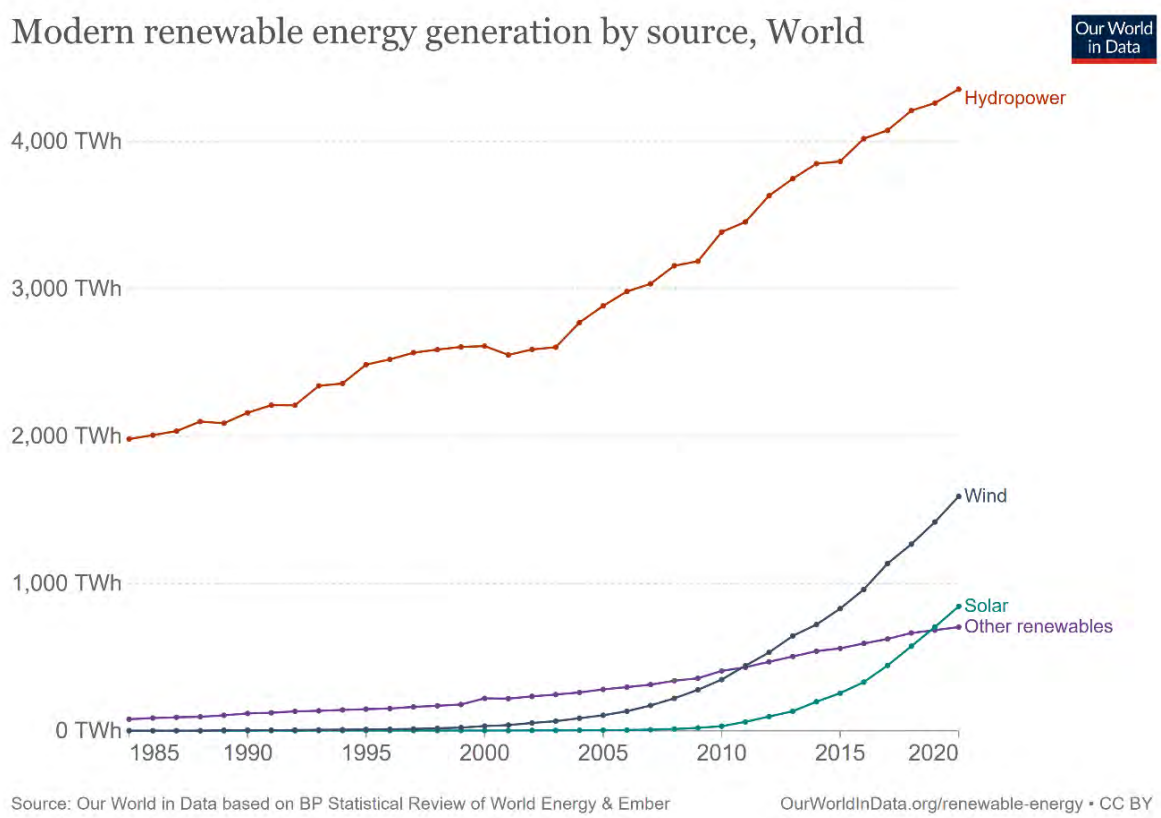

Fig. 1.2: Evolution of global energy generation by different renewable energy sources during 1985-2020.

1.2 Solar energy

The Sun is an abundant source of energy and most importantly, the solar energy received by the earth comes at no cost. In one year, the Sun provides approximately 174 000 TW of solar radiation [5]. The amount of solar energy falling on the Earth in one hour is greater than the total energy consumed by everyone in the world in one year. Solar energy reaching the Earth in the form of electromagnetic radiations extends from the ultraviolet (UV) to the deep infrared (IR) region. Solar irradiance is defined as the power per unit area received by the Earth in the form of light energy and it is measured by an instrument in a particular wavelength region of the electromagnetic waves. However, the irradiance is not uniform throughout the journey of radiation from the Sun to the Earth. Fig. 1.3 shows different intensities of irradiance as a

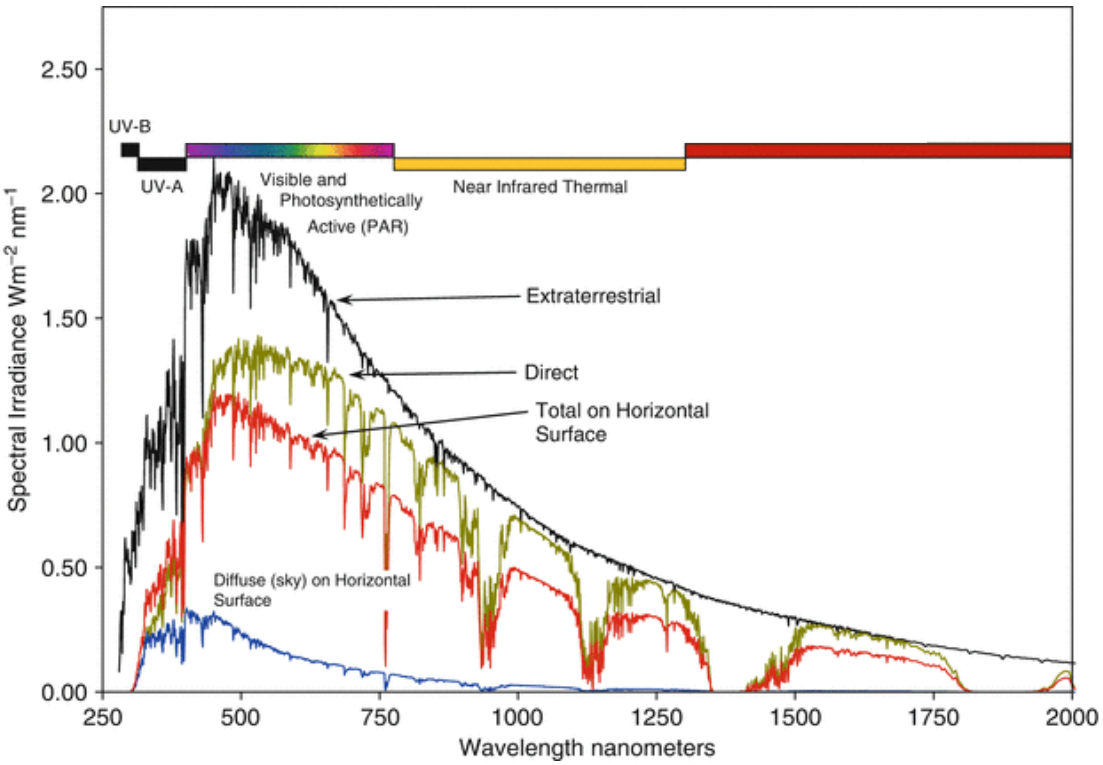

Fig. 1.3: Solar irradiance as a function of wavelength in the extra-terrestrial region, direct solar radiation, diffuse sky radiation, and total radiation on horizontal surface [6].

function of wavelength in the range from 250 nm to 2000 nm. As shown in Fig. 1.3, in extra-terrestrial space, the solar irradiance is highest (black line), and it decreases as the sunlight enters and propagates through the Earth's atmosphere. Due to the absorption, reflection, and scattering by the atmospheric components, the intensity of irradiance decreases. The direct

irradiance (yellow line) is measured on the Earth's surface at a given location and the surface element is taken perpendicular to the Sun, excluding the diffused radiations. Total on horizontal surface irradiance (red line) is the solar radiation measured in a similar manner as in the case of direct irradiance but with the surface element parallel to the Sun. Diffuse on horizontal surface irradiance (blue line) is the sum of light scattered by molecules and particles present in the atmosphere and it is measured on a horizontal surface. To have an idea of the numbers, the average annual solar irradiance is about 1361 W/m^2 in the extra-terrestrial region on top of the Earth's surface and it reduces to a value of 1000 W/m^2 for normal incidence at sea level on a clear day[7].

The performance of a solar cell, which converts incident solar light into electricity, fluctuates with the change in incident power and spectrum of light. As a result, to avoid the variations in the measurement conditions at different times and locations on the Earth, a standard spectrum and power density have been established for the electromagnetic radiation coming from the Sun. AM denotes the air mass, which is the path length travelled by the sunlight into the atmosphere normalized to the path length defined by the shortest possible distance between the Earth and the Sun. This also signifies the reduction of solar power after entering the atmosphere. AM0 and AM1.5 are defined as the standard spectrums outside the surface of the Earth and at the surface of the Earth, respectively. In the case of AM0, the light does not enter the Earth's surface and there is no decrease in power, hence this spectrum is utilized to calculate the efficiency of solar cells in outer space. For AM1.5G (G stands for global and incorporates direct and diffuse radiations) or AM1.5D (D indicates direct radiation only), the intensity of light is reduced by the absorption of air molecules and dust after entering Earth's atmosphere. The power density for AM1.5G has been approximately calculated to be $1kW/m^2$ and this has been globally used for the measurement of photovoltaic efficiencies.

1.3 Basic photovoltaic principles

When the sunlight falls on certain types of photoactive (PV) materials, it can be effectively converted into electricity at the atomic level. These materials display photoelectric effect and this phenomenon is called photovoltaics. French scientist, Edmund Becquerel, first discovered the photoelectric effect in 1839 [8]. In 1905, Albert Einstein explained the photoelectric effect by considering the discrete nature of light, which means light is made of particles called

photons with an energy proportional to the frequency of light, E = hν (h is the Plank's constant). When these photons enter the photovoltaic materials, they transfer their energy, and electrons are emitted from the material. Solar cells or photovoltaic cells also work on the same principle, where the absorbing layer of the cell absorbs the sunlight and converts it into freely flowing charge carriers [9]. The evolution of different photovoltaic technologies is briefly reviewed in the next section.

1.4 Evolution of different photovoltaic technologies

The first solar cell was developed in 1883 with the help of a Selenium crystal and a layer of Gold. This cell exhibited a very low power conversion efficiency (PCE) of 1%. In simple words, PCE is the efficiency by which a solar cell converts sunlight into electricity, and details about its calculation are discussed in Section 1.5.2. Later in 1954, the first solar cell based on Silicon was fabricated in Bell's lab and it converted the sunlight into electricity with an efficiency of 6% [10]. This gave birth to the first generation of solar cells, which are produced mainly from Silicon single crystal and bulk polycrystalline Silicon wafers [11]. Due to the usage of thick (160-200 μm) and rigid Silicon wafers, the first generation cells have the disadvantage of being dependent on the wafer size and have the limited possibility of cost reduction. Additionally, they have high production and environmental cost, which has encouraged researchers to look for other alternatives.

The second generation of solar cells, also known as thin-film solar cells, was developed in the 1980s, and this technology was based on thinner films (a few nm up to 10 μm) of the photoactive layer as compared to first-generation devices. Semiconducting materials such as amorphous Silicon, thin Silicon films, Copper Indium Gallium Selenide (CIGS), and Cadmium Telluride (CdTe) are used to fabricate the second-generation photovoltaic cells [11]. This class of solar cells has the advantage of less material usage as compared to the first generation. Furthermore, they can also be deposited on large-area substrates. However, the high production and environmental cost remain a problem in the second generation cells.

After several years of research, scientists have been able to find several materials for overcoming the challenges presented by first and second-generation solar cells. The third generation of solar cells uses the latest technologies for the production of high-performance solar cells and possesses the advantages of low-cost production and minor environmental

impact. They can be divided into organic photovoltaics, dye-sensitized solar cells (DSSC), quantum dot solar cells, and perovskite solar cells (PSC).

The DSSCs, also known as Grätzel cells, have several advantages over other photovoltaic technologies due to their simple processing, low cost, and flexibility. It was first invented by Michael Grätzel and Brian O'Regan in 1988 and they were able to achieve a PCE of ~7% [12]. In a typical DSSC device, a light-absorbing monomolecular layer of dye molecules (usually ruthenium complexes) is deposited on top of a porous TiO_2 nanoparticle layer. This bilayer is then immersed into a liquid electrolyte solution (an organic solvent containing iodide/triiodide couple), on top of which a catalyst layer based on platinum is deposited. The device is completed by depositing cathode and anode layers, both of which are made of either indium tin oxide (ITO) or fluorine-doped tin oxide (FTO), at the opposite sides of the electrolyte. When the light is incident on the device, dye molecules absorb the photons and generate electrons, which then travel to the TiO_2 layer. These electrons, after being collected at the electrode and flowing through the external circuit containing a load, re-enter the device from the back electrode and then flow towards the electrolyte. Subsequently, the electrons are transported back to the oxidized dye molecules by the electrolyte.

In the third-generation solar cells, the next important achievement was the development of PSCs, which originated from DSSCs in 2009. By replacing the dye molecules in the liquid electrolyte solution with perovskite nanocrystals, the solar cell produced an efficiency of 3.8% [13]. Later, modifications were made and an all-solid-state solar cell based on perovskite as the absorbing layer was developed in 2012, producing a high PCE of 9.7% [14]. Since then an enormous amount of effort has been put by researchers to boost the performance of perovskite-based solar cells. The development of PSC technology will be discussed in detail in the next sub-section. The high PCE, tunability of properties, easy processing, low-cost production, and usability in the flexible substrates make PSCs a strong contender to the commercially available Si-based photovoltaics [15,16,17,18]. The current record for the highest efficiency of PSC stands at a remarkable value of 25.7%, which is close to the theoretical limit [19]. This technology has been the most efficient and cheapest among other third-generation photovoltaic cells [16,20,21]. Although PSCs have shown huge progress in the last decade, challenges such as long-term stability, toxicity and scalability need to be addressed before they can be successfully commercialized [22,23]. These challenges will be broadly discussed in Section 1.9. Another crucial innovation in third-generation solar cells has been the evolution of tandem architectures.

In these devices, several absorber layers of different materials or the same materials with different bandgaps are stacked on top of each other instead of a single absorber layer.

The main goal of multiple layers is to maximize the absorption of sunlight for getting higher-performing photovoltaic cells and even going beyond the theoretical Shockley-Quessier efficiency limit (discussed in Section 1.5.1) [24]. Owing to the bandgap tunability of perovskites, they make a perfect candidate for tandem devices. In the tandem architecture, perovskites can be combined with other PV materials for fabricating high-efficiency devices [25]. Currently, the perovskite silicon tandem solar cells have achieved a record efficiency of 29.8% [26]. The evolution of different photovoltaic technologies over the past few decades is shown in Fig. 1.4.

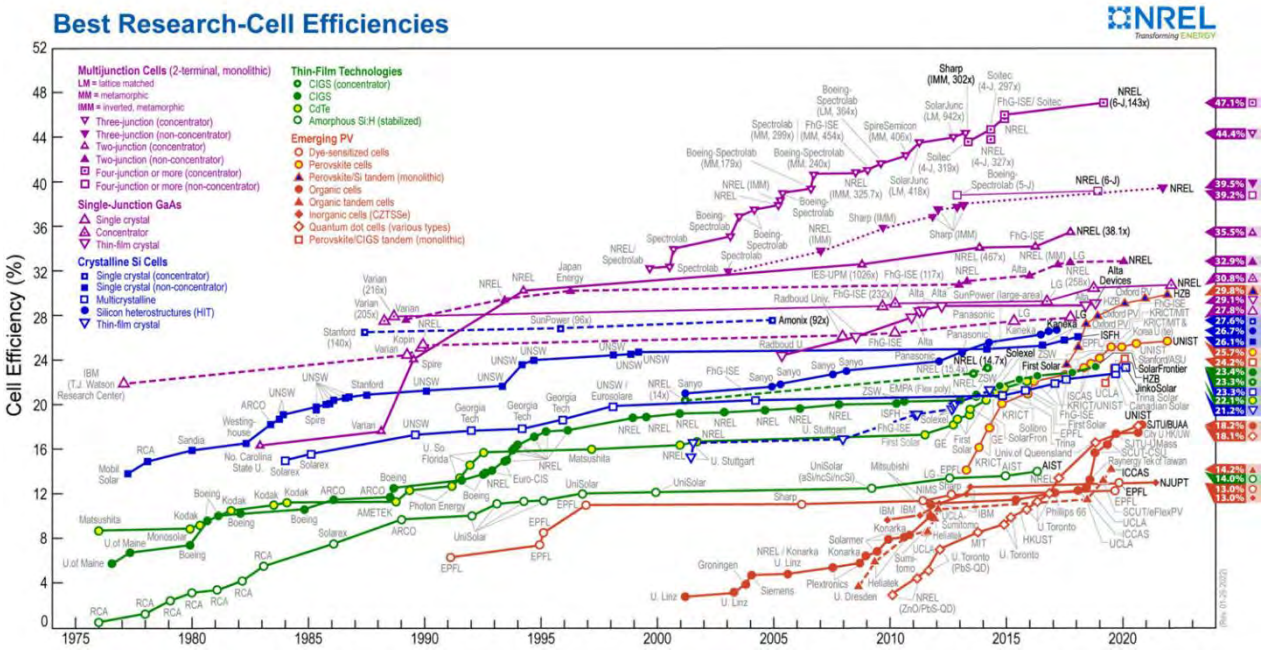

Fig. 1.4: Evolution of power conversion efficiencies of different photovoltaic technologies from 1975 to 2022 [19].

1.4.1 A general overview of the development of perovskite solar cells

The PSC is an exciting and thriving field, which has shown a huge progress in the past decade. As compared to the existing photovoltaic technologies based on Si, GaAs, CdTe, organic polymers, quantum dots, dyes, etc., the efficiency of PSCs has remarkably increased from 3.8% to 25.7% in a very short span of time [19] (Fig 1.4). The current solid-state architecture of the PSC was achieved by carrying out some modifications in the DSSC configuration as discussed

in the previous section. The first work of perovskite materials used in the DSSC configuration was reported by Kojima et al. in 2009 [13]. They fabricated methylammonium lead halides ($MAPbX_3$) and used them as a liquid sensitizer in the DSSC structure and achieved a PCE of 3.8%. The chemical compositions and crystal structures of lead halide perovskite materials are discussed comprehensively in Section 1.6. Unfortunately, the perovskite material had a tendency to dissolve into the liquid electrolyte and it restricted the improvement of solar cell efficiency. Later, in 2012, Kim et al. designed an all-solid-state device structure to solve the solubility issue. In their work, they used methylammonium lead iodide ($MAPbI_3$), and the solid-state mesoscopic heterojunction solar cells boosted PCE to 9.7% [14]. A breakthrough was achieved in 2016 when Saliba et al. incorporated the inorganic Cs into the mixed organic cation perovskite composition [27]. By doing so, they were able to produce pure perovskite films of the composition $Cs_x(MA_{0.17}FA_{0.83})_{(100-x)}Pb(I_{0.83}Br_{0.17})_3$ with monolithic grains and highly efficient and reproducible solar cells with efficiencies >20 %. Many research groups have been working on different components of the devices in order to further improve the PCEs and reach the theoretical Shockley-Queisser limit. Now, the device efficiencies >25% have been achieved for hybrid halide perovskite solar cells as shown in Fig. 1.5 As the PCE of perovskite-based

Fig. 1.5: Progress in PCE of Pb-based and Pb-free perovskite solar cells since 2009 (adapted from [28]).

solar cells are now reaching the theoretical limit, the next challenge that researchers are trying to solve is increasing the environmental stability as well as reducing the toxicity of perovskites. The operational stability of perovskites with organic A-site cations has major operational stability issues due to the high volatility of organic components and light-induced phase segregation. Therefore, researchers have turned their attention toward all-inorganic perovskite compositions to tackle the stability issues. The all-inorganic perovskites have Cs cation at the A-site and they tend to have a better thermal, chemical, and optoelectronic stability as compared to their organic counterparts [29]. Recently a high efficiency of >20 % was reported for $CsPbI_3$-based PSCs [30]. Although all inorganic perovskites have produced high-performing solar cells, the photoactive phase of $CsPbI_3$ perovskite is unstable at room temperature and the perovskite films have a large number of defects present in the bulk films hence PSCs based on these are still not as good as hybrid perovskites [31,32]. In order to address the toxicity issue of Pb, the efforts are directed toward producing Pb-free perovskite compositions. For replacing the Pb atom in the perovskite structure, other non-toxic divalent metals have been used [2833] (discussed in the next section. So far Pb-free PSCs have not achieved efficiencies comparable to that of Pb-based high-efficiency devices and a lot of research is going on for improving the performance of Pb-free devices. Furthermore, the next step in the field of PSC research is to bring this technology to market for practical use. However, the commercialization of PSCs faces several obstacles, and details about these are discussed in the following section.

1.5 Components and working principles of perovskite solar cells

As discussed earlier, a solar cell is an electrical device that covnerts solar light into electricity. It consists of several layers stacked on top of each other for extracting the photogenerated charge carriers. The most important layer is the photoactive absorber layer, which is made up of a semiconducting material with high optical absorption, high electrical conductivity, and a suitable bandgap. In regard to the topic of this thesis, the complete schematic of a conventional PCS device is shown in Fig. 1.6. In a complete device, there are several layers including the electrode layers, the electron transporting layer (ETL), the hole transporting layer (HTL), and perovskite as the light-absorbing layer. FTO, which is transparent as well as conducting, is generally used as the front electrode and is deposited on a glass substrate. The most commonly

used ETLs can be prepared from n-type semiconducting oxides such as TiO_2, SnO_2, and ZnO (details about the ETL are discussed in Section 1.8). The photoactive layer, which is made from halide perovskites can have a variety of different compositions such as single A-site cation, mixed A-site cation, or mixed halide (X-site) perovskites. (for details, refer to Section 1.6).

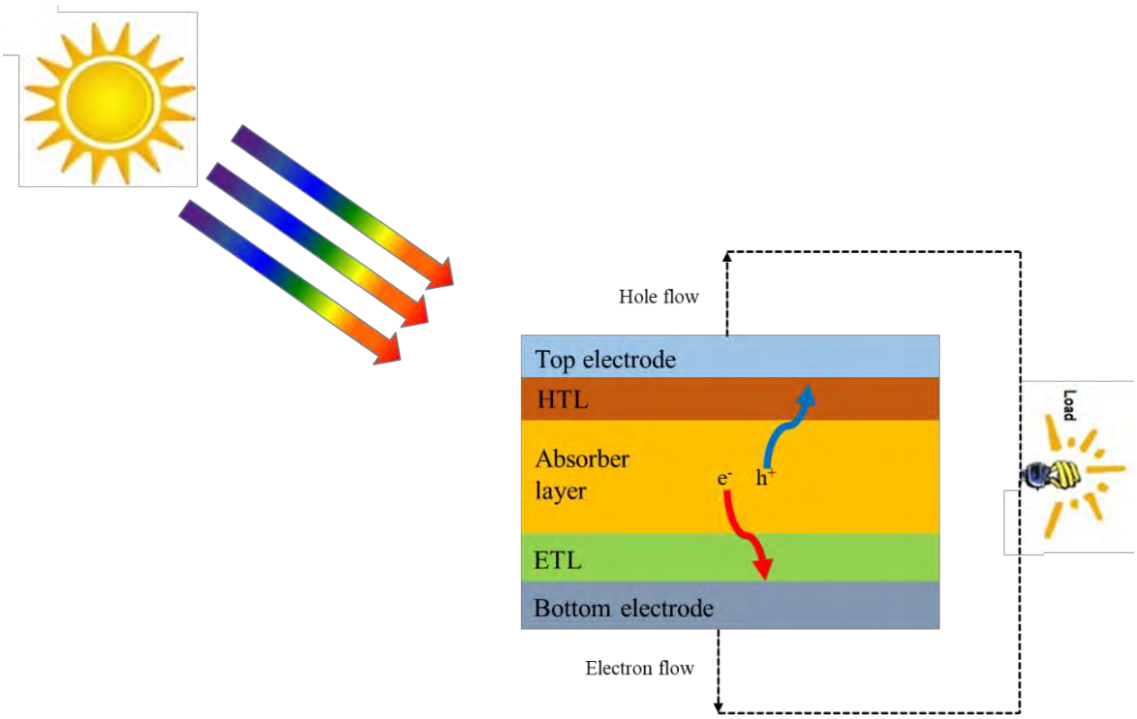

Fig 1.6: Schematic diagram of a conventional perovskite solar cell device and its working.

Spiro-OMeTAD (2,2',7,7'-tetrakis[N,N-di(4-methoxyphenyl)amino]-9,9'-spirobifluorene) and gold are generally used as HTL and back electrode in the high-efficiency PSCs. Fig. 1.7 shows the energy level alignment of different layers and the flow of charge carriers generated by the sunlight in a typical PSC. Once, the light enters the device from the FTO side of the device and reaches the perovskite layer, excitons (a bound state of e^- and h^+) are created. The dissociation of excitons takes place due to the presence of an in-built electric field inside the perovskite layer. After the charges are separated, the e^- is extracted from the lowest occupied molecular orbital (LUMO) of perovskite to the LUMO of ETL and finally to the FTO electrode. Similarly, h^+ is extracted from the highest occupied molecular orbital (HOMO) of perovskite to HOMO of HTL and then Au electrode. The photogenerated charge carriers start flowing when the device circuit is completed through to an external load and current is produced. During the above process, another phenomenon takes place, which is the recombination of charges before

they reach the respective electrodes. These recombinations are non-radiative in nature and lead to the lower performance of solar cells. One of the major causes of non-radiative recombination is the presence of defects. Several strategies have been followed to reduce these defects and they are discussed in detail in sub-section 1.9.2.

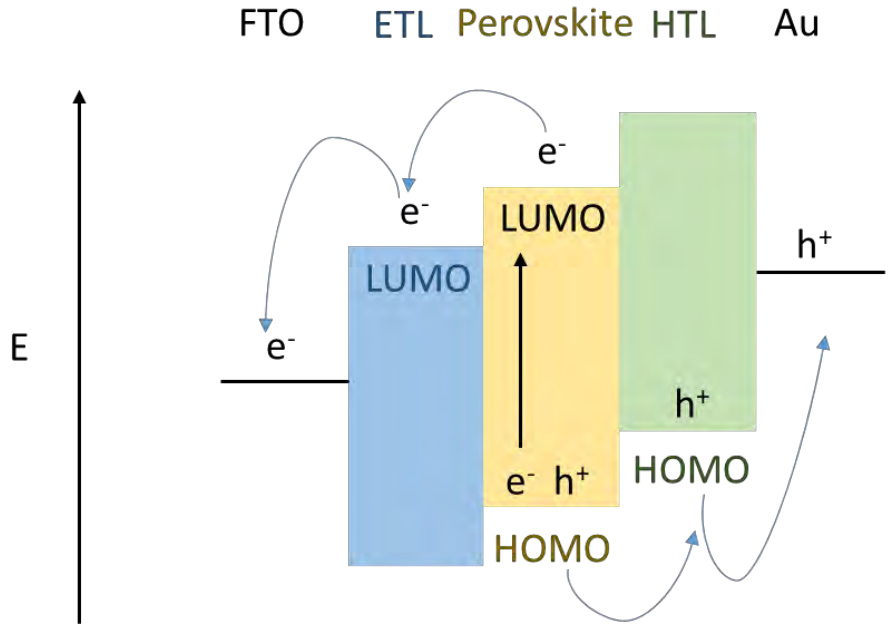

Fig. 1.7: Band alignment and flow of charge carriers in a conventional PSC.

1.5.1 Device Architectures

In the PSC devices, mainly two types of device configurations have been adopted by the researchers, namely normal and inverted. These configurations have the positions of ETL and HTL interchanged. The inverted structure is beyond the topic of this thesis, hence, it will not be discussed further. The normal configuration can be further divided into two categories: planar and mesoscopic. Between these two architectures, the main difference lies in the morphology of materials used in the ETL. More information about ETLs is discussed in detail in Section 1.7, with the emphasis on ZnO-based planar PSCs. As shown in Fig 1.8, in the case of planar structure, typically a compact layer of TiO_2, SnO_2, or ZnO is deposited as the ETL before the perovskite layer [34]. However, in the mesoscopic structure, an additional mesoporous scaffold of a metal oxide is deposited on top of the compact layer. Most commonly used mesoscopic nanoparticles are composed of TiO_2, Al_2O_3, ZrO_2, or SnO_2 [34]. This additional layer

provides a larger surface area, which is in contact with the perovskite layer and provides an improved charge transport. Therefore, due to the better electron extraction capability of mesoporous structures, higher-performing cells can be fabricated [35].

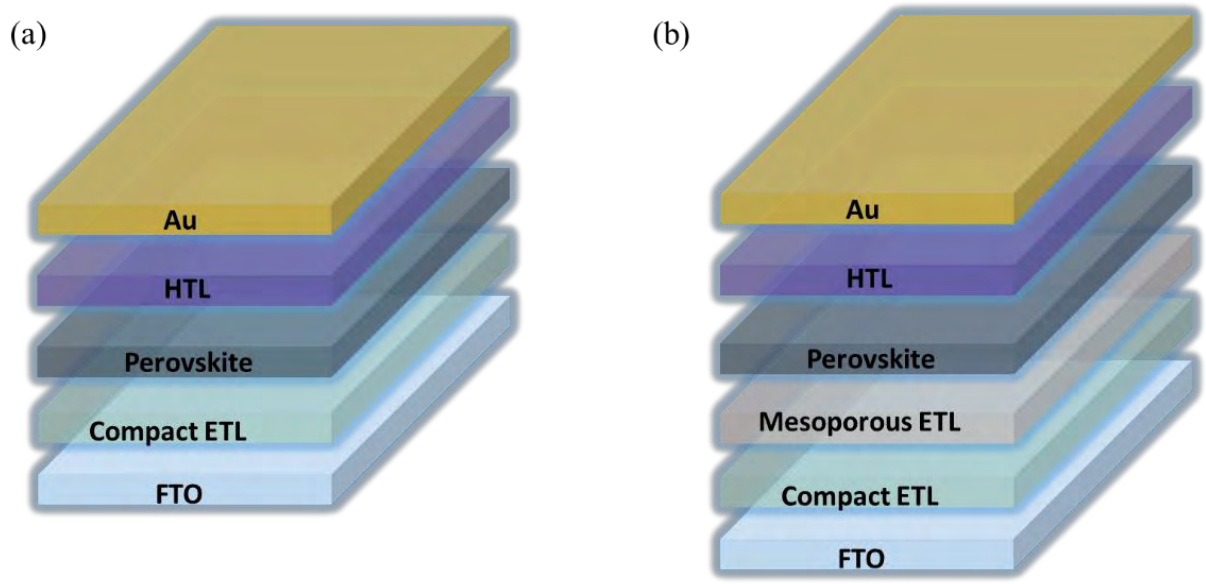

Fig. 1.8: Schematic of device architecture for (a) planar and (b) mesoscopic perovskite solar cells.

Remarkably, various defects are present at the grain boundaries and at the surface of both the electron transport and perovskite layers as well as the perovskite/ETL and perovskite/HTL interfaces [36]. These defects produce non-radiative recombination centers and cause misalignment of energy bands between perovskite and charge-transportting layers, which compromises the performance of solar cells by majorly reducing the flow of charges and stability of the devices [37]. The ion migration at the interface is another issue that needs to be resolved. Perovskite materials are also inherently unstable due to their easy degradation in the presence of moisture, oxygen, UV-light, and high temperature [38]. Therefore, in order to boost the efficiencies of PSCs further and obtain higher stability, the passivation of defects has been adopted widely by researchers as an effective strategy [36]. The passivation can be carried out for either the perovskite layer or charge transporting layers or both in a PSC. Two approaches have been followed for the passivation: 1) bulk passivation by mixing the passivation agent with the corresponding material followed by thin film deposition 2) surface passivation by depositing an extremely thin layer of the passivating agent on top of the desired layer. More about the types of materials used for the passivation of different layers is discussed later in Section 1.9.2.

Once the device structure is completed, it is subjected to various characterization methods in order to determine the performance and other properties. These characterizations are discussed in the following section.

1.5.2 Characterization of solar cell devices

The most common electrical characterization of solar cells is carried out by illuminating the cell at 1 Sun (at AM1.5 G conditions, 1 Sun is defined as the irradiance equal to 1000 W/m^2) and measuring its output current versus voltage (I-V) characteristics. Graphically, the relationship between current and voltage for a solar cell operating at a certain irradiance and temperature is similar to the curve as shown in Fig 1.9. This type of I-V characteristics gives information about the solar cell's capacity of converting sunlight into DC (direct current). When the circuit of the solar cell is in an open position i.e. solar cell is not connected to any load,

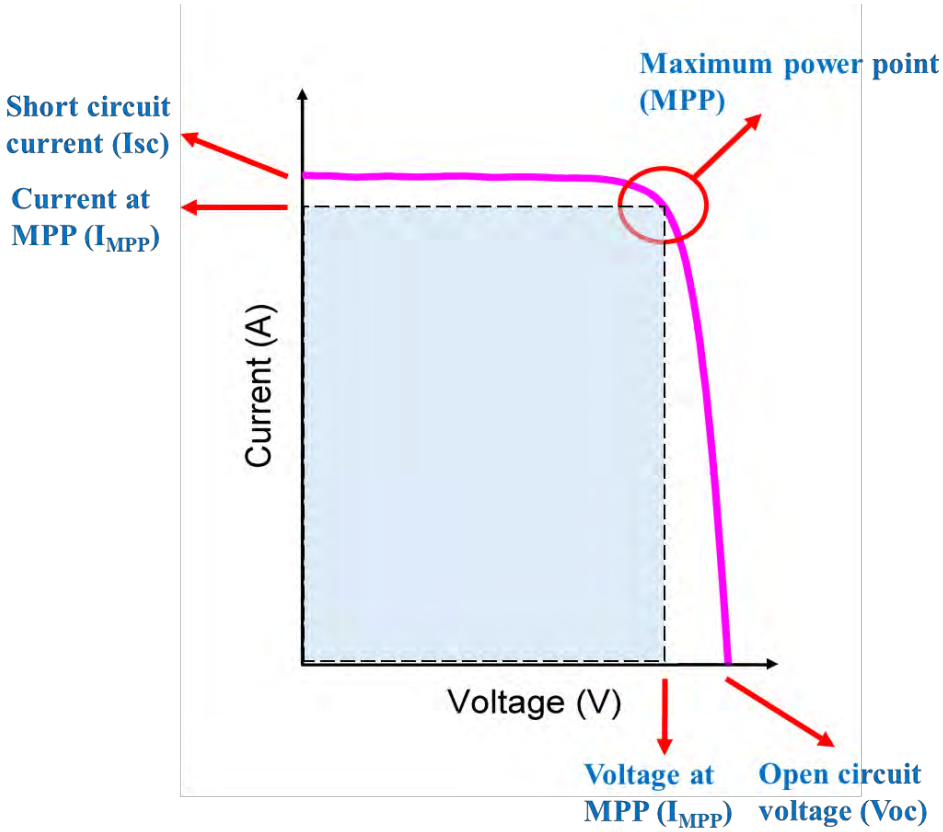

Fig 1.9: Typical I-V characteristics of a working solar cell device.

the current flowing through the cell is zero and the maximum voltage is obtained. This maximum voltage achieved from a solar cell is referred to as open-circuit voltage (V_{oc}). The V_{oc} is the point on the x-axis where the current is zero in the diagram. When the solar cell is in the short-circuit position i.e. the positive and negative terminals are joined together, the voltage obtained across the cell is zero. The current obtained from the cell has the maximum value in this arrangement, and it is referred to as short circuit current I_{sc} (point on the y-axis where voltage is zero). To eliminate the area dependency, the output current is divided by the active area of the solar cell, yielding current density or J (SI unit A/m^2). Therefore, the J-V curves are normally plotted for better understanding and they have been used to discuss the characteristics of PSCs in Chapters 4 and 5 in this thesis.

While I_{sc} and V_{oc} represent the highest current and voltage that a solar cell can produce, the output power is zero at these operating points since the product of current and voltage is zero. Therefore, another parameter known as the fill factor (FF) is employed to calculate the maximum power derived from the cells. The point on the I-V curve where the product of V and I is greatest or where the power is greatest is called the maximum power point (MPP). The fill factor is defined in this context as the ratio of the product of voltage and current at MPP to the product of V_{oc} and I_{sc}.

$$FF = \frac{V_{mpp}\, I_{mpp}}{V_{oc}\, I_{sc}}$$

where V_{mpp} and I_{mpp} are the voltage and current at the MPP, respectively, as indicated in the I-V curve. Graphically, FF represents the extent of the I-V curve's squareness as well as the rectangle with the largest area that can fit inside the I-V curve (shaded blue area in Fig. 1.9). It indicates that the higher the fill factor, the more square the I-V curve is. Finally, the power conversion efficiency (PCE) is the most significant parameter for assessing solar cell performance. It is defined as the ratio of solar cell output power to solar cell input power from the Sun. As discussed in section 1.2, the efficiency of a solar cell depends on the intensity as well as the spectrum of solar light. Therefore, the measurements are carried out at AM1.5G as a standard practice. The formula of efficiency is given by

$$\eta = \frac{P_{out}}{P_{in}} = \frac{V_{oc}\, I_{sc} FF}{P_{in}}$$

where η is the PCE, P_{out} is the maximum output power at MPP which is a product of V_{oc}, I_{sc}, and FF and P_{in} is the power of incident light (1000 W/m^2 at AM1.5G). Thus the efficiency

determines the fraction of input power that is converted into electricity. In 1961, William the Shockley and Hans-Joachim Queisser defined a theoretical limit for maximum efficiency that can be derived from a single junction solar cell. This limit, also known as Shockley Queisser limit, indicated that the maximum efficiency of 30% can be obtained from a solar cell made from an absorber material with a bandgap of 1.1 eV [24]. In their calculations, they considered the solar spectrum as the radiation coming from a black body with a temperature of 6000 K. Further improvements in the calculation were carried out by taking into account the solar spectrum at AM1.5G, which resulted in the value of 33.16% for a semiconductor material of 1.34 eV [39].

Other characterizations of solar cells include incident photon conversion efficiency (IPCE) or external quantum efficiency (EQE) measurements, maximum power point tracking (MPPT), and hysteresis. The IPCE or EQE of a solar cell is the fraction of incident photons that can be successfully converted into charge carriers. This measurement is carried out at short circuit conditions and it indicates the device performance as a function of wavelength. During the measurement, a broad spectrum of light (standard AM1.5 solar emission) is incident on the device, which is held at a constant voltage and the output current is measured. The conversion efficiency is calculated by the software by comparing the generated current to an incident photon flux. From the EQE data, the total J_{sc} of the device can also be derived by integrating the EQE over the entire spectrum. The stability of devices can be measured by tracking the device performance at MPP for a given amount of time. This measurement enables to determine the steady-state PCE of the solar cell as a function of time. Furthermore, the hysteresis behaviour of the device can be measured from the forward and backward I-V scans. Hysteresis is the difference in the I-V curve during backward scan from open-circuit to short circuit conditions and forward scan from short-circuit to open circuit conditions.

The inherent properties of the powders or thin films of photoactive layer are also studied by measurements such as X-ray diffraction (XRD), nuclear magnetic resonance (NMR) spectroscopy, ultraviolet-visible (UV-Vis) spectroscopy, photoluminescence (PL) measurements, time resolved photoluminescence (TRPL) measurements, atomic force microscopy (AFM), scanning electron microscopy (SEM) and ultraviolet photoelectron spectroscopy (UPS). The XRD studies reveal the crystalline structure of photoactive materials. They can also determine whether a sample is pure with only one phase or it contains multiple phases. The NMR measurements give information about the local structure, chemical environment, and dynamics of the materials at the molecular level [40]. Characterization

techniques such as UV-Vis spectroscopy and PL spectroscopy enables the investigation of optical properties of the materials such as light absorption in the solar spectrum and its emission. Moreover, the changes in PL emission spectra provide information about the recombination of charge carriers inside the material. The TRPL measurements are performed to estimate the lifetime of charge carriers before they recombine. Since, the morphology of films plays an important role in the device performance, it is usually studied by imaging techniques such as SEM and AFM. In addition to the morphology, AFM measurements also give the information about the surface roughness of the photoactive films. The UPS studies are used to probe the electronic structure and band alignment of the materials. X-ray photo electron spectroscopy (XPS), impedance spectroscopy, Fourier transformed infrared (FTIR) spectroscopy, X-ray fluorescence (XRF), mass spectroscopy, thermal gravimetric and differential thermal analysis (TG-DTA) etc. are among other characterization techniques used for studying photoactive materials.

1.6 Hybrid organic-inorganic metal halide perovskites and their application to solar cells

1.6.1 Structure and properties of 3D metal halide perovskites

The class of materials called perovskites was first discovered in 1839 by a German scientist named Gustav Rose during his expedition in Russia and the name perovskite was given in the honour of Russian mineralogist Lev von Perovski. The mineral discovered in Ural mountain had the chemical formula of $CaTiO_3$ and all the materials with the similar crystal structure were termed as perovskites. There are a large number of compounds that fall into this class of materials and they exhibit very stable structures with a number of interesting properties and many practical applications. They are broadly classified into two types: all inorganic metal halide perovskites and hybrid organic-inorganic halide perovskites. H. L. Wells was the first to synthesize all inorganic metal halide perovskite in 1892, when he created caesium lead halides [41]. Metal halide perovskites have the general formula ABX_3, where A is a monovalent inorganic cation (e.g. Cs^+ or Rb^+) or an organic cation (e.g. methylammonium or MA ($CH_3NH_3^+$), formamidinium or FA ($CH(NH_2)_2^+$), guanidinium or Gua ($NH_2C(=NH)NH_2^+$)), B is a divalent metal cation (e.g. Pb^{2+}, Sn^{2+}, Ge^{2+}) and X is the halide anion (e.g. Cl^-, Br^-, I^-).

The perovskite crystals have a cubic structure with cation B and anion X forming a corner sharing octahedral network of $[BX_6]^{4-}$ and cation A situated between these octahedrons, as seen in Fig. 1.10.

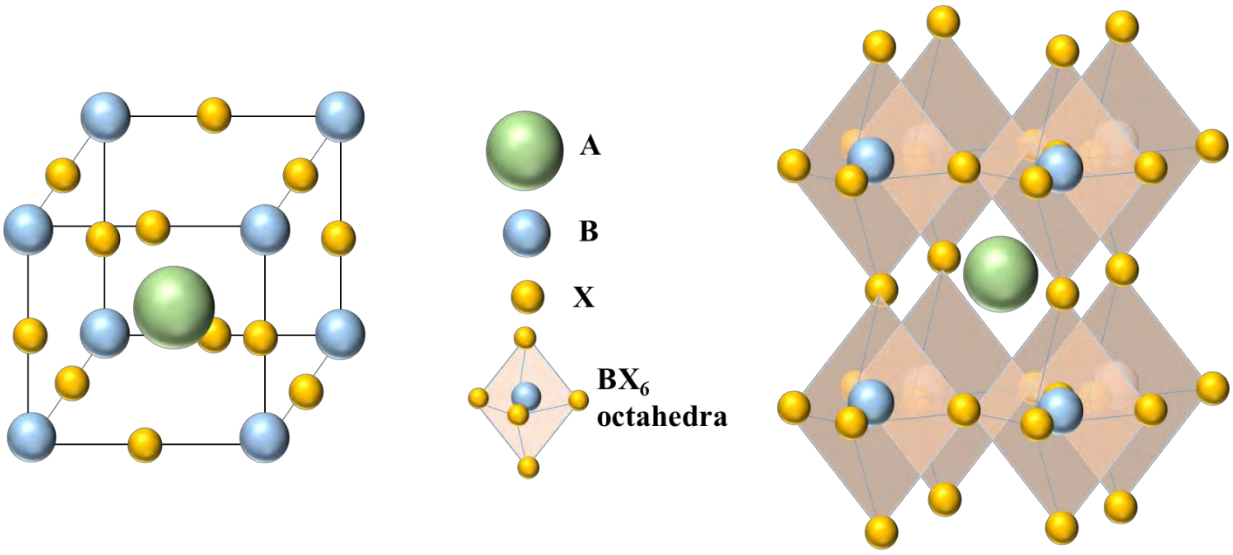

Fig 1.10: Schematic of crystal structure of perovskite and (left) and arrangement of BX_6 octahedra (right) in the crystal lattice.

However, several other perovskite crystal lattices can also be formed apart from the cubic structure depending upon the types of cations and anions involved. In order to predict the stability of perovskites structures with chemical formula ABX_3, Goldschmidt first proposed the formula:

$$t = \frac{r_A + r_X}{\sqrt{2}\,(r_B + r_X)}$$

Where t is the tolerance factor and r_A, r_B and r_X are ionic radius of molecules A, B and X respectively [42]. Usually, the A-site cation is larger as compared to the B-site cation with $r_A > r_B$. For organic-inorganic halide perovskites, when the value of tolerance factor t lies between $0.8 \leq t \leq 1$, the formation of three-dimensional perovskite structure takes place. The ideal cubic structure is formed when t ≈ 1 (Fig. 1.11 (d)). On the other hand, when there is a mismatch between the sizes of cations and anions, additional perovskite and non-perovskite structures are formed. For example, orthorhombic structure is created if the cation A is too small ($0.8<t<0.9$) and hexagonal or tetragonal structures result from larger A cations ($0.9<t<1$) as

depicted in Fig. 1.11 (b) and (c). The second formula for predicting the structural stability is called octahedral factor (μ) and it is given by

$$\mu = \frac{r_B}{r_X}$$

In order to form a stable BX_6 octahedra, the octahedral factor, must lie in the range of $0.44 < \mu < 0.72$ [43]. Additionally, a perovskite material with a given composition can have different crystal structures depending on the temperature and synthesis method. Furthermore, B-site cation can be replaced by either one tetravalent cation or one monovalent and one trivalent cation resulting into perovskites with general formulas of $A_2B(IV)X_6$ and $A_2B(I)B(III)X_6$ respectively. The composition $A_2B(I)B(III)X_6$ is called double perovskites and their properties can be adjusted by the selection of different B(I) and B(III) elements [44]. The ions that can be used as B(I) and B(III) include Na^+, Ag^+, Cu^+, K^+, In^+, and Tl^+, and Bi^{3+}, Sb^{3+}, In^{3+}, and rare earth ions (La^{3+}, Y^{3+}etc.), respectively [45].

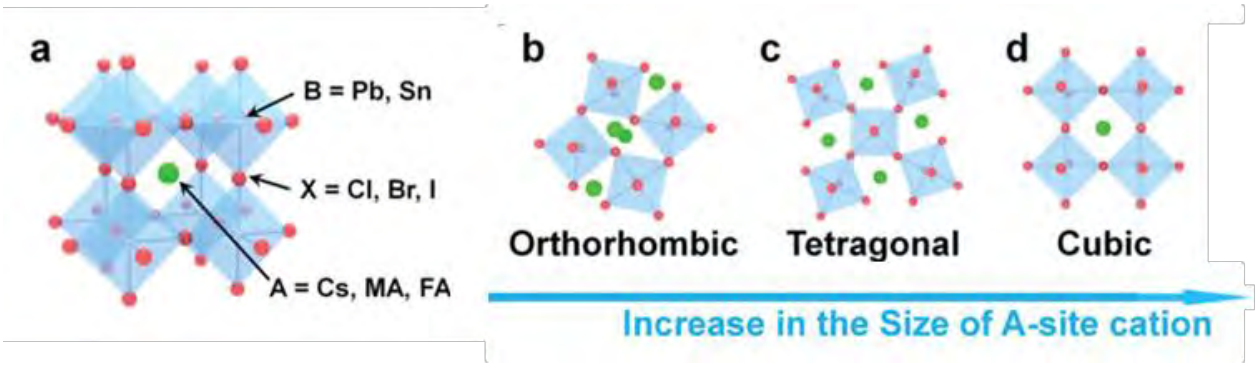

Fig. 1.11: Formation of different 3D perovskite crystal structures with increasing A-site cation (adapted from [46]).

Hybrid metal halide perovskite materials possess extraordinary chemical and optoelectronic properties. These outstanding properties include high absorption coefficient, charge mobility, direct and tuneable band gap, low excitons binding energy and long carrier diffusion lengths [47,48,49]. The comparison of various properties relative to the other commonly used photoactive semiconducting material is presented in Table 1. As compared to other photovoltaic materials, perovskites have a high absorption coefficient of the order of 10^5-10^6 cm^{-1}. The perovskite materials also have a tuneable band gap, which can be achieved by adjusting the A-site as well as X-site compositions and ratios [50,51,52,53]. Although, perovskites have a shorter carrier diffusion lengths as compared to the inorganic materials, they exhibit

higher photoluminescence efficiency [54]. All these properties make them a perfect candidate for the fabrication of high performance solar cells. Currently, 3D metal halide perovskites have been most commonly used for the fabrication of highly efficient PSCs. However, these 3D perovskites tend to have poor long term stability, which is a big hindrance in the commercialization of PSCs. Therefore, in recent years, attention has been shifting towards the development of 2D perovskites since they offer much higher stability of PSCs. More insights regarding these materials will be talked about later in Section 1.6.3.

Table 1: Properties of different types of photoactive materials used for fabricating solar cells.

Material	Absorption coefficient (cm^{-1})	Band gap (eV)	Exciton diffusion length (nm)
Si	10^3	1.1 (indirect)	$10^5 – 3x10^5$
Organic materials	10^5	1 – 2.3	1-10
CdTe	$3 x10^4$	1.4 (direct)	10^3
Perovskite (polycrystalline films)	10^5 - 10^6	1.5 – 3.2 (direct)	10^2 - 10^3

1.6.2 Compositional engineering of 3D metal halide perovskite for high-efficiency solar cells

The most important factor that affects the performance of a solar cell is the quality of absorbing layer. In the case of PSCs, the properties and characteristics of photoactive perovskite layer is dominated by its chemical composition. Accordingly, the properties can be altered by tuning the compositions at A, B and X sites for better performance and stability of devices.

1.6.2.1 Monovalent cations at A-site

In the perovskite composition ABX_3, the cation present at A-site plays an important role in tuning the properties of materials. Depending on the size of A-site cation, which directly affects the tolerance factor, different crystal structures are formed as shown in Fig. 1.12. The commonly used monovalent cations such as Cs, MA (methylammonium) and FA (formamidinium) form the 3D perovskite structures and large cations like GA (guanidinium), EA (ethylammonium), AA (acetamidinium) etc. form the non-perovskite phases [55]. However,

when a commonly used cation is mixed with a large cation, 2D perovskite structures are formed. Accordingly, these materials exhibit different properties. By substituting different monovalent cations at position A, not only the overall stability of solar cells can be improved but also the photovoltaic performance can be boosted [56]. In addition to the single cations, hybrid mixed cation 3D perovskites have also been synthesized and they have proved to be more effective in the solar cells. The following section will discuss more about different perovskite systems with single and multiple A-site cations.

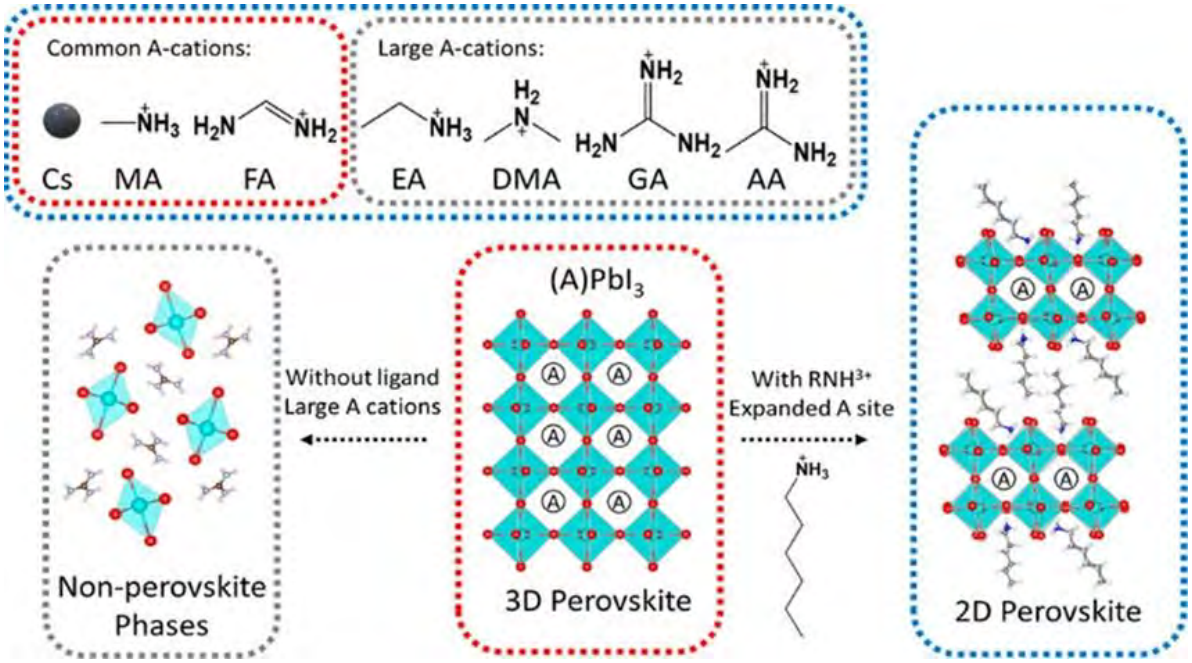

Fig. 1.12: Commonly explored A-site cations and formation of different perovskite structures according to the size of cations (adapted from [55]).

1.6.2.1.1 Single cation perovskite systems

The most frequently used monovalent cation for the A-site is MA, which produces the methylammonium lead iodide ($MAPbI_3$) perovskite composition. With these perovskite systems, PCEs over 20% have already been achieved for solar cells. However, MA-based perovskites exhibit poor stability under moisture, light, and oxygen [57]. Another cation, FA, which is more robust than MA and can also be substituted as the A-site cation in the perovskite lattice and it produces formamidinium lead iodide ($FAPbI_3$) composition. Generally, the band alignment of perovskites is influenced by the lead and halide ions present in the lattice, where valence band maximum is determined by the antibonding Pb-6s and I-5p and the conduction

band minimum is dependent on the bonding orbitals of Pb-6p [58]. The A cation either expands or contracts the crystal lattice or tilts the PbI_6 octahedrons [58]. When MA is replaced by FA cations, it results in the expansion of lattice due to the larger size of FA cation. This expansion further leads to the formation of better symmetry crystals from tetragonal structure for $MAPbI_3$ to the cubic structure for $FAPbI_3$ [59]. As a result, the $FAPbI_3$ perovskites with higher symmetry have lower band gap of 1.45 eV as compared to 1.52 eV for $MAPbI_3$, which is beneficial for better performing devices [59]. In spite of the advantage, at room temperature δ-phase of $FAPbI_3$ exists, which is not photoactive and the photoactive α-phase of $FAPbI_3$ is thermodynamically stable only at high temperatures above 150 °C [53,60,61]. The inorganic cation Cs has also been used to synthesize $CsPbX_3$, which showed good light and thermal stability [62]. Nevertheless, due to the conversion of these compounds into the non-perovskite orthorhombic forms at room temperature and a higher band gap, they have not been able to achieve high efficiencies in the solar cells [63]. Although single cation perovskites have a strong potential in solar cells, there is still a large room for improvement of crystallinity, morphology of films as well as the stability of materials. Therefore, cation mixing strategies have been adopted for fabricating highly efficient and stable devices.

1.6.2.1.2 Mixed cation perovskite systems

The degradation of $MAPbI_3$ in the ambient condition as well as instability of photoactive phase of $FAPbI_3$ and $CsPbX_3$ at room temperature has prompted reasearchers to look for strategies to improve the stabilility of perovskite materials. One of the approaches for achieving this is the mixing of A-site cations, which results into multi cation perovskite systems. In this way, double cation, triple cation and quadrupole cation metal halide perovskites can be synthesized. By taking suitable cations like MA, FA, Cs, K and Rb in appropriate stoichimetric ratios, highly efficient mixed cation perovskite compositions have been reported by researchers [27,64,65]. However, among these, double cation perovskites have an advantage of being easier to process and engineer due to less number of cations involved. The perovskites with triple and quadrupole cations are harder to engineer owing to their complex compositions. In case of double cation systems MA/FA, Cs/FA and Cs/MA mixtures have been explored [66,67,68,69].

1.6.2.1.2.1 Double cation perovskites based on FA and Cs

As discussed previously, $FAPbI_3$ perovskite has a lower band gap and enhanced thermal stability in comparison to the most commonly used perovskite, $MAPbI_3$ [70,71,72,73]. Nevertheless, the photoactive α-phase of $FAPbI_3$ is thermodynamically stable at high temperatures above 150 °C [53,60,61]. Substituting some of the large FA cations by smaller cations at A site optimizes the Goldschmidt tolerance factor and the phase transition to non-photoactive state can be inhibited leading to the improvement of device parameters as well as the stability. In order to stabilize the α-phase of $FAPbI_3$, initially MA cation was introduced into the crystal structure [74,75,76,77]. However, due to volatile nature of MA, this mixed cation system of $MA_xFA_{1-x}PbI_3$ was thermally unstable [78]. Therefore, research focus was shifted to inorganic cation Cs with a smaller ionic radius (1.81 Å) as compared to MA (2.70 Å) and FA (2.79 Å) [79]. The incorporation of Cs cation into $FAPbI_3$ resulting into the composition $Cs_xFA_{1-x}PbI_3$ proved to be beneficial for the stability of devices under humidity and thermal stress [80,81,82]. A PCE of 16.5% was achieved with $Cs_{0.1}FA_{0.9}PbI_3$-based PSC [67]. Replacing 10% of FA by Cs lead to the enhancement of photo and moisture stability due to the modification of cubo-octahedral volume inside the lattice and increased interaction between FA and iodide. Later, Yi et al proved that 20% of Cs addition supports the α-phase crystallization of $FAPbI_3$ forming $Cs_{0.2}FA_{0.8}PbI_3$, which was structurally stable and yielded a PCE of 15.69% [66]. An improved solution processing approach was developed by Zhou et al. where they achieved a PCE of 18.6%. They used a mixture of FAI and FACl while the sequential deposition step, which allowed the formation of large sized perovskite grains and enhanced the charge transport and collection [83,84]. In spite of having excellent stability of the mixed cation perovskite system based on Cs and FA, the PCE of solar cells fabricated from these perovskites did not reach PCEs over 20%. Therefore, efforts are needed to develop synthetic methods and device engineering for fabricating high performance $Cs_xFA_{1-x}PbI_3$-based PSCs.

1.6.2.2 Divalent cations at B-site

Perovskite materials with Pb^{2+} as the B-site cation have been most comprehensively explored and they have exhibited the best properties so far. Due to this reason, the commonly studied perovskite materials for solar cells applications are based on Pb^{2+}. Lead, which is a group IVA element, has the ionic radii of 119 pm. Nevertheless, lead is a toxic element, which is hazardous

to humans and environment. Therefore, other divalent cations such as Sn^{2+} and Ge^{2+} have also been used (discussed in Section 1.9.1). However, due to the easy oxidation of Sn^{2+} to Sn^{4+} and low chemical stability of Ge^{2+}, they have limited applications in high-efficiency solar cells. During the research carried out included in this thesis only materials based on lead have been used.

1.6.2.3 Monovalent anions at X-site

For the X-site anion in ABX_3 composition, halides from group VIIA such as, Cl, Br and I have been used. The size of halide anions increases as we go down the group, enabling perovskites to absorb light of higher wavelengths. Therefore, I has been most extensively used in the perovskite compositions. Moreover, mixtures of these halide ions have also been investigated for tuning the band gap and increasing the stability of materials. For example, theoretical and experimental studies of $MAPbX_3$-based perovskites have revealed a shift in the bandgap from about 2.25 eV for $MAPbBr_3$ to about 1.55 eV for $MAPbI_3$. The mixed iodide bromide composition in $MAPbX_3$ also produces devices with higher moisture stability as compared to pure $MAPbI_3$ [85]. The work included in this thesis is only focused on materials with I as the halide anion.

1.6.3 Structure and properties of 2D metal halide perovskites

Hybrid organic-inorganic halide perovskites also exist in the form of two-dimensional (2D) structures and this is a new emerging group of materials prospective for photovoltaic applications. The most common 2D perovskite is called Ruddlesden-Popper (RP) perovskite, which has a 2D layered structure. The general formula for layered RP perovskites is $A'_2A''_{n-1}B_nX_{3n+1}$, where A' is a large organic cation (aromatic or aliphatic alkyl ammonium cation), A'' is a monovalent cation (Cs^+, $CH_3NH_3^+$, or $CH(NH_2)_2^+$), B is the divalent metal cation (Pb^{2+}, Sn^{2+}, Ge^{2+}) and X is the halide anion (Cl^-, Br^- or I^-). In this composition, A' acts as the spacer cation between the octahedral inorganic layers of BX_6 due to its bulky nature and confines the perovskite in two dimensions [86]. The integer n denotes the number of inorganic layers separated by the A' cation and 3D structures are formed when n is very large ($n=\infty$). The value of n can be tuned by adjusting the stoichiometric ratios between A' and A'' during

the synthesis. Arrangement of atoms in the 2D RP perovskite structures for n = 1, 2, and 3 is shown in the Fig 1.13.

The 2D layers of perovskites can be visualized as slicing of 3D perovskite materials along different crystallographic planes such as <100>, <110> and <111>. These layers can hold bigger and complex organic molecules between them [87,88]. Owing to their reduced dimensionality in 2D, these perovskites also exhibit higher band gap values as compared to

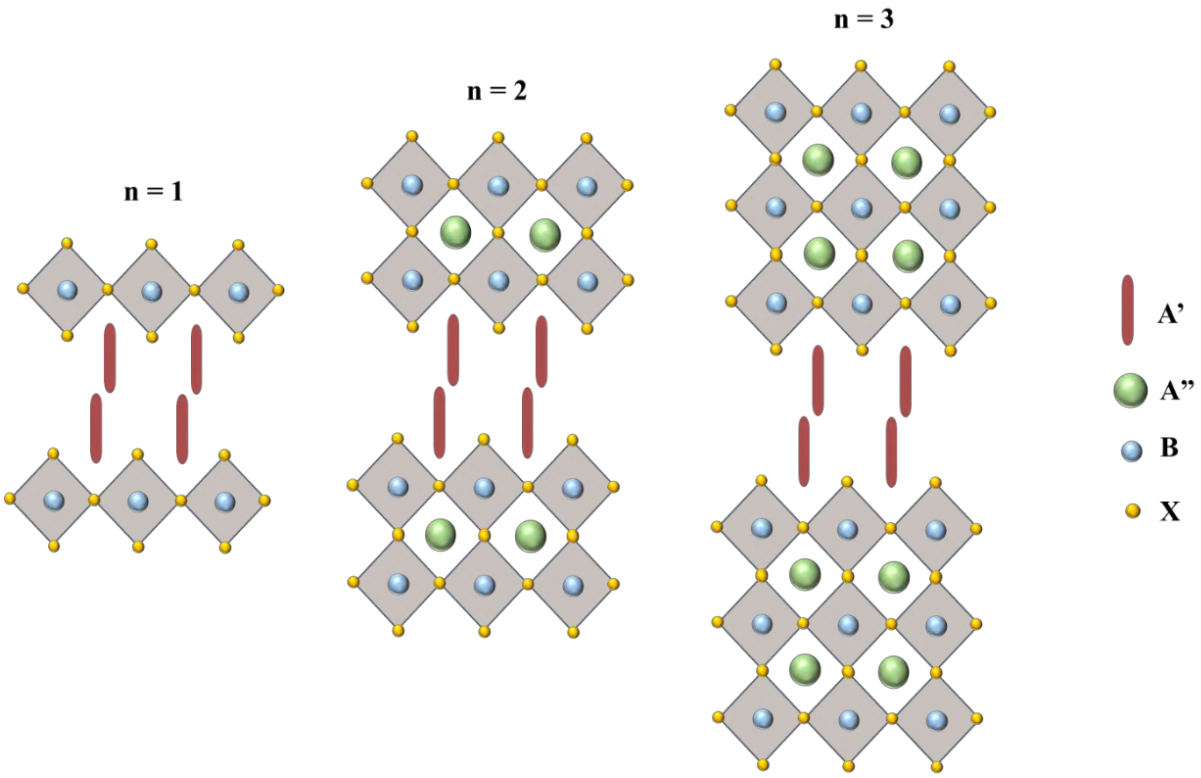

Fig. 1.13: Illustration of 2D Ruddlesden-Popper layered perovskites for n = 1, 2 & 3.

their 3D counterparts [89]. 2D perovskites have large optical band gap (>2.2 eV) and poor charge transporting properties due to the presence of organic bulky groups. The presence of hydrophobic and Columbic forces between the stacked layers helps in maintaining the structural integrity in the 2D system. Moreover, the strong hydrogen bonds between the inorganic and organic layer makes them more structurally stable. The layered 2D perovskites have an advantage of being more resistant towards degradation from humidity and light as compared to their 3D analogues. The hydrophobic long chain or aromatic carbon present in the spacer cations blocks the absorption of moisture and makes the 2D compound more stable [90].

These large cations also help in suppressing the migration of ions in-plane and out-plane in the layered structures. The research on 2D layered perovskites is still in the embryonic state and they have been employed in PSCs. The most commonly explored spacer cations in the 2D metal halide perovskites are n-butylammonium ($C_4NH_{11}^+$) and 2-phenylethylammonium ($C_{18}N_8H_{36}^+$) and they increase the stability of PSCs [91,92,93]. Other cations such as monoammonium linear cations (ethylammonium, propylanmmonium, pentylammonium, octylammonium etc.), cyclic monoammonium cations (cyclopropylammonium, cyclobutylammonium, cyclopetylammonium etc.), aromatic monoammonium cations (benzylammonium, 2-naphthylethylammonium etc.) and inorganic cations (guanidinium, Cs^+) have also been utilized for the synthesis of 2D perovskites [93,94]. To get the benefits of excellent stability as well as reduce the effect of large band gap and limited charge transport, 2D perovskites are utilized in the form of mixed 3D/2D perovskites as the photoactive layer in PSCs [95,96,97,98,99,100]. For example, in a recent work, we showed that the mixture of 2D perovskites based on spacer cations 2-phenylethylammonium (PEA^+) and 2-(perfluorophenyl)ethylammonium (FEA^+), when deposited on top of 3D perovskite layer, improved the device PCE up to 21% [101]. Besides the success in achieving improved efficiency and stability of PSCs based on 2D perovskites, these materials have mostly been synthesized by the solution processing and vapour deposition techniques [92,93]. These synthesis techniques have several drawbacks, which will be discussed in detail in Section 1.8. As a result, there is a constant need for the development of novel and efficient ways for producing these perovskite materials.

1.7 Electron transporting layers in perovskite solar cells

In the solar cell device configuration, the ETL is in contact with the perovskite layer and plays a crucial role in the performance of devices. After the photoexcitation, the generated electrons travel through the ETL and then transported to the electrode. The effective separation of photo generated charge carriers and their transfer to the respective transport layers before recombination is extremely important. As discussed previously in Section 1.5. the n-type semiconducting metal oxides such as TiO_2, SnO_2, and ZnO have been widely studied as promising ETLs in the solar cells [34,102]. A good ETL should have the following properties [103]

1) The conduction band and valence band should be well aligned with the perovskite layer for the fast extraction and transport of electrons.
2) In order to reduce the charge accumulation and recombination at the interface, the electron mobility inside the ETL should be high.
3) The transmittance as well as UV light tolerance should be sufficient enough for the photo generation in the perovskite layer.
4) The ETL should be resistant to the moisture to ensure the stability of devices.
5) There should be a good contact between ETL and perovskite layer for facilitating the crystallization of perovskites and reduce the traps at the interface.

At present, TiO_2 has been the most extensively studied electron transporting material for superior photovoltaic cells with PCE reaching over 20% [104,105]. Due to the favourable alignment of conduction band with the perovskites, wide band gap (~ 3.1 eV), and long carrier lifetime, they make a suitable material for fabricating high performance solar cells [106]. Nevertheless, TiO_2 has some shortcomings such as low mobility of electrons (0.1-4 $cm^2 V^{-1} s^{-1}$), instability under ultraviolet light, associated non-radiative recombination and high sintering temperatures for forming layers [107,108,109]. SnO_2 is another widely explored material for the electron selective layer. It shows improved optoelectronic properties, better band alignment to the absorber perovskite layer and overall stability as compared to the TiO_2 [110]. It also has a high optical transparency which makes it suitable for highly efficient photovoltaic cells [111]. Unfortunately, the presence of dangling Sn bonds on the surface makes it susceptible to react with moisture and oxygen leading to the degradation [112,113]. Additionally, electrons can also be trapped in these loose bond locations and further result into non-radiative recombination. Other n-type oxides explored for ETL includes ZnO, Zn_2SO_4, WO_3, In_2O_3, $SrTiO_3$, Nb_2O_5, and $BaSnO_3$ [111,114,115,116,117,118]. Among these ZnO has shown a promising potential which is discussed in the next section.

1.7.1 ZnO as the electron transporting layer

ZnO, which is an n-type semiconductor, has attracted a lot of attention for being investigated as ETL in PSCs owing to its excellent optoelectronic properties. As compared to TiO_2, ZnO possesses a wider band gap of ~3.3 eV, a higher mobility of electron (200–300 $cm^2 V^{-1} s^{-1}$) and excellent transmittance in the visible region [119,120]. Additionally, it is easily processable

and can be prepared at low temperatures making the production low cost relative to TiO_2 and suitable for flexible substrates. Although, ZnO is a promising alternative to polycrystalline TiO_2, it has certain disadvantages related to the defect density and chemical instability of ZnO/perovskite interfaces. Moreover, due to the presence of UV light and the annealing of perovskite layer, the hydroxyl groups present on the surface of ZnO react with perovskites and produce lead iodide. This induced degradation reduces the overall device efficiency and stability [121,122]. The mechanism of degradation is depicted in Fig. 1.14.

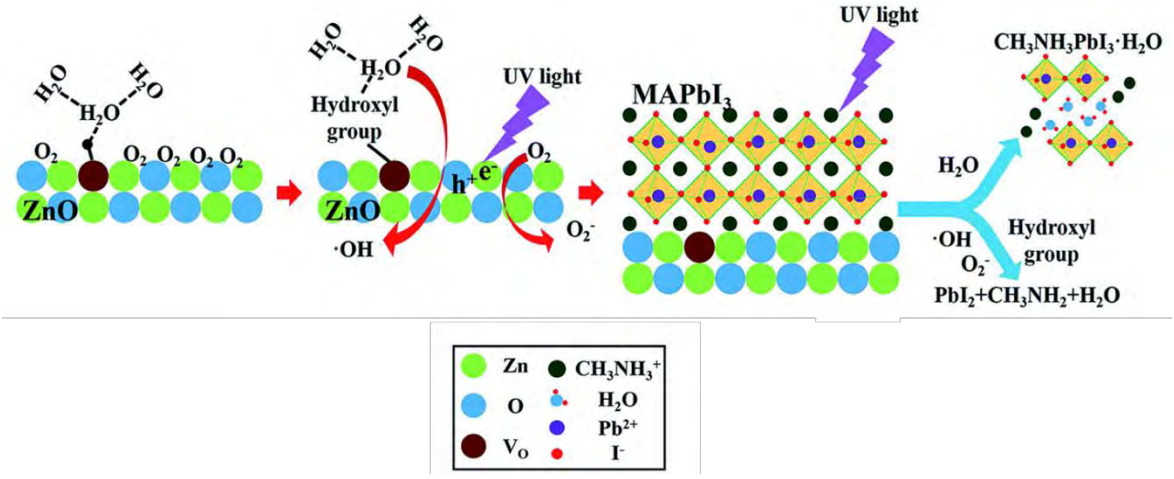

Fig. 1.14: Schematic representation of the degradation mechanism of perovskite deposited on top ZnO layer. (adapted from [123])

Several nanostructures of ZnO such as nanoparticle, nanorods, nanotubes and quantum dots (QDs) have been explored for the application in PSCs [124,125]. In case of QDs, the injection of electrons is increased by the production of multiple excitons while absorbing UV light [18]. Additionally, the deposition of QDs results into more compact films compared to bulk ZnO and hence allows the formation of unconstrained perovskite crystals on top [126,127]. Nevertheless, the intrinsic defects present on the surface of these nanostructures make way for charge recombination and account for low performing cells [128,129]. During the process of thermal annealing, perovskite crystals, which are in direct contact with ZnO, tend to degrade due to the presence of hydroxide on the surface of ZnO [130]. Therefore, efforts are needed to improve the surface of ZnO as well as ZnO/perovskite interface for better charge transport and device efficiencies. One approach followed by researchers is the passivation of ZnO layer with different molecules. Passivation reduces the chemical activity as well as improves the interfacial contact between perovskite and ZnO layer. Cao et al. demonstrated the passivation

by a thin layer of MgO and protonated ethanolamine (EA), promoting the fabrication of high-efficiency, hysteresis free, and stable PSCs [131]. Introduction of MgO inhibits charge recombination at the interface of ZnO/perovskite and EA enhances the charge transport leading to a high-efficiency of 21.1%. Other surface passivation have been carried out by depositing thin layers of inorganic materials like Nb_2O_5 [132], Al_2O_3 [133], alkali metals [134], self-assembled monolayer of methoxybenzoic acid [135], organic materials like graphene [136], fullerenes [137], and PCBM [138]. While inorganic layers assist in improving the chemical stability, the organic passivation layers inhibits the direct proton transfer and hence improving the efficiency. Another strategy for improving the PCE of ZnO-based solar cells is the surface modification ZnO. More recently, Wang and co-workers developed ZnO complexed with ethylene diamine tetraacetic acid, improving the electron mobility and band alignment with the perovskite layer [139]. Using this modified ZnO, they were able to fabricate solar cell with high-efficiency of 20.39% and the best device retained 95% of its efficiency after an exposure to ambient atmosphere for 3604 h. In spite of the progress in using ZnO for PSCs, very high efficiencies have not been achieved and there is a lot of scope for improvement.

1.8 Synthetic methods for the preparation of metal halide perovskites and respective films fabrication

The most important factor that affects the performance of a PSC is the quality of perovskite film. High efficiencies can be achieved when these films are smooth, uniform, crystalline, and phase pure. Fortunately, development of several fabrication methods has made a pathway for modifying these parameters. Largely, these methods can be divided into two categories: wet chemical processing and solid state processing. These methods provide opportunity for tuning the morphology and the uniformity of perovskite films by altering growth and overall crystallinity. These techniques will be discussed in more detail in the following sections.

1.8.1 Wet chemical synthesis

Wet chemical synthesis is the most commonly followed approach for the preparation of perovskite materials. In this synthesis procedure, generally, the precursors are dissolved in a solvent and then deposited on the substrate by spin-coating or dip coating to form the final

films. Among various solution processed techniques, one-step deposition was the very first method used for the deposition of perovskite layer in the solar cells. This method has the advantage of being facile and inexpensive among all the other perovskite fabrication methods. In this processing technique, all the organic and inorganic precursors are dissolved in a common aprotic polar solvents like dimethyl formamide (DMF), dimethyl sulfoxide (DMSO), n-methyl-2-pyrrolidone (NMP), γ-butyrolactone (GBL), or n,n-dimethylacetamide (DMAC) [140,141,142]. Further, the precursor solution is deposited on top of the ETL by spin-coating and subsequent annealing leads to the formation of perovskite film (Fig. 1.15 (a)). The high boiling point and low vapour pressure of the solvents allow the perovskite solution to become supersaturated and promote the crystallization. Subsequent annealing of this film leads to the removal of extra solvents and assist in the enlargement of crystal grains [143]. Although, one-step method is comparatively easy due to lesser number of steps involved, it produces rough and non-uniform films having pinholes. The slow formation of perovskite crystals and incomplete coverage of underlying TiO_2 layer have the effect of high charge recombination at the interface [144].

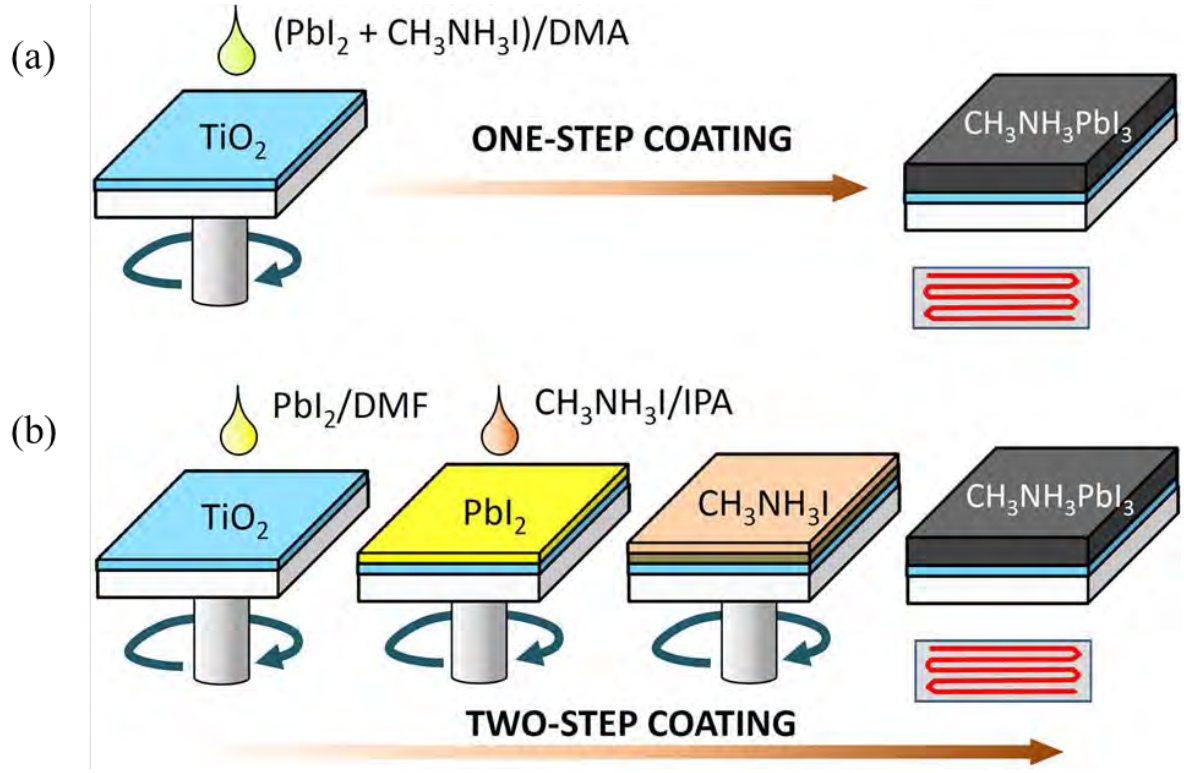

Fig. 1.15: Schematic diagram of (a) one-step and (b) two-step deposition of perovskite solutions (adapted from [145]).

Another procedure, which included two steps, was developed to overcome the poor film quality produced by one-step deposition method. As shown in Fig. 1.15 (b), first step involves deposition of metal halide precursor film and the second step is the introduction of organic halide precursor on top. Additionally, the second step can be carried out either by spin-coating or dipping the metal halide film into organic precursor solution or annealing the metal halide film in the vapours of organic precursors. During the dipping process, ammonium halide infuses into the crystallized metal halide lattice at the grain boundaries. When the film is dipped for a longer time, large perovskite grains are formed by Ostwald ripening [146]. However, during the spin-coating, there is an immediate interaction between the organic solution and metal halide film, resulting into the change of film colour [147]. Further annealing allows the crystallization and growth of perovskite grains.

A modification to the one-step deposition approach for improving the film morphology was achieved by using an anti-solvent while depositing the perovskite solution and it is called anti-solvent assisted deposition. This is a well-established and highly efficient method for the fabrication of perovskite films, where solvent engineering is applied to the one-step deposition. An anti-solvent is dropped on top of the perovskite films just few seconds before finishing the spin-coating process. This leads to the oversaturation of perovskite solution and further promotes the crystallization process [148]. In order to initiate the crystallization and nucleation, the anti-solvent should be added before the formation of the crystalline intermediate [149]. Solvents such as chlorobenzene, dichlorobenzene, toluene, trifluorotoluene have been investigated for the formation of high quality perovskite films [60,150,151]. This anti-solvent assisted deposition method has been used for fabricating perovskite films for solar cells during the research work included in this thesis.

Despite being the most commonly used method for perovskites synthesis, wet methods have certain disadvantages. The drawbacks of utilizing the wet method are use of toxic solvents, solubility of precursors in the solvents, changes in composition stoichiometry of perovskite after long storage time of precursor solution and more energy consumption for the solvothermal conditions [152,153,154]. Therefore, the demand for processes involving less toxic solvents as well as solid state processes is increasing.

1.8.2 Solid-phase synthesis

In order to overcome the shortcomings of solution processing methods, several solid state techniques have been developed for producing metal halide perovskite films. This type of synthesis process does not include use of any liquids as suggested by the name. First solid state synthesis of metal halide perovskite was done by vapour deposition of precursors [71]. The precursors MAI and $PbCl_2$ were heated at very high temperatures inside a vacuum chamber to convert them into their vapour form and subsequently deposited on the compact TiO_2 coated substrate (Fig. 1.16). In this case, two different sources for evaporating organic and inorganic precursors were used. It was found that films coated in this way were highly homogeneous as compared to the films made by solution processing and they were able to achieve a PCE of 15.4 %. The deposition of evaporated precursors onto the substrate can be carried out by either co-evaporating the precursors simultaneously or sequentially in two steps. Now, mixed halide inorganic perovskites as well as mixed halide and mixed cation perovskites is being deposited by the evaporation techniques and high PCEs (>21 %) of solar cells have been achieved [155]. Large-area PSC devices are also produced by these methods [156]. Nevertheless, these processes involve expensive instruments and high temperature processing, increasing the overall cost of

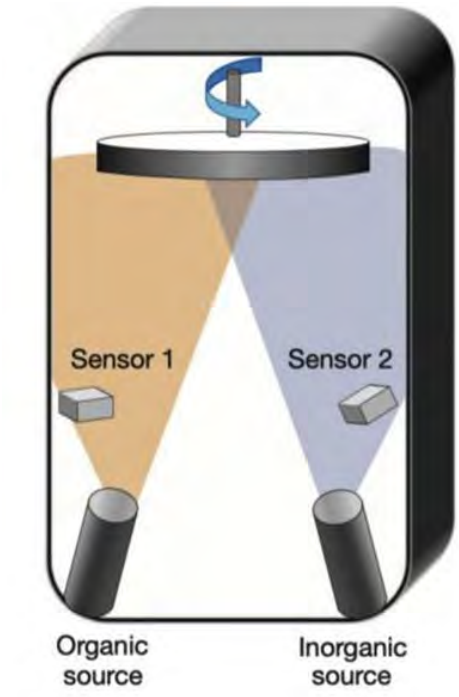

Fig. 1.16: Co-evaporation of perovskite precursors inside a vacuum chamber for producing perovskite films (adapted from [71])

PSCs. Controlling the evaporation rate of precursors during the vacuum deposition is also a problem that researchers are trying to solve. Recently, another solid state technique, also known as mechanosynthesis, has emerged as a promising low cost and greener alternative for the fabrication of perovskite materials [77,157–159]. The scope of this process and its application to perovskites synthesis is discussed in the next sub-section.

1.8.2.1 Mechanochemical synthesis

Mechanochemistry is a powerful synthetic approach for the synthesis of organic [160] and inorganic compounds [161], and various functional materials including metal organic frameworks [162] and energy storage materials [163]. In recent years, the mechanosynthesis has emerged as a promising greener alternative for the fabrication of perovskite materials as well [159]. This solid state technique, where the starting reagents react in the dry environment, has several advantages over the traditional wet chemical method. The method is very simple, environment friendly, energy efficient, and produces compounds with high purity, which effectively increases the efficiency of devices. Since, there are no solvents involved, the choice of reactants used is not restricted by the solubility. The mechanochemical processes are scalable to produce large amount of products and reduce the synthesis time. A large yield of pure products can be obtained with excellent batch to batch reproducibility. Moreover, a higher degree of stoichiometric control and phase purity can be achieved with the thin films made from mechanochemistry. Additionally, the perovskite powders prepared from this method are more stable as compared to the perovskite solutions. The devices made from these films also have better reproducibility and stability. The working principle of this technique will be discussed in Chapter 2.

The use of mechanochemical method for the synthesis of halide perovskites and their applications for PSCs was first pioneered by the Lewiński and Grätzel in 2015, when a highly phase pure $MAPbI_3$ polycrystalline powder was prepared and then applied for the device fabrication (Fig. 1.17) [157]. The authors showed that the devices based on mechanochemically synthesized perovskites exhibited superior performance as compared to the conventional devices made from the solution-processed method. Subsequently, the Lewinski and Grätzel groups systematically screened the compositions and synthesized stable materials of mixed cation perovskites $(MA)_x(FA)_{1-x}PbI_3$ and $(Gua)_x(MA)_{1-x}PbI_3$ [77,164]. In a following work, they

also showed that the incorporation of Cs^+ into the perovskite was possible through the mechanochemical grinding of precursors, which was not feasible earlier through the solution processing methods due to the insolubility of CsCl in the common solvents for perovskites [158]. By this approach, they used CsCl as a new source of precursor for incorporating Cs^+ into the triple cation system and achieved a high PCE of 19.12% was for triple cation $Cs_x(MA_{0.17}FA_{0.83})_{(100-x)}Pb(I_{0.83}Br_{0.17})_3$ perovskite based solar cells. Following these pioneering work, several other groups also reported the synthesis of perovskites with mixed compositions by grinding the appropriate amount of precursors in solid form. Compositions with mono-cation mixed halide of $FAPb(Cl_xBr_{1-x})_3$, $FAPb(Br_xI_{1-x})_3$, and $MAPb(Br_xI_{1-x})_3$ have been mechanochemically synthesized by gradually changing the halide precursor ratios, which resulted into materials with better phase purity as compared to the solution processed perovskites [165,166,167]. The mechanochemical grinding of precursors has also enabled the synthesis of all inorganic $CsPbX_3$ perovskites in the form of bulk materials as well as quantum dots [168,169,170,171]. Owing to the poor solubility of Caesium halides in commonly used solvents, the conventional synthesis of $CsPbX_3$ from solution processing methods is challenging. The

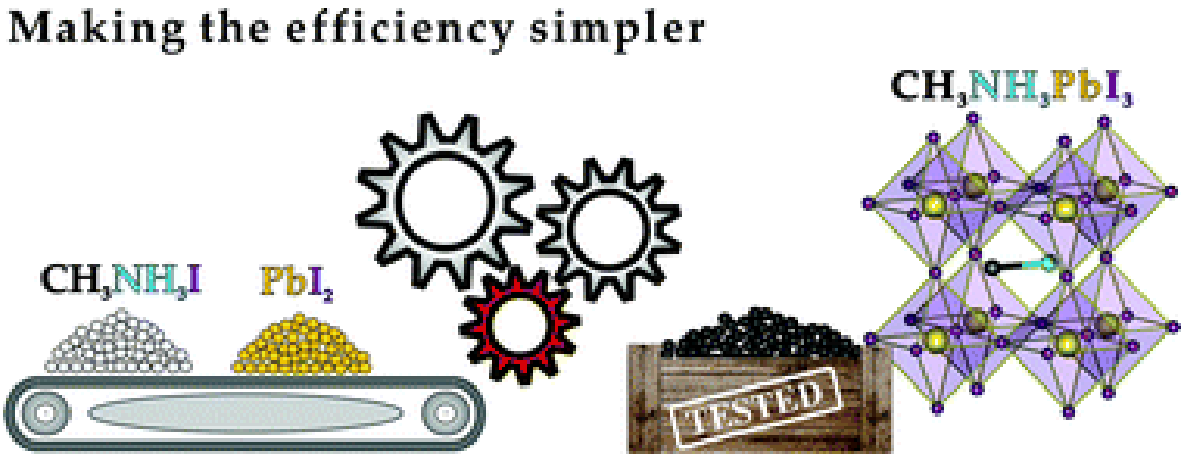

Fig. 1.17: Mechanochemical synthesis of methylammonium lead iodide. (adapted from [157])

mechanochemistry provides an alternative way for synthesizing these materials in a simple, fast and more efficient manner. In a report, Bolink et al. showed the fabrication of thin films by single-source vacuum deposition of mechanochemically produced inorganic $CsPbX_3$ [171]. They found that high quality perovskite films were formed by the evaporation of grinded powders without any pre-annealing of the precursors, which was not possible in the case of

standard dual source evaporation of pristine precursors. The mechanochemistry has also been utilized for the synthesis of lead free perovskites and double perovskites. Recently, the Lewiński group reported the phase pure Sn-based mixed halides perovskites produced by mechanochemical grinding [172]. They successfully synthesized perovskites with the general formula of $ASnX_3$ and used different A-site cations and halide anions. In another work, the dry mechanosynthesis of Sn-, Ge-, and Zn-substituted powders of lead free double perovskite, $Cs_2AgBiBr_6$, was reported [173]. Thin films of Sn-based double perovskites was also deposited by single-source vacuum deposition. Furthermore, the mechanochemically synthesized perovskite powders have a major advantage of being investigated by the solid state NMR for probing the atomic level structures. The solid state NMR is a powerful characterization technique for studying the structural dynamics at atomic level. This solid state characterization method also avoids the solvent impurities as compared to the conventional liquid state NMR measurements. The perovskite powders produced by mechanochemical grinding have been recently utilized for studying the structure of perovskites, halide mixing, phase segregation, local properties and dynamics by the solid state NMR [40]. Besides, the accomplishment achieved in the mechanosynthesis of 3D perovskites, the synthesis of pure phase 2D hybrid halide perovskites following mechanochemistry, has remained a challenge so far [159].

1.9 Challenges towards commercialization of perovskite solar cells

As discussed in previous sections, the efficiencies of lab-scale PSCs are reaching the theoretical limit. The current focus of perovskite research is slowly shifting towards bringing perovskite PV technology into market for practical purposes. However, several challenges still remain as a barrier before the successful commercialization of this technology. The challenges and efforts to overcome them are briefly summarized in the sub-sections.

1.9.1 Pb toxicity issue

One of the problems in PSCs is the use of lead, which is a toxic element and presents health hazards to humans. In order to address the toxicity issue of Pb, the efforts are directed towards producing Pb-free perovskite compositions. For replacing the Pb atom at the B-site in the

perovskite structure, other non-toxic divalent metals such as Sn, Ge and Bi have been used [28,33]. Among these, Sn-based PSCs have shown best efficiency up to ~13 %, however, their efficiencies still lag far behind the best Pb-based PSCs [174,175]. Additionally, Sn-based PSCs have major stability issues due to easy oxidation of Sn^{2+} to Sn^{4+}. Therefore, other transition metals like Cu, Fe, Zn, Sb and Mn are also being explored as the B-site cations [33]. Nevertheless, due to their cation radii, they can only form 2D layered structures with the formula A_2BX_6. Other lead free composition include double perovskites and 0D perovskite derivatives [33,45].

1.9.2 Long term stability

The other major issue related to the hybrid organic-inorganic perovskite materials is their instability in the ambient conditions. As mentioned previously, the instability of perovskite materials in the presence of moisture, O_2, UV-light, heat as well as chemical instability is well recognized [38,85]. Therefore, a lot of efforts are directed in the direction of stabilizing the materials for producing PSCs with longer life. The photoactive perovskite layer tend to degrade very quickly in the presence of the abovementioned components and lead to poor PSC performances. The perovskites with organic A-site cations have major operational stability issues due to their high volatility and light induced phase segregation. Therefore, in order for this technology to be commercialized, the issue of long term stability needs to be fixed. Compositional engineering is one of the ways that has been used extensively for increasing the phase stability of different perovskites as explained previously. Moreover, researchers have started investigating the all inorganic perovskite compositions due to their superior stability (discussed in Section 1.4.1). The defects present at various locations in a PSC also play a critical role in their low stability. Therefore, passivation by different types of additives for stabilizing the hybrid perovskites have been implemented. Bulk passivation of perovskites has been done by addition of alkali metals such as Li, Na, K, Cs and Rb [176]. It has been shown that due to the ionic radii of alkali metals, incorporating them at A-site leads to the formation of more stable perovskite structures with better tolerance factors [177,178]. Addition of halide anion like Cl^- into the perovskite composition has also displayed the passivation of grain boundaries and surfaces. Other additives used for the surface and grain boundary passivation for perovskite layer includes PbI_2, wide band gap materials, alkylammonium halogen, Lewis acids and bases, and hydrophobic materials [36]. To increase the stability of devices, 2D perovskites have also been used in the form of bulk passivator or surface passivator of 3D perovskite layer as

discussed in previous Section 1.6.3. The resulting quasi 2D materials and 2D-3D heterostructures have shown more resistance towards degradation from humidity, heat and light [179]. Additionally, passivation of perovskite/HTL and perovskite/ETL has also been carried out to increase the overall stability of PSCs [180]. These interfacial passivation strategies account for better charge transport, band alignment and lower defects.

1.9.3 Fabrication of large-area devices

To shift from lab scale synthesis to industry scale manufacturing of metal halide perovskites based solar cells, scalability of synthesis methods for large-area processing is also a necessary requirement. Several techniques such as doctor blade coating, spray pyrolysis, slot die coating, inkjet printing and vapour based techniques have been developed for the fabrication of large-area devices [181,182]. A lot of research is going on in the direction of producing large-area solar cells for industrial purposes [181,182,183,184]. PCE as high as 17.9 % for an active area of 804 cm^2 has already been achieved for the PSC [185].

1.10 Objective and outline of this thesis

The rapid progress shown in the research of perovskite materials and their application to solar cells solar cells in the past decade are unprecedented and it has led to the achievement of very high PCEs comparable to the existing Si-based photovoltaics. As a result of simple and low cost processing, perovskite technology has an immense potetial to be commercialized. Due to the chemical composition of perovskites, there is a large possibility for tuning the properties of these materials. A lot of efforts have already been made for the improvement of either material properties or the quality of deposited films or other layers of the solar cells in order to get highly efficient and stable devices. However, there is still a continous need to produce stable perovskite materials via synthetic methods which are environment friendly. It is also required to develop more efficient methods for obtaining perovskite films with superior qualities and can exhibit high efficiencies of solar cells. Additionally, improvements are also desired in the charge selective layers of devices for better electronic properties.

In this thesis three main issues have been addressed

1) Material development of 2D layered perovskites by using an environmental friendly method.
2) Synthesis of single and double cation single crystals and understanding their inherent properties.
3) Development of 3D perovskite films with double A-site cations and their passivation for high-efficiency mesoscopic PSCs.
4) Modifications in ETL and ETL/perovskite interface for high-efficiency planar PSCs.

In order to achieve the aforementioned goals, several approaches have been followed. Chapter 3 focuses on the synthesis and characterization of various perovskite materials including 2D perovskites and single crystals. The 2D layered perovskites with different spacer cations were synthesized by following the highly efficient and solvent-free mechanochemical approach. Single crystals of single and double cation perovskites were synthesized by the inverse temperature crystallization procedure. Chapter 4 focuses on the fabrication of high-efficiency mesoporous solar cells. By modifying the solution processing approach, high quality films of 3D metal halide perovskite with mixed Cs and Formamidinium was deposited, improving the efficiency of PSCs significantly. Further the perovskite layer was also passivated in order to reduce the surface defects. Chapter 5 discusses the incorporation of a novel ZnO QD as the ETL in the planar PSC architecture and improvement of ZnO/perovskite interface for increasing device performance. After the addition of different ammonium halides as the passivation agents at the interface of ZnO and perovskite layer, the solar cells exhibited very high-efficiency.

Chapter 2: Experimental methods and characterization techniques

2.1 Experimental techniques and procedures

2.1.1 Mechanochemical synthesis of hybrid inorganic-organic metal halide perovskites

As discussed in Chapter 1, mechanochemistry is a well-established synthetic procedure that has been used for the synthesis of a variety of organic and inorganic materials [160,161,162,163]. In this solid-state processing technique, mechanical forces are utilized for carrying out the chemical reactions. In order to get the products, the precursors are taken in the solid form and they are grinded or ball milled inside a jar with the grinding balls. The grinding jars are usually made up of materials such as agate, teflon, zirconia, chrome steel etc. and the grinding balls are made from agate, hardened steel, zirconia, chrome steel, alumina, stainless steel etc. There

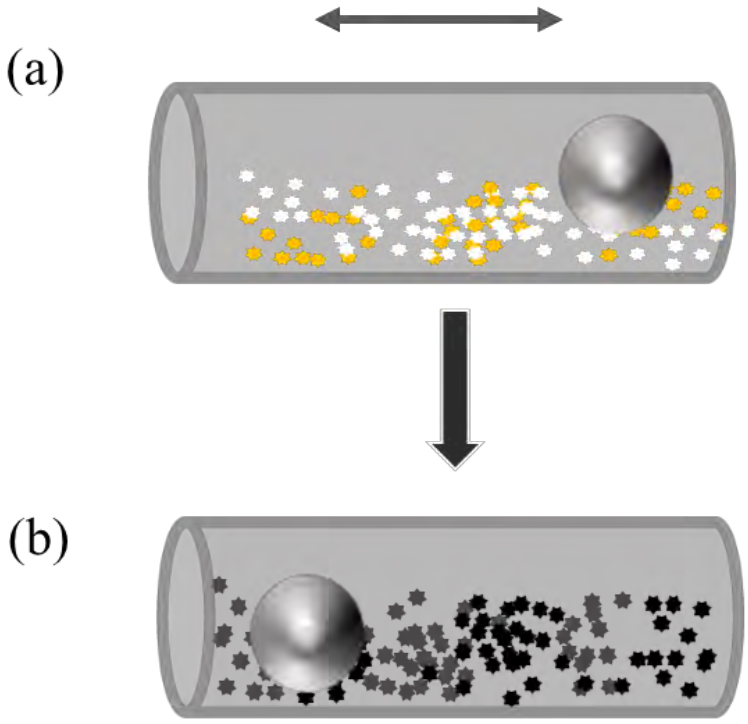

Figure 2.1: Schematic illustration of mechanochemical grinding inside a shaker mill (a) Horizontal motion of agate jar containing the precursors and agate balls and (b) Final product after the mechanochemical grinding.

are several types of ball mills used for the mechanochemical procedure. For the research work included in this thesis, vibration mill or shaker mill was used for carrying out the reactions. The schematic of this technique is shown in Fig. 2.1, depicting the horizontal motion of the jar containing precursors and milling balls. Here, the mechanical force is exerted on the reactants in the form of high speed vibrations. The horizontally placed jar vibrates back and forth and due to collisions between the balls and wall of the jar, friction is created. This frictional force allows the precursors to react with each other and form the final product.

Instrument

Mechanosynthesis of compounds was carried out in a Retsch MM - 400 mixer mill. The reactions were performed in agate jar of 10 mL volume and an agate ball of 10 mm diameter was added to assist the grinding. The resulting perovskite materials were later characterized by vast array of techniques.

Materials

All precursors were obtained from commercial sources and used without any further purification. BAI (n-butylammonium iodide), PEAI (2-phenylethylammonium iodide) were purchased from Sigma Aldrich. PbI_2 and MAI (methylammonium iodide) were purchased from TCI. 2H-pyrimido[1,2-a]pyrimidine-1,3,4,6,7,8-hexahydro-hydroiodide (c-GuaI) was synthesized in house.

Mechanosynthesis of $BA_2MA_{n-1}Pb_nI_{3n+1}$ series

For the 2D perovskite materials with n=1, the precursors BAI and PbI_2 were carefully weighed in the molar ratio of 2:1 and grinded together at an optimized frequency of 30 Hz for 30 min in the shaker mill. After the grinding was finished, a homogenous powder of BA_2PbI_4 was obtained as shown in Fig. 2.2 (left image). Similarly, the precursors BAI, MAI and PbI_2 were taken in stoichiometric ratios of 2:1:2 and 2:2:3 for materials with n=2 & 3 respectively. After grinding for 30 min at 30 Hz, the polycrystalline powders of $BA_2MAPb_2I_7$ (Fig. 2.2, middle image) and $BA_2MA_2Pb_3I_{10}$ (Fig. 2.2, right image) were obtained. Furthermore, for getting better crystallinity, the powders were further annealed at 80 ^oC for 3-4 h in the oven. The powder for n=3 was kept inside the glove box for a week for aging.

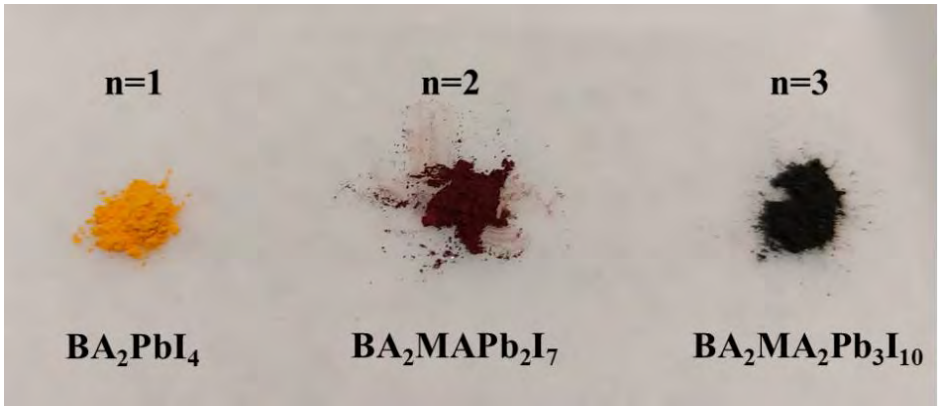

Figure 2.2: Photographic images of obtained polycrystalline powders of $BA_2MA_{n-1}Pb_nI_{3n+1}$ series.

Mechanosynthesis of $PEA_2MA_{n-1}Pb_nI_{3n+1}$ series

For the 2D perovskite materials with n=1, the precursors PEAI and PbI_2 were carefully weighed in the molar ratio of 2:1 and grinded together at an optimized frequency of 30 Hz for 30 min in the shaker mill. Similarly, the stoichiometric ratios of the precursors PEAI, MAI and PbI_2 (2:1:2 and 2:2:3 for materials with n=2 & 3 respectively) were taken in separate containers and grinded for 30 min at 30 Hz. The images of obtained polycrystalline powders for BA_2PbI_4, $PEA_2MAPb_2I_7$ and $PEA_2MA_2Pb_3I_{10}$ are shown in Fig 2.3. For getting better crystallinity of the products, the grinding time was increased to 60 min and 75 min. Furthermore, these powders were further annealed at 80 ºC for 3-4 h in the oven and aged for few days in the glove box.

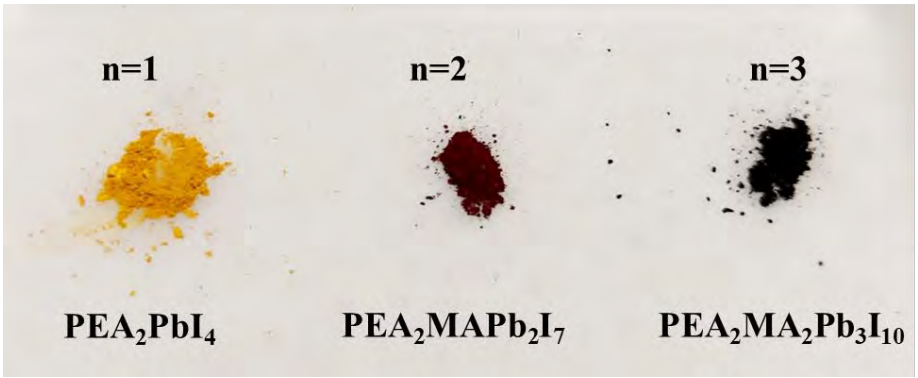

Figure 2.3: Photographic images of obtained polycrystalline powders of $PEA_2MA_{n-1}Pb_nI_{3n+1}$ series.

Mechanosynthesis of (c-Gua)$_2$MA$_{n-1}$Pb$_n$I$_{3n+1}$ series

The precursors c-GuaI, MAI and PbI_2 were precisely measured in the molar ratio of 2:0:1 (for n=1), 2:1:2 (for n=2) and 2:2:3 (for n=3) in separate agate jars. The grinding was performed in the at 30 Hz for 30, 60 and 75 min for each material. Further, the obtained powders were annealed at 80^o C for 60 min up to 3-4 h in the oven.

2.1.2 Inverse temperature crystallization method for the synthesis of perovskite single crystals

The inverse temperature crystallization (ITC) is an efficient procedure which is very fast as compared to other crystallization methods. In this technique, the precursors are dissolved in an appropriate solvent and heated at high temperatures. The solvent is chosen in such a way that the solubility of compound is high up to certain temperatures and it decreases with increasing temperature. Due to this property of inverse solubility, after heating at high temperatures, the precursor solution becomes saturated and small seed crystals are formed. In the next step, this solution is heated at lower temperatures, allowing the seed crystals to grow bigger. The schematic representation of this process is shown in Fig. 2.4 .

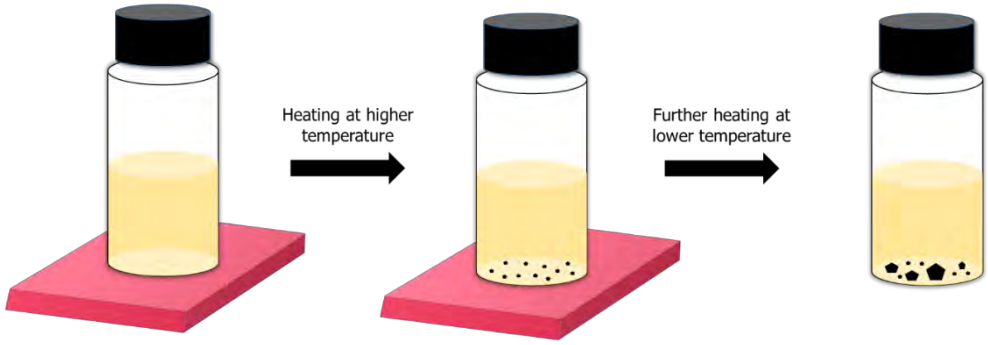

Fig. 2.4: Schematic of formation of crystals in the ITC method.

Materials

All precursors were obtained from commercial sources and used without any further purification. PbI_2, MAI (methylammonium iodide), GuaI (guanidinium iodide) and γ-butyrolactone (GBL) were purchased from TCI.

Synthesis of $MAPbI_3$ single crystals

The single crystals of $MAPbI_3$ were grown by using a 1.0 M $MAPbI_3$ solution in GBL. The solution was prepared by dissolving equimolar quantities of MAI and PbI_2 in GBL and it was kept on a hot plate at 60 °C overnight. Before crystallization, the precursor solution was filtered using a polytetrafluoroethylene (PTFE) filter with a pore size of 0.2 μm. Subsequently, 2 mL of this filtered solution was heated at 160°C for 30 min in an oil bath. This initial heating at high temperature resulted in the growth of very small seed crystals. Further, the seed crystal solution was heated at a lower temperature of 120°C for 3 h, allowing the crystals to grow in size. Finally, the remaining solution was discarded and the crystals were washed with acetone 2−3 times to remove any remaining solution present of the surface and then dried.

Synthesis of $Gua_xMA_{1-x}PbI_3$ single crystals

As in the case of synthesis procedure of $MAPbI_3$ single crystals, 1M perovskite solutions containing precursors PbI_2, MAI and GuaI in a molar ratio of 1:0.8:0.2 was prepared in GBL in separate glass vials and kept at 60 °C overnight. Before crystallization, the precursor solutions were filtered using a PTFE filter with a pore size of 0.2 μm. Subsequently, 2 mL of this filtered solution was heated at 160 °C for 30 min in an oil bath. This initial heating at high temperature resulted in the growth of very small seed crystals. Further, the seed crystal solution was heated at a lower temperature of 120°C for 3 h, allowing the crystals to grow in size. Finally, the remaining solution was discarded and the crystals were washed with acetone 2−3 times to remove any remaining solution present of the surface and then dried. Attempts to obtain crystals from the solutions containing precursors PbI_2, MAI and GuaI in a molar ratio of 1:0.7:0.3 and 1:0.6:0.4 were also made, however, no crystals could be formed.

2.1.3 Solar cell device fabrication

2.1.3.1 Methods used for thin film deposition

2.1.3.1.1 Spray pyrolysis

Spray pyrolysis is an inexpensive and simple process for deposition of thin films. In this technique, the reactants dissolved in a solvent are sprayed on a heated substrate and the final product is formed on the substrate. The reactants and solvents are selected in such a way that

the undesired by-products and the solvent is evaporated at the temperature of deposition [186]. The schematic diagram of this technique is shown in Fig. 2.5. In a simplistic arrangement, the precursor solution is poured into a container which is connected to the spray gun with the help of a pump or the spray gun is directly dipped inside the container. The spray set-up is also connected to a supply of compressed gas with a regulator to control the pressure. When this gas is released into the spray gun at a controlled pressure, the solution is forced to reach the nozzle and spray starts in the form of small droplets of solution. The substrate, which is heated at a desired temperature on the hotplate, is kept directly below the nozzle. After the droplets reach the hot substrate surface, they undergo endothermic decomposition. The thermal energy provided by the substrate aids in the initial decomposition and subsequent recombination of the constituents. Further sintering at high temperatures leads to the crystallization of constituent species and finally a smooth film.

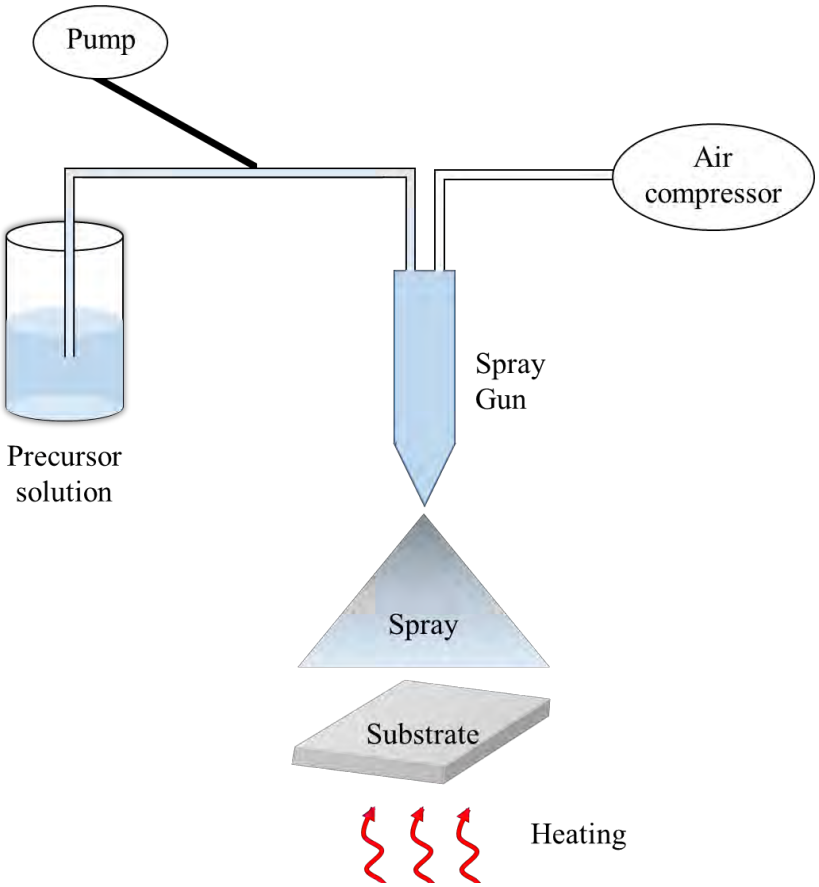

Fig 2.5: Components and working of spray pyrolysis technique.

The size of droplets depends on shape of nozzle as well as the pressure of the compressed gas. Final thickness of the deposited film is influenced by the distance and angle between the spray nozzle and substrate, concentration and amount of solution used and substrate temperature. Additionally, the quality of film depends on the ratio of reactants, carrier gas, size of droplets, substrate temperature, ambient atmosphere and lastly on the cooling rate after deposition.

2.1.3.1.2 Spin-coating

Spin-coating is another very simple and widely used technique for the deposition of thin films on the desired substrate. Usually, the substrate is carefully mounted on the centre of substrate holder, which holds it tightly with the help of vacuum. The compound is first dissolved in a suitable solvent and then dropped on the substrate, which is further rotated at high speed. Due to the centripetal force and surface tension of the solvent, the solution is forced to spread as a uniform layer on top of the substrate. This spin-coating process can be divided into 4 steps (Fig. 2.6)

1) Deposition – This is the first step where solution is dropped on the surface of substrate. The deposition can be done on the substrate either when it is static or rotating.
2) Spin-up – After the substrate reaches its maximum speed, most of the solution is thrown away from the surface due to the centrifugal forces.
3) Spin-off – In this step, the thickness of solution on the surface begins to thin due to the viscous forces of the solvent.
4) Evaporation – In the last step, the ejection of liquid stops and the layer starts to form by the evaporation of solvent. The rate of evaporation relies on the vapour pressure and volatility of solvent used.

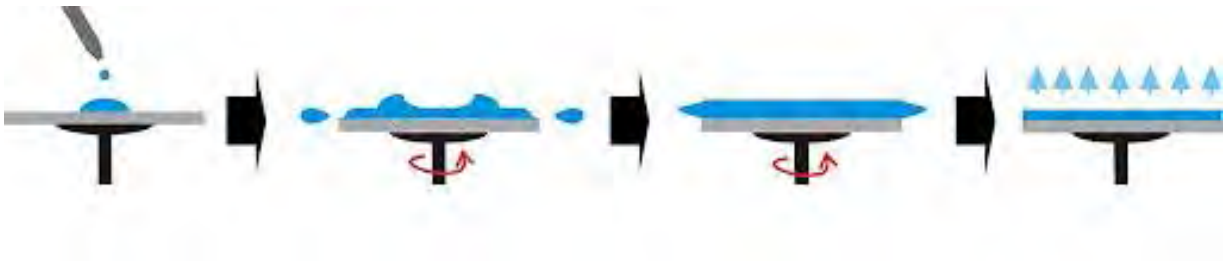

Fig 2.6: Different steps in the spin-coating technique (adapted from [187]).

Multi-layered films can also be deposited by repeating the above steps for desired number of times. Generally, the thickness of films deposited by the spin-coating technique is inversely proportional to the angular velocity and given by the equation

$$t = \frac{1}{\sqrt{\omega}}$$

Where t is the final thickness of the film and ω is the angular velocity of the spin coater. In addition to the spinning speed, the thickness also depends on the concentration of the solution and the properties of solvents.

2.1.3.1.3 Thermal evaporation

Thermal evaporation is a solid state method used for the deposition of thin films and coatings by vaporizing a target material, transporting it in vacuum, and condensing it on a substrate. A typical thermal evaporator has several components as illustrated in the schematics in Fig. 2.7. The pumping line is used to evacuate vacuum chamber to pressures of the order of 10^{-6} Torr. The vacuum gauge measures the pressure inside the chamber. A metal boat keeps the target material, which needs to be deposited. When electric current is passed through the boat, it starts heating up and when the required temperature is reached, the target materials starts evaporating. The desired substrate is placed on the holder, directly above the metal boat. The holder is built in such a way that, it can rotate or tilt along the vertical axis depending upon the requirements of deposition. These options help to avoid undesirable shadows. A thickness monitor based on a quartz crystal microbalance (QCM), which is present close to the substrate controls the thickness of the evaporated film by measuring the variation of deposited mass on the surface of a quartz crystal resonator. The crystal should be kept at a constant temperature for high

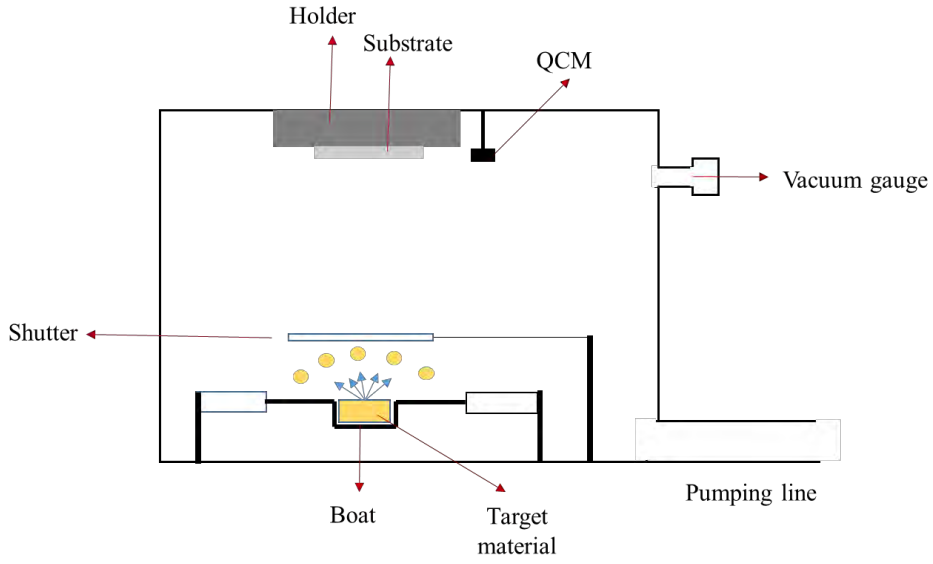

Fig 2.7: Schematic illustration of different components of a thermal evaporator set-up.

accuracy measurements. The shutter is closed until the desired boat temperature is reached and material vaporization begins. It is again closed when the evaporation process finishes. Thus mainly two factors control the evaporation process: current through the boat and the shutter position.

2.1.3.2 Device fabrication of $Cs_xFA_{1-x}PbI_3$-based mesoporous perovskite solar cells

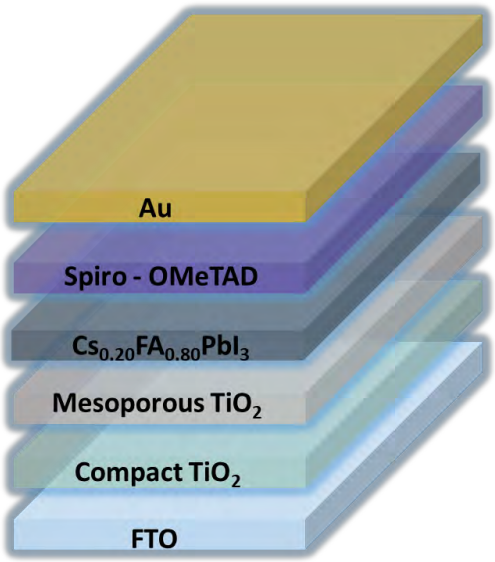

Fig 2.8: Schematic illustration for the device architecture of mesoporous PSC with $Cs_xFA_{1-x}PbI_3$-based perovskite layer.

Materials

FAI and MABr were purchased from dyesol; PbI_2, $PbBr_2$, 1- adamantylamine, and guanidinium iodide were purchased from TCI; CsI/CsCl salts were purchased from abcr GmbH; titanium diisopropoxide bis(acetylacetonate) (75 wt % in isopropanol), lithium bis(trifluoro methanesulfonyl)imide (Li-TFSI), and 4-tert-butylpyridine were received from Sigma-Aldrich; chlorobenzene (99.8%), isopropyl alcohol (IPA, 99.8%), dimethyl sulfoxide (DMSO, 99.8%), N,N-dimethylformamide (DMF, 99.7%), and acetonitrile (99.9%) were purchased from Arcos Organics.

Etching and cleaning of FTO coated glass substrates

Chemical etching of FTO substrates (10Ω sq^{-1} Nippon sheet glass) with the desired pattern was carried out with zinc power and HCl solution (concentrated HCl:water=1:5 v/v). Further, etched FTO substrates were first cleaned with 2% Hellmanex solution in deionized (DI) water, followed by acetone and ethanol. The substrates were kept in each solution for sonication for 15-20 min. Finally, after cleaning with ethanol, the substrates were dried by air gun. Before the deposition of next layer, substrates were UV-ozone treated for 15 min.

Solution preparation of TiO_2 and deposition of respective compact layer

After the substrates were etched and cleaned, the compact layer was deposited by spray coating of a TiO_2 solution at 450 °C in air. The solution was prepared by mixing 9 ml of ethanol solution with 0.6 mL of titanium diisopropoxide bis-(acetylacetonate) solution (75% in 2-propanol, Sigma-Aldrich) and 0.4 mL of acetylacetone. After cooling down the substrates, they were again UV-ozone treated for 15 min.

Solution preparation of TiO_2 and deposition of respective mesoporous layer

A thick mesoporous layer of TiO_2 was deposited on top of the compact TiO_2 electron transport layer by spin-coating. The 30 nm-sized nanoparticles (Dyesol 30NRD, Dyesol) were diluted in ethanol (1:6 wt/wt) and deposited by spin-coating at 5000 rpm for 10 s. Then, the films were gradually heated to 500 °C and sintered at that temperature for 1.5 h under oxygen atmosphere. The substrate was cooled and kept for UV-ozone treatment for 15 min before transferring to glove box for the deposition of perovskite layer.

Solution preparation of $Cs_{0.20}FA_{0.80}PbI_3$ and deposition of respective layer

The perovskite solutions were prepared in 1 mL of anhydrous DMF/DMSO (4:1; v/v) solvent mixture. For reference perovskite $Cs_{0.20}FA_{0.80}PbI_3$, PbI_2 (1 mmol; 0.461 g), FAI (0.80 mmol, 0.137 g), and CsI (0.2 mmol, 0.051 g) was dissolved in the solvent by vigorous stirring at 60 °C for ≈12 h till the cloudy solution yields to a transparent yellow solution. The 1M stock solution of $Cs_{0.20}FA_{0.80}PbI_3$ by our modified method was prepared by dissolving PbI_2 (1 mol; 0.461 g), FAI (1 mmol, 0.172 g), and CsCl (0.2 mmol,0.033 g) in 1 ml of anhydrous DMF/DMSO (4:1; v/v) at 60 °C for ≈12 h till the cloudy solution yields to a transparent yellow solution. Afterwards, the perovskite solutions were spin-coated by a one-step spin-coating program with two steps at 1000 rpm for 10 s and 6000 rpm for 20 s. In the second step, 100 μL of chlorobenzene (CB) was dropped on top of the spinning film 10 s prior to the end of the

program. After deposition, the film was annealed at 150 °C for 30 min in a dry box under controlled atmospheric conditions.

Solution preparation and deposition of respective passivation layer

The passivation solutions of ADA (1- adamantylamine) were prepared by dissolving 1, 3 and 5 mg of ADA in 1 mL of isopropyl alcohol (IPA) in separate glass vials. Similarly GuaI (guanidinium iodide) solutions in IPA were prepared with concentration of 3, 5 and 10 mg/mL. These solutions were deposited on top of perovskite layer by spin-coating at 5000 rpm for 30 s followed by annealing at 100 °C for 10 min.

Solution preparation of spiro-OMeTAD and deposition of respective layer

The hole transporting material (HTM) solution was prepared by dissolving 90 mg spiro-OMeTAD, 20.6 μL of Li-TFSI (stock solution of Li-TFSI 520 mg/mL in acetonitrile) and 35.6 μL tert-butylpyridine in 1 mL of chlorobenzene. This solution was spin-coated at 4000 rpm for 20 s.

Deposition of Au layer

The final layer of gold as a thin top electrode (~80 nm) was deposited by thermal evaporation under high vacuum using a Leica thermal evaporator.

2.1.3.3 Device fabrication of $FA_{0.97}MA_{0.03}Pb(I_{0.97}Br_{0.03})_3$-based planar perovskite solar cells

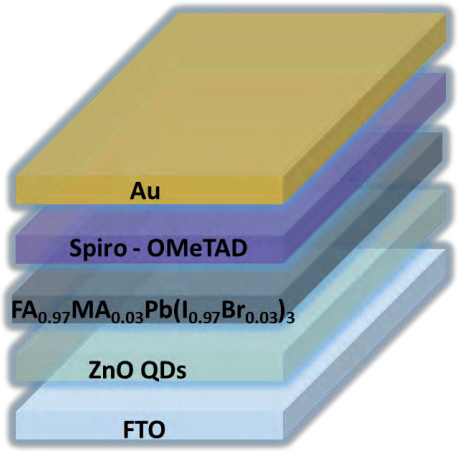

Fig 2.9: Schematic illustration for the device architecture of planar PSC with ZnO QDs-based electron transporting layer.

Materials

FAI, MAI, and MABr were purchased from dyesol; PbI_2 and $PbBr_2$ were purchased from TCI; titanium diisopropoxide bis(acetylacetonate) (75 wt % in isopropanol), lithium bis(trifluoro methanesulfonyl)imide (Li-TFSI), and 4-tert-butylpyridine were received from Sigma-Aldrich; chlorobenzene (99.8%), isopropyl alcohol (IPA, 99.8%), dimethyl sulfoxide (DMSO, 99.8%), N,N-dimethylformamide (DMF, 99.7%), and acetonitrile (99.9%) were purchased from Arcos Organics. Novel zwitterion coated ZnO quantum dots (QDs) were synthesized according to the newly developed procedure by PhD student Zygmunt Drużyński from the Lewiński group at Warsaw University of Technology.

Etching and Cleaning of FTO coated glass substrates

As explained in the previous section, chemical etching of FTO substrates (10Ω sq^{-1} Nippon sheet glass) with the desired pattern was carried out with zinc power and HCl solution (concentrated HCl:water=1:5 v/v). Further, etched FTO substrates were first cleaned with 2% Hellmanex solution in deionized (DI) water, followed by acetone and ethanol. The substrates were kept in each solution for sonication for 15-20 min. Finally, after cleaning with ethanol, the substrates were dried by air gun. Before the deposition of next layer, substrates were UV-ozone treated for 15 min.

Solution preparation of ZnO QDs and deposition of respective layer

A colloidal solution of ZnO QDs was prepared by dissolution of a microcrystalline ZnO powder (5 mg) powder was dissolved in 1 mL of ethanol. Sonicating this solution for 25-30 min and then filtering with a PTFE filter of pore size 0.45 μm resulted in a clear solution. Next the resulting colloidal solution was deposited on top of FTO substrates by spin-coating at 3000 rpm for 20 s followed by annealing at 150 ^oC for 1 hour in air. Multiple layers of ZnO were also deposited with the same deposition parameters and an intermediate annealing was done at 150 ^oC for 10 min before the deposition of the next layer. Finally, these multilayer films were again heated at 150 ^oC for 1 hour in air.

Solution preparation of NH_4X and deposition of respective passivation layer

The solutions of ammonium halides (NH_4F, NH_4Cl and NH_4Br) with concentrations of 1, 3 and 5 mg/mL were prepared in two ways. First, different amounts of ammonium halides were dissolved in the 5 mg/mL ZnO solution in ethanol. For example, 1 mg of NH_4F was dissolved by sonication in the 5 mg/mL ZnO solution to get a mixed solution. Similarly, 3 and 5 mg of

NH_4F and 1, 3, and 5 mg of NH_4Cl and NH_4Br were mixed with ZnO solution in separate containers in order to get different solution concentrations. Subsequently, these solutions were filtered with a PTFE filter of pore size 0.45 μm and deposited on top of FTO substrates by spin-coating at 3000 rpm for 20 s followed by annealing at 150 ºC for 1 hour in air. In the second strategy, the ammonium halide solutions were prepared separately by dissolving them in the deionized water. In this case, again three concentrations of 1 mg/mL, 3 mg/mL and 5 mg/mL for each NH_4F, NH_4Cl and NH_4Br were prepared by dissolving appropriate amounts in 1 mL of deionized water. The powders dissolved completely in the DI water immediately without the need of sonication. These solutions were further filtered with a PTFE filter of pore size 0.45 μm before deposition. The solution was spin coated on top of ZnO layer at 5000 rpm for 20s and subsequently annealed at 150 ºC for 30 min.

Solution preparation of $FA_{0.97}MA_{0.03}Pb(I_{0.97}Br_{0.03})_3$ and deposition of the respective layer

The perovskite films were deposited from the precursor solution using a single-step deposition method. The precursor solution was prepared in the Argon atmosphere with a concentration of 1.45 M containing FAI, MABr, PbI_2, and $PbBr_2$ in anhydrous DMF/DMSO (4:1; v/v) to achieve the desired composition: $FA_{0.97}MA_{0.03}Pb(I_{0.97}Br_{0.03})_3$ (3% PbI_2 excess). 0.1 M of MAI+I_2 was prepared by dissolving in IPA and stirred at 70°C. Then, 5 mM of this mixture was added to the perovskite composition as reported [188]. The perovskite solution was deposited on by a one-step spin-coating program with two steps at 1000 rpm for 10 s and 5000 rpm for 30 s, respectively. In the second step, 270 μl of chlorobenzene was dropped on the spinning substrate. This was followed by annealing the films at 150 °C for 35 to 40 min. All the devices were fabricated inside a dry air box, under controlled atmospheric conditions

Solution preparation of EAI and deposition of respective passivation layer

After the substrate with deposited perovskite layer was cooled down to room temperature, all the films were surface passivated by ethylammonium iodide (EAI) (3 mg mL^{-1} in IPA), The EAI solution was spin coated at 6000 rpm for 30 s followed by the annealing at 70 °C for 10-15 min.

Solution preparation of spiro-OMeTAD and deposition of respective layer

The HTM solution was prepared by dissolving 90 mg spiro-OMeTAD, 23.2 μL of Li-TFSI (stock solution of Li-TFSI 520 mg/mL in acetonitrile) and 36 μL of tert-butylpyridine in 1 mL of chlorobenzene. This solution was spin-coated at 5000 rpm for 30 s.

Deposition of Au layer

The final layer of gold as a thin top electrode (~80 nm) was deposited by thermal evaporation under high vacuum using Leica thermal evaporator.

2.2 Characterization techniques

2.2.1 X-Ray Diffraction

Characterization of mechanochemically synthesized 2D perovskite powders

Diffraction pattern of perovskite powder was recorded with an Empyrean diffractometer (PANalytical) equipped with a copper lamp (40 kV, 40 mA) and a secondary graphite (002) monochromator. For the measurements, Ni-filtered Cu Kα (λ = 0.154 nm) radiation was used and was detected with an X'Celerator 1D detector in the Bragg−Brentano θ−θ geometry. The measurement was carried out in the 2θ angle range of 3° to 30° without rotating the sample using a low background Si sample holder.

Temperature dependent characterization of powdered single crystals of $MAPbI_3$

Temperature-dependent diffraction patterns of powdered single crystals were recorded with an Empyrean diffractometer (PANalytical) equipped with a copper lamp (40 kV, 40 mA). The samples were mounted inside the Anton Paar TTK-450 sample chamber for nonambient X-ray diffraction experiments. For the measurements, Ni-filtered Cu Kα (λ = 0.154 nm) radiation was used and was detected with an X'Celerator 1D detector in the Bragg−Brentano θ−θ geometry. The XRD patterns were recorded over a 2θ range of 10−50° without rotating the sample using a low background Si sample holder.

Characterization of powdered single crystals of $Gua_xMA_{1-x}PbI_3$

Diffraction pattern of powdered single crystals was recorded with an Empyrean diffractometer (PANalytical) equipped with a copper lamp (40 kV, 40 mA) and a secondary graphite (002) monochromator. For the measurements, Ni-filtered Cu Kα (λ = 0.154 nm) radiation was used and was detected with an X'Celerator 1D detector in the Bragg−Brentano θ−θ geometry. The measurement for finely ground crystals was carried out in the 2θ angle range of 10° to 30° without rotating the sample using a low background Si sample holder.

Characterization of thin films of $Cs_{0.20}FA_{0.80}PbI_3$ and $FA_{0.97}MA_{0.03}Pb(I_{0.97}Br_{0.03})_3$

Diffraction pattern of perovskite thin film was recorded by an X'Pert MPD PRO (PANalytical) diffractometer containing a Cu anode (λ = 1.54060 Å), an RTMS X'celerator (Panalytical) and a secondary graphite (002).The samples were measured in the 2θ angle range of 5° to 40° without rotating the sample.

2.2.2 UV-Vis spectroscopy

Characterization of mechanochemically synthesized 2D perovskite powders

Optical absorption (UV-Vis) spectra for mechanochemically synthesized perovskite were recorded on a Hitachi U-2910 spectrophotometer.

Characterization of powdered single crystals of $MAPbI_3$ and $Gua_xMA_{1-x}PbI_3$

Optical absorption (UV-Vis) spectra for ground perovskite crystals were recorded on a Hitachi U-2910 spectrophotometer.

Characterization of thin films of $Cs_{0.20}FA_{0.80}PbI_3$

Optical absorption (UV-Vis) spectra for perovskite films were recorded by a Varian Cary 5 spectrophotometer.

2.2.3 Steady-state photoluminescence

Characterization of $Cs_{0.20}FA_{0.80}PbI_3$ and $FA_{0.97}MA_{0.03}Pb(I_{0.97}Br_{0.03})_3$ thin films

Photoluminescence spectra of perovskite films were recorded with Fluorolog 322 (Horiba Jobin Ybon Ltd)

2.2.4 Time-resolved photoluminescence

Characterization of $Cs_{0.20}FA_{0.80}PbI_3$ thin films

Time resolved photoluminescence (TRPL) spectra of $Cs_xFA_{1-x}PbI_3$ were obtained with a picosecond pulsed diode laser EPL-405 with an excitation wavelength of 405 nm and pulse

width of 49 ps. For fitting, a biexponential equation was employed and the lifetime was determined using the following equation: $\tau_{avr} = \tau_1 * \tau_2 / (\tau_1 + \tau_2)$

Characterization of $FA_{0.97}MA_{0.03}Pb(I_{0.97}Br_{0.03})_3$ thin films

Time resolved photoluminescence (TRPL) spectra were obtained via time-correlated single-photon counting (TCSPC) using a LifeSpec II (Edinburgh Instruments) fluorescence spectrometer with a picosecond pulsed diode laser (EPL-510, Edinburgh Instruments) with an excitation wavelength of 510 nm and pulse width of 85 ps. For fitting, a monoexponential equation was employed and the lifetime was determined using the following equation: $\tau_{carrier} = 2\tau_{decay}$

2.2.5 Nuclear Magnetic Resonance

Characterization of mechanochemically synthesized 2D perovskite powders

Solid−state MAS NMR spectra of ^{1}H (700.1), ^{13}C (176.0 MHz) and ^{2}H (107.5 MHz) were recorded on a Bruker Avance III 16.4 T spectrometer equipped with 4 mm CPMAS probe. The recycle delays in 1H-13C cross-polarization (CP) experiments were set based on the measured ^{1}H T_1 values and were between 3 and 5 s. MAS spin rate of 12 kHz was used and ^{1}H decoupling (80 kHz) was applied during acquisition. ^{2}H spectra were recorded at 4 kHz MAS using a Bloch decay pulse sequence and a recycle delays of 0.06 s (PEA_2PbI_4) 0.5 s (BA_2PbI_4), 2 s (BAI-d_3, PEAI-d_3) and 12 s (MAI-d_3). The spectra were processed with MestReNova software.

Characterization of single crystals of $Gua_xMA_{1-x}PbI_3$

The liquid state ^{1}H NMR spectra were collected at 298 K using a Bruker 600 AVANAC III spectrometer and processed with MestReNova software.

2.2.6 Scanning electron microscopy

Characterization of $Cs_{0.20}FA_{0.80}PbI_3$ and $FA_{0.97}MA_{0.03}Pb(I_{0.97}Br_{0.03})_3$ thin films

The morphology and cross-section of perovskite films were studied by high-resolution Zeiss Merlin SEM.

2.2.7 Atomic force microscopy

Characterization of $Cs_{0.20}FA_{0.80}PbI_3$ thin films

The morphology and surface roughness of perovskite films was studied by NanoScope IIIa/Dimension 3100 AFM.

2.2.8 Ultraviolet spectroscopy

Characterization of $Cs_{0.20}FA_{0.80}PbI_3$, $FA_{0.97}MA_{0.03}Pb(I_{0.97}Br_{0.03})_3$ and ZnO QD thin films

The valence and Fermi levels of respective films were recorded by using an ultraviolet photoelectron spectrometer (AXIS NOVA, Kratos Analytical Ltd, UK) with He I (21.2 eV) as the photon source.

2.2.9 J-V characterization

Characterization of $Cs_{0.20}FA_{0.80}PbI_3$ and $FA_{0.97}MA_{0.03}Pb(I_{0.97}Br_{0.03})_3$-based solar cells

The J-V curves for solar cells were recorded using a Keithley (model 2400) digital source meter. A 450 W xenon lamp (Oriel) with a Schott K113 Tempax sunlight filter (Praezisions Glas & Optik GmbH) was used to match the emission spectra to the AM1.5G standard in the 350-750 nm region. A dark coloured metal mask was used to mask the devices for J-V measurements, resulting in an active area of 0.16 cm^2 (for mesoscopic devices) and 0.158 cm^2 (for planar devices). The light intensity was ranging between 0.98 to 1 Sun.

2.2.10 IPCE measurements

Characterization of $Cs_{0.20}FA_{0.80}PbI_3$-based solar cells

Incident photoelectron conversion efficiency (IPCE) measurements were performed using a LED light source (Ariadne EQE from Cicci Research)

Characterization of $FA_{0.97}MA_{0.03}Pb(I_{0.97}Br_{0.03})_3$-based solar cells

The IPCE was measured with a steady white light bias of around 5 mW cm^{-2} provided by a white light-emitting diode array. The excitation beam was focussed using a Gemini-180 double

monochromator (Jobin Yvon Ltd) and chopped at about 2 Hz using a 300 W Xenon lamp (ILC Technology). A Model SR830 DSP Lock-In Amplifier (Stanford Research Systems) was used to record the signal.

2.2.11 Operational stability measurements

Characterization of $Cs_{0.20}FA_{0.}80PbI3$-based solar cells

The shelf life was recorded for 7 days by keeping the devices in a dry air box with a relative humidity of 30% and monitoring every 24 hours in the backward scan direction (10 mV as the step voltage).

Characterization of $FA_{0.97}MA_{0.03}Pb(I_{0.97}Br_{0.03})_3$-based solar cells

The Biologic MPG2 potentiostat was used to assess stability under a full AM 1.5 Sun-equivalent white LED bulb. Under continuous illumination at room temperature, the devices were tested using a maximum power point (MPP) tracking technique. A typical perturb and observe strategy was used to update the MPP every 10 seconds. A J-V curve was captured every minute in order to trace the change of specific JV parameters.

Chapter 3: Synthesis and characterization of lead based halide perovskite materials

Part A- Mechanosynthesis and characterization of lead based 2D Ruddlesden-popper perovskites

3.1 Introduction

The 2D Ruddlesden-popper layered perovskites have a general formula of $A'_2A''_{n-1}B_nX_{3n+1}$, where A' is a large organic cation (aromatic or aliphatic alkyl ammonium cation), A'' is a monovalent cation (Cs^+, $CH_3NH_3^+$, or $CH(NH_2)_2^+$), B is the divalent metal cation (Pb^{2+}, Sn^{2+}) and X is the halide anion (Cl^-, Br^- or I^-), and integer n denotes the number of inorganic layers separated by the A' cation. Remarkably, these 2D perovskites are more resistant towards degradation from moisture as compared to their 3D analogues. Reason behind this stability lays in the hydrophobic nature of the spacer A' cations. Additionally, they are more structurally stable and resistant to the degradation caused by light [90]. The 2D perovskites based on lead as the B-site cation, methylammonium as the monovalent cation and iodide as the halide anion have attracted significant attentions due to their unique and efficient performance in solar cells [91,92]. Additionally, the most utilized spacer cations are n-butylammonium (C_4NH_{11}) and 2-phenylethylammonium ($C_{18}N_8H_{36}$). However, the synthesis of 2D perovskites based on these cations has only been restricted to the solution based and vapor deposition methods [92,93], which present several disadvantages. The solution processing techniques often utilize solvents which are not environment friendly as well as provide inherent impurities from the solvents and vapor deposition methods increase the cost of production. Therefore, there is a continuous need for the development of new efficient methods for the preparation of these perovskite materials. While mechanochemistry has become one of the common procedures for synthesizing 3D perovskites due to its simple and environment friendly process, the mechanosynthesis of 2D perovskites is still in an embryonic stage.

In this work, a solvent-free mechanochemical method was used for the synthesis of lead based 2D Ruddlesden-popper layered perovskites with the general formula of $A'_2MA_{n-1}Pb_nI_{3n+1}$.

Three different spacer cations were investigated for the synthesis namely, n-butylammonium (BA), 2-phenylethylammonium (PEA), and 2H-pyrimido[1,2-a]pyrimidine-1,3,4,6,7,8-hexahydro-hydroiodide as a cyclic guanidinium (c-Gua). The resulting microcrystalline powders of these materials were further characterized by powder X-Ray diffraction (PXRD), UV-Vis absorption spectroscopy, and solid state Nuclear magnetic resonance (NMR) spectroscopy. The XRD analysis revealed that among the three spacer cations, BA and PEA cations successfully produced 2D layered perovskites with n=1, 2, and 3, while c-Gua produced non-perovskite structures. The UV-Vis spectra confirmed the decrease in bandgap of the layered materials with increasing value of n. Purity and local molecular structure of the layered materials were also established by the ^{1}H and ^{13}C solid state NMR spectra.

3.2 Results and discussions

3.2.1 Selection of spacer cations for 2D Ruddlesden-popper layered perovskites

As discussed in Chapter 1 (Section 1.6.3), when a large organic spacer cation is incorporated into the 3D perovskite structure, the crystal lattice is transformed into inorganic layers of corner sharing BX_6 octahedra separated by the spacer cations. Usually, these layers are oriented along the (100), (110), and (111) planes of 3D crystals. It can be visualized as the slicing along one of these crystallographic planes to form a 2D sheet like structure. This leads to the formation of a 2D quantum-well nanostructure as the inorganic and organic layers are arranged in alternating fashion. Due to this quantum confinement, the 2D layered perovskites exhibit higher bandgap values as compared to their 3D counterparts [189,190]. For the work included in this thesis, three different types of organic moieties were investigated as the spacer cations – linear, aromatic, and cyclic. The molecular structures of these cations are presented in Fig. 3.1. All these molecules have ammonium cation with a linear carbon chain in BA, aromatic carbon chain in PEA and a cyclic chain in c-Gua.

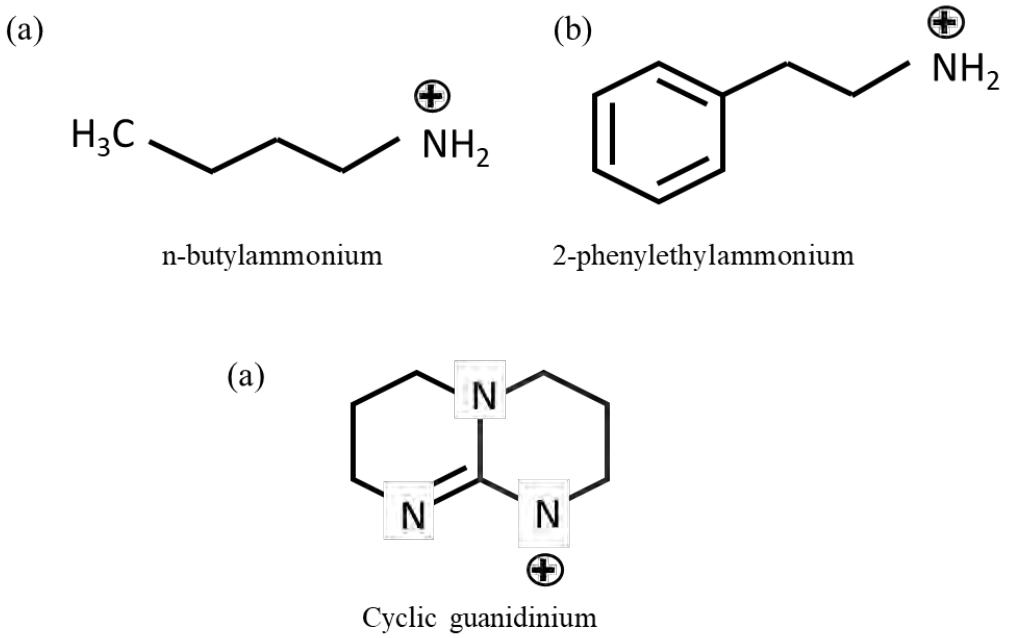

Fig. 3.1: Molecular structure of the investigated spacer cations.

3.2.2 2D layered perovskites with n-butylammonium as the spacer cation

The synthesis of $BA_2MA_{n-1}Pb_nI_{3n+1}$ for n=1 Ruddlesden-Popper structure was carried out as described in the experimental section of Chapter 2. The precursors BAI and PbI_2 were grinded together in the appropriate ratios for 30 min at a shaking speed of 30 Hz. The final product was obtained in the form of an orange colored uniform microcrystalline powder (Fig. 2.2). Further, the sample was analyzed by PXRD in order to study the crystal structure of the resulting materials. One of the important characteristics of 2D perovskites is the presence of low angle diffraction peaks (i.e., (0k0) reflections) as reported for the materials synthesized by a solution processing technique [191]. The peak at 6.4° for the crystallographic plane corresponding to (002) plane was observed, revealing the formation of BA_2PbI_4 phase (orange curve in Fig. 3.2). Other characteristic peaks were also observed from the diffraction planes (004), (006), and (008) at 2θ angles of 12.8°, 19.3° and 25.8° respectively. Generally, 2D perovskites with n=1 preferentially grow along the (110) direction, and hence, display the reflection peaks of the planes corresponding to (00l), which is parallel to the substrate [87]. Moreover, the absence of peak around 12° showed that there was no PbI_2 present in the sample, indicating the high purity of final product.

For the synthesis of next 2D perovskite of the series with n=2 ($BA_2MAPb_2I_7$), initially two separate batches of the precursors, BAI and PbI_2 (molar ratio 2:1) as well as MAI and PbI_2 (molar ratio 1:1), were independently grinded at 30 Hz for 30 min to form BA_2PbI_4 and $MAPbI_3$ materials. Next, these powders were mixed together in a ratio 1:1 in order to get the product with correct stoichiometry and grinded for another 30 min at 30 Hz. However, this 2-step grinding method resulted into a product with very low crystallinity with broad PXRD peaks. Besides, the characteristic peak for the expected n=2 layered perovskite was also not observed below 10°. Therefore, for the next control experiment, another approach was followed where the precursors BAI, MAI, and PbI_2 in the ratio 2:1:2 were grinded together in the same jar and subsequently annealed (for details see the experimental section of Chapter 2). In this case, the resulting material was uniform and dark maroon in color (Fig. 2.2). The PXRD data revealed the characteristic low angle peaks at diffraction angles of 4.5° and 9° corresponding to (020) and (040) planes for the expected n=2 layered perovskite material with formula $BA_2MAPb_2I_7$ (maroon curve in Fig. 3.2). Interestingly, when the MA cation is added into the system, it tries to promote the growth of crystal out of the planar layers whereas the BA cation ensures the confined growth within the layer. Therefore, in addition to the peaks from (0k0) planes, reflections from (111) and (202) are also observed in the PXRD pattern, which displays the

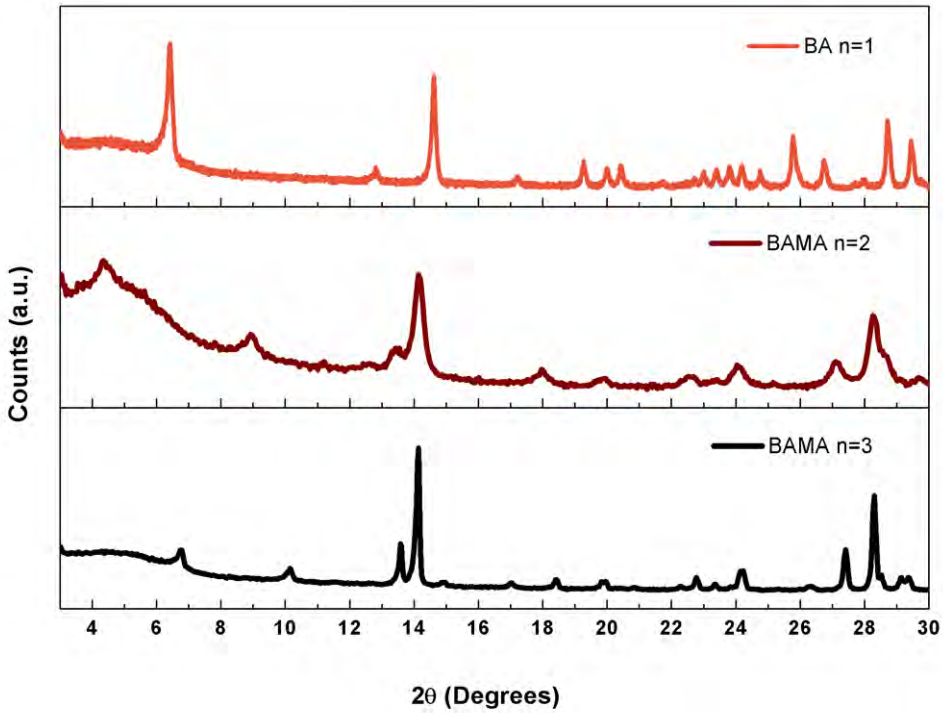

Fig. 3.2: PXRD pattern of synthesized 2D $BA_2MA_{n-1}Pb_nI_{3n+1}$ perovskite materials with spacer cation BA for n=1 (orange curve), n=2 (maroon curve) and n=3 (black curve).

vertical growth of the crystal lattice on the substrate [88]. In the synthesized mechanopowders, these peaks from (111) and (202) were seen at 14.3° and 28.4°, respectively. Additionally, characteristic reflections also appeared at diffraction angles of 13.5°, 18.1°, and 28.7° by the planes (060), (080), and (222). This shows that mechanochemical synthesis only results in the formation of desired products when precursors are grinded in a particular order.

With regard to the developed mechanochemical procedure for the n=2 layered perovskites, similar reaction conditions were used for the preparation of n=3 perovskites ($BA_2MA_2Pb_3I_{10}$). This mechanoperovskite material was synthesized by taking the precursors BAI, MAI and PbI_2 in a ratio of 2:2:3 and after the grinding was finished a uniform black multicrystalline powder was obtained (Fig. 2.2). Initially, the PXRD pattern of resulting powder showed that the formation of the expected 3 layered structure was not complete as some of the characteristic peaks were absent. The subsequent annealing of powders at 80 °C for 3-4 h also had no effect on the crystallinity of powder. It has been reported that in some mechanochemical reactions, after the mechanosynthesis, further ageing of compounds lead to the formation desired products [192]. Therefore, in order to check if aging had any effect on the material, they were kept inside the glove box. Finally, after aging the powder for a week and repeating the PXRD measurements, the characteristic peaks for layered perovskite systems with n =3 were visible. The reflections resulting from (040) and (060) planes appeared at 6.7° and 10.1° diffraction angles (black curve in Fig. 3.2). Due to the limitation of PXRD method, the peak for plane (020) below 3 ° could not be observed. It can be noted that the peak position corresponding to (040) plane shifts to lower angle from 9° to 6.7° when number of inorganic layers in the 2D structure changes from 2 to 3. This is directly related to the thickness of 2D inorganic layers, which increases with increasing value of n. Furthermore, the vertical growth of crystal is confirmed by the appearance of peaks at angles 14.1° and 28.3° for the planes (111) and (202).

Next, the optical properties of synthesized 2D $BA_2MA_{n-1}Pb_nI_{3n+1}$ perovskites were studied by the UV-Visible spectroscopy. The absorption of powdered materials was recorded in the region from 350 to 850 nm. As shown in Fig. 3.3, the absorption onset shifts to higher wavelength as the value of n increases. The absorption behavior of these samples with 2D Ruddlesden-Popper structure matched well with the observed colors, which changed from orange to black, indicating light absorption of perovskites at higher wavelength for larger n values. This bathochromic shift in the absorption band edge is attributed to the increase in number of inorganic layers in the 2D perovskite system. The optical bandgaps (E_g) were calculated from

the absorption onset giving values of 2.21 eV, 1.85 Ev, and 1.61 eV for the materials BA_2PbI_4, $BA_2MAPb_2I_7$, and $BA_2MA_2Pb_3I_{10}$, respectively. As the inorganic layer becomes thicker, the perovskite becomes more conducting and the band gap decreases. Additionally, a peak was observed in the lower wavelength region around 505 nm for BA_2PbI_4 sample due to the presence of excitonic state [193]. A local electrostatic field is created between the BA^+ ions and the negatively charged inorganic layer, which prevents the separation of photogenerated excitons. Hence, the binding energy decreases with increasing number of layers [194]. The excitonic peak was also observed for the $BA_2MAPb_2I_7$ material at ~566 nm but it almost vanishes in the case of $BA_2MA_2Pb_3I_{10}$ material. The disappearance of excitonic peak for $BA_2MA_2Pb_3I_{10}$ as a n=3 layered structure material can be explained by the weakening of electrostatic field with increasing thickness of inorganic layers which allows the dissociation of excitons.

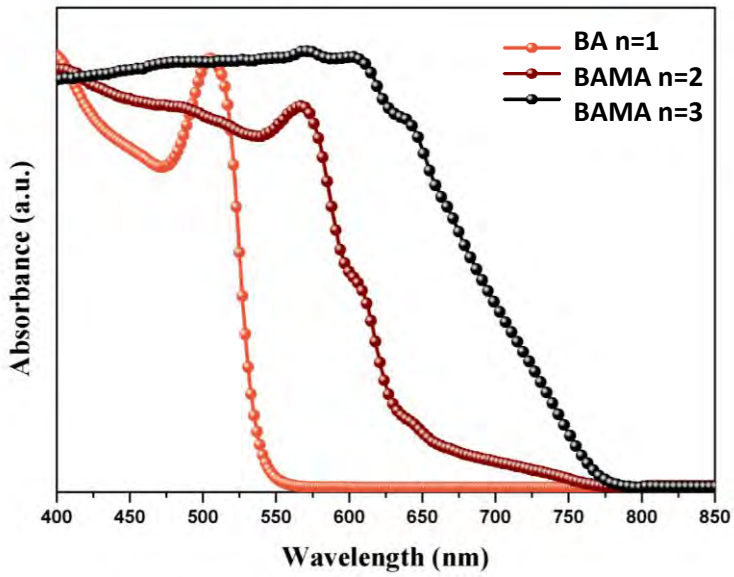

Fig. 3.3: Normalized UV-Vis spectra of the synthesized 2D $BA_2MA_{n-1}Pb_nI_{3n+1}$ perovskite materials with the cationic BA spacer for n=1 (orange curve), n=2 (maroon curve) and n=3 (black curve).

The local molecular structure of these 2D layered perovskites was analyzed by solid state nuclear NMR measurements. This powerful spectroscopic tool can provide information about the structure of spacer cation and inorganic layer inside the perovskite crystals. Therefore, to get deeper insights, the perovskite powders were sent to Dr. Dominik Kubicki in the group of Prof. Clare Grey at Cambridge University, United Kingdom for solid-state NMR

measurements. First, ^{1}H NMR spectra of perovskite powders, BA_2PbI_4, $BA_2MAPb_2I_7$, and $BA_2MA_2Pb_3I_{10}$ as n=1, 2, and 3 materials were recorded and they are presented in Fig. 3.4. The major signals for hydrogen atom of BA cation in case of the n=1 material were observed at 7.18, 3.59, and 1.20 ppm. Moreover, the signals for the hydrogen atoms at positions 1, 2, and 3 of the aliphatic chain (as marked in the molecular structure in Fig. 3.4) are overlapped and give a significantly broad peak around 1.20 ppm. Due to the existence of several internal spin interaction in the solid state, the solid state NMR peaks width is broader as compared to that observed in liquid state. Here, this broadening is the result of the presence of ^{1}H-^{1}H dipolar couplings which are not fully averaged out by Magic Angle Spinning (MAS). As the MA cation is introduced to the n=2 and n=3 perovskite systems, two additional peaks are observed at 3.39 and 6.47 ppm for two different hydrogen atoms of methyl and ammonium groups, respectively. Additionally, it was noted that as the number of inorganic layers increases (for n = 2 & 3), the resonance from ammonium hydrogens shifts to lower values.

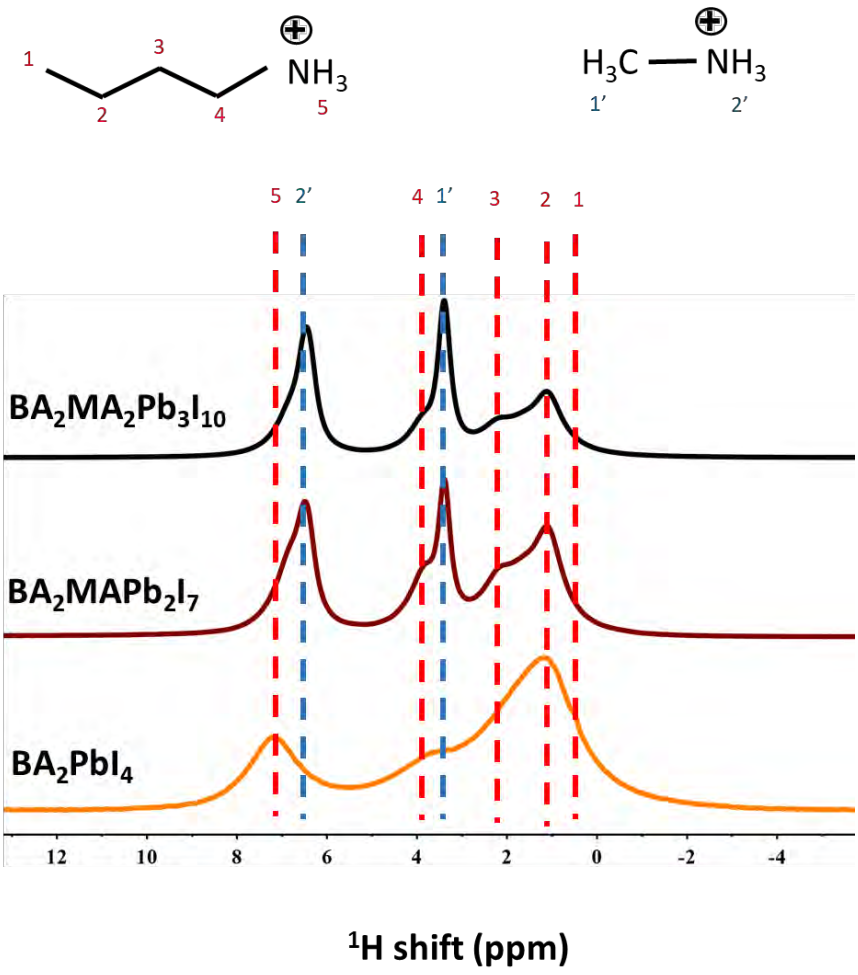

Fig. 3.4: ^{1}H NMR spectra of the synthesized 2D $BA_2MA_{n-1}Pb_nI_{3n+1}$ perovskite materials with the cationic BA spacer for n=1 (orange curve), n=2 (maroon curve) and n=3 (black curve).

Next, in order to investigate the local structure of carbon atoms, ^{13}C NMR spectra of the materials BA_2PbI_4, $BA_2MAPb_2I_7$, and $BA_2MA_2Pb_3I_{10}$ were recorded. As shown in Fig. 3.5 (orange curve), the NMR signals from the carbon atoms of BA cation in BA_2PbI_4 material appear at 16.15, 20.9, 30.72, and 42.35 ppm. After the addition of MA cation and producing $BA_2MAPb_2I_7$ and $BA_2MA_2Pb_3I_{10}$ samples i.e. the n=2 and n=3 layered materials, an additional peak appears at 31.22 ppm corresponding to methyl carbon. It can also be noted that the NMR signal for carbon closest to ammonium group shifted to higher resonance value of 43.88 ppm in n>1 samples.

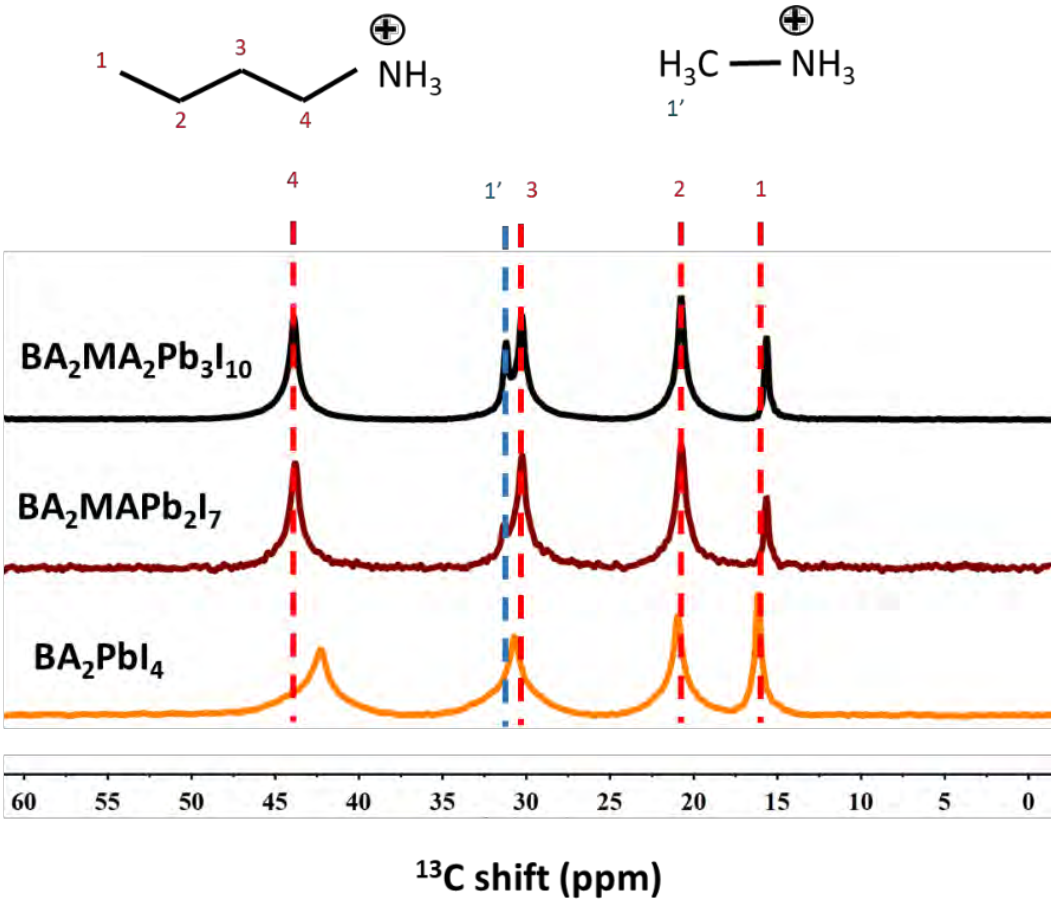

Fig. 3.5: ^{13}C NMR spectra of the synthesized 2D $BA_2MA_{n-1}Pb_nI_{3n+1}$ perovskite materials with the cationic BA spacer for n=1 (orange curve), n=2 (maroon curve) and n=3 (black curve).

To study the dynamics of MA and BA moieties in these materials, ^{2}H NMR spectra were also recorded for the deuterated precursors as well as the deuterated layered perovskite samples. However, the NMR spectra revealed that the ^{2}H peaks for BA and MA cations in the precursors and mechanochemically synthesized BA_2PbI_4 perovskite exhibited similar chemical shift

values (Fig. 3.6). This overlap of ^{2}H signals in different samples restricted the further analysis of the dynamics of organic molecules present in the system. Therefore no conclusion could be drawn from these results and no further ^{2}H NMR measurements were carried out for other samples.

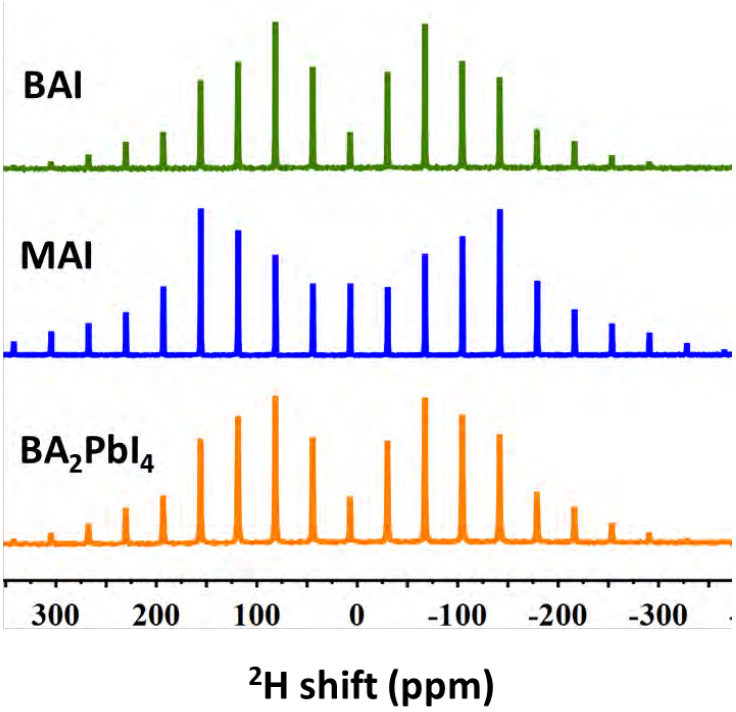

Fig. 3.6: ^{2}H NMR spectra of the precursors BAI (green curve), MAI (blue curve) and 2D perovskite material BA_2PbI_4 (orange curve).

3.2.3 2D layered perovskites with 2-phenylethylammonium as the spacer cation

The next series of 2D perovskites with Ruddlesden-Popper structure were synthesized with 2-phenylethylammonium (PEA) as the spacer cation. To obtain monolayer PEA_2PbI_4 perovskite, the precursors PEAI and PbI_2 were grinded together in a ratio of 2:1 ratio as described in the experimental section of Chapter 2. The resultant material was obtained in the form of microcrystalline powder with yellow color (Fig. 2.3). The initial PXRD measurements of this powder without post synthesis annealing revealed the successful formation of the expected 2D layered perovskite with n=1 (magenta curve in Fig. 3.7). The characteristic low angle reflection peak from (002) plane was seen at 5.4°. The presence of this highly intense peak indicated the preferred orientation of the 2D layers along the <001> direction, which is parallel to the

substrate [195]. Other characteristic reflections of 2D layered structure with n=1 from the crystallographic planes (004), (006), (008), and (00$\underline{10}$) were also observed at 10.8° , 16.2°, 20.4°, and 27.2°, respectively. In case of the preparation of $PEA_2MAPb_2I_7$ (n=2) and $PEA_2MA_2Pb_3I_{10}$ (n=3), all the precursors were grinded together in appropriate ratios for 30 min at 30 Hz, however, this resulted in materials with broad PXRD peaks indicating low crystallinity of the materials. Therefore, in the next control experiments, the grinding time was increased from 30 min to 60 min and 75 min and PXRD patterns were subsequently recorded. It was found that longer grinding time of 75 min resulted into the slight improvement in crystallinity of these perovskite materials. Nonetheless, both the perovskites, $PEA_2MAPb_2I_7$ and $PEA_2MA_2Pb_3I_{10}$ exhibited relatively low crystallinity relative to the respective n=1 sample as evidenced by the broad PXRD peaks. While the characteristic reflections of 2D layered

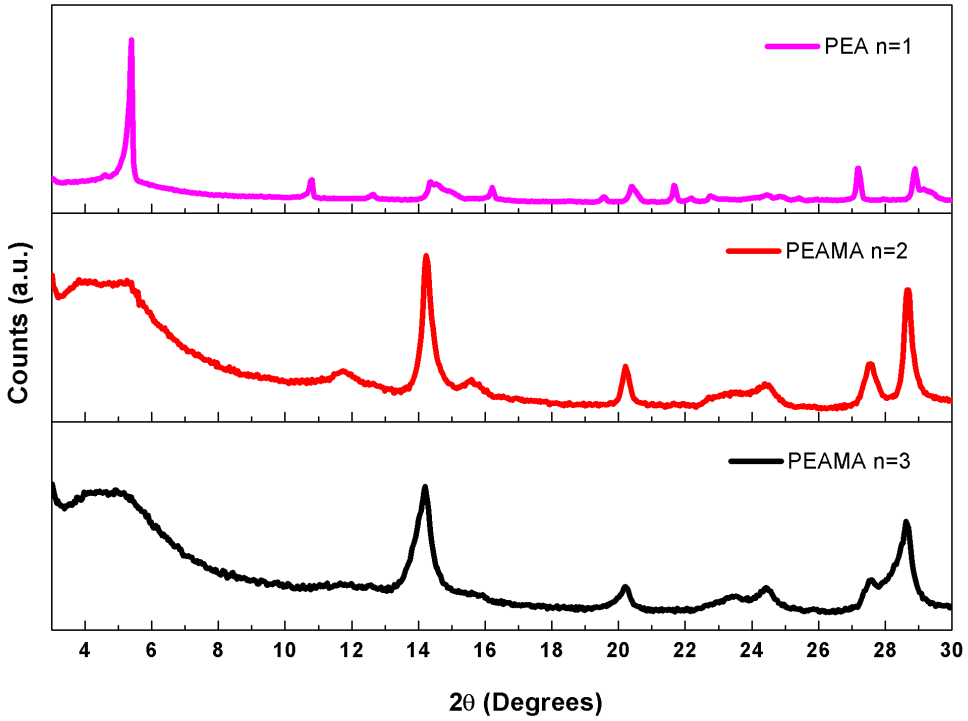

Fig. 3.7: PXRD pattern of synthesized 2D $PEA_2MA_{n-1}Pb_nI_{3n+1}$ perovskite powders with PEA spacer cation for n=1 (magenta curve), n=2 (red curve) and n=3 (black curve).

perovskites below 10° could not be distinguished due to the broad signal, the peaks from (111) plane were present at 14.25° and 14.18° for the n=2 and n=3 samples, respectively. The broadness of low angle peaks could be explained by the lesser no of perovskite crystal planes lying in the parallel direction to substrate. Additionally, the other dominant peaks show that as

the n increases, the inorganic layers inside the perovskite start growing in perpendicular direction to the substrate and stronger signals are obtained. For these materials further experiments with subsequent annealing as well as ageing were also performed, however, they did not improve the crystallinity of materials. The difficulty in producing pure and highly crystalline 2D perovskites with PEA spacer cation for the n=2 and n=3 phases of $PEA_2MA_{n-1}Pb_nI_{3n+1}$ could be attributed to the bulky nature of PEA molecule.

The optical characteristics of synthesized PEA-based 2D perovskites were further analyzed by measuring the light absorption in the UV-Visible region. A similar trend in the absorption spectra of these perovskites was observed as for the materials made with BA spacer cations. There was a pronounce shift in the absorption onset to higher wavelength values for 2D $PEA_2MA_{n-1}Pb_nI_{3n+1}$ materials when the value of n increased (Fig. 3.8). The layered perovskite with the n=1 showed an excitonic peak around 500 nm. As explained in the case of BA cation based 2D perovskites, a local electrostatic field is created between the PEA^+ ions and the negatively charged inorganic layer, which prevents the separation of photo generated excitons. The other two materials of the series, $PEA_2MAPb_2I_7$ and $PEA_2MA_2Pb_3I_{10}$, exhibited multiple peaks around 500 nm, 570 nm and 610 nm. The absorption peak near 610 nm and 570 nm can be assigned to the excitonic absorptions from the n=3 and n=2 perovskites, respectively. The peak around 500 nm matches with the excitonic peak of n=1 material. This indicates that the

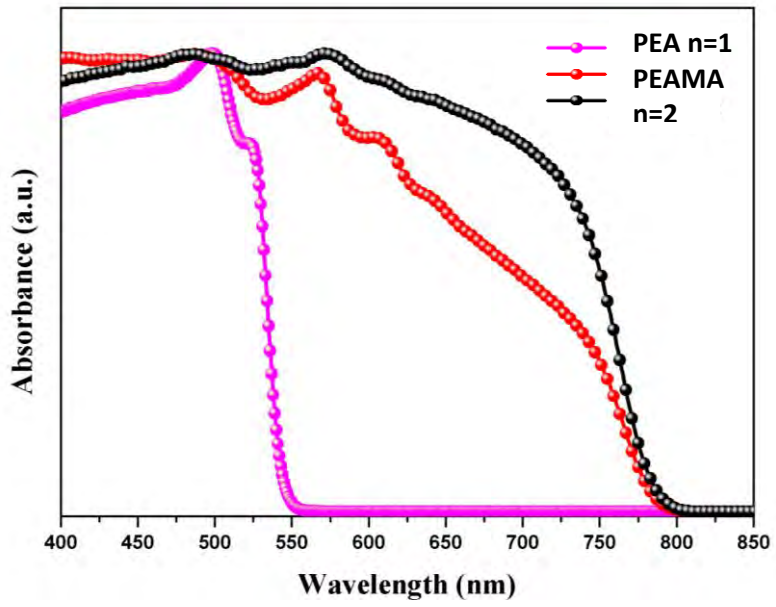

Fig. 3.8: Normalized UV-Vis spectra of the synthesized 2D $PEA_2MA_{n-1}Pb_nI_{3n+1}$ perovskite powders with cationic PEA spacer for n=1 (magenta curve), n=2 (red curve) and n=3 (black curve).

perovskites with n=2 and n=3 contain trace amount of n=1 material as well. The calculated optical bandgap values resulted to be 2.23 eV, 2.11 Ev, and 1.98 eV for 2D PEA_2PbI_4, $PEA_2MAPb_2I_7$, and $PEA_2MA_2Pb_3I_{10}$ perovskites, respectively.

Furthermore, the local molecular structure for this series of 2D materials was studied by the solid state NMR measurements. Dr. Kubicki recorded the NMR spectra of these samples. Fig. 3.9 shows the ^{13}C NMR spectra of the 2D perovskites with PEA spacer cation for n=1, 2, and 3. In case of the monolayer PEA_2PbI_4, the signals from two alkyl carbons appear at 33.91 and 44.36 ppm and the signals from aromatic carbon appear at higher chemical shift values of 130.64, 127.48, and 137.33 ppm, respectively. The second and third member of the series, show an additional peak at 34.13 ppm originating from carbon atom of the MA methyl group. This confirms the incorporation of MA cation into the 2D perovskite structure. For further understanding the dynamics of different molecules, ^{2}H NMR spectra of deuterated precursors

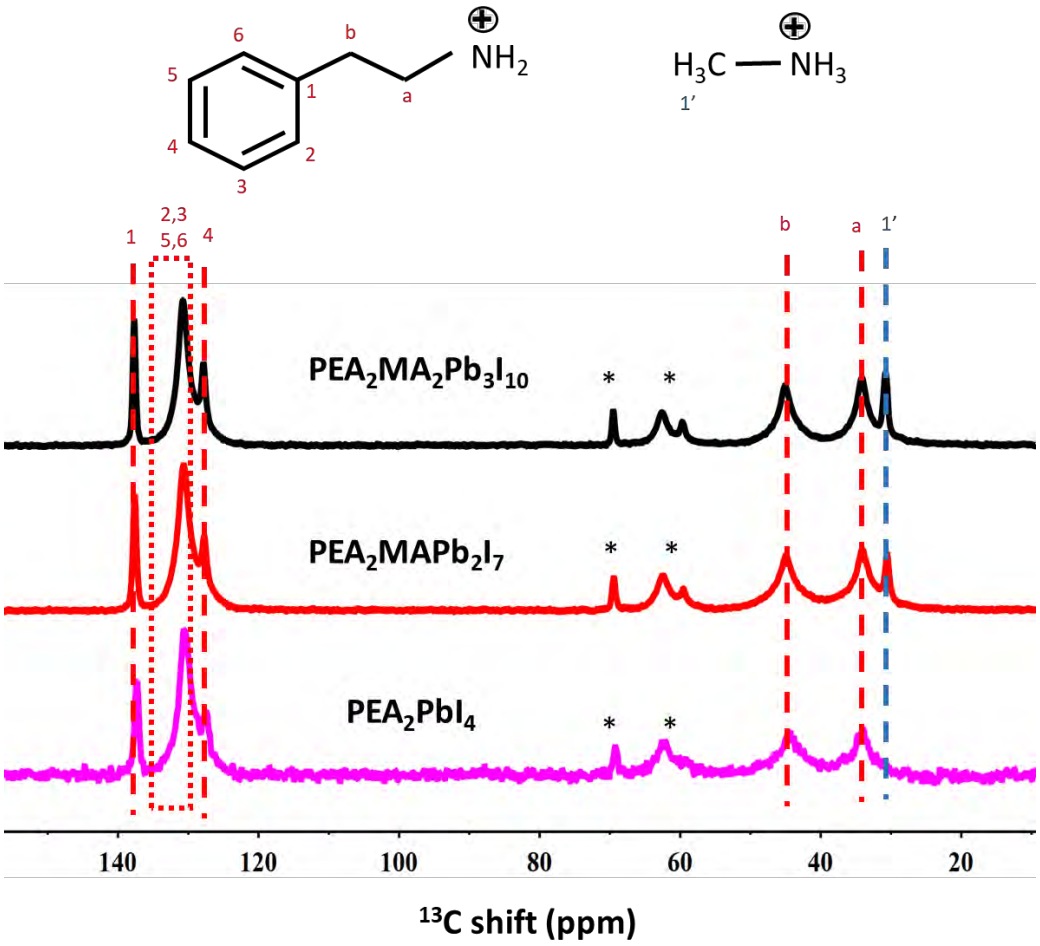

Fig. 3.9: ^{13}C NMR spectra of the synthesized 2D $PEA_2MA_{n-1}Pb_nI_{3n+1}$ perovskite powders with PEA spacer cation for n=1 (magenta curve), n=2 (red curve) and n=3 (black curve).

and mechanosynthesized PEA-based perovskite powders were recorded. However, again the signals from the deuterated hydrogen of PEA and MA appeared at the same chemical shifts as shown in Fig. 3.10. When the ^{2}H spectra were recorded for PEA_2PbI_4, the peaks from precursors could not be distinguished and no conclusion about the local dynamics could be drawn.

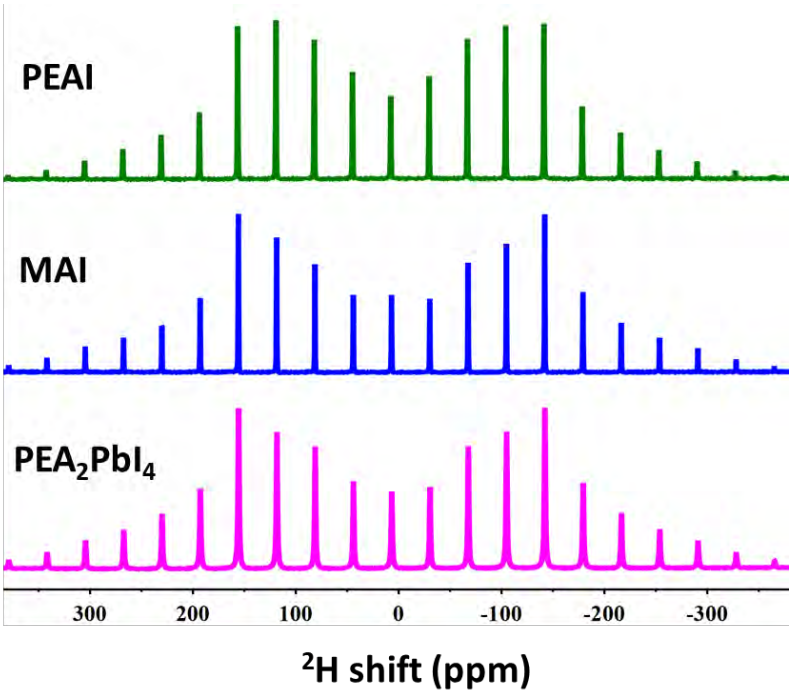

Fig. 3.10: ^{1}H NMR spectra of the precursors PEAI (green curve), MAI (blue curve) and 2D PEA_2PbI_4 material (magenta curve).

3.2.4 Attempts to synthesize inorganic-organic hybrid materials involving a cyclic guanidinium

Next, 2H-pyrimido[1,2-a]pyrimidine-1,3,4,6,7,8-hyxahydro-hydroiodide (c-GuaI) was utilized as a potential spacer cation for the synthesis of a series of materials with the general formula $(c\text{-}Gua)_2MA_{n-1}Pb_nI_{3n+1}$. Using the similar procedures described above for the synthesis of BA and PEA-based 2D layered perovskites, c-GuaI was also grinded with other precursors in order to get 2D structures. For example, c-GuaI and PbI_2 were grinded together in a ratio of 2:1 at 30 Hz for 30 min (for details see the experimental section of Chapter 2) for synthesizing the

expected n=1 Ruddlesden-Popper structured materials. Similarly, the precursors c-GuaI, MAI and PbI_2 in the stoichiometric ratios of 2:1:2, 2:2:3 precursors were grinded in order to obtain the expected layered materials for n=2 and 3 respectively. The obtained powders for all the materials were pale yellow in color. However, the PXRD measurements showed no characteristic peaks for a layered perovskite structure at low angles below 10° (Fig. 3.11). The synthesized material for the expected n=1 layered structure exhibited several peaks in the region from 15 ° to 30 °, however, they were difficult to interpret. Two strong peaks were also seen around 9.3 ° and 10.1 °, which didn't match with any of the perovskite plane. Interestingly, when MA cation was added to the $(c\text{-}Gua)_2PbI_4$ material in order to get the anticipated n=2 and n=3 phases, the resulting materials also showed several XRD peaks in the region from 15 ° to 30 °. In case of the materials with precursors mixed for n=3 phase, two small peaks appeared around 11.4 ° and 14.1 °. The peak at 14.1 ° might be the result of diffraction from (111) plane of perovskite phase, however no other peaks were identified from the crystalline perovskite structure. The absence of any characteristic 2D perovskite diffraction peak in these materials could be due to the formation of non-perovskite polymeric structure when c-Gua is used as the potential spacer cation. Therefore, for the next set of experiments, milling time was increased from 30 min to 60 min and 75 min. The increase in reaction time also displayed no effect on

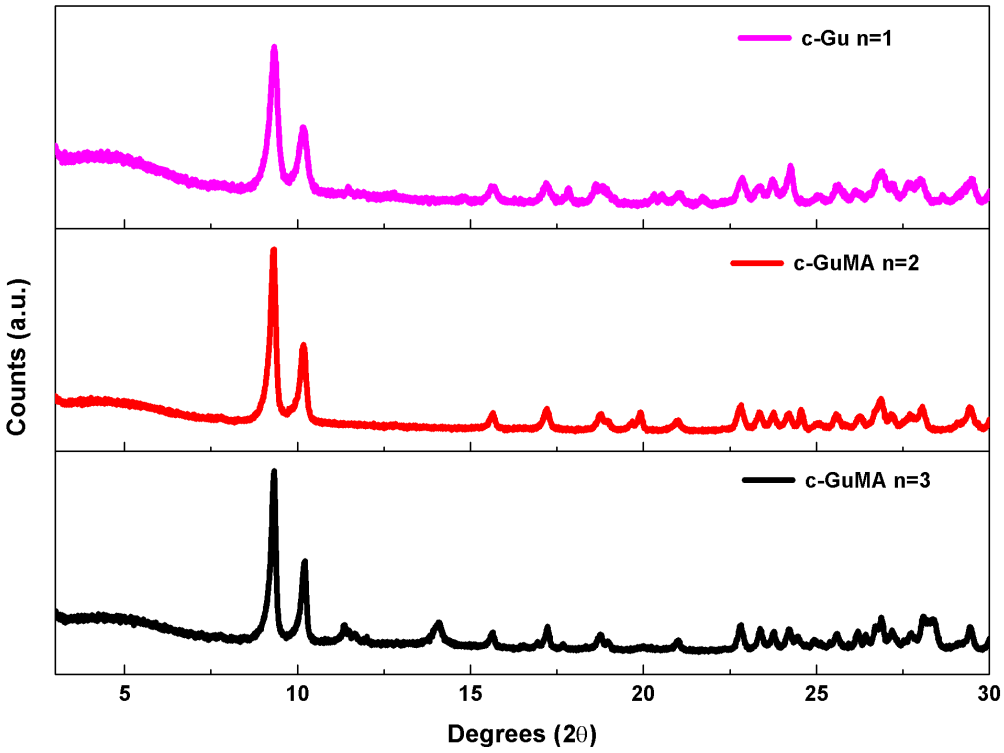

Fig. 3.11: XRD pattern of hybrid inorganic organic materials involving c-Gua cation for n=1 (magenta curve), n=2 (red curve) and n=3 (black curve).

the structure of materials as measured by PXRD. The powders were subsequently annealed at 80 ºC for varying time of 60 min to few hours, however, no change in the crystallinity of materials could be seen. The series of experiments indicated that c-Gua cannot be incorporated into the 2D perovskite structure and therefore no further experiments were conducted with this cation.

3.3 Conclusions

In conclusion, the simple and solvent-free mechanochemical procedure was followed for the synthesis of 2D layered perovskite materials of the general formula $A_2MA_{n-1}Pb_nI_{3n+1}$. Three different types of cations namely, n-butylammonium (BA), 2-phenylethylammonium (PEA) and 2H-pyrimido[1,2-a]pyrimidine-1,3,4,6,7,8-hexahydro-hydroiodide as a cyclic guanidinium (c-Gua) were investigated as potential spacer cations. After grinding the precursors in the shaker mill and optimizing the reaction conditions, a series of phase pure 2D layered perovskites with the n=1, 2 and 3 Ruddlesden-Popper structure were obtained in case of the BA cation. The mechanosynthesis involving PEA cation resulted in the formation of phase pure 2D perovskites with the n=1 Ruddlesden-Popper structure, however, mixed phase 2D perovskites were obtained for the n=2 and n=3 materials. Nevertheless, the c-Gua cation could not be incorporated into a 2D perovskite structure and the process resulted into the formation of ill-defined non-perovskite materials. Characterization techniques like PXRD, UV-vis spectroscopy and solid state NMR confirmed the formation of 2D layered materials with the n=1, 2 and 3 structures for BA and PEA spacer cations. The results nicely demonstrate that the mechanochemical approach is a powerful synthesis technique, which can be extended for the pure phase synthesis of high quality 2D Ruddlesden-Popper perovskite powders by optimizing the reaction conditions.

Part B: Investigating fundamental properties of lead based halide perovskite single crystals

3.4 Introduction

In the second part of this chapter, the synthesis and properties of single cation and double cation metal halide perovskite crystals are discussed. Metal halide perovskites in the form of single crystals are more suitable for the study of the inherent optical and electronic properties on a more fundamental level than the polycrystalline perovskite thin films. Due to the substantially limited grain boundaries in single crystals, they offer better transport of charge carriers and reduced defect density, making them more favourable for optoelectronic applications [49,196,197,198]. Interestingly, single crystals of the simplest and commonly explored halide perovskite, $MAPbI_3$, have shown reduced defects and a higher carrier lifetime and carrier diffusion length [49,199]. Therefore, a lot of efforts have been dedicated for investigating the growth mechanism and properties of perovskite single crystals. Furthermore, in perovskite solar cells (PSCs), the efficiency and stability of devices depend on the ion migration inside the perovskite materials. In $MAPbI_3$, the major ions contributing to the ion migration are MA^+, I^-, H^+, and Pb^{2+} [200,201]. Among these, H^+ ions have a negligible role due to their low concentration and Pb^{2+} ions have a high activation energy for the migration as compared to that of other ions [202,203]. The ions MA^+ and I^- have low binding energy and they play a significant role in the hysteresis behaviour in the current-voltage scan and stability of $MAPbI_3$-based solar cells [204,205]. One way to reduce the hysteresis of PSCs is controlling the chemical arrangement and replacing some of I^- with other smaller halides such as Br^- [206,207]. Another way is to dope the A-site MA^+ cation with other cations to reduces the ion migration. For this purpose, guanidinium (Gua) cation was investigated theoretically due to its zero dipole moment and larger size relative to the MA cation [208,209]. However, the studies revealed that including Gua into the $MAPbI_3$ perovskite structure increases the hysteresis effect in current-voltage measurements when compared to pure $MAPbI_3$-based PSCs. Therefore, further detailed investigation of Gua doping of $MAPbI_3$ perovskite crystal lattice needs to be carried out in order to understand the ion transport mechanism.

In the following section, the synthesis of high quality $MAPbI_3$ single crystals using the inverse temperature crystallization (ITC) method is discussed. The basic characterization of crystals

was performed using XRD and UV-vis spectroscopy. The temperature dependent XRD measurements showed that the crystals were stable up to 363 K. These single crystals were then sent to our collaborator Dr. Pankaj Yadav at Pandit Deendayal Petroleum University, India for further analysis using electrochemical impedance spectroscopy (EIS) and capacitance spectroscopy. Following this work, a double cation single crystal was synthesized, where a small amount of Gua cation was introduced into the $MAPbI_3$ crystal to replace some of the MA cations. This resulted in the formation of single crystals with formula $Gua_xMA_{1-x}PbI_3$ (x=1.5). Subsequently, the crystal structure of $Gua_xMA_{1-x}PbI_3$ was confirmed by XRD and the ratio of MA and Gua cations introduced into the perovskite structure was calculated by the liquid state NMR measurements. In order to study the effect of Gua incorporation on the electronic properties of $MAPbI_3$, the crystals were then sent to Dr. Pankaj Yadav for electrochemical characterization. These studies have enabled to investigate the in-depth properties of single cation and double cation perovskite single crystals.

3.5 Results and discussions

3.5.1 Properties of $MAPbI_3$ single crystals

$MAPbI_3$ single crystals were synthesized by dissolving MAI and PbI_2 (ratio 1:1) in γ-butyrolactone (GBL) following the ITC method (for experimental details, see Chapter 2). A 2-step heating of precursor solution at 160 °C and 120 °C, respectively, resulted in the formation of well-shaped single crystals as shown in Fig. 3.12.

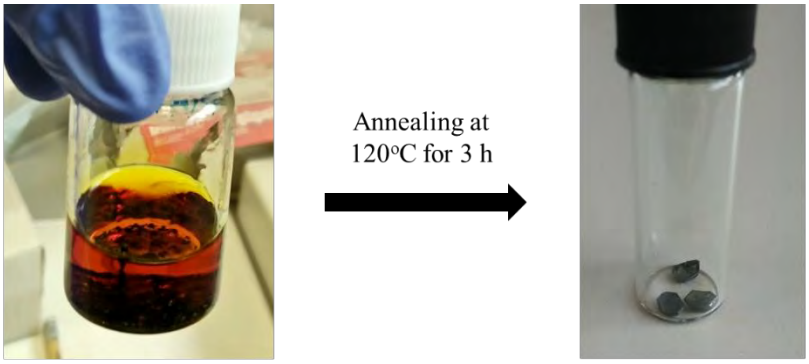

$MAPbI_3$ seed crystals in solution $MAPbI_3$ crystals after drying

Fig. 3.12: Images of seed crystals in precursor solution (left) and dried single crystals (right) of $MAPbI_3$.

Fig. 3.13 (black) shows the room temperature XRD measurement at 298 K and it revealed the presence of characteristic peaks for tetragonal crystal structure. Reflection peaks were observed at 14.4°, 40.6°, and 43.3° from the crystallographic planes (110), (224,) and (314), respectively. Next, the XRD patterns were recorded with increasing temperature starting from 298 to 393 K in order to determine the thermal stability of the materials. As it can be seen in Fig. 3.13, the temperature dependant measurements indicated that the crystals remained stable upon heating up to 363 K ;no additional peaks were observed in the XRD patterns measured at higher temperatures, showing no decomposition was taking place. Furthermore, a phase transition from tetragonal to cubic structure was observed between 323 and 333 K, which is typical for $MAPbI_3$ [210]. The reflection peak at 23.7°, corresponding to plane (211) in the tetragonal phase, disappears when the crystal structure changes to cubic. Additionally, the appearance of a peak at 28.5°, which is a characteristic of (200) plane in the cubic phase, confirms the transition.

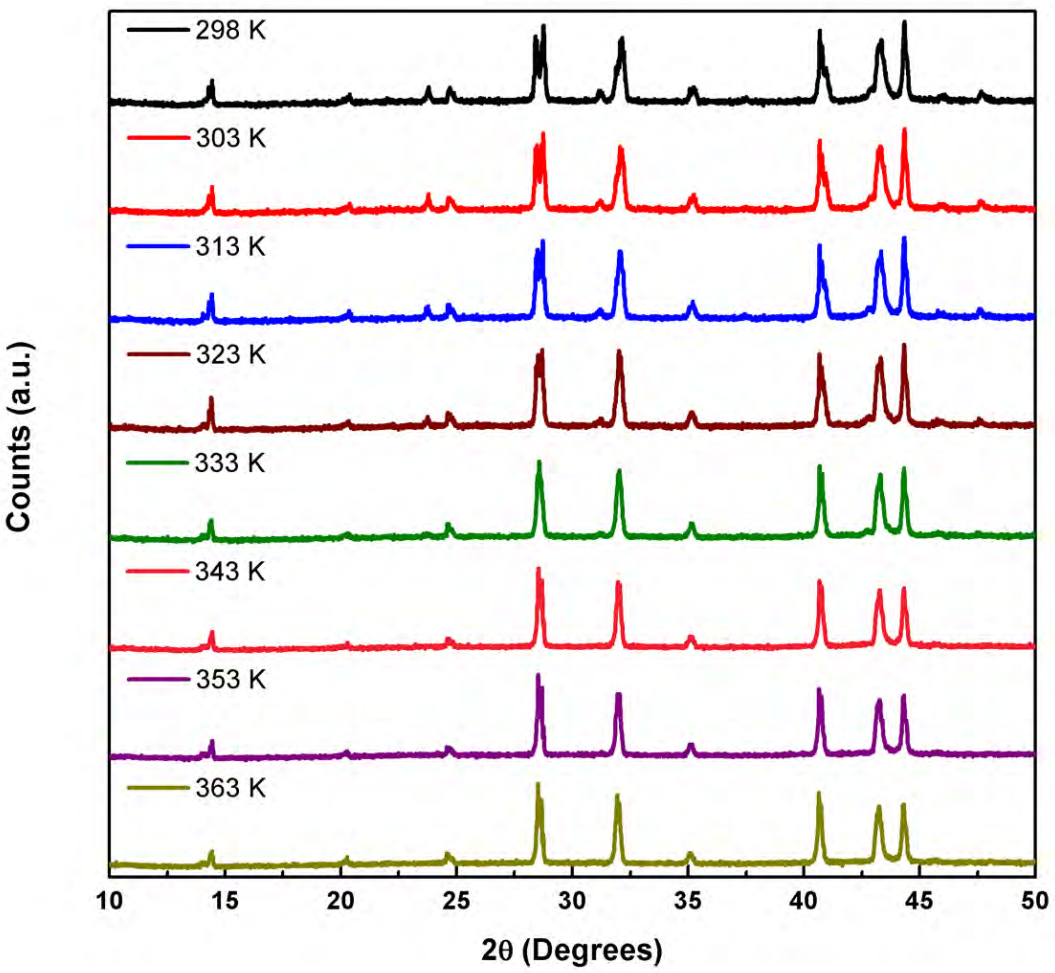

Fig. 3.13: Temperature dependent XRD patterns of grounded $MAPbI_3$ single crystals.

Next, the effect of heating on absorption characteristics of $MAPbI_3$ crystals was analysed by UV-Vis spectroscopy. The absorption spectra in Fig. 3.14 show that there was no significant change in the light absorption of crystals at room temperature and after heating at 363 K in the range of 500 nm to 900 nm. This also indicates that the bandgap of crystals does not change after heating.

For further investigations of electronic properties of these single crystals materials, they were sent to our collaborator Dr Pankaj Yadav. By using the EIS method, the temperature and bias dependent impedance behavior of single crystalline $MAPbI_3$ were investigated for the first time. It was determined that the low frequency capacitance of $MAPbI_3$ is affected by the ion density and mobility inside the crystal. The net impedance spectrum was found to be a combination of ionic capacitance and conductivity related resistance. Additionally, the study revealed that the single crystals had a very low trap density of 0.96×10^{10} cm^{-3} and an activation energy of 0.53−0.54 eV.

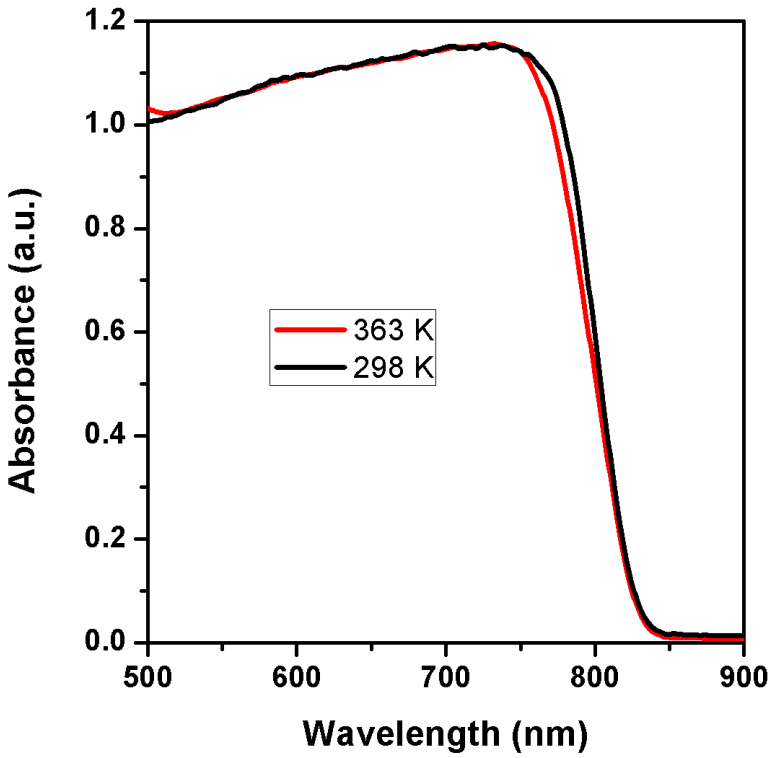

Fig. 3.14: Absorption spectra of grounded $MAPbI_3$ single crystals at 298 and 363 K.

3.5.2 Properties of $Gua_xMA_{1-x}PbI_3$ –type single crystals

In the following work, the A-site MA cations were doped with Gua cations in order to form perovskite crystals with the formula of $Gua_xMA_{1-x}PbI_3$. Again, the ITC technique was followed to create mixed cation perovskite single crystals in GBL and for reference $MAPbI_3$ crystals were also synthesized. A 1 M precursor solution comprising of PbI_2, MAI, and GuaI in the molar ratios of 1: 0.8: 0.2 was used to make $Gua_xMA_{1-x}PbI_3$ single crystals (for further information, see the Experimental section), resulting in a single crystal material of the formula $Gua_{0.015}MA_{0.985}PbI_3$. By dissolving one distinct crystal in 500 µL of DMSO-d_6, the ratio of organic cations integrated into the perovskite structure was measured using liquid-state ^{1}H NMR analysis (Fig. 3.15).

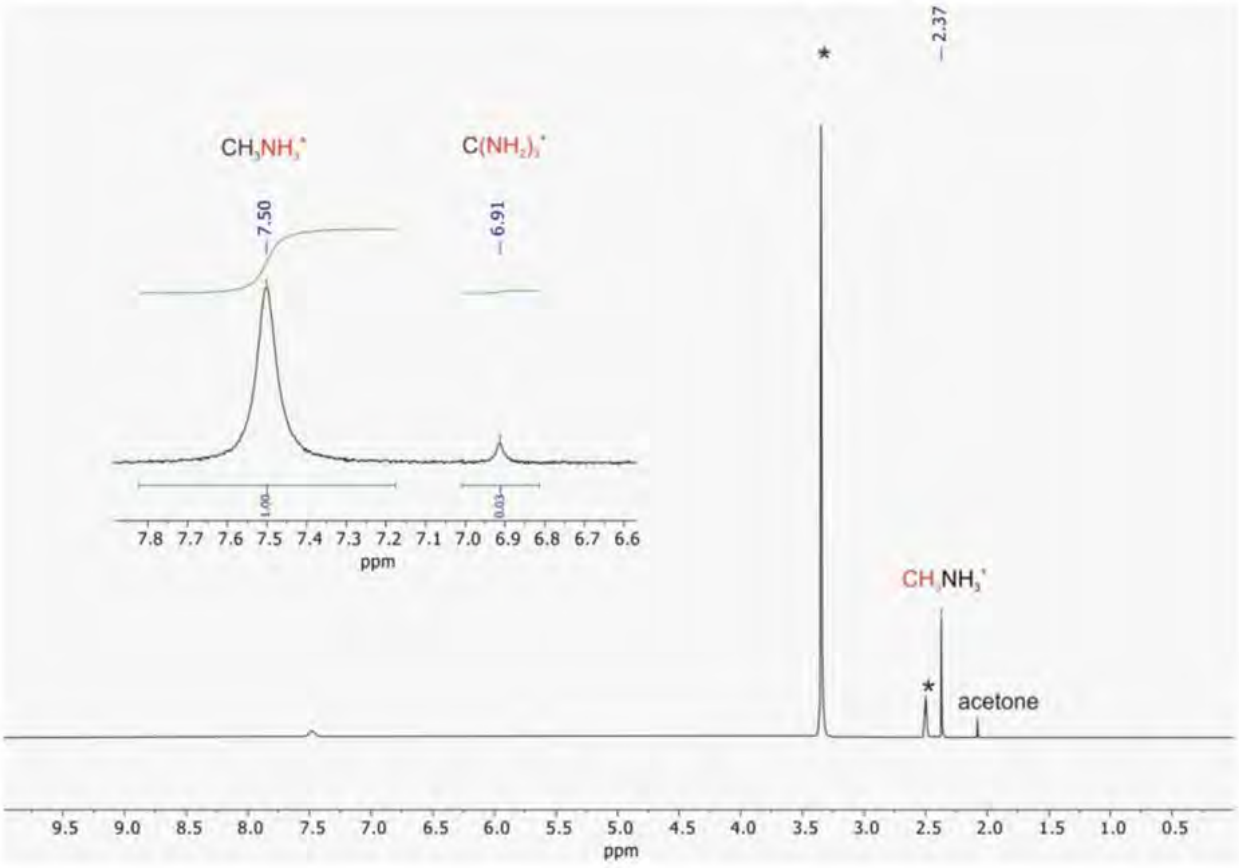

Fig. 3.15: ^{1}H NMR spectra of $MAPbI_3$ and $Gua_{0.015}MA_{0.985}PbI_3$ single crystals dissolved in DMSO-d_6. The * peak relates to DMSO-d_6 and water (adapted from [211]).

In the $Gua_xMA_{1-x}PbI_3$ crystal, the Gua/MA ratio was determined using the integrated values for the amine group resonances of Gua (6.91 ppm) and MA (7.50 ppm) as following

Number of H atoms in the amine group of Gua ($(NH_2)_3^+$) = 6

Number of H atoms in MA (NH_3^+) = 3

Therefore, integrated values for $(NH_2)_3^+$ and (NH_3^+) resonances in the NMR spectra are

X = [$(NH_2)_3^+$ / 6] = 0.03/6 = 0.005

Y = [(NH_3^+) / 3] = 1/3 = 0.333

Now,

$$\% \text{ Gua} = \frac{X}{X+Y} * 100 = \frac{0.005}{0.005+0.33} * 100 \cong 1.5\%$$

$$\% \text{ MA} = \frac{Y}{X+Y} * 100 = \frac{0.33}{0.005+0.33} * 100 \cong 98.5\%$$

From the calculated values, it was discovered that the real MA/Gua ratio was equal to 0.985:0.015 . In order to confirm these results, more crystals from the same batch were again analyzed by the ^{1}H NMR and all of them showed similar ratios. The reason behind this large difference in Gua content inside the crystal and precursor solution could be due to the low solubility of perovskite precursors in GBL, which leads to low yield during the crystallization process. Next, in order to increase the Gua incorporation into the $MAPbI_3$ crystals, higher amount of GuaI was taken in the precursor solution. For example, two different precursor solution were prepared by combining PbI_2, MAI, and GuaI in molar ratios of 1:0.7: 0.3 and 1:0.6:0.4. Nonetheless, these solutions failed to produce any crystals.

Consequently, for further investigations of the effect of Gua incorporation, the crystals with formula of $Gua_{0.015}MA_{0.985}PbI_3$ were utilized. XRD measurements were conducted on the resultant crystals of $MAPbI_3$ and $Gua_{0.015}MA_{0.985}PbI_3$ to verify their phase purity and crystalline structure. The XRD patterns showed that both the samples had equivalent perovskite crystal structure, as illustrated in Fig. 3.16 (a). The diffraction peaks centered at 14.07°, 28.1°, and 31.8° were observed from the crystallographic planes (110), (220), and (222). The insertion of Gua cations resulted in a modest shift of the diffraction peaks to lower angles (Fig. 3.16 (b)), which is also consistent with the literature [164].

These $Gua_{0.015}MA_{0.985}PbI_3$ crystals along with $MAPbI_3$ were then sent to Dr Pankaj Yadav for further EIS measurements. For investigating the influence of Gua cation incorporation on the ion transport dynamics, the temperature dependent EIS studies were carried out on the single crystalline $Gua_xMA_{1-x}PbI_3$ perovskite composition. It was observed that replacing some of the MA cations with Gua decreases the activation energy for iodide ion migration as compared to pure $MAPbI_3$. The reason behind this lies in the lattice enlargement due to the presence of a large Gua cation in a 3D perovskite structure, which in turn disturbs atomic interactions within the perovskite lattice. As a result, the $Gua_xMA_{1-x}PbI_3$ crystals show larger hysteresis during the J–V measurements than that observed for pure $MAPbI_3$ single crystal.

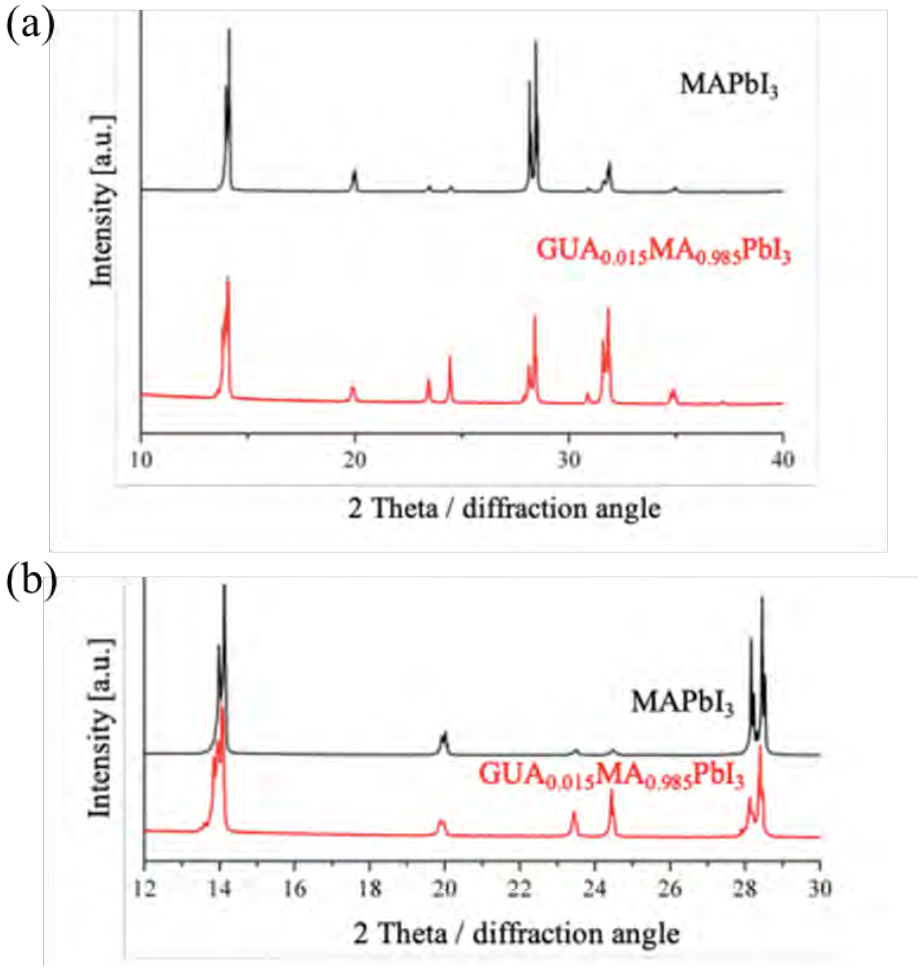

Fig. 3.16: XRD spectra of powdered $MAPbI_3$ and $Gua_{0.015}MA_{0.985}PbI_3$ single crystals for diffraction angle of (a) 10° – 40° and (b) 12° – 30° (adapted from [211]).

3.6 Conclusions

In conclusion, single crystals of pure $MAPbI_3$ and Gua incorporated $MAPbI_3$ perovskite were obtained following the ITC method. The thermal stability of $MAPbI_3$ crystals was confirmed by the temperature dependent XRD measurements and UV-Vis absorption spectroscopy, which revealed that the crystals were stable up to 363 K. The temperature and bias dependent EIS measurements revealed that the ion density and mobility inside the $MAPbI_3$ crystal affect the low frequency capacitance, and the net impedance spectrum was due to the ionic capacitance and conductivity related resistance of the crystals. It was also found that the crystals had very low trap density. The next single crystal was synthesized by introducing Gua cation into the $MAPbI_3$ lattice, resulting in the formation of crystals with a composition of $Gua_{0.015}MA_{0.985}PbI_3$. XRD measurements confirmed that the lattice structure of these crystals was similar to $MAPbI_3$. By carrying out the EIS measurements, our collaborators showed that the activation energy of iodide migration decreases due to the lattice enlargement after the incorporation of Gua cation. This leads to higher hysteresis during the J-V measurements of $Gua_{0.015}MA_{0.985}PbI_3$ single crystals as compared to that of pure $MAPbI_3$. These results were significant in understanding the underlying electrical characteristics of the $MAPbI_3$ as well as $Gua_xMA_{1-x}PbI_3$-type single crystal, which may be relevant in the future towards the development of perovskite single-crystal based applications.

Chapter 4: Engineering of Cs and formamidinium based double cation perovskites and their passivation for high-efficiency mesoscopic solar cells

4.1 Introduction

The double cation lead halide perovskites based on Cs and formamidinium (FA) as A-site cations have been widely used for the fabrication of high-performance perovskite solar cells (PSCs). As discussed in Chapter 1, substituting some of the FA cations with Cs cations in the $FAPbI_3$ perovskite structure stabilizes the photoactive α-phase crystallization of $FAPbI_3$ and results in perovskites with a general formula of $Cs_xFA_{1-x}PbI_3$. In this chapter, device fabrication of high-efficiency mesoscopic perovskite solar cells (PSCs) based on $Cs_xFA_{1-x}PbI_3$ perovskite via a modified one-step spin-coating approach is discussed. Following this simple and effective newly developed technique, the $Cs_xFA_{1-x}PbI_3$ perovskites were synthesized and then employed in solar cell devices. Generally, for the synthesis of $Cs_xFA_{1-x}PbI_3$ perovskite composition, precursor CsI is used as the source of Cs cation (Fig. 4.1 (a)) [66,67]. In this improved procedure, CsCl was used as the source of Cs cation instead of CsI. When 20% of CsCl is added in the excess amount into the equimolar solution of PbI_2 and FAI and the spin-coated perovskite film is annealed, perovskite composition of $Cs_{0.2}FA_{0.8}PbI_3$ is formed. During the annealing process, the Cs cation is introduced into the $FAPbI_3$ crystal lattice and the initially introduced Cl anion is evaporated in the form of FACl. Remarkably, it is shown that this new approach leads to the formation of highly uniform and high-quality films with large grains of micrometre size, reduced non-radiative charge recombination, and longer carrier lifetimes. Next, applying this film in the mesoporous solar cells with the device architecture of FTO/c-TiO_2/m-TiO_2/$Cs_xFA_{1-x}PbI_3$/spiro-OMeTAD/Au (where c-TiO_2 is the compact layer and m-TiO_2 is the mesoporous layer) yielded a champion PCE of 20.6% and stabilized PCE of 19.85%. In the next subtask, 1- adamantylamine (ADA) and guanidinium iodide (GuaI) were utilized as the passivating agents to reduce the defects in the perovskite layer and improve the device efficiency. The passivation by GuaI resulted in the improvement of interface between the perovskite and the

hole transporting layers, which slightly increased the open circuit voltage (V_{oc}) and power conversion efficiency (PCE) of devices.

4.2 Results and discussions

4.2.1 Formation of $Cs_xFA_{1-x}PbI_3$ perovskite films by the modified approach

As discussed in the introduction, the conventional synthesis of $Cs_xFA_{1-x}PbI_3$ perovskite uses the precursor CsI to provide the Cs cation. One-step spin-coating of precursor perovskite solution is the most commonly used method for the fabrication of perovskite films. In case of $Cs_xFA_{1-x}PbI_3$ perovskite, a precursor solution with CsI, FAI, and PbI_2 in appropriate ratios are dissolved in the desired solvent and spin-coated on the substrate followed by thermal annealing [66,67]. On the other hand, in a two-step deposition method, first a precursor solution of CsI and

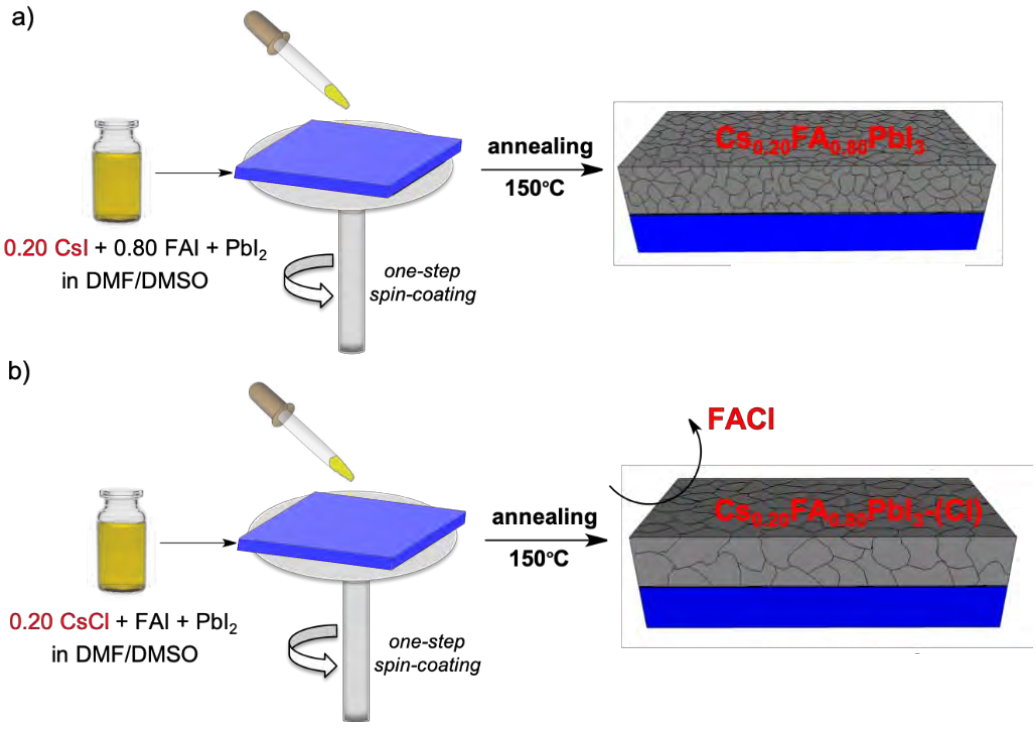

Fig. 4.1: Illustration of one-step deposition methods for $Cs_{0.2}FA_{0.8}PbI_3$ by (a) traditional method using CsI as the source of Cs cation and (b) our modified method using CsCl as the source of Cs cation (adapted from [212]).

PbI_2 is spin-coated and then FAI solution is deposited on top [213]. In this work, a modified one-step deposition approach was devised, where CsCl was used as the source of Cs cation. The precursor solution was prepared by dissolving FAI, PbI_2, and CsCl mixture in a molar ratio of 1:1:0.2. The perovskite film was deposited on top of the TiO_2 coated substrate and further annealed at 150 °C for 30 min, yielding the perovskite layer with a composition of $Cs_{0.2}FA_{0.8}PbI_3$ as illustrated in Fig. 4.1(b) (see details in the experimental section of Chapter 2). For comparison, a reference device was also fabricated, where the perovskite absorber layer of $Cs_{0.2}FA_{0.8}PbI_3$ was spin-coated by depositing the precursor solution with FAI, PbI_2, and CsI in molar ratio of 0.8:1:0.2 and further annealing under same conditions (Fig. 4.1(a)). From now on, perovskite film prepared using CsI and CsCl will be termed as CsFA-I and CsFA-Cl, respectively. In case of CsFA-Cl, the amount of CsCl was optimized to 20% and annealing of these films lead to the removal of excessive amount of Cl^- and FA^+ in the form of sublimed FACl at higher temperatures. Therefore, the final composition contained 20% of Cs cations and 80% of FA cation. The resulting films exhibited improved morphology with large grain sizes and reduced recombination centres and these are discussed in the following sections.

4.2.2 Properties of the resulting $Cs_{0.2}FA_{0.8}PbI_3$ perovskite films

Morphological studies of the spin-coated and subsequently annealed perovskite films of CsFA-Cl and CsFA-I were carried out by the scanning electron microscopy (SEM) and atomic force microscopy (AFM). The top view SEM images of CsFA-Cl and CsFA-I perovskites reveal the high quality of films without pinholes and excellent uniformity as shown in Fig. 4.2 (a) & (b). Additionally, it can be seen that the film based on CsFA-Cl displayed larger grain size up to ~1 µm as compared to the reference, which had grains of less than 500 nm. Besides, white spots were detected in the film due to the presence of PbI_2. The AFM images (Fig. 4.2 (c) & (d)) also present similar information about the morphology of both the films. Larger grains were observed in case of the CsFA-Cl perovskite film as compared to that of the reference film. Next, roughness of these films were measured by AFM and the root mean square (RMS) surface roughness values were estimated to be 18 nm and 35 nm for CsFA-Cl and CsFA-I films, respectively. It is also evident in the 3D AFM images (Fig. 4.2 (e) & (f)) that the surface of reference film is rougher as compared to that based on CsFA-Cl. The presence of chloride anion in the precursor solution thus promotes the formation of smoother films with larger grain sizes and hence improving the device performance as reported previously [214].

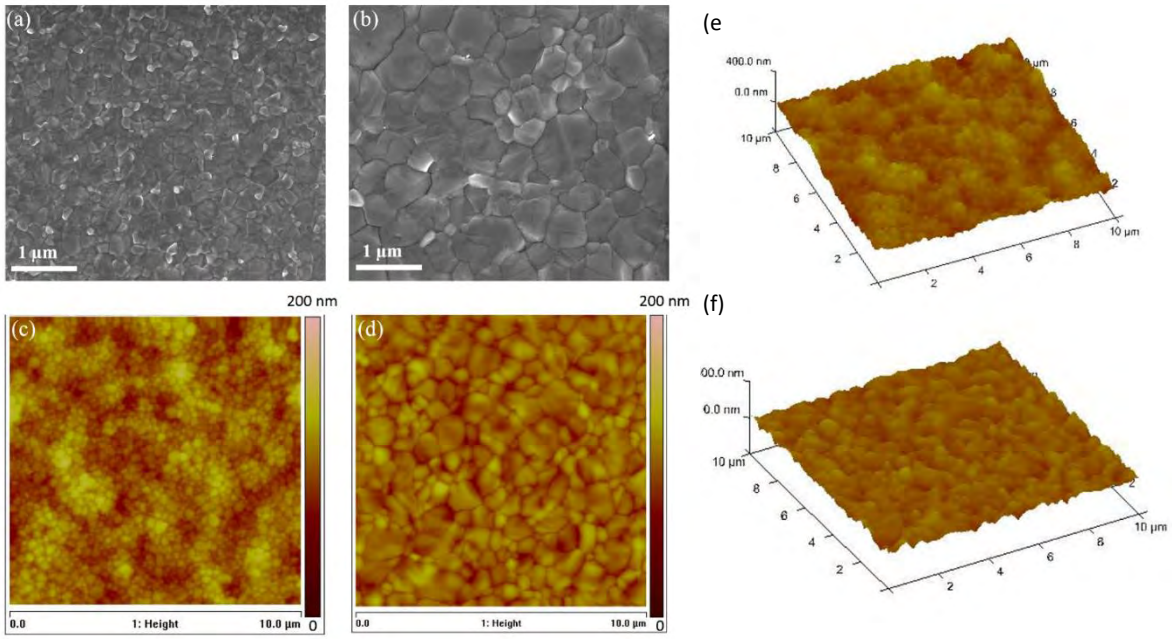

Fig. 4.2: Top view SEM, AFM and 3-D AFM images of perovskite films deposited on FTO/compact TiO_2/mesoporous TiO_2 for a-c-e) CsFA-I and b-d-f) CsFA-Cl (adapted from [212]).

The crystal structure of perovskite films was studied by the powder X-ray diffraction (XRD) measurements. Both CsFA-Cl and CsFA-I based films were deposited and annealed at 150 ºC before recording the XRD patterns. As presented in Fig. 4.3(a), the perovskite films of reference and CsFA-Cl showed similar crystal structures with the occurrence of XRD peaks at similar 2θ angles. The diffraction peaks for (001), (002) and (012) planes were observed at 14.07°, 28.3°, and 31.7°, respectively, indicating the formation of the stable black α-phase of $Cs_{0.2}FA_{0.8}PbI_3$ perovskite. An additional peak with higher intensity in the reference sample was observed at 12.7°, corresponding to the presence of pure PbI_2 in the perovskite film. This observation also matched well with the revelation of PbI_2 in the SEM images of the corresponding perovskite film. The existence of PbI_2 could be attributed to the decomposition of perovskite at high temperature annealing [215]. Moreover, the crystallinity of the films prepared with CsFA-Cl was improved in comparison to that of CsFA-I based reference films, as indicated by the enhanced intensity of XRD peaks.

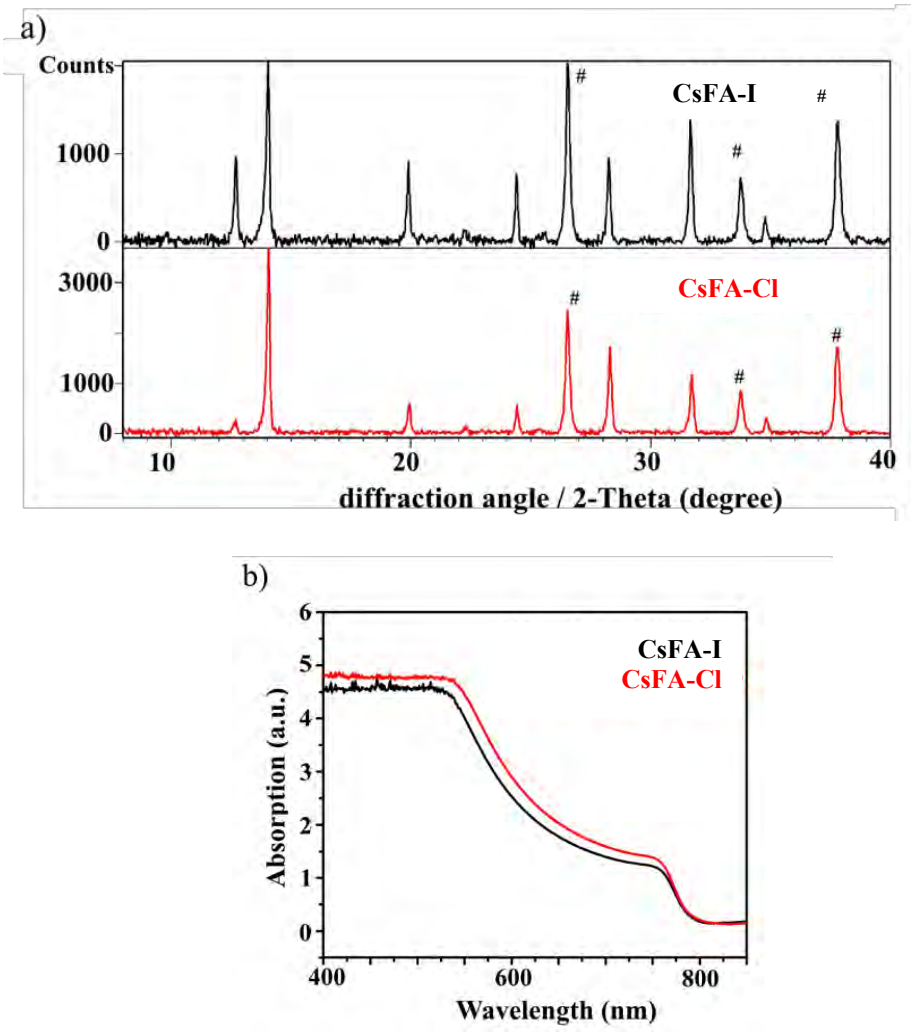

Fig. 4.3: (a) XRD pattern of CsFA-I (black) and CsFA-Cl (red) perovskite films on FTO substrates (peaks marked with # corresponds to FTO). (b) UV-Vis absorption spectra of both the films (adapted from [212]).

The UV-Vis absorption spectra were also recorded for CsFA-Cl and CsFA-I films and similar absorption characteristics were observed in the region from 400 nm to 850 nm (Fig. 4.3 (b)). The absorption onset was close to 800 nm for both the perovskite films and the bandgap calculated from the absorption onset gave a value of ~1.56 eV. The photoluminescence (PL) spectra of the films displayed a single peak around 804 nm in both cases (Fig. 4.4 (a)). It was observed that the intensity of PL peak was significantly increased for CsFA-Cl film as compared to that of reference. The enhanced PL intensity indicates the reduction in non-radiative recombination in the CsFA-Cl based perovskite film, which further leads to an increased V_{oc} values of devices [216]. This predicted enhancement of V_{oc} was later confirmed

by the J-V measurement of solar cells (discussed in Section 4.2.3). Furthermore, the charge carrier dynamics of perovskite was studied by time resolved PL (TRPL) measurements. The TRPL spectra showed a slower PL decay of CsFA-Cl film as compared to that of CsFA-I based film (Fig 4.4 (b)). Estimated carrier lifetimes from these measurements were found to be 108.4 ns and 38.6 ns for CsFA-Cl and CsFA-I films, respectively. The extended carrier lifetime in case of CsFA-Cl perovskite indicates that the addition of CsCl in the precursor solution reduces the non-radiative recombination related to the traps and defects present in the perovskite.

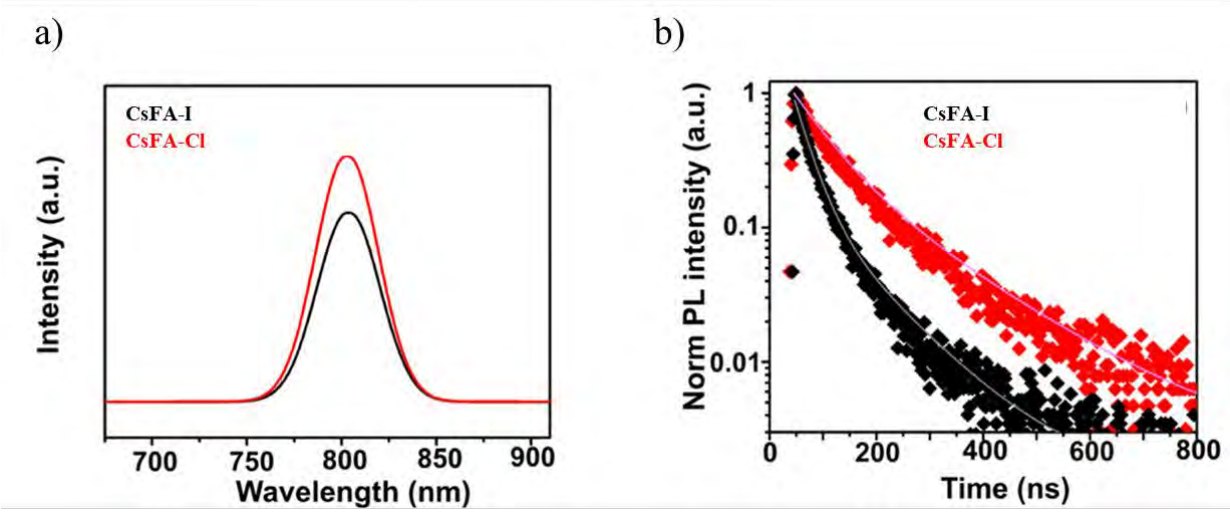

Fig. 4.4: (a) PL emission spectra of CsFA-I (black) and CsFA-Cl (red) perovskite films. (b) UV-Vis absorption spectra of both the films (adapted from [212]).

The energy levels of the perovskite materials prepared from both CsI and CsCl were analysed by ultraviolet photoelectron spectroscopy (UPS). In case of the CsFA-Cl material, the fermi level is shifted deeper from -4.62 eV (reference) to -4.89 eV (Fig 4.5 (a)). This shift shows that the addition of CsCl makes the perovskite more p-type, leading to a higher electrostatic field at the interface of perovskite and ETL and hence better charge transport. The difference between valence band and Fermi level was calculated from the onset energy in the low binding energy region (Fig. 4.5 (b)). A small difference was observed in the estimated valence band values between CsFA-Cl (-5.39 eV) and CsFA-I (-5.37 eV) films, which can be attributed to the difference in the amount of FA cations present in the abovementioned perovskite compositions. By using the calculated band gap values, the conduction band was also determined to be -3.78 eV and -3.8 eV for CsFA-I and CsFA-Cl films, respectively. The alignment of energy levels for these two perovskite films is shown in Fig. 4.5 (c).

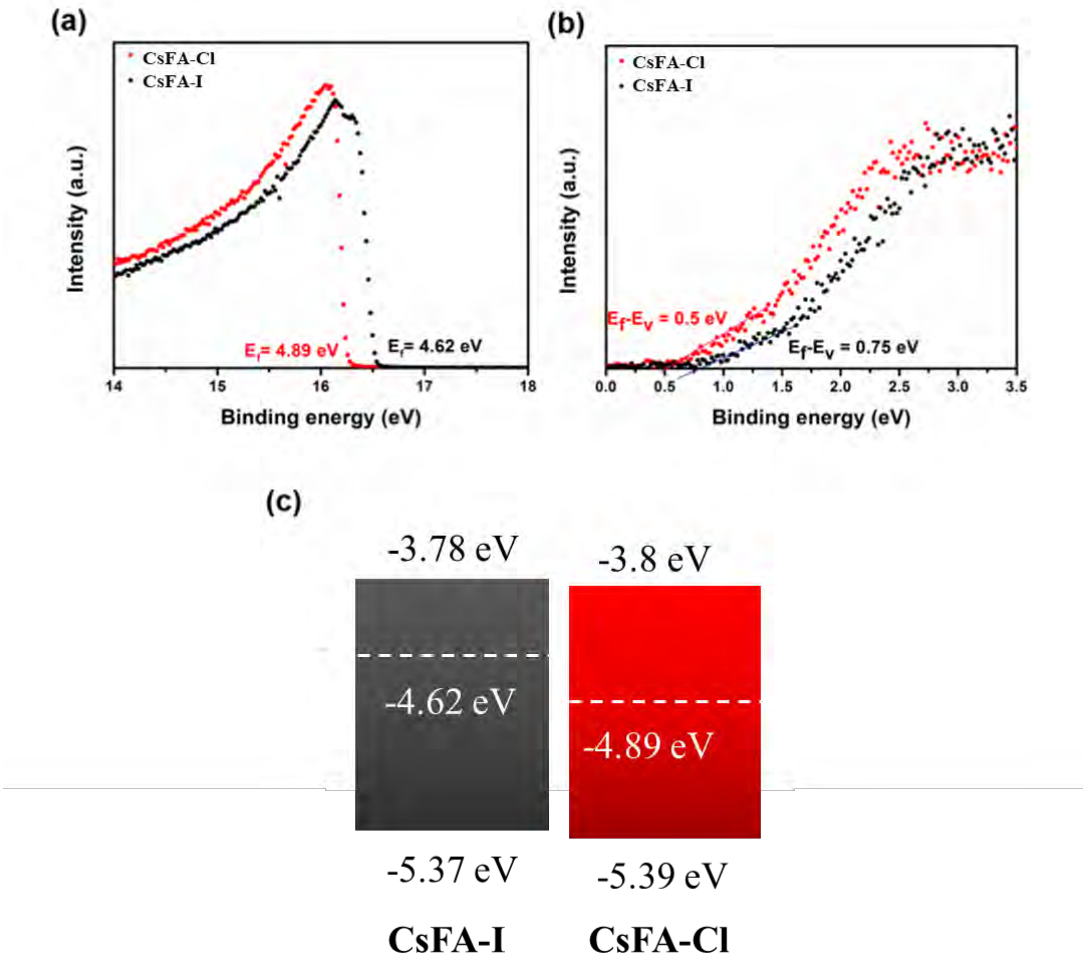

Fig. 4.5: UPS measurements of CsFA-I (black) and CsFA-Cl (red) films representing the (a) Fermi levels and (b) difference between Fermi level and valence band. (c) band alignment of respective films (adapted from [212]).

4.2.3 Fabrication and characterization of $Cs_{0.2}FA_{0.8}PbI_3$-based mesoscopic solar cells

In order to see the performance of solar cells based on CsFA-Cl, as compared to the reference one based on CsFA-I, the mesoscopic device architecture of glass/FTO/c-TiO_2/m-TiO_2/$Cs_xFA_{1-x}PbI_3$/spiro-OMeTAD/Au was adopted. As discussed in the experimental section of Chapter 2, devices were fabricated on cleaned FTO substrates and a combination of compact and mesoporous layer of TiO_2 was deposited as the ETL. Next, the perovskite precursor solution of $Cs_{0.2}FA_{0.8}PbI_3$ was spin-coated by both a modified as well as the traditional approach (explained in section 4.2.1). Finally, the devices were completed by spin-coating

spiro-OMeTAD as the HTL and gold was evaporated as the back electrode. These solar cells were subsequently characterized by the current density-voltage (J-V) measurements. Fig. 4.6 (a) shows the J-V curve of best solar cells fabricated from CsFA-Cl and CsFA-I measured under AM 1.5G irradiation at 100 mWcm^{-2}. The reference device showed the PCE of 15.87% with a J_{sc} of 22.78 mA cm^{-2}, a V_{oc} of 1.01 V, and a FF of 68.7%. However, when the CsFA-Cl perovskite active layer was employed into the device, a significantly higher efficiency of 20.6% was achieved. As compared to the reference PCE, this was a striking increase of ~30 %. In this case, other device parameters were also improved with a high J_{sc} of 24.1 mA cm^{-2}, a V_{oc} of 1.10 V, and a FF of 77.6%. The performance of the best cell for CsFA-Cl was also studied by tracking the stabilized power output at maximum power point (MPP) for a period of 60 seconds as shown in Fig. 4.6 (b). As discussed in Chapter 1, the power output at MPP is the product of current (I_{MPP}) and voltage (V_{MPP}) and it gives the maximum power that a solar cell can deliver. A steady-state efficiency as high as 19.85% was obtained for the CsFA-Cl based cells, showing the high stability of devices.

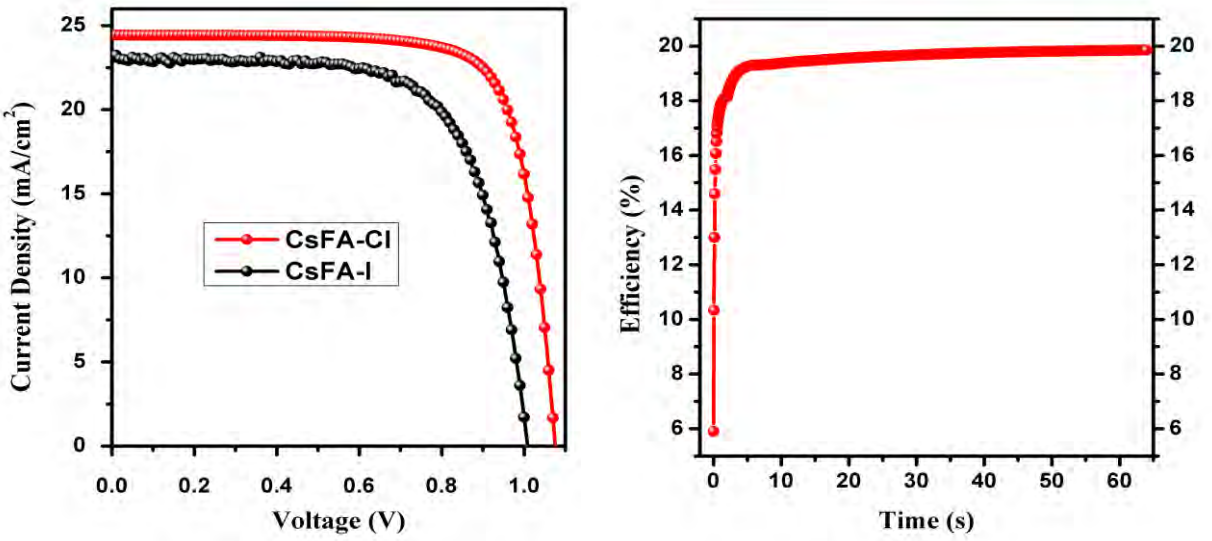

Fig. 4.6: (a) J-V characteristics of champion devices based on CsFA-Cl (red) and CsFA-I (black) perovskites (b) Maximum power point tracking of champion device for CsFA-Cl [212].

In order to check the reproducibility, several devices were fabricated for both CsFA-I and CsFA-Cl perovskite materials. The statistical distribution of device parameters is shown in the form of box plots in Fig. 4.7. It was found that devices showed very good reproducibility with

the average device efficiency of 19.15 ± 0.63 %. An overall improvement was observed in every parameter as compared to the reference devices. It is well known that V_{oc} is directly related to the recombination of mobile charge carriers at defects in the perovskite layer [217]. Therefore, the increase in the V_{oc} of CsFA-Cl devices, which correlated with the enhancement of PL intensity, indicates that the defect concentrations in the perovskite layer are reduced. The average value of all the device parameters as well as parameters for best performing cells are listed in Table 4.1.

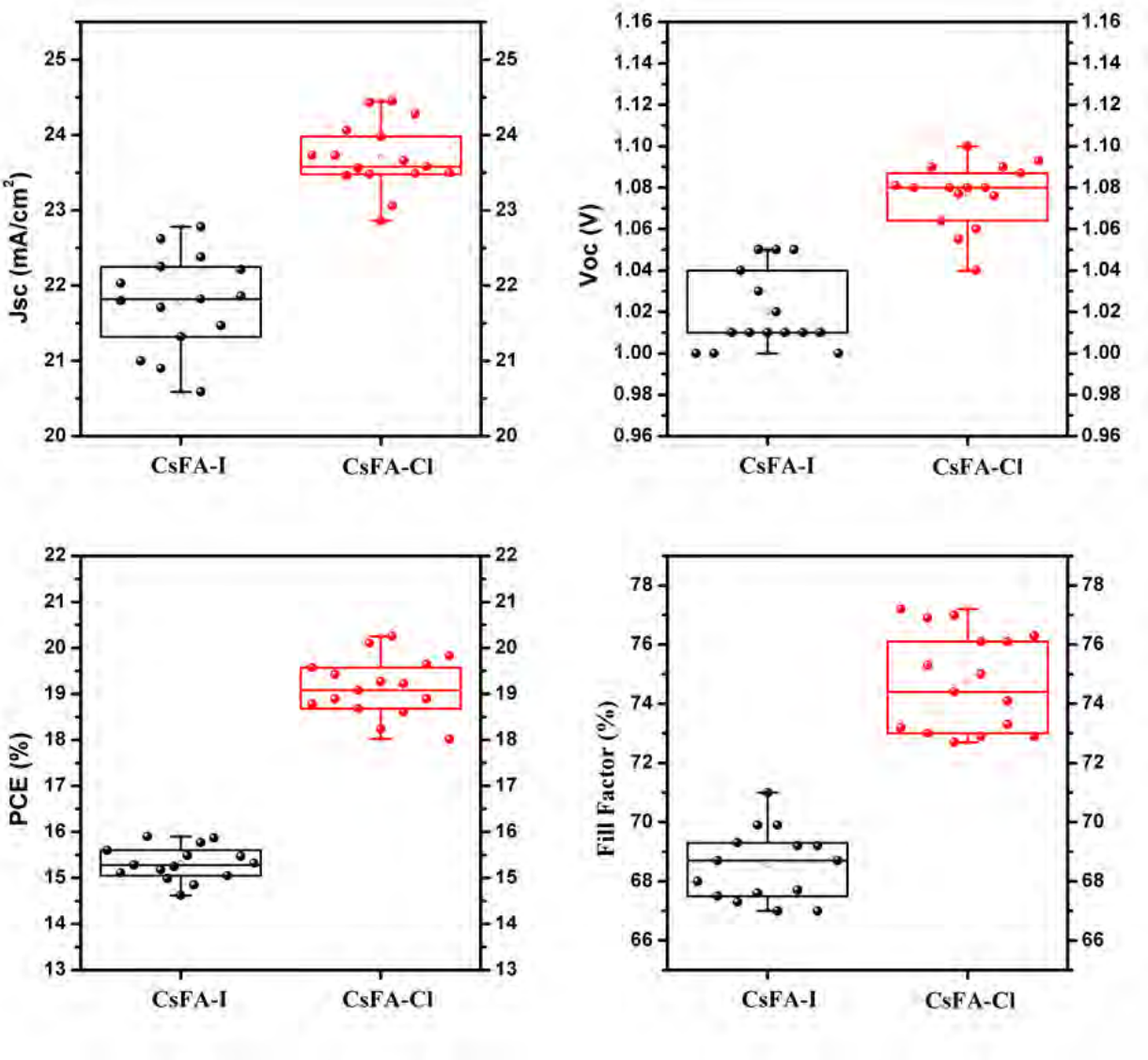

Fig. 4.7: Statistics of J_{sc}, V_{oc}, PCE and FF for several devices made with CsFA-I and CsFA-Cl perovskites [212].

Table 4.1: Device parameters for best performing cell and averaged values of several cells based on CsFA-I and CsFA-Cl perovskites.

Perovskite	Device	Jsc ($mAcm^{-2}$)	V_{oc} (V)	FF (%)	PCE (%)
CsFA-I	Best	22.78	1.01	68.7	15.87
	Average	21.78±0.63	1.02±0.02	68.5±1.2	15.31±0.37
CsFA-Cl	Best	24.1	1.10	77.6	20.6
	Average	23.70±0.44	1.07±0.02	74.8±1.6	19.15±0.63

Incident photon to current efficiency (IPCE) spectrum was recorded for perovskite films, which confirmed the improvement of external quantum efficiency for CsFA-Cl perovskite as compared to the reference. The IPCE value at a particular wavelength is the total current that a solar cell will generate when photons of that wavelength will be incident on it. To get the current density (J_{sc}), IPCE values are integrated all over the solar spectrum. Both IPCE and calculated current density plots are shown in Fig. 4.8. The J_{sc} value of CsFA-Cl based cells calculated from IPCE spectrum was found to be 23.70 $mAcm^{-2}$, which is within 2% error of the J_{sc} value obtained from the J-V curve.

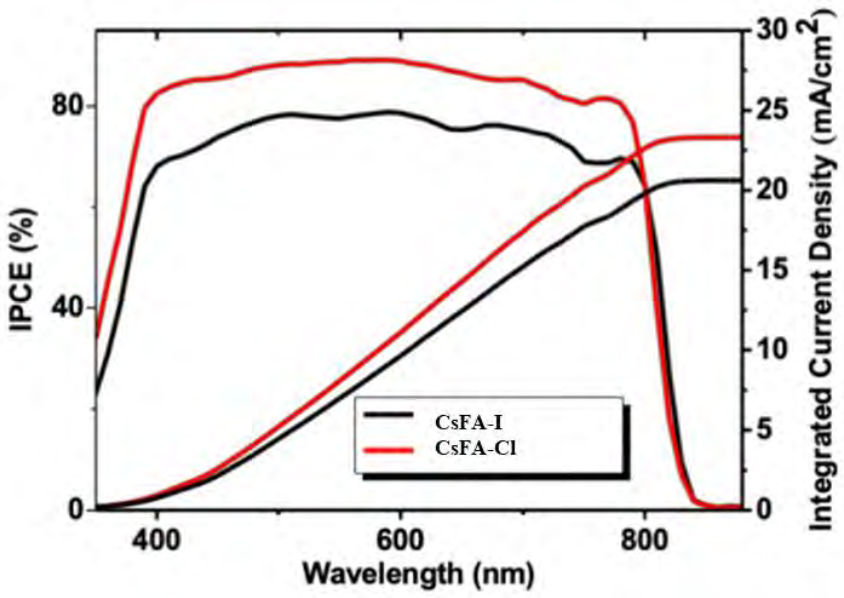

Fig. 4.8: IPCE spectra and calculated J_{sc} for films made with CsFA-I (black curve) and CsFA-Cl (red curve) perovskites [212].

Next, the hysteresis behaviour of devices was also studied by measuring the forward and backward J-V scans. Hysteresis is the difference in J-V curves during backward scan from open-circuit to short circuit conditions and forward scan from short-circuit to open circuit conditions. As shown in Fig. 4.9, the difference in backward and forward scans is higher in case of the CsFA-I based device as compared to that based on CsFA-Cl. Due to the improved morphology and larger grain size in case of CsFA-Cl perovskite layers, the charge transfer is better as compared to the reference films and this leads to the lower hysteresis [218].

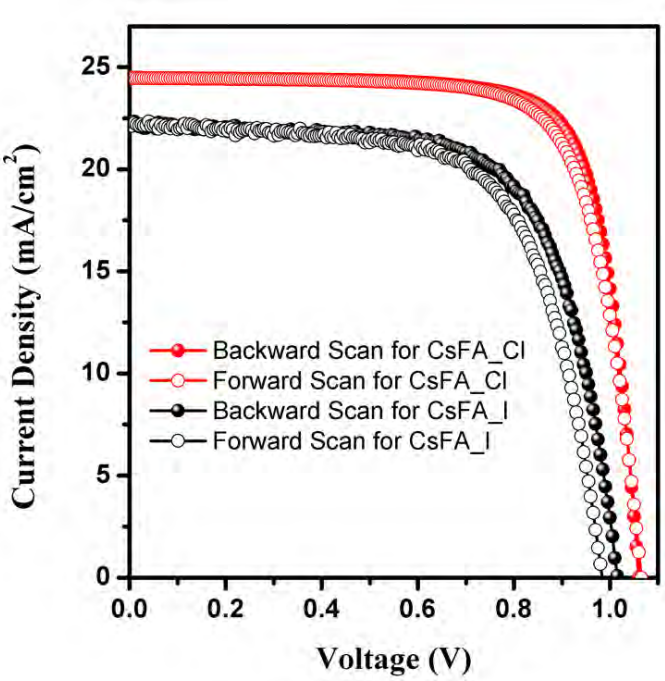

Fig. 4.9: Backward and forward J-V scans for CsFA-Cl (red curves) and CsFA-I (black curves) perovskites based devices [212].

The hysteresis index was calculated for devices made from CsFA-Cl and CsFA-I materials by applying the formula $h = 100 \times (PCE_{BS} - PCE_{FS})/ PCE_{BS}$, where PCE_{BS} is the PCE for backward scan and PCE_{FS} is the PCE forward scan. These values are listed in Table 4.2 and it can be seen that the hysteresis index of CsFA-Cl based devices is lower as compared to that of reference devices. The CsFA-Cl based cells show lower hysteresis due to the larger perovskite grains and a reduced grain boundary, which facilitates better charge transfer.

Table 4.2: Device parameters and hysteresis indices for CsFA-Cl and CsFA-I devices for forward and backward JV scans at a scan rate of 200 mV/s.

Device	Scan direction	V_{oc} (V)	J_{sc} (mA/cm^2)	FF (%)	PCE (%)	ΔPCE
CsFA-I perovskite based	Backward	0.99	22.94	67.9	15.57	**0.92**
	Forward	0.96	22.88	66.1	14.65	
	Backward	1.01	22.12	67.8	15.36	**0.82**
	Forward	0.98	22.20	66.0	14.54	
	Backward	0.98	22.54	67.2	14.95	**0.87**
	Forward	0.94	22.70	65.5	14.08	
CsFA-Cl perovskite based	Backward	1.07	24.10	77.2	19.94	**0.56**
	Forward	1.07	24.10	74.9	19.38	
	Backward	1.06	23.79	76.5	19.37	**0.59**
	Forward	1.06	23.77	73.9	18.78	
	Backward	1.04	24.51	75.5	19.33	**0.63**
	Forward	1.04	24.50	73.0	18.70	

4.2.4 Improvement of solar cell performance by passivation of perovskite layer

In the next sub-task, the aim was to further improve device performance by reducing the defects in the perovskite layer. The polycrystalline film deposited by spin-coating method usually contain large amount of defects in the form of crystallographic disorder, grain boundary disorder or vacancy defects [36,219]. These deformities promote the non-radiative charge carrier recombination and ion transport at the interface, leading to poor device performances. Additionally, perovskite films with defects tend to degrade faster in the presence of moisture. Therefore, these defects need to be mitigated in order to have better charge transport at the interface of perovskite and HTL. One of the most common ways to reduce these defects is the surface passivation of perovskite layer via various organic or inorganic additives, that makes the perovskite layer less affected by external environment [36,176]. These additives improve the device efficiencies by filling the vacancy defects, improving interfacial contact, improving

band alignment, blocking humidity and gold atom from penetrating inside the perovskite layer. or blocking the minority carriers at the interface.

In this work, two different organic additives were used for the passivation of CsFA-Cl perovskite layer: 1-adamantylamine (ADA) and guanidinium iodide (GuaI). As explained in the experimental section of Chapter 2, these compounds were dissolved in isopropyl alcohol (IPA) in different concentrations and they were deposited on top of the CsFA-Cl perovskite layer followed by annealing at 100 °C for 10 min. To see the effect of passivation, reference devices with only CsFA-Cl layer were also fabricated for comparison. In case of ADA, three solution concentrations of 1 mg/mL, 3 mg/mL and 5 mg/mL (ADA 1, ADA 3 and ADA 5) were prepared and the respective devices were fabricated with a thin layer of ADA passivation between the perovskite and spiro-OMeTAD layer. The subsequent J-V measurements of these photovoltaic cells indicated that there was no improvement in the device efficiencies after the

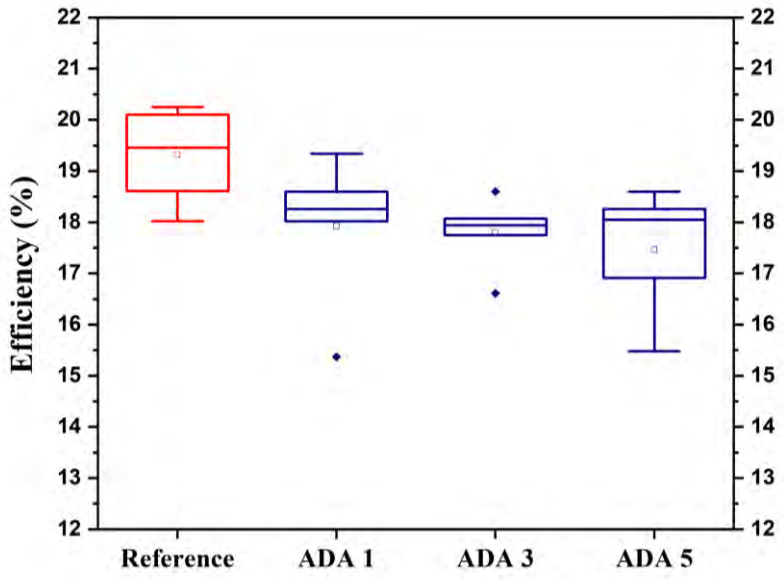

Fig. 4.10: Statistics of PCE for several devices made from CsFA-Cl perovskites with passivation of different ADA solution concentrations.

addition of ADA. Fig. 4.10 shows the PCE of several devices made for each conditions and it can be clearly seen that all the passivated devices had lower performances than the reference devices without passivation layer. Additionally, the efficiencies of solar cells decreased with increasing ADA concentrations. Therefore, no further devices were fabricated with the ADA passivation.

Next, the molecule GuaI was explored for the passivation of CsFA-Cl perovskite layer. Since the molecular weight of GuaI (186.98 g/mol) is larger than the ADA (151.25 g/mol), higher GuaI solution concentrations were investigated in order to avoid the extremely diluted solutions. Three solutions of GuaI in IPA were prepared with concentrations of 3 mg/mL, 5 mg/mL, and 10 mg/mL (Gua 3, Gua 5 and Gua 10). Following the same reaction conditions as in the case of ADA passivation, a thin passivation layer of Gua solution was deposited on top of the perovskite layer and other layers were deposited to complete the device structure as explained previously. These passivated devices along with the reference device without passivation were further characterized by J-V measurements. Fig. 4.11 shows the statistics of

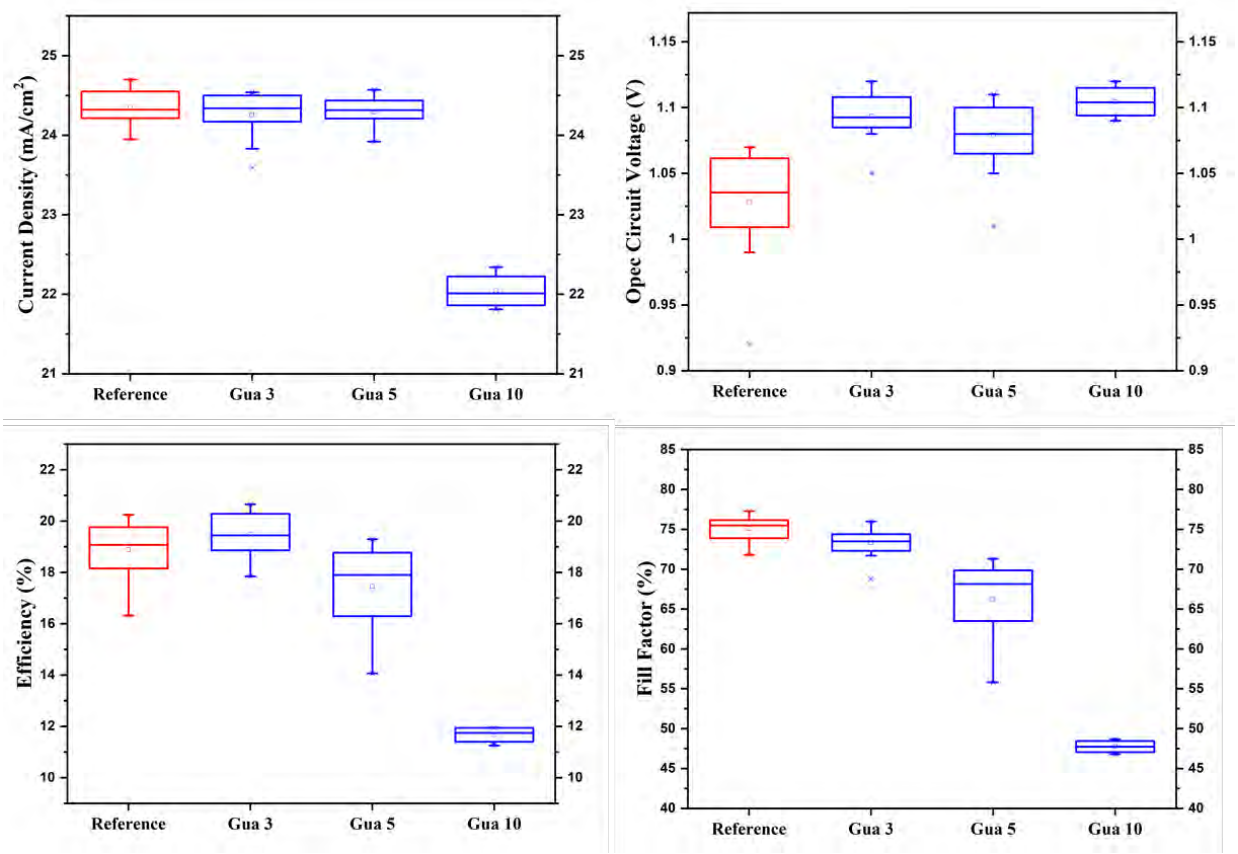

Fig. 4.11: Statistics of J_{sc}, V_{oc}, FF and PCE for several devices made from CsFA-Cl perovskites with passivation of different Gua solution concentrations.

device parameters of several devices made with each Gua solution as compared to the reference devices. The passivation from 3 mg/mL Gua solution showed improvement in the V_{oc} and PCE as compared to the reference device. Other Gua solutions with higher concentration also showed an increase in overall V_{oc} of passivated devices. V_{oc} as high as 1.12 V was obtained

after passivation with the Gua 3 solution. The enhancement in V_{oc} is indicative of the improved perovskite/spiro-OMeTAD interface due to the reduction in defect states. However, FF decreased with increasing the Gua solution concentration and hence devices showed poor performances as compared to that of the reference. The highest PCE achieved with the passivation using 3 mg/mL Gua solution was 20.66%. In case of the passivation with Gua 10 solution, the J_{sc} and FF reduced drastically and hence the resulting PCE was lowest.

The IPCE measurement of devices with the Gua passivation from different solution concentrations also showed similar characteristics. As compared to the reference, devices with Gua 3 and Gua 5 passivation had similar external quantum efficiencies (Fig. 4.12 (a)). On the other hand, passivation with Gua 10 solution decreased the external quantum efficiencies and hence the J_{sc} values. The integrated current density plot as a function of wavelength in Fig. 4.12 (b) shows the decreasing trend in the J_{sc} values with increasing Gua solution concentration. The J_{sc} for the reference device and devices with passivation from Gua 3 and Gua 5 solutions were calculated to be 23.67 mA/cm^2 23.72 mA/cm^2, and 23.43 mA/cm^2, respectively. However, solution passivation by Gua 10 decreased J_{sc} to the lowest value of 22.89 mA/cm^2.

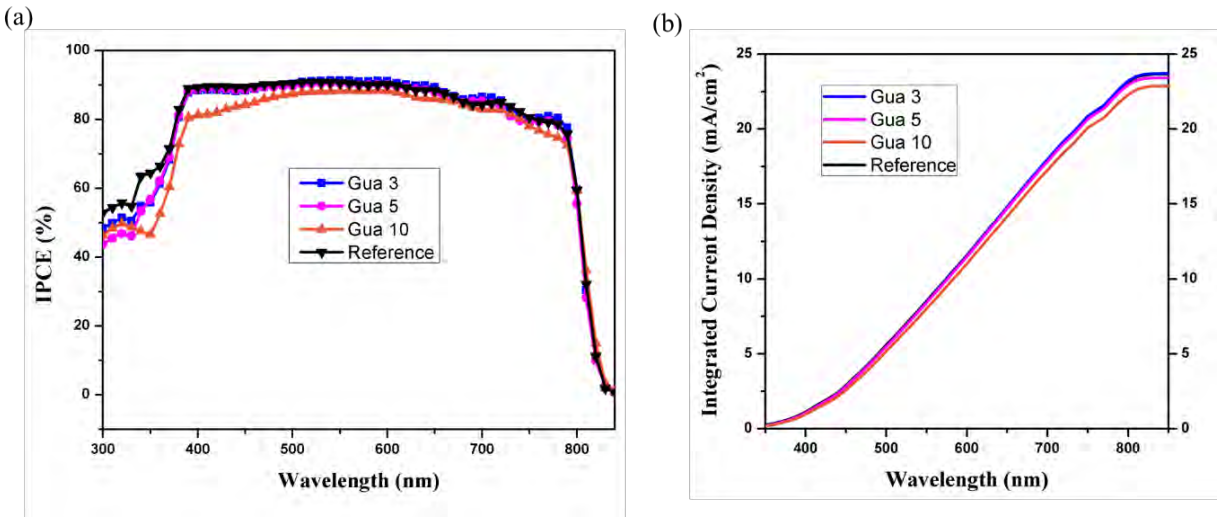

Fig. 4.12: (a) IPCE spectra and (b) calculated J_{sc} of reference and passivated devices made with CsFA-Cl perovskites

Furthermore, the effect of adding thin layer of 3mg/mL Gua solution on the CsFA-Cl perovskite layer was studied by optical characterization techniques such as UV-Vis and steady state PL spectroscopy. As shown in Fig. 4.13 (a), no notable difference was observed in the absorption characteristics of reference perovskite film and passivated film by Gua 3 solution.

The absorption onset was close to 800 nm for both the films, which means there was no change in the bandgap. A slight change in the slope of absorption curve was observed around 550 nm for the passivated film, which could be attributed to the formation of a 2D perovskite phase on top of the CsFA-Cl perovskite [36]. Subsequently, the PL measurements of the aforementioned perovskite films showed that the emission was significantly enhanced after the passivation from Gua 3 solution (Fig. 4.13 (b)). This increase in the PL intensity suggests the suppression of non-radiative recombination in the passivated perovskite film, which resulted in the increase of V_{oc} of passivated devices. However, a shoulder was observed in the passivated film at around 750 nm as opposed to that of the reference [36]. The shoulder peak can be due to the creation of a potential 2D perovskite phase on the surface of CsFA-Cl perovskite layer and this observation is in accordance with UV spectra of films.

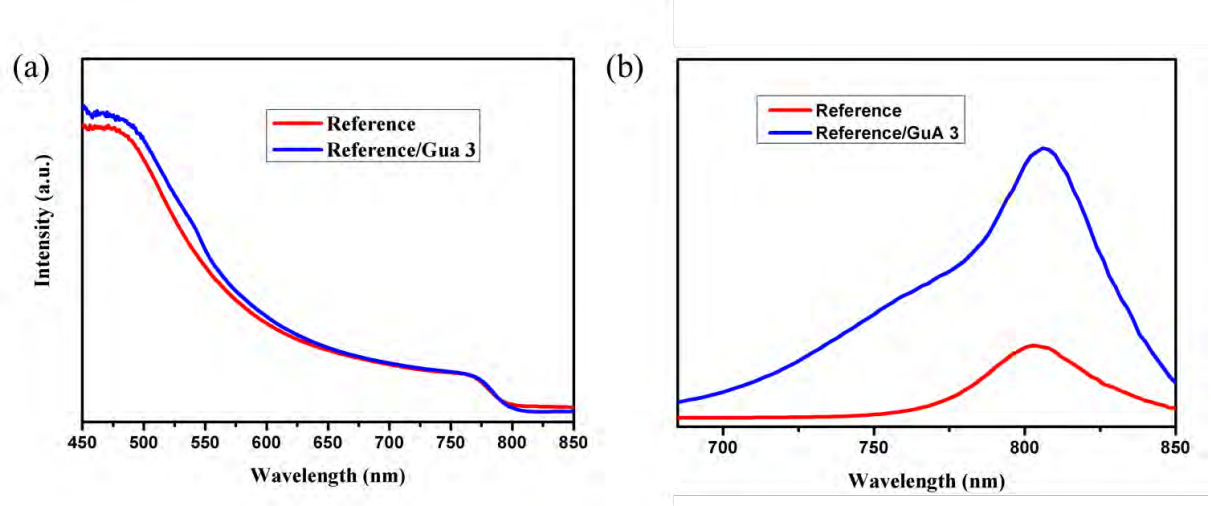

Fig. 4.13: (a) UV-Vis absorption spectra and (b) PL emission of CsFA-Cl perovskite film without passivation (red curve) and passivated film with Gua 3 solution (blue curve).

4.3 Conclusions

In conclusion, high-efficiency solar cells based on double cation $Cs_xFA_{1-x}PbI_3$ perovskite layers were fabricated by devising a modified one-step solution processing approach. This method proved to be very effective for the preparation of highly uniform $Cs_{0.2}FA_{0.8}PbI_3$ films by using CsCl as the source of Cs cation. Upon addition of excess CsCl to the $FAPbI_3$ precursor solution, the resultant perovskite films showed large size and high quality of grains. The improved

crystallinity and larger grain size as compared to the reference film led to longer carrier lifetimes. The champion solar cell device in the mesoscopic architecture showed a high-efficiency of 20.6% with a stabilized PCE of 19.85% and a low hysteresis. Furthermore, two organic molecular additives namely, 1-adamantylamine (ADA) and guanidinium iodide (GuaI), were investigated for the passivation of the CsFA-Cl perovskite layer. While adding a thin passivation film of ADA resulted in lower device efficiencies, the GuaI layer between perovskite layer and hole transporting layer slightly enhanced the solar cell performance. Due to the GuaI passivation, the interface improved through the reduction of defects and suppressed non-radiative recombination, which caused slight enhancement in V_{oc} and PCE of solar cells. These results suggested that the newly devised solution processing method effectively produces excellent perovskite films and passivation by GuaI reduces defects in the perovskite films, resulting into high performance mesoporous PSCs.

Chapter 5: Interfacial engineering of ZnO quantum dots based electron transporting layer for high-efficiency planar perovskite solar cells

5.1 Introduction

Zinc oxide (ZnO) being an n-type semiconductor, has attracted a lot of attention in PSC research as a replacement for the commonly used electron transporting material, TiO_2 [119,120,220] as discussed in Chapter 1. Moreover, nanostructured materials of ZnO can be easily processed at low temperatures and are thus applicable to flexible perovskite solar cell (PSC) devices [17,221,222]. Various ZnO nanostructures such as nanoparticles, nanorods, nanotubes, and quantum dots (QDs) have been investigated for application in PSCs [124,125,223]. Notably, in the case of QDs, the electron injection is increased due to the production of multiple excitons while absorbing UV light [18]. Additionally, the deposition of QDs results in tighter, more compact ZnO film structures and subsequently supports the formation of unconstrained perovskite microcrystalline layer [126,127].

In this chapter, the device fabrication of high-efficiency planar PSCs based on novel ZnO QDs is discussed. The newly developed ZnO QDs coated by the zwitterionic surfactant betaine were utilized as the electron transporting layer (ETL) in the planar device structure, resulting in a maximum power conversion efficiency (PCE) of 16.7%. For further improving the interface between the ETL and the perovskite layer, passivation with various ammonium halides (NH_4F, NH_4Cl, and NH_4Br) was carried out. By systematically studying the effect of these additives on device performances, it was observed that the passivation with ammonium halides leads to a significant increase in the PCE of solar cells. They effectively improve the ZnO/perovskite interface by reducing the non-radiative recombination that resulted in increased open-circuit voltage. Additionally, ammonium halide passivation leads to an improved energy level alignment between ZnO and perovskite. This band alignment caused a substantial increase of fill factor (FF) from 71.5 % to 80.3 % in case of NH_4F passivation. As a result, the best device with NH_4F passivation produced a champion efficiency of 21.9%. Remarkably, the highest PCE of NH_4F passivated device was ~31 % higher than that of the reference device without

any passivation. The solar cells were also relatively stable, retaining ~78% of the initial efficiency after a continuous exposure to 1 Sun illumination for 250 h.

5.2 Results and Discussions

5.2.1 Thin film formation of ZnO QDs and device fabrication of planar PSCs

The newly developed ZnO QDs coated by the zwitterionic surfactant betaine were utilized as the ETL in a planar device structure of FTO/ZnO/$(FAPbI_3)_{0.97}(MAPbBr_3)_{0.03}$/EAI/spiro-OMeTAD/Au. The ZnO QDs were synthesized by the Ph.D. student Zygmunt Drużyński from the Lewiński group at the Warsaw University of Technology. The as obtained microcrystalline ZnO powder was initially dissolved in ethanol with a concentration of 5 mg/mL and sonicated for 25-30 min as described in the experimental section of Chapter 2. Before spin-coating, the ZnO solution was filtered to avoid any aggregates. Next, this solution was spin-coated on the cleaned FTO substrate followed by thermal annealing at 150 ºC for 30 min. Various thicknesses of ZnO layers were formed by depositing the solution multiple times with intermediate annealing at 150 ºC for the removal of solvents. Subsequently, in order to examine the working of devices based on these ZnO QDs as ETL, planar PSCs with a device structure of

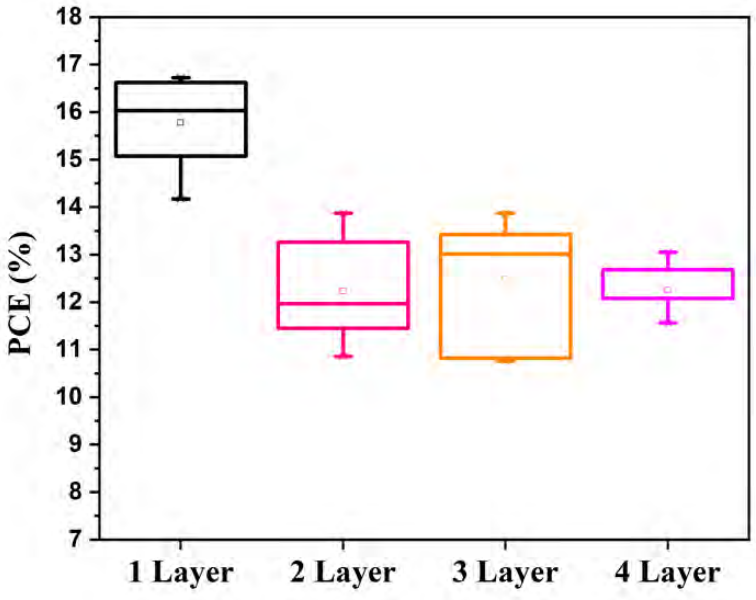

Fig. 5.1: Statistical distribution of devices with different number of ZnO QDs layers from 5 mg/mL solution.

FTO/ZnO/$(FAPbI_3)_{0.97}(MAPbBr_3)_{0.03}$/EAI/Spiro-OMeTAD/Au were fabricated. ZnO layer was deposited as explained previously and a solution concentration of 5mg/mL of the solution was utilized. Next, the perovskite precursor solution was spin coated by one-step deposition technique using chlorobenzene as the antisolvent, followed by annealing at 150 ºC for 30-40 min (details in the experimental section of Chapter 2). After being cooled down to room temperature, a thin passivation layer of ethylammonium iodide (EAI) was formed on top of perovskite layer. Finally the device structure was completed by spin-coating the spiro-OMeTAD solution and evaporating the gold layer. These devices were then characterized by the current density-voltage (J-V) measurements under 1 Sun illumination. The statistical distribution of devices made with different numbers of deposited layers with 5 mg/mL ZnO QD solution is presented in Fig. 5.1. Among these, devices with one layer of 5mg/mL ZnO QD solution showed the highest efficiency of 16.7% with a short circuit current density (J_{sc}) of 22.7 mA/cm^2, a fill factor (FF) of 71.5% and an open circuit voltage (V_{oc}) of 1.03 V. Films with multiple layers of ZnO QD solution produced lower efficiency devices. Therefore, one layer of 5mg/mL ZnO solution was employed for further optimization of devices.

5.2.2 Introduction of ammonium halides between the ZnO and perovskite layer and respective device properties

As explained in Section 1.7 of Chapter 1, the PSCs based on ZnO ETL are susceptible to degradation due to the surface defects and chemical instability of ZnO. Therefore, a lot of efforts are being made to passivate the interface between the ZnO layer and perovskite for the improvement of the photovoltaic performance of planar PSCs. A previous work has shown the use of quaternary ammonium halides for the passivation of defects and trap states present on the surface of metal halide perovskites [224]. Due to the chemical structure of $NR^{+4}X^{-}$, where R is an alkyl or aryl group and X is a halide, they effectively passivate both positively and negatively charged defects through quaternary ammonium and halide ions. For the effective passivation of ZnO/perovskite interface, amine halides have also been utilized as an additive [225,226]. In another report, ammonium fluoride was used as the surface passivation agent of SnO_2-based ETL in the planar PSC [227]. The authors showed that the ammonium fluoride reduced the surface defect sites and adjusted the Fermi energy level of SnO_2, leading to enhanced photovoltaic efficiencies. Therefore, in next sub-task, the aim was to investigate several ammonium halides (NH_4F, NH_4Cl, and NH_4Br) as passivation agents between the ZnO QDs ETL and perovskite layer for improving the device performance.

To see the effect of introducing ammonium halides at the interface of ZnO/perovskites, two strategies were followed: 1) mixing of ammonium halides with 5 mg/mL ZnO solution and subsequent film deposition and 2) post treatment surface passivation of ZnO films by ammonium halide solution. Three concentrations (1, 3, and 5 mg/mL) of NH_4F, NH_4Cl, and NH_4Br solution were investigated in each case of passivation. In the first strategy, the solutions were prepared by adding appropriate amounts of ZnO QDs and NH_4X together in ethanol (for details, see the experimental section of Chapter 2). This solution was filtered and then spin coated on the cleaned FTO substrate and annealed at 150 ^oC for removing the solvent. After depositing the perovskite, spiro-OMeTAD, and Au layers, the device performances were analysed by the J-V measurements. For comparison, reference devices containing ZnO layer without any passivation were also fabricated and characterized. It was found that among all the passivation solutions explored, the highest PCEs were achieved with the films of mixed ZnO QDs (5mg/mL) and NH_4F (1 mg/mL), ZnO QDs (5mg/mL) and NH_4Cl (3 mg/mL), and ZnO QDs (5mg/mL) and NH_4Br (1 mg/mL), respectively. The highest efficiency of 19.2 % was achieved with NH_4F, 18.6 % with NH_4Cl, and 18.1 % with NH_4Br additions. The J-V characteristics of devices with mixed ammonium halides and ZnO QDs are shown in Fig. 5.2 (a). These results showed that mixing the passivating agents with ETL resulted into an overall increase in the device performance. In the second strategy of passivation, a thin passivation layer of ammonium halide solution (in DI water) was deposited on the surface of the ZnO QDs layer. Again three concentrations (1, 3 and 5 mg/mL) of each ammonium halides were investigated as in the case of mixing during the first strategy. After the deposition of ammonium halides as a surface passivation layer on top of ZnO, subsequent annealing was also carried out at 150 ^oC. The device structure was completed by deposition of other layers and the J-V characteristics of devices were recorded. Correspondingly control devices without passivation were also fabricated and characterized for comparison. The J-V measurements showed a significant improvement in device performance from the second approach as compared to that of the first strategy. A champion PCE of 21.9% was achieved in case of NH_4F with the second strategy of post treatment passivation. It was a remarkable ~ 31% increase of PCE relative to the reference device without passivation. The NH_4F passivated device showed highest increase in case of FF (from 71.5 to 80.3%) and a slight increase in V_{oc} was also observed, pointing toward the improvement of ZnO/perovskite interface. NH_4Cl and NH_4Br passivation also resulted into the improvement of device performances with the best PCEs of

20.8% and 20.1%, respectively. The device parameters for champion cells made from the second strategy without and with different passivation are listed in Table 1.

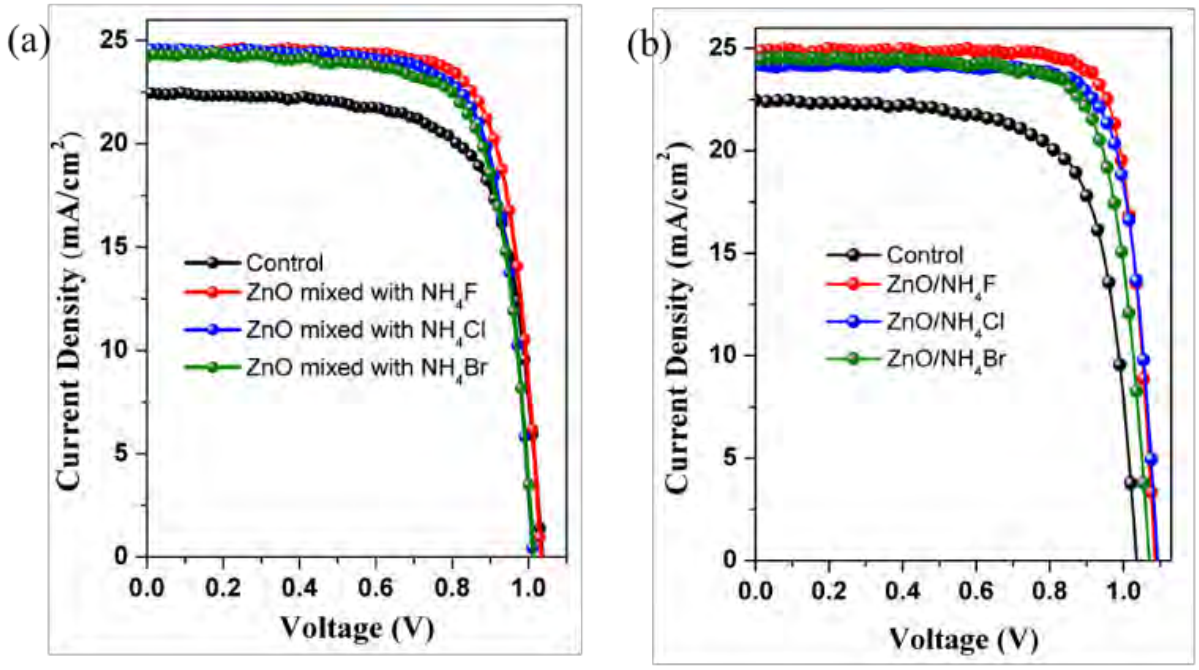

Fig. 5.2: J-V characteristics of devices (a) with mixed ammonium halides in ZnO solution (b) with ammonium halides post treatment passivation of ZnO layer.

Table 1: Device parameters for best performing cell with and without post treatment NH_4X passivation.

Device	**J_{sc} (mAcm^{-2})**	**V_{oc} (V)**	**FF (%)**	**PCE (%)**
Control (ZnO)	22.7	1.03	71.5	16.7
ZnO/NH_4F	25.0	1.09	80.3	21.9
ZnO/NH_4Cl	24.4	1.10	77.4	20.8
ZnO/NH_4Br	24.4	1.08	76.4	20.1

Fig 5.2 (b) shows the J-V characteristics of devices with passivation as compared to the control device without passivation. Since the second strategy of post treatment passivation produced the best results, only devices and films made from this strategy were further investigated. PSCs are known to be prone to hysteresis and PCE is susceptible to scan direction in the J-V measurements. The origin of hysteresis might be due to the perovskite's unique interactions

with ambient moisture, resulting in freely migrating species in addition to inherent point defects [37]. Hence, in order to check the hysteresis behaviour, forward and backward scans were performed for the passivated devices. As shown in Fig. 5.3 (a-c), the device with NH_4F passivation displayed the least hysteresis and the device with NH_4Br passivation displayed the largest hysteresis in J-V scan. The lower hysteresis in the first case could be attributed to the better charge transfer due to the improved ZnO/perovskite interface.

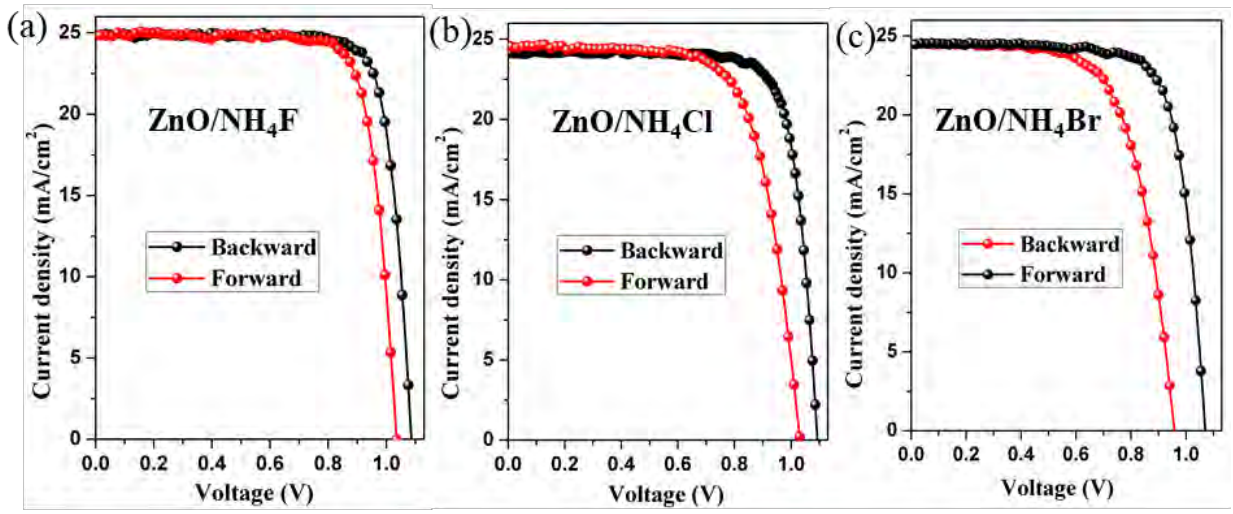

.

Fig. 5.3: Forward and backward scans of devices with the post treatment passivation of (a) NH_4F (b) NH_4Cl and (c) NH_4Br.

The high performance of solar cell devices was also verified by measuring the scan independent power output at maximum power point (MPP) under 1 Sun illumination. While monitoring the efficiency for 60 s, a steady state efficiency of 20.8%, 19.3%, and 17.5% was obtained for passivated devices with NH_4F, NH_4Cl, and NH_4Br, respectively (Fig 5.4).

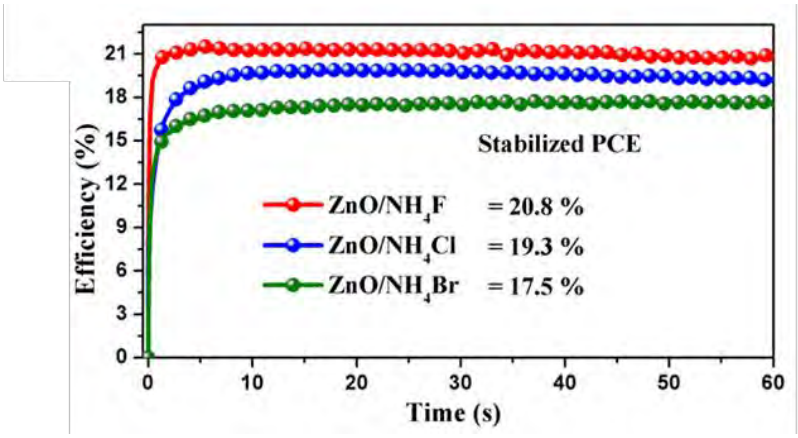

Fig. 5.4: Stabilized PCE of passivated devices monitored at MPP for 60 s.

The consistency of device performances was next examined by fabricating several devices in the same conditions and they were analysed by measuring the J-V curves. Statistical distribution of the device parameters for several devices made for each condition is presented in Fig 5.5. It was observed that the reproducibility of solar cells increases after the addition of passivation layer of NH_4X on top of ZnO QDs layer, as indicated by lesser variations in the PCE of passivated devices. As compared to the control devices, the average FF, V_{oc}, and J_{sc} are higher in the passivated devices. Interestingly, the highest increase was observed in the FF, signifying the improved interface between ETL and perovskite layer. The average V_{oc} of devices after passivation was also increased slightly relative to the control devices. During these J-V characterization of devices with post treatment passivation, it was realized that NH_4F passivation consistently produced best results as compared to other two ammonium halides, therefore, further detailed analysis was carried out only for films and devices with NH_4F passivation.

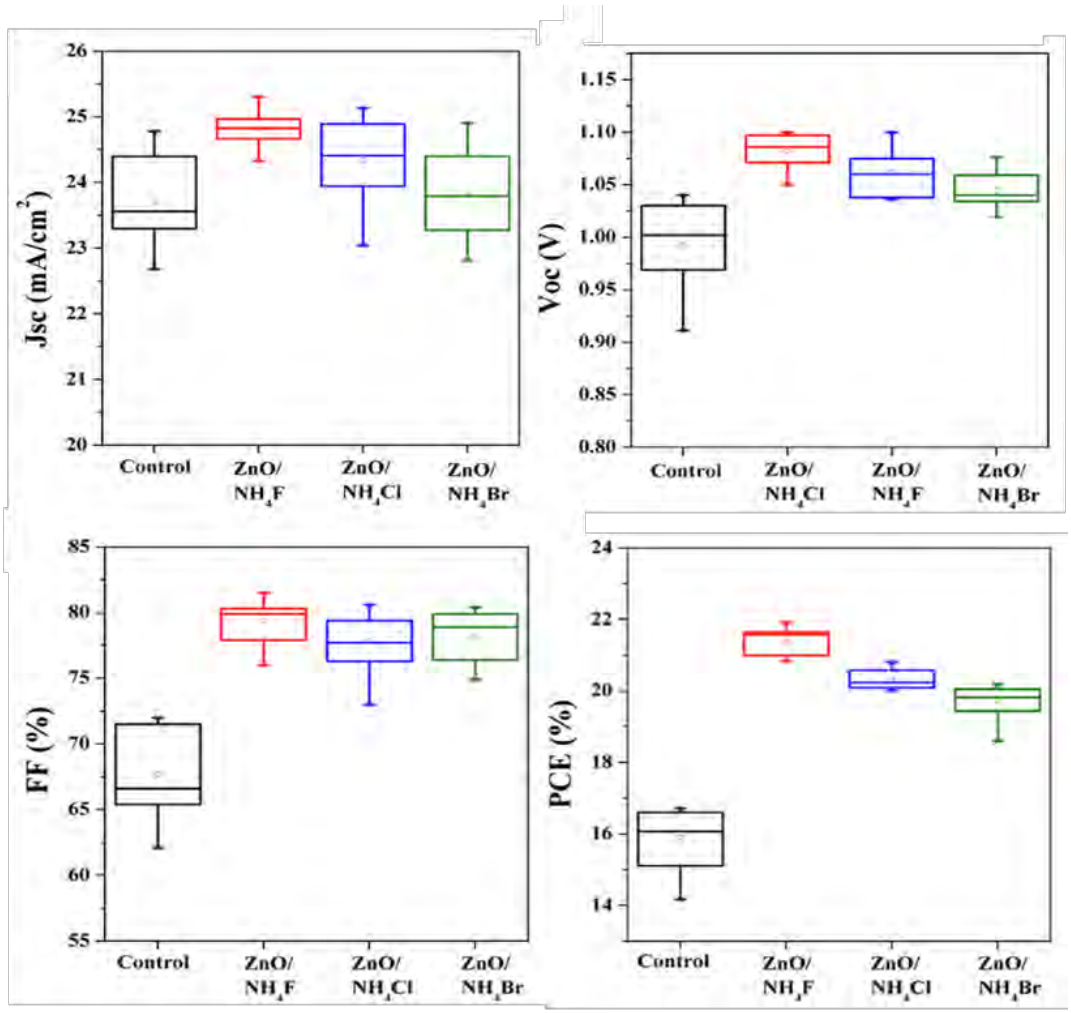

Fig 5.5: Statistical distribution of Jsc, V_{oc}, FF and PCE for devices fabricated with post treatment passivation of for each condition.

5.2.3 Film properties and device stability studies after ammonium fluoride passivation

The crystal structure of perovskite films was studied by the X-ray diffraction (XRD) measurements for both control perovskite film and perovskite film with the underlying Zno layer with NH_4F passivation. The XRD patterns shown in Fig. 5.6 indicate that the crystal structure of perovskite remains the same after the incorporation of passivation layer underneath. Both the films show characteristic peaks at 13.6°, 24°, and 27.8° corresponding to the (110), (202), and (220) crystallographic planes of $(FAPbI_3)_{0.97}(MAPbBr_3)_{0.03}$ perovskite phase. The presence of XRD peaks at same 2θ angles show that the crystal structure of perovskite remained unaltered after the passivation. Appearance of a small peak at 12.3° corresponds to the existence of unreacted PbI_2, which could be due to the presence of excess PbI_2 in the perovskite composition.

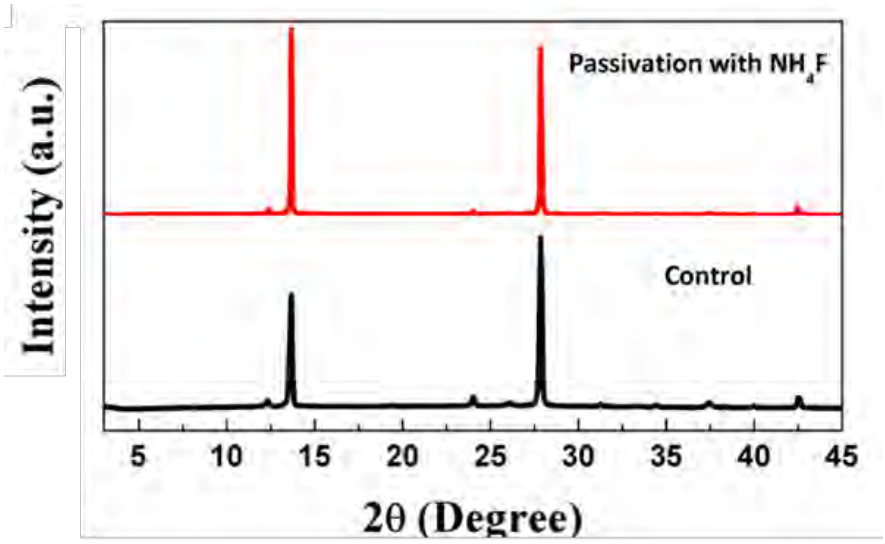

Fig. 5.6: XRD patterns of perovskite layer with underlying ZnO layer with and without NH_4F passivation.

The morphological study of the perovskite films was carried out by scanning electron microscopy (SEM). The images in Fig. 5.7 (a-b) show the formation of smooth perovskite films without pinholes. The bright areas seen on the surface is due to the presence of trace amount of PbI_2, as also confirmed by the XRD measurements. Both control and passivated films had similar morphologies with grain sizes of the order of few hundred nanometres up to a micrometre. The similarity in morphology is in well accordance with the XRD results, which

indicates that the passivation layer beneath does not affect the perovskite crystal structure as well as the morphology of the film. The cross sectional SEM images of reference and passivated devices (with NH_4F) are also shown in Fig. 5.7 (c-d) where different layers can be easily seen.

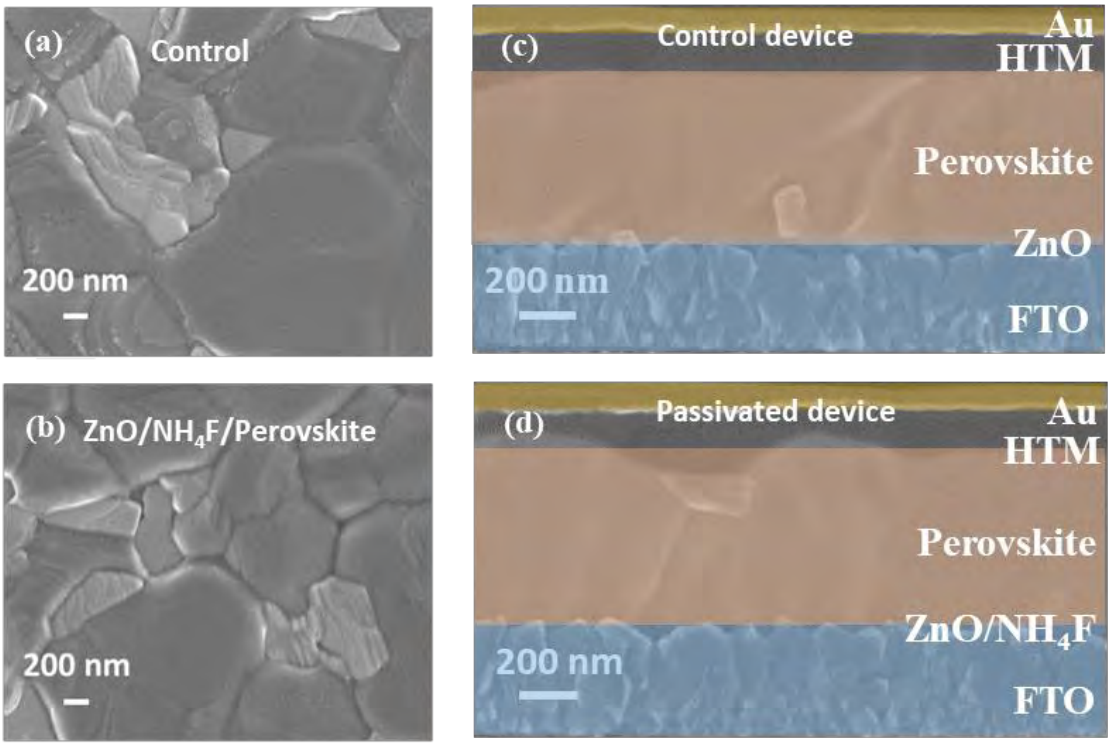

Fig. 5.7: SEM images of perovskite layer with underlying (a) ZnO, (b) ZnO/NH_4F. Cross sectional image of (c) reference device and (d) device with NH_4F passivation.

In order to understand the charge transfer and surface recombination at the interface of ETL/perovskite, the steady state photoluminescence (PL) measurement was carried out. The PL intensity of perovskite films deposited on top of ZnO layer with and without NH_4F passivation (average of two films for the same conditions) is shown in Fig. 5.8. A strong emission was observed at ~791 nm for both the films. Additionally, it is well evident that there is a significant increases in the PL intensity after the surface passivation of ZnO QDs layer by NH_4F, suggesting the suppression of non-radiative recombination and passivation of defects. It has also been observed that the local bonding of the FAI terminated surface of the perovskite layer is altered by establishing a hydrogen bond between the closely present F^- and FA^+ ions [228]. Incorporation of F^- ions also helps to maintain the local structure by raising the ionic charge on the surrounding Pb site. Through strong ionic interactions, these ions minimize the

losses caused by charge recombination. This observation also validates the improved V_{oc} of devices after passivation.

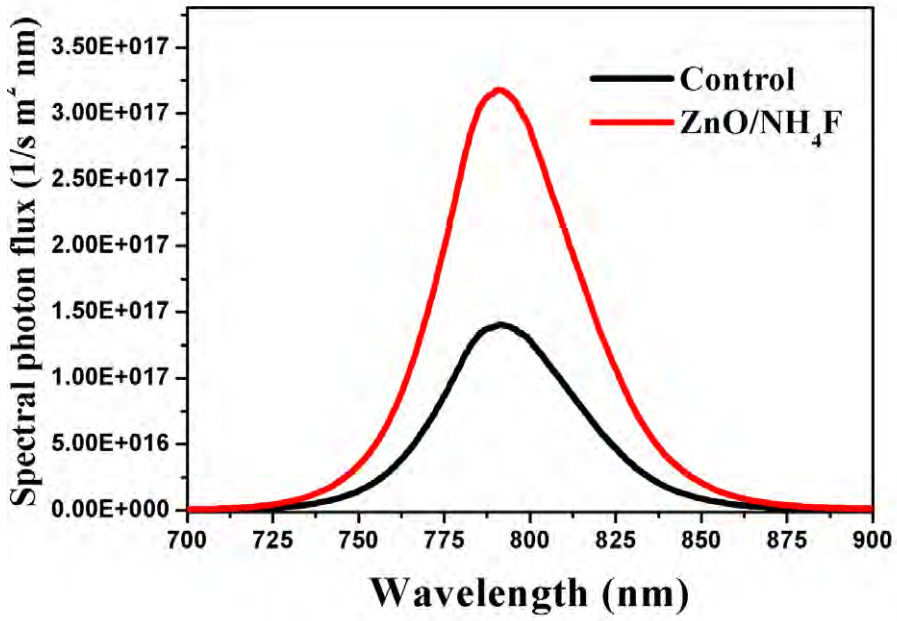

Fig. 5.8: Steady state PL of perovskite films with underlying ZnO layer with and without NH_4F passivation (average of two films for each condition).

The detailed analysis of recombination dynamics at the ZnO/perovskite interface was carried out by transient photoluminescence (TRPL) studies. Typically, the carrier lifetime depends on the density of traps or defects present inside the semiconducting materials. In the region from 100 nm to 600 nm of the TRPL curve, the decay is generally dominated by non-radiative recombination. Hence, by fitting the TRPL decay curve in this region (Fig. 5.9) with monoexponential function, the control device exhibited an average carrier lifetime (of 2 devices) of 350 ± 40 ns and after the passivation with NH_4F, the carrier lifetime increased to 470 ± 140 ns. This enhancement in charge carrier lifetime after NH_4F passivation is indicative of reduced non-radiative recombination, which matches well with the trend observed in the PL measurements. Additionally, it shows that the films have lower trap state density, which implies the recombination of charge carriers takes longer time. Another possibility of reduction in the defects states could be due to the zwitterionic capping of ZnO QDs. The presence of betaine containing both negatively charged and positively charged groups on the surface of ZnO could also assist in passivation of ionic defects present in the perovskite.

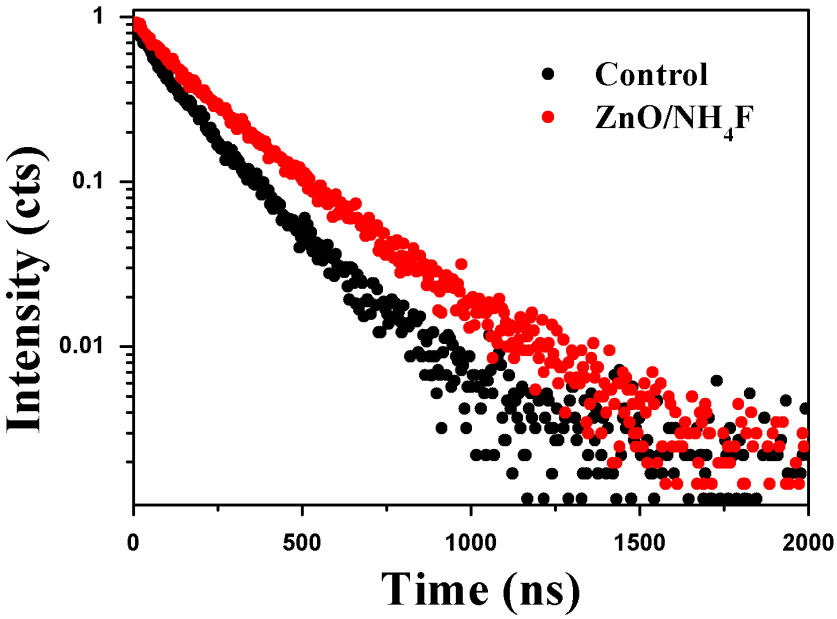

Fig. 5.9: TRPL decay curves of perovskite films with underlying ZnO layer with and without NH_4F passivation (average of two films for each condition).

The optical bandgap of ZnO QDs was calculated from the absorption spectra (Fig. 5.10) which gave a value of 3.35 eV. Next, in order to evaluate the band structure of the ZnO films with and without NH_4F passivation in more detail, ultraviolet photoelectron spectrometer (UPS) measurements were carried out for these films.

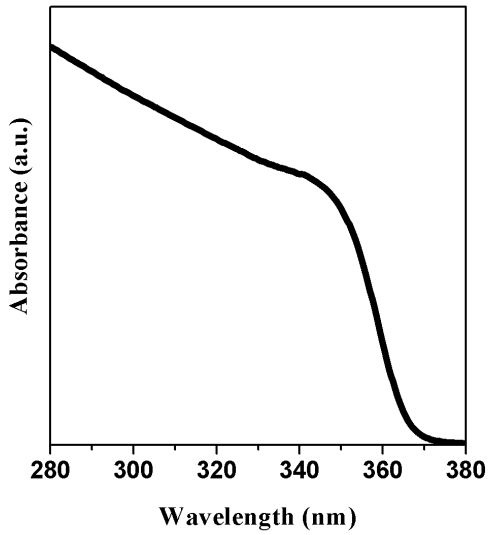

Fig. 5.10: UV-Vis absorption spectra of ZnO QDs.

Fig. 5.11 (a-b) shows the kinetic energy and binding energy of the ZnO films with and without passivation. The valence band energy level of the films were calculated from the onset of valence band maxima in the region of low binding energy giving a value of -7.02 eV and -7.14 eV for control ZnO and ZnO/NH_4F films respectively. Similarly, the Fermi levels were estimated from the onset of kinetic energy of electron (Fig. 5.11 (a)) resulting into values of -3.73 eV and -3.85 eV for control film and films with NH_4F passivation. The corresponding conduction band energy levels were -3.67 eV and -3.79 eV. Schematics of band alignment of ZnO layers with and without passivation is shown in Fig. 5.11 (c). It can be seen from these values that passivation with ammonium halide downshifts the Fermi energy level with a shift

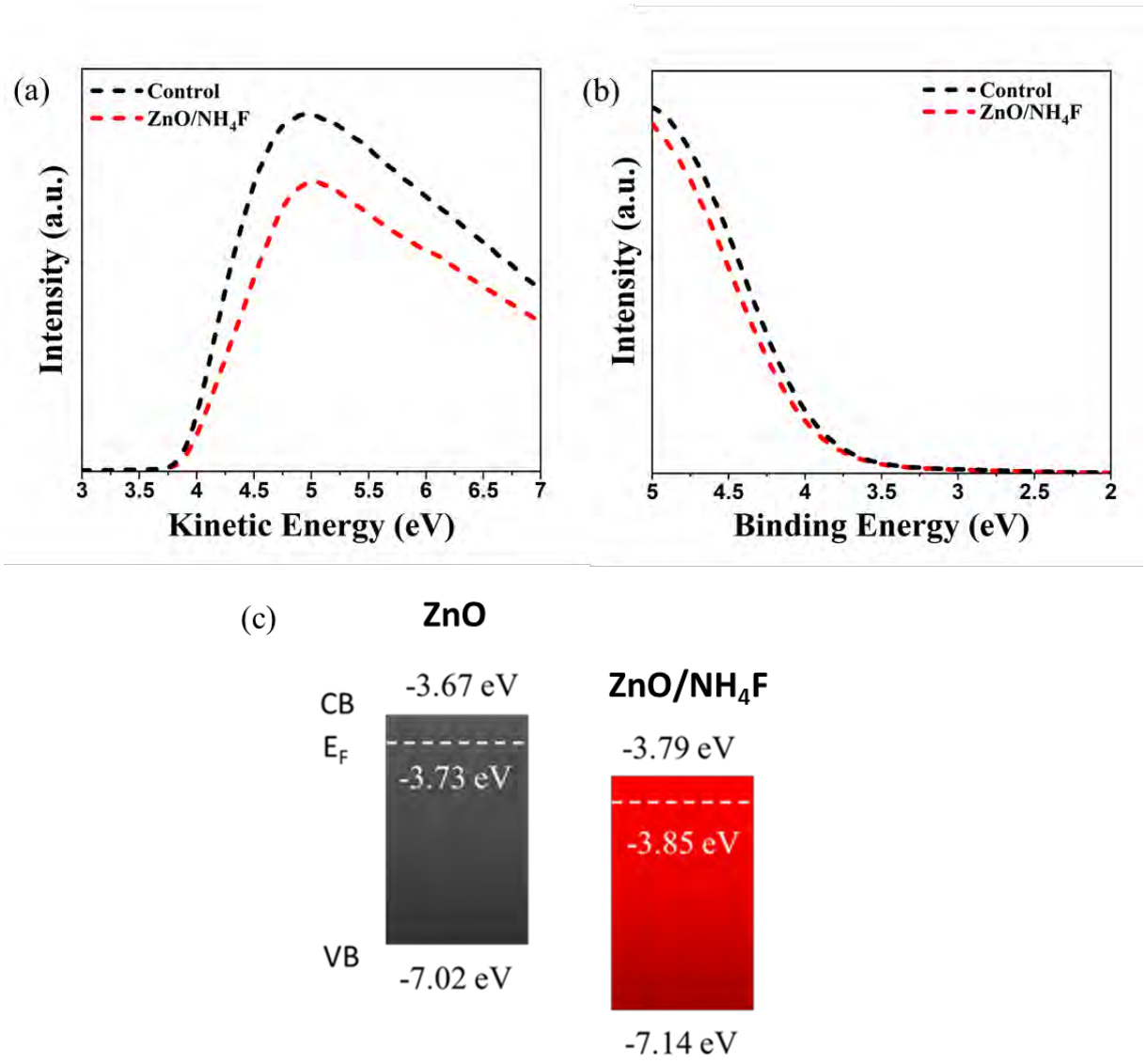

Fig. 5.11: UPS measurements of ZnO films with and without NH_4X passivation showing their (a) fermi levels and (b) valence band maximum. (c) Schematic of corresponding energy levels of respective films.

of ~0.12 eV. This shift in the Fermi energy levels suggests that band bending at the ZnO/perovskite interface can be modulated by the addition of ammonium halide. In case of control device, the conduction band is at higher energy level, which presents a barrier to the electron transfer from the perovskite layer and results into a low FF. However, when the ZnO layer is passivated with NH_4F, the conduction band is shifted to lower energy values and electron transfer is promoted. As a result of better energy level alignment, the charge transfer improves between the ZnO and perovskite layers, resulting into significant increase in the FF after passivation. This indicates that electron transfer from perovskite to the electron transporting layer is much easier in case of ZnO/NH_4F which leads to higher FF and better device efficiency as compared to the reference.

The operational stability of the unencapsulated control and best device with NH_4F passivation was measured in the nitrogen atmosphere. At room temperature, the devices were constantly illuminated under 1 Sun. After 250 h of measurement, the control device degrades significantly and reached an efficiency of ~42 % of its initial value (Fig. 5.12). However, the device passivated with NH_4F showed improved operational stability and retained ~78% of the initial PCE after 250 h of measurement. This showed that both efficiency and stability of devices were improved after the passivation with NH_4F.

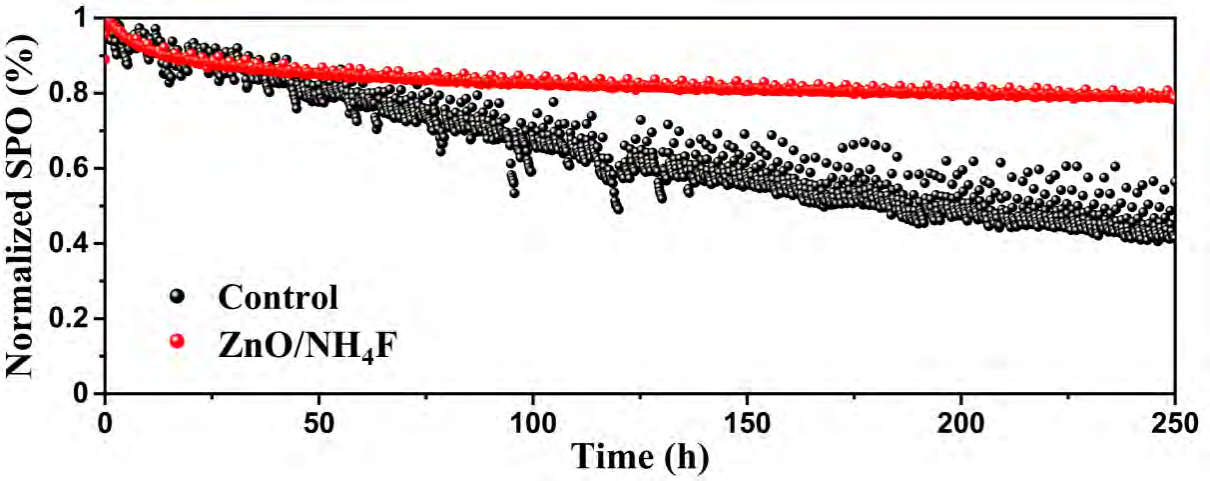

Fig. 5.12: Operational stability measurement of solar cells without the passivation (black) and with NH_4F passivation (blue).

5.3 Conclusions

In conclusion, the use of novel ZnO QDs capped with zwitterionic surfactant betaine has been shown as an efficient electron transporting layer in the planar perovskite solar cell structure. By using only ZnO QDs as the ETL, a maximum efficiency of 16.7% was achieved for the PSCs. The presence of defects on the surface of ZnO and the degradation of perovskite by reacting with ZnO limits the efficiency of ZnO-based PSCs. Therefore, several ammonium halides (NH_4F, NH_4Cl, and NH_4Br) were explored as passivation agents for the ZnO QDs layer to improve the performance of planar PSCs. Further, it was shown that the addition of ammonium halides as the passivation layer significantly improves the efficiency up to 21.9% in case of NH_4F. X-ray diffraction patterns and scanning electron microscopy images showed that the passivation does not affect the crystal structure and morphology of the perovskite layer. The steady state photoluminescence and transient photoluminescence spectra revealed that the ammonium halides passivation resulted into reduction of non-radiative recombination and hence improvement in V_{oc}. Ultraviolet photoelectron spectroscopy indicated the shift of energy levels of ZnO QDs layer after passivation, facilitating better charge transport from perovskite to ETL and led to a significant improvement of FF up to 80.3% in case of NH_4F passivation. These results suggested that modified ZnO QDs with betaine capping and ammonium halide passivation act as an excellent ETL for high-efficiency planar perovskite solar cells.

Chapter 6: Conclusions and future outlook

Hybrid organic-inorganic metal halide perovskites have emerged as a fascinating photovoltaic material in the past decade. These materials possess extraordinary optical and electrical properties, which make them suitable for multiple applications ranging from photodetectors, light-emitting diodes, sensors, X-ray detectors to solar cells. The perovskites exhibit excellent photoconversion efficiency, high absorption coefficient, long diffusion lengths and long lifetimes of charge carriers, low trap densities, and low cost of starting materials. Owing to these properties, they have been utilized for photoelectric conversion in solar cells and produced remarkable power conversion efficiencies. In addition to the excellent performance, the easy and low-cost processing of perovskite photovoltaic technology presents an enormous commercialization potential. However, there are several issues that need to be addressed before bringing this technology to market. One of the issues is that the most widely adopted wet chemical solution processing approach for the synthesis of perovskites requires dissolving perovskite precursors in a solvent. The commonly used solvents limit the precursor solubility, change the compositional stoichiometry of precursor solution during the long storage period, require more energy for the solvothermal conditions and they are not environmentally friendly. In particular, pure phase 2D perovskites, which are more stable than their 3D counterparts, have largely been synthesized by the solution processing methods. Another issue is producing 3D perovskite compositions with an optimal band gap, decent thermal stability, and brilliant optoelectronic properties, suitable for high-efficiency PSCs. Reducing the high-temperature processing for commonly used ETL in the PSCs in order to reduce the overall production cost is another challenge that researchers are facing. Many attempts have previously been made either to enhance the material characteristics or improve the quality of deposited perovskite films or other layers of solar cell devices in order to achieve high-efficiency and stability. However, there is still a need to develop high-quality, stable materials using synthetic technologies that are environmentally benign and can be used on a wide scale.

The investigations in this thesis were aimed at various aspects of perovskite research including the engineering of perovskite materials and their application to solar cells. In particular, the research work was focused on synthesizing 2D perovskites using an efficient and environment-friendly mechanochemical approach, better understanding the properties of perovskite single crystals, improving the 3D $Cs_xFA_{1-x}PbI_3$-type perovskite layer for fabricating high-efficiency mesoscopic solar cells. The inherent innovative part concerned the interfacial engineering of a

novel ZnO quantum dots(QD) based electron transporting layer towards fabricating high-efficiency planar perovskite solar cells.

In order to achieve the aforementioned goals, several approaches were followed. In the first part of the research, the focus was on the development of 2D Ruddlesden-popper layered perovskite with a general formula of $A_2MA_{n-1}Pb_nI_{3n+1}$ by following the highly efficient solvent-free mechanochemical approach. Using this synthetic method, three different potential spacer cations (A-site cation) viz., n-butylammonium (BA), 2-phenylethylammonium (PEA), and 2H-pyrimido[1,2-a]pyrimidine-1,3,4,6,7,8-hexahydro-hydroiodide as a cyclic guanidinium (c-Gua) were explored. The PXRD data revealed the successful formation of pure phase 2D perovskite materials for n=1, 2, and 3 Ruddlesden-popper phases in the case of the BA cation. When the PEA cation was used as the spacer cation, pure 2D perovskites were obtained for the n=1 phase and mixed-phase perovskite materials were obtained for n=2 & 3 layered structures. Nevertheless, the c-Gua cation could not be incorporated into the 2D layered Ruddlesden-popper structures and resulted in non-perovskite materials. Next, UV-Vis absorption spectroscopy confirmed the decreasing bandgap of 2D perovskite materials prepared with BA and PEA with an increasing value of n. The purity and local molecular structure of these materials was confirmed by the solid-state NMR measurements. These results are in preparation for publication.

The Guanidinium (Gua) cation can be used to replace some of the A-site MA^+ cations for increasing the performance of $MAPbI_3$-based PSCs. However, it has been reported that the incorporation of Gua cation increases the hysteresis of devices and an understanding of ion migration is required to explain this behavior. Therefore in the next task, perovskite single crystals were synthesized in order to understand the electronic properties of single cation and double cation perovskites. $MAPbI_3$ and $Gua_xMA_{1-x}PbI_3$ single crystals were synthesized from the inverse temperature crystallization method. The temperature dependant powder XRD measurements revealed the stability of $MAPbI_3$ single crystals up to a temperature of 363 K. Also, it was found that $Gua_xMA_{1-x}PbI_3$ perovskite had a similar crystal structure and bandgap as compared to that of $MAPbI_3$. Further EIS measurements by our collaborators indicated that $MAPbI_3$ crystals had very low trap density and the net impedance spectrum of this perovskite material was due to the ionic capacitance and conductivity-related resistance. The effect of Gua incorporation in the $MAPbI_3$ crystal lattice on ion migration was also studied by our collaborators. It was found that the activation energy of iodide migration decreases in the $Gua_xMA_{1-x}PbI_3$ crystals due to the expansion of lattice, which further leads to the increased

hysteresis during the J-V measurements of these crystals as compared to that of pristine $MAPbI_3$. These results were published in *J. Phys. Chem. C* 2020, 124, 6 and *Phys. Chem. Chem. Phys.*, 2020,22, 11467-11473.

The next task focused on the fabrication of high-efficiency mesoscopic solar cells based on a 3D double cation perovskite system with the general formula of $Cs_xFA_{1-x}PbI_3$. By using a newly developed solution processing approach, thin films of $Cs_{0.2}FA_{0.8}PbI_3$ were deposited and later employed in the mesoscopic solar cells with an architecture of FTO/c-TiO_2/m-TiO_2/ $Cs_{0.2}FA_{0.8}PbI_3$/spiro-OMeTAD/Au. In this modified one-step solution processing approach, CsCl was used in the precursor solution as the source of Cs cation. The resulting 3D perovskite composition, when deposited by the spin-coating method, produced a highly uniform and smooth perovskite layer with large grains up to a micrometre in size. The highest PCE obtained with $Cs_{0.2}FA_{0.8}PbI_3$ perovskite based mesoscopic devices was as high as 20.6% with a stabilized PCE of 19.85%. Additionally, the devices showed low hysteresis and suppressed non-radiative recombination. Further, two organic additives 1- adamantylamine (ADA) and guanidinium iodide (GuaI) were used for the passivation of the perovskite layer to reduce the defects. Among these two agents, GuaI showed a slight enhancement of device parameters. A part of these results was published in *Chem. Mater*. 2019, 31, 5, 1620–1627.

The most commonly explored electron transport material for high-efficiency PSC, TiO_2, needs high-temperature processing and ZnO has emerged as an exciting alternative in recent years. Hence, the next highly innovative research step was devoted to using a novel ZnO quantum dot (QD) capped with betaine as the zwitterions in the planar PSC. When a layer of ZnO QDs was employed as the electron transporting layer in the solar cell with an architecture of FTO/ZnO/$(FAPbI_3)_{0.97}(MAPbBr_3)_{0.03}$/EAI/spiro-OMeTAD/Au, efficiency up to 16.7% could be achieved. In order to further improve the ZnO/perovskite interface, several ammonium halide (NH_4F, NH_4Cl, and NH_4Br) additives were introduced as passivation agents. As a result, the band alignment between the ZnO/perovskite was improved and non-radiative recombinations were reduced. The maximum increase was observed in the case of FF of the device, which increased significantly from 71.5% for the reference device to 80.3% for NH_4F passivated device. The best device with NH_4F passivation exhibited a champion PCE of 21.9%, which is a remarkable increase of ~ 31% from the reference device. The passivate solar cells were also stable up to 250 h of constant 1 Sun illumination, retaining ~78% of the initial PCE. These results contributed to a manuscript submitted in a highly ranked journal.

The research outcomes presented in this thesis focused on several aspects of perovskite research and gave insights into both the development of synthesis methods and the understanding inherent properties of the resulting materials. Furthermore, the fabrication of high-performance PSCs in the mesoporous architecture based on double cation perovskite composition as well as in the planar architecture with a novel ZnO QD-based ETL was also elaborately discussed. However, there are several questions that are still needed to be answered and to be researched upon

1) How to use solvent-free mechanochemistry for producing large amounts of pure phase perovskites and utilize the mechanochemically synthesized materials directly for the fabrication of PSCs?
2) How to utilize 2D perovskite efficiently to achieve more stable PSC devices?
3) How to further improve the efficiency and stability of ZnO-based devices?
4) How to retain the high efficiencies along with the stability of Pb-based PSCs by using proper passivating agents?
5) How to scale the device fabrication processes to large-areas without compromising the power conversion efficiencies for industrial applications?
6) How to properly encapsulate and device a recycling mechanism of the Pb-based PSCs for environmental safety?

References

[1] Ahmad, T.; Zhang, D. A Critical Review of Comparative Global Historical Energy Consumption and Future Demand : The Story Told so Far. *Energy Reports* **2020**, *6*, 1973–1991.

[2] Energy Production and Consumption - Our World in Data https://ourworldindata.org/energy-production-consumption (accessed 2021 -08 -17).

[3] OECD iLibrary | CO_2 Emissions from Fuel Combustion 2018 https://www.oecd-ilibrary.org/energy/co2-emissions-from-fuel-combustion-2018_co2_fuel-2018-en (accessed 2021 -08 -17).

[4] Renewable Energy - Our World in Data https://ourworldindata.org/renewable-energy (accessed 2021 -09 -13).

[5] Smil, V. *General Energetics: Energy in the Biosphere and Civilization*; 1991.

[6] Solar Radiation for Solar Energy Utilization | SpringerLink https://link.springer.com/referenceworkentry/10.1007/978-1-4419-0851-3_450 (accessed 2021 -08 -16).

[7] Coddington, O.; Lean, J. L.; Pilewskie, P.; Snow, M.; Lindholm, D. A SOLAR IRRADIANCE CLIMATE DATA RECORD. *Bull. Am. Meteorol. Soc.* **2016**, *97* (7), 1265–1282.

[8] Becquerel, E. Mémoire Sur Les Effets Électriques Produits Sous l'influence Des Rayons Solaires. *Comptes Rendus* **1839**, *9*, 561–567.

[9] Würfel, P.; Würfel, U. *Physics of Solar Cells from Basic Principles to Advanced Concepts*, 3rd edition.; Wiley-VCH, 2016.

[10] April 25, 1954: Bell Labs Demonstrates the First Practical Silicon Solar Cell. *APS News, Am. Phys. Soc.* **2009**, *18* (2).

[11] Badawy, W. A. A Review on Solar Cells from Si-Single Crystals to Porous Materials and Quantum Dots. *J. Adv. Res.* **2015**, *6* (2), 123–132.

[12] Regan, B. O.; Graetzel, M. A Low-Cost, High-Efficiency Solar Cell Based on Dye-Sensitized Colloidal TiO_2 Films. *Nature* **1991**, *353*, 737–740.

[13] Kojima, A.; Teshima, K.; Shirai, Y.; Miyasaka, T. Organometal Halide Perovskites as Visible-Light Sensitizers for Photovoltaic Cells. *J. AM. CHEM. SOC* **2009**, *131*, 6050–6051.

[14] Kim, H. S.; Lee, C. R.; Im, J. H.; Lee, K. B.; Moehl, T.; Marchioro, A.; Moon, S. J.;

Humphry-Baker, R.; Yum, J. H.; Moser, J. E.; Grätzel, M.; Park, N. G. Lead Iodide Perovskite Sensitized All-Solid-State Submicron Thin Film Mesoscopic Solar Cell with Efficiency Exceeding 9%. *Sci. Rep.* **2012**, *2*, 1–7.

[15] Jena, A. K.; Kulkarni, A.; Miyasaka, T. Halide Perovskite Photovoltaics: Background, Status, and Future Prospects. *Chem. Rev.* **2019**, *119* (5), 3036–3103.

[16] Kim, J. Y.; Lee, J.-W.; Jung, H. S.; Shin, H.; Park, N.-G. High-Efficiency Perovskite Solar Cells. *Chem. Rev.* **2020**, *120* (15), 7867–7918.

[17] Tang, G.; Yan, F. Recent Progress of Flexible Perovskite Solar Cells. *Nano Today* **2021**, *39*, 101155.

[18] Suresh Kumar, N.; Chandra Babu Naidu, K. A Review on Perovskite Solar Cells (PSCs), Materials and Applications. *J. Mater.* **2021**, *7* (5), 940–956.

[19] Best Research-Cell Efficiency Chart | Photovoltaic Research | NREL https://www.nrel.gov/pv/cell-efficiency.html (accessed 2022 -03 -04).

[20] Ansari, M. I. H.; Qurashi, A.; Nazeeruddin, M. K. Frontiers, Opportunities, and Challenges in Perovskite Solar Cells: A Critical Review. *J. Photochem. Photobiol. C Photochem. Rev.* **2018**, *35*, 1–24.

[21] Fagiolari, L.; Bella, F. Carbon-Based Materials for Stable, Cheaper and Large-Scale Processable Perovskite Solar Cells. *Energy Environ. Sci.* **2019**, *12* (12), 3437–3472.

[22] Park, N.-G. Research Direction toward Scalable, Stable, and High Efficiency Perovskite Solar Cells. *Adv. Energy Mater.* **2020**, *10* (13), 1903106.

[23] Yan, J.; Savenije, T. J.; Mazzarella, L.; Isabella, O. Progress and Challenges on Scaling up of Perovskite Solar Cell Technology. *Sustain. Energy Fuels* **2022**, *6* (2), 243–266.

[24] Shockley, W.; Queisser, H. J. Detailed Balance Limit of Efficiency of P-n Junction Solar Cells. *J. Appl. Phys.* **1961**, *32* (2).

[25] Wang, R.; Huang, T.; Xue, J.; Tong, J.; Zhu, K.; Yang, Y. Prospects for Metal Halide Perovskite-Based Tandem Solar Cells. *Nat. Photonics* **2021**, *15* (6), 411–425.

[26] Al-Ashouri, A.; Köhnen, E.; Li, B.; Magomedov, A.; Hempel, H.; Caprioglio, P.; Márquez, J. A.; Vilches, A. B. M.; Kasparavicius, E.; Smith, J. A.; Phung, N.; Menzel, D.; Grischek, M.; Kegelmann, L.; Skroblin, D.; Gollwitzer, C.; Malinauskas, T.; Jošt, M.; Matič, G.; Rech, B.; Schlatmann, R.; Topič, M.; Korte, L.; Abate, A.; Stannowski, B.; Neher, D.; Stolterfoht, M.; Unold, T.; Getautis, V.; Albrecht, S. Monolithic Perovskite/Silicon Tandem Solar Cell with >29% Efficiency by Enhanced Hole Extraction. *Science (80-.).* **2020**, *370* (6522), 1300–1309.

[27] Saliba, M.; Matsui, T.; Seo, J.-Y.; Domanski, K.; Nazeeruddin, M. K.; Baena, J. C.; Zakeeruddin, S. M.; Tress, W.; Abate, A.; Hagfeldt, A.; Gratzel, M. Cesium-Containing Triple Cation Perovskite Solar Cells: Improved Stability, Reproducibility and High Efficien. **2016**, *9* (6).

[28] Jeon, I.; Kim, K.; Jokar, E.; Park, M.; Lee, H.-W.; Diau, E. W. Environmentally Compatible Lead-Free Perovskite Solar Cells and Their Potential as Light Harvesters in Energy Storage Systems. *Nanomaterials* . 2021.

[29] Xiang, W.; Tress, W. Review on Recent Progress of All-Inorganic Metal Halide Perovskites and Solar Cells. *Adv. Mater.* **2019**, *31* (44), 1902851.

[30] Yu, B.; Shi, J.; Tan, S.; Cui, Y.; Zhao, W.; Wu, H.; Luo, Y.; Li, D.; Meng, Q. Efficient (>20 %) and Stable All-Inorganic Cesium Lead Triiodide Solar Cell Enabled by Thiocyanate Molten Salts. *Angew. Chemie Int. Ed.* **2021**, *60* (24), 13436–13443.

[31] Ouedraogo, N. A. N.; Chen, Y.; Xiao, Y. Y.; Meng, Q.; Han, C. B.; Yan, H.; Zhang, Y. Stability of All-Inorganic Perovskite Solar Cells. *Nano Energy* **2020**, *67*, 104249.

[32] Liang, J.; Qi, Y. B. Recent Progress on All-Inorganic Metal Halide Perovskite Solar Cells. *Mater. Today Nano* **2021**, *16*, 100143.

[33] Li, J.; Duan, J.; Yang, X.; Duan, Y.; Yang, P.; Tang, Q. Review on Recent Progress of Lead-Free Halide Perovskites in Optoelectronic Applications. *Nano Energy* **2021**, *80*, 105526.

[34] Mohamad Noh, M. F.; Teh, C. H.; Daik, R.; Lim, E. L.; Yap, C. C.; Ibrahim, M. A.; Ahmad Ludin, N.; Mohd Yusoff, A. R. bin; Jang, J.; Mat Teridi, M. A. The Architecture of the Electron Transport Layer for a Perovskite Solar Cell. *J. Mater. Chem. C* **2018**, *6* (4), 682–712.

[35] Chen, W.; Yin, X.; Que, M.; Xie, H.; Liu, J.; Yang, C.; Guo, Y.; Wu, Y.; Que, W. A Comparative Study of Planar and Mesoporous Perovskite Solar Cells with Printable Carbon Electrodes. *J. Power Sources* **2019**, *412*, 118–124.

[36] Gao, F.; Zhao, Y.; Zhang, X.; You, J. Recent Progresses on Defect Passivation toward Efficient Perovskite Solar Cells. *Adv. Energy Mater.* **2020**, *10* (13), 1902650.

[37] Ball, J. M.; Petrozza, A. Defects in Perovskite-Halides and Their Effects in Solar Cells. *Nat. Energy* **2016**, *1* (11), 16149.

[38] Asghar, M. I.; Zhang, J.; Wang, H.; Lund, P. D. Device Stability of Perovskite Solar Cells – A Review. *Renew. Sustain. Energy Rev.* **2017**, *77*, 131–146.

[39] Ruhle, S. Tabulated Values of the Shockley – Queisser Limit for Single Junction Solar Cells. *Sol. Energy* **2016**, *130*, 139–147.

[40] Kubicki, D. J.; Stranks, S. D.; Grey, C. P.; Emsley, L. NMR Spectroscopy Probes Microstructure, Dynamics and Doping of Metal Halide Perovskites. *Nat. Rev. Chem.* **2021**, *5* (9), 624–645.

[41] Well, H. L. Uber Die Casium- Und Kalium-Blei Halogenide. *Sheffiel Sci. Sch.* **1892**.

[42] Goldschmidt, V. M. Die Gesetze Der Krystallochemie. *Naturwissenschaften* **1926**, *14*, 477–485.

[43] Yi, Z.; Ladi, H.; Shai, X.; Li, H.; Shen, Y.; Wang, M. Will Organic – Inorganic Hybrid Halide Lead Perovskites Be Eliminated from Optoelectronic Applications? *Nanoscale Adv.* **2019**, *1*, 1276–1289.

[44] Khalfin, S.; Bekenstein, Y. Advances in Lead-Free Double Perovskite Nanocrystals, Engineering Band-Gaps and Enhancing Stability through Composition Tunability. *Nanoscale* **2019**, *11* (18), 8665–8679.

[45] Gao, Y.; Pan, Y.; Zhou, F.; Niu, G.; Yan, C. Lead-Free Halide Perovskites: A Review of the Structure–Property Relationship and Applications in Light Emitting Devices and Radiation Detectors. *J. Mater. Chem. A* **2021**, *9* (20), 11931–11943.

[46] Gao, W.; Chen, C.; Ran, C.; Zheng, H.; Dong, H.; Xia, Y.; Chen, Y.; Huang, W. A-Site Cation Engineering of Metal Halide Perovskites: Version 3.0 of Efficient Tin-Based Lead-Free Perovskite Solar Cells. *Adv. Funct. Mater.* **2020**, *30* (34), 2000794.

[47] Stranks, S. D.; Eperon, G. E.; Grancini, G.; Menelaou, C.; Alcocer, M. J. P.; Leijtens, T.; Herz, L. M.; Petrozza, A.; Snaith, H. J. Electron-Hole Diffusion Lengths Exceeding 1 Micrometer in an Organometal Trihalide Perovskite Absorber. *Science (80-.).* **2013**, *342*, 341–345.

[48] Wehrenfennig, C.; Eperon, G. E.; Johnston, M. B.; Snaith, H. J.; Herz, L. M. High Charge Carrier Mobilities and Lifetimes in Organolead Trihalide Perovskites. *Adv. Mater.* **2014**, *26*, 1584–1589.

[49] Shi, D.; Adinolfi, V.; Comin, R.; Yuan, M.; Alarousu, E.; Buin, A.; Chen, Y.; Hoogland, S.; Rothenberger, A.; Katsiev, K.; Losovyj, Y.; Zhang, X.; Dowben, P. A.; Mohammed, O. F.; Sargent, E. H.; Bakr, O. M. Low Trap-State Density and Long Carrier Diffusion in Organolead Trihalide Perovskite Single Crystals. *Science (80-.).* **2015**, *347* (6221).

[50] Li, Y.; Lu, Y.; Huo, X.; Wei, D.; Meng, J.; Dong, J.; Qiao, B.; Zhao, S.; Song, D. Bandgap Tuning Strategy by Cations and Halide Ions of Lead Halide Perovskites Learned from Machine Learning. *RSC Adv* **2021**, *11*, 15688–15694.

[51] Noh, J. H.; Im, S. H.; Heo, J. H.; Mandal, T. N.; Seok, S. Il. Chemical Management for

Colorful, E Ffi Cient, and Stable Inorganic − Organic Hybrid Nanostructured Solar Cells. *Nano Lett.* **2013**, *13*, 1764–1769.

[52] Albero, J.; Asiri, M.; Garcia, H. Influence of the Composition of Hybrid Perovskites on Their Performance in Solar Cells. *J. Mater. Chem. A* **2016**, *4*, 4353–4364.

[53] Eperon, G. E.; Stranks, S. D.; Menelaou, C.; Johnston, M. B.; Herz, L. M.; Snaith, H. J. Formamidinium Lead Trihalide : A Broadly Tunable Perovskite for Efficient Planar Heterojunction Solar. *Energy Environ. Sci.* **2014**, *7*, 982–988.

[54] Zhang, F.; Castaneda, J. F.; Chen, S.; Wu, W.; Dinezza, M. J.; Lassise, M.; Nie, W.; Mohite, A.; Liu, Y.; Liu, S.; Friedman, D.; Liu, H.; Chen, Q.; Zhang, Y.; Huang, J.; Zhang, Y. Comparative Studies of Optoelectrical Properties of Prominent PV Materials : Halide Perovskite , CdTe, and GaAs. *Mater. Today* **2020**, *36*, 18–29.

[55] Hautzinger, M. P.; Pan, D.; Pigg, A. K.; Fu, Y.; Morrow, D. J.; Leng, M.; Kuo, M.-Y.; Spitha, N.; Lafayette, D. P.; Kohler, D. D.; Wright, J. C.; Jin, S. Band Edge Tuning of Two-Dimensional Ruddlesden–Popper Perovskites by A Cation Size Revealed through Nanoplates. *ACS Energy Lett.* **2020**, *5* (5), 1430–1437.

[56] Bush, K. A.; Frohna, K.; Prasanna, R.; Beal, R. E.; Leijtens, T.; Swifter, S. A.; Mcgehee, M. D. Compositional Engineering for Efficient Wide Band Gap Perovskites with Improved Stability to Photoinduced Phase Segregation. *ACS Energy Lett.* **2018**, *3*, 428–435.

[57] Ouyang, Y.; Li, Y.; Zhu, P.; Li, Q.; Gao, Y.; Tong, J.; Shi, L.; Zhou, Q.; Ling, C.; Chen, Q.; Deng, Z.; Tan, H.; Deng, W.; Wang, J. Photo-Oxidative Degradation of Methylammonium Lead Iodide Perovskite : Mechanism and Protection. *J. Mater. Chem. A* **2019**, *7*, 2275–2282.

[58] Rothlisberger, U. Valence and Conduction Band Tuning in Halide Perovskites for Solar Cell Applications. *J. Mater. Chem. A* **2016**, *4*, 15997–16002.

[59] Kim, H.; Hagfeldt, A.; Park, N. Morphological and Compositional Progress in Halide Perovskite Solar Cells. *Chem. Commun.* **2019**, *55*, 1192–1200.

[60] Jeon, N. J.; Noh, J. H.; Kim, Y. C.; Yang, W. S.; Ryu, S.; Seok, S. Il. Solvent Engineering for High-Performance Inorganic-Organic Hybrid Perovskite Solar Cells. *Nat. Mater.* **2014**, *13*, 897–903.

[61] Stoumpos, C. C.; Malliakas, C. D.; Kanatzidis, M. G. Semiconducting Tin and Lead Iodide Perovskites with Organic Cations: Phase Transitions, High Mobilities, and Near-Infrared Photoluminescent Properties. *Inorg. Chem.* **2013**, *52*, 9019–9038.

[62] Aamir, M.; Adhikari, T.; Sher, M.; Revaprasadu, N.; Khalid, W.; Akhtar, J.; Nunzi, J.

Fabrication of Planar Heterojunction $CsPbBr_2I$ Perovskite Solar Cells Using ZnO as an Electron Transport Layer and Improved Solar Energy Conversion Efficiency. *New J. Chem* **2018**, *42*, 14104–14110.

[63] Nair, S.; Patel, S. B.; Gohel, J. V. Recent Trends in Efficiency-Stability Improvement in Perovskite Solar Cells. *Mater. Today Energy* **2020**, *17*, 100449.

[64] Bu, T.; Liu, X.; Zhou, Y.; Yi, J.; Huang, X.; Luo, L.; Xiao, J.; Ku, Z.; Peng, Y.; Huang, F.; Cheng, Y.; Zhong, J. A Novel Quadruple-Cation Absorber for Universal Hysteresis Elimination for High Efficiency and Stable Perovskite Solar Cells. *Energy Environ. Sci.* **2017**, *10*, 2509–2515.

[65] Patil, J. V; Hong, C. K. A Thiourea Additive-Based Quadruple Cation Lead Halide Perovskite with an Ultra-Large Grain Size for Efficient Perovskite Solar Cells. *Nanoscale* **2019**, *11*, 21824–21833.

[66] Yi, C.; Luo, J.; Meloni, S.; Boziki, A.; Astani, N. A.; Graetzel, C.; Zakeeruddin, S. M.; Rothlisberger, U.; Graetzel, M. Entropic Stabilization of Mixed A-Cation ABX_3 Metal Halide Perovskites for High Performance Perovskite Solar Cells. *Energy Environ. Sci.* **2016**, *9*, 656–662.

[67] Lee, J.; Kim, D.; Kim, H.; Seo, S.; Cho, S. M.; Park, N. Formamidinium and Cesium Hybridization for Photo- and Moisture-Stable Perovskite Solar Cell. *Adv. Energy Mater.* **2015**, *5*.

[68] Choi, H.; Jeong, J.; Kim, H.; Kim, S.; Walker, B.; Kim, G.; Young, J. Y. Cesium-Doped Methylammonium Lead Iodide Perovskite Light Absorber for Hybrid Solar Cells. *Nano Energy* **2014**, *7*, 80–85.

[69] Bi, D.; Tress, W.; Dar, M. I.; Gao, P.; Luo, J.; Renevier, C.; Schenk, K.; Abate, A.; Giordano, F.; Baena, J. C.; Decoppet, J.; Zakeeruddin, S. M.; Nazeeruddin, M. K.; Grätzel, M.; Hagfeldt, A. Efficient Luminescent Solar Cells Based on Tailored Mixed-Cation Perovskites. *Sci. Adv.* **2016**, *2*.

[70] Burschka, J.; Pellet, N.; Moon, S.-J.; Baker, H. R.; Gao, P.; Nazeeruddin, M. K.; Graetzel, M. Sequential Deposition as a Route to High-Performance Perovskite-Sensitized Solar Cells. *Nature* **2013**, *499*.

[71] Liu, M.; Johnston, M. B.; Snaith, H. J. Efficient Planar Heterojunction Perovskite Solar Cells by Vapour Deposition. *Nature* **2013**, *501*, 395–398.

[72] Son, D.; Lee, J.; Choi, Y. J.; Jang, I.; Lee, S.; Yoo, P. J.; Shin, H.; Ahn, N.; Choi, M.; Kim, D.; Park, N. Self-Formed Grain Boundary Healing Layer for Highly Efficient $CH_3NH_3PbI_3$ Perovskite Solar Cells. *Nat. Energy* **2016**, *1*, 1–8.

[73] Yang, W. S.; Noh, J. H.; Jeon, N. J.; Kim, Y. C.; Ryu, S.; Seo, J.; Seok, S. I. High-Performance Photovoltaic Perovskite Layers Fabricated through Intramolecular Exchange. *Science (80-.).* **2015**, *348* (6240), 1234–1238.

[74] Pellet, N.; Gao, P.; Gregori, G.; Yang, T.; Nazeeruddin, M. K.; Maier, J.; Grätzel, M. Mixed-Organic-Cation Perovskite Photovoltaics for Enhanced Solar- Light Harvesting. *Angew.Chem.Int. Ed* **2014**, *53*, 3151–3157.

[75] Ji, F.; Wang, L.; Pang, S.; Gao, P.; Xu, H.; Xie, G.; Zhang, J.; Cui, G. A Balanced Cation Exchange Reaction toward Highly Uniform and Pure Phase $FA_{1-x}MA_xPbI_3$ Perovskite Films. *J. Mater. Chem. A* **2016**, *4*, 14437–14443.

[76] Yang, Z.; Chueh, C.; Liang, P.; Crump, M.; Lin, F.; Zhu, Z.; Jen, A. K. Effects of Formamidinium and Bromide Ion Substitution in Methylammonium Lead Triiodide toward High-Performance Perovskite Solar Cells. *Nano Energy* **2016**, *22*, 328–337.

[77] Prochowicz, D.; Yadav, P.; Saliba, M.; Saski, M.; Zakeeruddin, S. M.; Lewinski, J.; Gratzel, M. Mechanosynthesis of Pure Phase Mixed-Cation $MA_xFA_{1-X}PbI_3$ Hybrid Perovskites: Photovoltaic Performance and Electrochemical Properties. *Sustain. Energy Fuels* **2017**, 689–693.

[78] Binek, A.; Hanusch, F. C.; Docampo, P.; Bein, T. Stabilization of the Trigonal High-Temperature Phase of Formamidinium Lead Iodide. *J. Phys. Chem. Lett* **2015**, *6*, 1249–1253.

[79] Rehman, W.; Mcmeekin, D. P.; Patel, J. B.; Milot, R. L.; Johnston, M. B.; Snaith, H. J.; Herz, L. M. Photovoltaic Mixed-Cation Lead Mixed-Halide Perovskites: Links between Crystallinity, Photo-Stability and Electronic Properties. *Energy Environ. Sci.* **2017**, *10*, 361–369.

[80] Li, Z.; Yang, M.; Park, J.; Wei, S.; Berry, J. J.; Zhu, K. Stabilizing Perovskite Structures by Tuning Tolerance Factor: Formation of Formamidinium and Cesium Lead Iodide Solid-State Alloys. *Chem. Mater* **2016**, *28*, 284–292.

[81] Liu, T.; Zong, Y.; Zhou, Y.; Yang, M.; Li, Z.; Game, O. S.; Zhu, K.; Zhu, R.; Gong, Q.; Padture, N. P. High-Performance Formamidinium-Based Perovskite Solar Cells via Microstructure-Mediated δ - to - α Phase Transformation. *Chem. Mater* **2017**, *29*, 3246–3250.

[82] Bella, F.; Renzi, P.; Cavallo, C.; Gerbaldi, C. Caesium for Perovskite Solar Cells : An Overview. *Chem. Eur* **2018**, *24*, 12183–12205.

[83] Zhou, N.; Shen, Y.; Zhang, Y.; Xu, Z.; Zheng, G.; Li, L.; Chen, Q.; Zhou, H. CsI Pre-Intercalation in the Inorganic Framework for CsI Pre-Intercalation in the Inorganic

Framework for Efficient and Stable $FA_{1-x}Cs_xPbI_3(Cl)$ Perovskite Solar Cells. *Small* **2017**, *3*, 1–9.

[84] Chen, J.; Xu, J.; Zhao, C.; Zhang, B.; Liu, X.; Dai, S.; Yao, J. Efficient Planar Heterojunction $FA_{(1-x)}Cs_xPbI_3$ Perovskite Solar Cells with Suppressed Carrier Recombination and Enhanced Open Circuit Voltage via Anion-Exchange Process. *ACS Appl. Mater. Interfaces* **2019**, *11*, 4597–4606.

[85] Salhi, B.; Wudil, Y. S.; Hossain, M. K.; Al-Ahmed, A.; Al-Sulaiman, F. A. Review of Recent Developments and Persistent Challenges in Stability of Perovskite Solar Cells. *Renew. Sustain. Energy Rev.* **2018**, *90*, 210–222.

[86] Calabrese, J.; Jones, N. L.; Harlow, R. L.; Herron, N.; Thorn, D. L.; Wang, Y. Preparation and Characterization of Layered Lead Halide Compounds. *J. AM. CHEM. SOC* **1991**, *113*, 2328–2330.

[87] Chen, Y.; Sun, Y.; Peng, J.; Tang, J.; Zheng, K.; Liang, Z. 2D Ruddlesden – Popper Perovskites for Optoelectronics. *Adv. Mater.* **2018**, *30*.

[88] Cao, D. H.; Stoumpos, C. C.; Farha, O. K.; Hupp, J. T.; Kanatzidis, M. G. 2D Homologous Perovskites as Light-Absorbing Materials for Solar Cell Applications. *J. AM. CHEM. SOC* **2015**, *137*, 7843–7850.

[89] Gangadharan, D. T.; Ma, D. Searching for Stability at Lower Dimensions: Current Trends and Future Prospects of Layered Perovskite Solar Cells. *Energy Environ. Sci.* **2019**, *12*, 2860–2889.

[90] Mitzi, D. B. Synthesis, Structure, and Properties of Organic-Inorganic Perovskites and Related Materials. *Prog. Inorg. Chem.* **2007**, *48*, 1–121.

[91] Wu, G.; Liang, R.; Zhang, Z.; Ge, M.; Xing, G.; Sun, G. 2D Hybrid Halide Perovskites: Structure, Properties, and Applications in Solar Cells. *Small* **2021**, *17* (43), 2103514.

[92] Kim, E.-B.; Akhtar, M. S.; Shin, H.-S.; Ameen, S.; Nazeeruddin, M. K. A Review on Two-Dimensional (2D) and 2D-3D Multidimensional Perovskite Solar Cells: Perovskites Structures, Stability, and Photovoltaic Performances. *J. Photochem. Photobiol. C Photochem. Rev.* **2021**, *48*, 100405.

[93] Li, X.; Hoffman, J. M.; Kanatzidis, M. G. The 2D Halide Perovskite Rulebook: How the Spacer Influences Everything from the Structure to Optoelectronic Device Efficiency. *Chem. Rev.* **2021**, *121* (4), 2230–2291.

[94] Parikh, N.; Tavakoli, M. M.; Pandey, M.; Kalam, A.; Prochowicz, D.; Yadav, P. Role of the Spacer Cation in the Growth and Crystal Orientation of Two-Dimensional

Perovskites. *Sustain. Energy Fuels* **2021**, *5* (5), 1255–1279.

[95] Huang, Y.; Li, Y.; Lim, E. L.; Kong, T.; Zhang, Y.; Song, J.; Hagfeldt, A.; Bi, D. Stable Layered 2D Perovskite Solar Cells with an Efficiency of over 19% via Multifunctional Interfacial Engineering. *J. AM. CHEM. SOC* **2021**, *143*, 3911–3917.

[96] Tsai, H.; Nie, W.; Blancon, J.; Stoumpos, C. C.; Asadpour, R.; Harutyunyan, B.; Neukirch, A. J.; Verduzco, R.; Crochet, J. J.; Tretiak, S.; Pedesseau, L.; Even, J.; Alam, M. A.; Gupta, G.; Lou, J.; Ajayan, P. M.; Bedzyk, M. J.; Kanatzidis, M. G.; Mohite, A. D. High-Efficiency Two-Dimensional Ruddlesden–Popper Perovskite Solar Cells. *Nature* **2016**, *536*, 312.

[97] Cho, Y.; Soufiani, A. M.; Yun, J. S.; Kim, J.; Lee, D. S.; Seidel, J.; Deng, X.; Green, M. A.; Huang, S.; Ho-baillie, A. W. Y. Mixed 3D – 2D Passivation Treatment for Mixed-Cation Lead Mixed-Halide Perovskite Solar Cells for Higher Efficiency and Better Stability. *Adv. Energy Mater.* **2018**, *8*, 1703392.

[98] Jang, Y.; Lee, S.; Yeom, K. M.; Jeong, K.; Choi, K.; Choi, M.; Noh, J. H. Intact 2D/3D Halide Junction Perovskite Solar Cells via Solid-Phase in-Plane Growth. *Nat. Energy* **2021**, *6* (January), 63–71.

[99] Milić, J. V; Zakeeruddin, S. M.; Grätzel, M. Layered Hybrid Formamidinium Lead Iodide Perovskites: Challenges and Opportunities. *Acc. Chem. Res.* **2021**, *54* (12), 2729–2740.

[100] Gélvez-Rueda, M. C.; Ahlawat, P.; Merten, L.; Jahanbakhshi, F.; Mladenović, M.; Hinderhofer, A.; Dar, M. I.; Li, Y.; Dučinskas, A.; Carlsen, B.; Tress, W.; Ummadisingu, A.; Zakeeruddin, S. M.; Schreiber, F.; Hagfeldt, A.; Rothlisberger, U.; Grozema, F. C.; Milić, J. V; Graetzel, M. Formamidinium-Based Dion-Jacobson Layered Hybrid Perovskites: Structural Complexity and Optoelectronic Properties. *Adv. Funct. Mater.* **2020**, *30* (38), 2003428.

[101] Hope, M. A.; Nakamura, T.; Ahlawat, P.; Mishra, A.; Cordova, M.; Jahanbakhshi, F.; Mladenović, M.; Runjhun, R.; Merten, L.; Hinderhofer, A.; Carlsen, B. I.; Kubicki, D. J.; Gershoni-Poranne, R.; Schneeberger, T.; Carbone, L. C.; Liu, Y.; Zakeeruddin, S. M.; Lewinski, J.; Hagfeldt, A.; Schreiber, F.; Rothlisberger, U.; Grätzel, M.; Milić, J. V; Emsley, L. Nanoscale Phase Segregation in Supramolecular π-Templating for Hybrid Perovskite Photovoltaics from NMR Crystallography. *J. Am. Chem. Soc.* **2021**, *143* (3), 1529–1538.

[102] Lin, L.; Jones, T. W.; Yang, T. C.-J.; Duffy, N. W.; Li, J.; Zhao, L.; Chi, B.; Wang, X.; Wilson, G. J. Inorganic Electron Transport Materials in Perovskite Solar Cells. *Adv.*

Funct. Mater. **2021**, *31* (5), 2008300.

[103] Online, V. A. Metal Oxide Alternatives for Efficient Electron Transport in Perovskite Solar Cells : Beyond TiO_2 and SnO_2. *J. Mater. Chem. A* **2020**, *8*, 19768–19787.

[104] Akin, S.; Bauer, M.; Uchida, R.; Arora, N.; Jacopin, G.; Liu, Y.; Zakeeruddin, S. M.; Hertel, D.; Meerholz, K.; Mena-osteritz, E.; Ba, P.; Dar, M. I.; Gra, M. Cyclopentadithiophene-Based Hole-Transporting Material for Highly Stable Perovskite Solar Cells with Stabilized E Ffi Ciencies Approaching 21 %. *ACS Appl. Energy Mater.* **2020**, *3*, 7456−7463.

[105] Liu, Y.; Akin, S.; Hinderhofer, A.; Eickemeyer, F. T.; Zhu, H.; Seo, Y.; Zhang, J.; Schreiber, F.; Zhang, H.; Zakeeruddin, S. M.; Hagfeldt, A.; Dar, M. I.; Gr, M. Stabilization of Highly Efficient and Stable Phase-Pure FAPbI 3 Perovskite Solar Cells by Molecularly Tailored 2D-Overlayers. *Angew.Chem.Int. Ed* **2020**, *59*, 15688–15694.

[106] Zhiyuan Cao, Chengbo Li, Xiaoyu Deng, Shurong Wang, Yuan Yuan, Yuanming Chen,a Zhi Wang, Yaqing Liu, L. D. and F. H. Metal Oxide Alternatives for e Ffi Cient Electron Transport in Perovskite Solar Cells : Beyond TiO_2 and SnO_2. *J. Mater. Chem. A* **2020**, *8*, 19768–19787.

[107] Zhen, C.; Wu, T.; Chen, R.; Wang, L.; Liu, G.; Cheng, H. Strategies for Modifying TiO_2 Based Electron Transport Layers to Boost Perovskite Solar Cells. *ACS Sustain. Chem. Eng* **2019**, *7*, 4586−4618.

[108] Ito, S.; Tanaka, S.; Manabe, K.; Nishino, H. Effects of Surface Blocking Layer of Sb_2S_3 on Nanocrystalline TiO_2 for $CH_3NH_3PbI_3$ Perovskite Solar Cells. *J. Phys. Chem. C* **2014**, *118*, 16995−17000.

[109] Zhou, Y.; Li, X.; Lin, H. To Be Higher and Stronger — Metal Oxide Electron Transport Materials for Perovskite Solar Cells. *Small* **2020**, *16*.

[110] Xiong, L.; Guo, Y.; Wen, J.; Liu, H.; Yang, G.; Qin, P.; Fang, G. Review on the Application of SnO2 in Perovskite Solar Cells. *Adv. Funct. Mater.* **2018**, *28*.

[111] Yeom, E. J.; Shin, S. S.; Yang, W. S.; Lee, S. J.; Yin, W.; Kim, D.; Noh, J. H.; Ahn, T. K.; Seok, S. Il. Controllable Synthesis of Single Crystalline Sn-Based Oxides and Their Application in Perovskite Solar Cells. *J. Mater. Chem. A* **2017**, *5*, 79–86.

[112] Ai, Y.; Liu, W.; Shou, C.; Yan, J.; Li, N.; Yang, Z.; Song, W.; Yan, B.; Sheng, J.; Ye, J. SnO2 Surface Defects Tuned by $(NH_4)_2S$ for High-Efficiency Perovskite Solar Cells. *Sol. Energy* **2019**, *194*, 541–547.

[113] Slater, B.; Catlow, C. R. A.; Williams, E.; Stoneham, A. M. Dissociation of O_2 on the Reduced SnO_2(110) Surface. *Chem. Commun.* **2000**, *2*, 1235–1236.

[114] Wang, K.; Shi, Y.; Dong, Q.; Li, Y.; Wang, S.; Yu, X.; Wu, M.; Ma, T. Low-Temperature and Solution-Processed Amorphous WO_x as Electron-Selective Layer for Perovskite Solar Cells. *J. Phys. Chem. Lett* **2015**, *6*, 755–759.

[115] Bera, A.; Wu, K.; Sheikh, A.; Alarousu, E.; Mohammed, O. F.; Wu, T. Perovskite Oxide $SrTiO_3$ as an Efficient Electron Transporter for Hybrid Perovskite Solar Cells. *J. Phys. Chem. C* **2014**, *118*, 28494–28501.

[116] Shin, S. S.; Yeom, E. J.; Yang, W. S.; Hur, S.; Kim, M. G.; Im, J.; Seo, J.; Noh, J. H.; Seok, S. Il. Colloidally Prepared La-Doped $BaSnO_3$ Electrodes for Efficient, Photostable Perovskite Solar Cells. *Science (80-.).* **2017**, *356*, 167–171.

[117] Qin, M.; Ma, J.; Ke, W.; Qin, P.; Lei, H.; Tao, H.; Zheng, X.; Xiong, L.; Liu, Q.; Chen, Z.; Lu, J.; Yang, G.; Fang, G. Perovskite Solar Cells Based on Low-Temperature Processed Indium Oxide Electron Selective Layers. *ACS Appl. Mater. Interfaces* **2016**, *8*, 8460–8466.

[118] Kogo, A.; Numata, Y.; Ikegami, M.; Tsutomu, M. Nb2O5 Blocking Layer for High Open-Circuit Voltage Perovskite Solar Cells. *Chem. Lett* **2015**, *44*, 829–830.

[119] Özgür, Ü.; Alivov, Y. I.; Liu, C.; Teke, A.; Reshchikov, M. A.; Do, S.; Avrutin, V. A Comprehensive Review of ZnO Materials and Devices. *J. Appl. Phys.* **2005**, *98*.

[120] Zhang, B. Q.; Dandeneau, C. S.; Zhou, X.; Cao, G. ZnO Nanostructures for Dye-Sensitized Solar Cells. *Adv. Mater.* **2009**, *21*, 4087–4108.

[121] Shao, S.; Loi, M. A. The Role of the Interfaces in Perovskite Solar Cells. *Adv. Mater. Interfaces* **2020**, *7*, 1901469.

[122] Boyd, C. C.; Cheacharoen, R.; Leijtens, T.; McGehee, M. D. Understanding Degradation Mechanisms and Improving Stability of Perovskite Photovoltaics. *Chem. Rev.* **2019**, *119* (5), 3418–3451.

[123] Zhang, P.; Wu, J.; Wang, Y.; Sarvari, H.; Liu, D.; Chen, Z. D.; Li, S. Enhanced Efficiency and Environmental Stability of Planar Perovskite Solar Cells by Suppressing Photocatalytic Decomposition. *J. Mater. Chem. A* **2017**, *5*, 17368–17378.

[124] Luo, J.; Wang, Y.; Zhang, Q. Progress in Perovskite Solar Cells Based on ZnO Nanostructures. *Sol. Energy* **2018**, *163*, 289–306.

[125] Zhang, P.; Wu, J.; Zhang, T.; Wang, Y.; Liu, D.; Chen, H.; Ji, L.; Liu, C.; Ahmad, W.; Chen, Z. D.; Li, S. Perovskite Solar Cells with ZnO Electron-Transporting Materials. *Adv. Mater.* **2018**, *30*, 1–20.

[126] Nomaan, A. T.; Ahmed, A. A.; Ahmed, N. M.; Idris, M. I.; Hashim, M. R.; Rashid, M. ZnO Quantum Dot Based Thin Films as Promising Electron Transport Layer :

Influence of Surface-to-Volume Ratio on the Photoelectric Properties. *Ceram. Int.* **2021**, *47* (9), 12397–12409.

[127] Liu, D.; Kelly, T. L. Perovskite Solar Cells with a Planar Heterojunction Structure Prepared Using Room-Temperature Solution Processing Techniques. *Nat. Photonics* **2014**, *8*.

[128] You, A.; Be, M. A. Y.; In, I. Dominant Effect of Near-Interface Native Point Defects on ZnO Schottky Barriers. *Appl. Phys. Lett.* **2007**, *90*.

[129] Chen, S.; Small, C. E.; Amb, C. M.; Subbiah, J.; Lai, T.; Tsang, W.; Manders, J. R.; Reynolds, J. R.; So, F. Inverted Polymer Solar Cells with Reduced Interface Recombination. *Adv. Energy Mater.* **2012**, *2*, 1333–1337.

[130] Yang, J.; Siempelkamp, B. D.; Mosconi, E.; De Angelis, F.; Kelly, T. L. Origin of the Thermal Instability in $CH_3NH_3PbI_3$ Thin Films Deposited on ZnO. *Chem. Mater.* **2015**, *27* (12), 4229–4236.

[131] Cao, J.; Wu, B.; Chen, R.; Wu, Y.; Hui, Y.; Mao, B.; Zheng, N. Efficient , Hysteresis-Free , and Stable Perovskite Solar Cells with ZnO as Electron-Transport Layer : Effect of Surface Passivation. *Adv. Mater.* **2018**, *30*, 1705596.

[132] Zhang, P.; Yang, F.; Kapil, G.; Shen, Q.; Toyoda, T.; Yoshino, K.; Minemoto, T.; S Pandey, S.; Ma, T.; Hayase, S. Enhanced Performance of ZnO Based Perovskite Solar Cells by Nb_2O_5 Surface Passivation. *Org. Electron.* **2018**, *62*, 615–620.

[133] Li, S.; Zhang, P.; Wang, Y.; Sarvari, H.; Liu, D.; Wu, J.; Yang, Y.; Wang, Z.; Chen, Z. Interface Engineering of High Efficiency Perovskite Solar Cells Based on ZnO Nanorods Using Atomic Layer Deposition. *Nano Res.* **2017**, *10* (3), 1092–1103.

[134] Azmi, R.; Hwang, S.; Yin, W.; Kim, T.; Ahn, T. K.; Jang, S. High Efficiency Low-Temperature Processed Perovskite Solar Cells Integrated with Alkali Metal Doped ZnO Electron Transport Layers. *ACS Energy Lett.* **2018**, *3*, 1241–1246.

[135] Han, J.; Kwon, H.; Kim, E.; Kim, D.; Son, H. J.; Ha, D. Interfacial Engineering of a ZnO Electron Transporting Layer Using Self-Assembled Monolayers for High Performance and Stable Perovskite Solar Cells. *J. Mater. Chem. A* **2020**, *8*, 2105–2113.

[136] Tavakoli, M. M.; Tavakoli, R.; Yadav, P.; Kong, J. A Graphene / ZnO Electron Transfer Layer Together with Perovskite Passivation Enables Highly Efficient and Stable Perovskite Solar Cells. *J. Mater. Chem. A* **2019**, *7*, 679–686.

[137] Yao, K.; Leng, S.; Zhou, L.; Yao, K.; Leng, S.; Liu, Z.; Fei, L.; Chen, Y.; Li, S.; Zhou, N.; Zhang, J.; Xu, Y.-X.; Zhou, L.; Huang, H.; Jen, A. K. Fullerene-Anchored Core-

Shell ZnO Nanoparticles for Efficient and Stable Dual- Sensitized Perovskite Solar Cells Nanoparticles for Efficient and Stable Dual-Sensitized Perovskite Solar Cells. *Joule* **2019**, *3*, 417–431.

[138] Dong, Q.; Hoi, C.; Ho, Y.; Yu, H.; Salehi, A.; So, F. Defect Passivation by Fullerene Derivative in Perovskite Solar Cells with Aluminum-Doped Zinc Oxide as Electron Transporting Layer. *Chem. Mater* **2019**, *31*, 6833–6840.

[139] Wang, Z.; Zhu, X.; Feng, J.; Wang, C.; Zhang, C.; Ren, X.; Priya, S.; Liu, S.; Yang, D. Antisolvent- and Annealing-Free Deposition for Highly Stable Efficient Perovskite Solar Cells via Modified ZnO. *Adv. Sci.* **2021**, *8*, 2002860.

[140] Lee, J. W.; Kim, H. S.; Park, N. G. Lewis Acid-Base Adduct Approach for High Efficiency Perovskite Solar Cells. *Acc. Chem. Res.* **2016**, *49*, 311–319.

[141] Lv, M.; Dong, X.; Fang, X.; Lin, B.; Zhang, S.; Ding, J.; Yuan, N. A Promising Alternative Solvent of Perovskite to Induce Rapid Crystallization for High-Efficiency Photovoltaic Devices. *RSC Adv.* **2015**, *5* (26), 20521–20529.

[142] Zhou, Y.; Yang, M.; Wu, W.; Vasiliev, A. L.; Zhu, K.; Padture, N. P. Room-Temperature Crystallization of Hybrid-Perovskite Thin Films via Solvent-Solvent Extraction for High-Performance Solar Cells. *J. Mater. Chem. A* **2015**, *3*, 8178–8184.

[143] Dualeh, A.; Tétreault, N.; Moehl, T.; Gao, P.; Nazeeruddin, M. K.; Grätzel, M. Effect of Annealing Temperature on Film Morphology of Organic-Inorganic Hybrid Pervoskite Solid-State Solar Cells. *Adv. Funct. Mater.* **2014**, *24*, 3250–3258.

[144] Stranks, S. D.; Eperon, G. E.; Grancini, G.; Menelaou, C.; Alcocer, M. J. P.; Leijtens, T.; Herz, L. M.; Petrozza, A.; Snaith, H. J. Electron-Hole Diffusion Lengths Exceeding Trihalide Perovskite Absorber. *Science (80-.).* **2013**, *342*, 341–344.

[145] Im, J.-H.; Kim, H.-S.; Park, N.-G. Morphology-Photovoltaic Property Correlation in Perovskite Solar Cells: One-Step versus Two-Step Deposition of $CH_3NH_3PbI_3$. *APL Mater.* **2014**, *2* (8), 81510.

[146] Ummadisingu, A.; Grätzel, M. Revealing the Detailed Path of Sequential Deposition for Metal Halide Perovskite Formation. *Sci. Adv.* **2018**, *4*.

[147] Bi, C.; Shao, Y.; Yuan, Y.; Xiao, Z.; Wang, C.; Gao, Y.; Huang, J. Understanding the Formation and Evolution of Interdiffusion Grown Organolead Halide Perovskite Thin Films by Thermal Annealing. *J. Mater. Chem. A* **2014**, *2*, 18508–18514.

[148] Zeng, L.; Chen, S.; Forberich, K.; Brabec, C. J.; Mai, Y.; Guo, F. Controlling the Crystallization Dynamics of Photovoltaic Perovskite Layers on Larger-Area Coatings. *Energy Environ. Sci.* **2020**, *13*, 4666–4690.

[149] Bruening, K.; Tassone, C. J. Antisolvent Processing of Lead Halide Perovskite Thin Films Studied by: In Situ X-Ray Diffraction. *J. Mater. Chem. A* **2018**, *6*, 18865–18870.

[150] Paek, S.; Schouwink, P.; Athanasopoulou, E. N.; Cho, K. T.; Grancini, G.; Lee, Y.; Zhang, Y.; Stellacci, F.; Nazeeruddin, M. K.; Gao, P. From Nano- to Micrometer Scale: The Role of Antisolvent Treatment on High Performance Perovskite Solar Cells. *Chem. Mater.* **2017**, *29*, 3490–3498.

[151] Xiao, M.; Huang, F.; Huang, W.; Dkhissi, Y.; Zhu, Y.; Etheridge, J.; Gray-Weale, A.; Bach, U.; Cheng, Y. B.; Spiccia, L. A Fast Deposition-Crystallization Procedure for Highly Efficient Lead Iodide Perovskite Thin-Film Solar Cells. *Angew. Chemie - Int. Ed.* **2014**, *53*, 9898–9903.

[152] Dou, B.; Wheeler, L. M.; Christians, A.; Moore, D. T.; Harvey, S. P.; Berry, J. J.; Barnes, F. S.; Shaheen, S. E.; Hest, M. F. A. M. Van. Degradation of Highly Alloyed Metal Halide Perovskite Precursor Inks: Mechanism and Storage. *ACS Energy Lett.* **2018**, *3*, 979–985.

[153] Chao, L.; Niu, T.; Gao, W.; Ran, C.; Song, L.; Chen, Y.; Huang, W. Solvent Engineering of the Precursor Solution toward Large-Area Production of Perovskite Solar Cells. *Adv. Mater.* **2021**, *33*.

[154] Chem, J. M.; Song, T.; Chen, Q.; Zhou, H.; Jiang, C.; Wang, H.; Yang, M.; Liu, Y. Perovskite Solar Cells: Film Formation and Properties. *J. Mater. Chem. A* **2015**, *3*, 9032–9050.

[155] Gil-Escrig, L.; Momblona, C.; La-Placa, M.-G.; Boix, P. P.; Sessolo, M.; Bolink, H. J. Vacuum Deposited Triple-Cation Mixed-Halide Perovskite Solar Cells. *Adv. Energy Mater.* **2018**, *8* (14), 1703506.

[156] Feng, J.; Jiao, Y.; Wang, H.; Zhu, X.; Sun, Y.; Du, M.; Cao, Y.; Yang, D.; Liu, S. (Frank). High-Throughput Large-Area Vacuum Deposition for High-Performance Formamidine-Based Perovskite Solar Cells. *Energy Environ. Sci.* **2021**, *14* (5), 3035–3043.

[157] Prochowicz, D.; Franckevicius, M.; Cieslak, A. M.; Zakeeruddin, S. M.; Gratzel, M.; Lewinski, J. Mechanosynthesis of the Hybrid Perovskite $CH_3NH_3PbI_3$: Characterization and the Corresponding Solar Cell Efficiency. *J. Mater. Chem. A* **2015**, *3*, 20772–20777.

[158] Prochowicz, D.; Yadav, P.; Saliba, M.; Kubicki, D. J.; Mahdi, M.; Zakeeruddin, S. M.; Lewi, J.; Emsley, L.; Grätzel, M. One-Step Mechanochemical Incorporation of an

Insoluble Cesium Additive for High Performance Planar Heterojunction Solar Cells. *Nano Energy* **2018**, *49*, 523–528.

[159] Prochowicz, D.; Saski, M.; Yadav, P.; Graetzel, M.; Lewinski, J. Mechanoperovskites for Photovoltaic Applications : Preparation , Characterization , and Device Fabrication. *Acc. Chem. Res* **2019**, *52* (11), 3233–3243.

[160] Margetic, D.; Strukil, V. Recent Advances in Mechanochemical Orgainic Synthesis. In *Organic Snthesis: A Nascent Relook*; 2020.

[161] James, S. L.; Adams, C. J.; Bolm, C.; Braga, D.; Collier, P.; Friščić, T.; Grepioni, F.; Harris, K. D. M.; Hyett, G.; Jones, W.; Krebs, A.; Mack, J.; Maini, L.; Orpen, A. G.; Parkin, I. P.; Shearouse, W. C.; Steed, J. W.; Waddell, D. C. Mechanochemistry: Opportunities for New and Cleaner Synthesis. *Chem. Soc. Rev.* **2012**, *41* (1), 413–447.

[162] Głowniak, S.; Szczęśniak, B.; Choma, J.; Jaroniec, M. Mechanochemistry: Toward Green Synthesis of Metal–Organic Frameworks. *Mater. Today* **2021**, *46*, 109–124.

[163] Schlem, R.; Burmeister, C. F.; Michalowski, P.; Ohno, S.; Dewald, G. F.; Kwade, A.; Zeier, W. G. Energy Storage Materials for Solid-State Batteries: Design by Mechanochemistry. *Adv. Energy Mater.* **2021**, *11* (30), 2101022.

[164] Kubicki, D.; Prochowicz, D.; Hofstetter, A.; Saski, M.; Yadav, P.; Bi, D.; Pellet, N.; Lewin, J.; Zakeeruddin, S. M.; Gratzel, M.; Emsley, L. Formation of Stable Mixed Guanidinium − Methylammonium Phases with Exceptionally Long Carrier Lifetimes for High-Efficiency Lead Iodide-Based Perovskite Photovoltaics. *J. AM. CHEM. SOC* **2018**, *140*, 3345–3351.

[165] Askar, A. M.; Karmakar, A.; Bernard, G. M.; Ha, M.; Terskikh, V. V; Wiltshire, B. D.; Patel, S.; Fleet, J.; Shankar, K.; Michaelis, V. K. Composition-Tunable Formamidinium Lead Mixed Halide Perovskites via Solvent-Free Mechanochemical Synthesis: Decoding the Pb Environments Using Solid-State NMR Spectroscopy. *J. Phys. Chem. Lett* **2018**, *9*, 2671–2677.

[166] Karmakar, A.; Askar, A. M.; Bernard, G. M.; Terskikh, V. V; Ha, M.; Patel, S.; Shankar, K.; Michaelis, V. K. Mechanochemical Synthesis of Methylammonium Lead Mixed − Halide Perovskites: Unraveling the Solid-Solution Behavior Using Solid-State NMR. *Chem. Mater* **2018**, *30*, 2309–2321.

[167] Sadhukhan, P.; Kundu, S.; Roy, A.; Ray, A.; Maji, P.; Dutta, H.; Pradhan, S. K.; Das, S. Solvent-Free Solid-State Synthesis of High Yield Mixed Halide Perovskites for Easily Tunable Composition and Band Gap. *Cryst. Growth Des.* **2018**, *18*, 3428–3432.

[168] Protesescu, L.; Yakunin, S.; Nazarenko, O.; Dirin, D. N.; Kovalenko, M. V. Low-Cost

Synthesis of Highly Luminescent Colloidal Lead Halide Perovskite Nanocrystals by Wet Ball Milling. *ACS Appl. Nano Mater.* **2018**, *1*, 1300–1308.

[169] Zhu, Z.; Yang, Q.; Gao, L.; Zhang, L.; Shi, A.; Sun, C.; Wang, Q.; Zhang, H. Solvent-Free Mechanosynthesis of Composition-Tunable Cesium Lead Halide Perovskite Quantum Dots. *J. Phys. Chem. Lett* **2017**, *8*, 1610–1614.

[170] Palazon, F.; Ajjouri, Y. El; Sebastia-Luna, P.; Lauciello, S.; Mana, L.; Bolink, H. J. Mechanochemical Synthesis of Inorganic Halide Perovskites: Evolution of Phase-Purity, Morphology, and Photoluminescence. *J. Mater. Chem. C* **2019**, *7*, 11406.

[171] Ajjouri, Y. El; Palazon, F.; Sessolo, M.; Bolink, H. J. Single-Source Vacuum Deposition of Mechanosynthesized Inorganic Halide Perovskites. *Chem. Mater* **2018**, *30*, 7423–7427.

[172] Saski, M.; Prochowicz, D.; Marynowski, W.; Lewiński, J. Mechanosynthesis, Optical, and Morphological Properties of MA, FA, Cs-SnX_3 (X = I , Br) and Phase-Pure Mixed-Halide $MASnI_xBr_{3-x}$ Perovskites. *Eur. J. Inorg. Chem.* **2019**, 2680–2684.

[173] Sebasti, P.; Sessolo, M.; Palaz, F.; Ort, E.; Bolink, H. J. Tuning the Optical Absorption of Sn- ,Ge-, and Zn-Substituted Cs2AgBiBr6 Double Perovskites : Structural and Electronic Effects. *Chem. Mater* **2021**, *33*, 8028–8035.

[174] Wu, T.; Liu, X.; Luo, X.; Lin, X.; Cui, D.; Wang, Y.; Segawa, H.; Zhang, Y.; Han, L. Lead-Free Tin Perovskite Solar Cells. *Joule* **2021**, *5* (4), 863–886.

[175] Cao, J.; Feng, Y. Recent Progress in Tin-Based Perovskite Solar Cells. *Energy Environ. Sci.* **2021**, *14*, 1286–1325.

[176] Wang, Y.; Manohari, G.; Mahmoudi, T.; Mai, Y.; Hahn, Y. A Critical Review of Materials Innovation and Interface Stabilization for Efficient and Stable Perovskite Photovoltaics. *Nano Energy* **2021**, *87* (January), 106141.

[177] Saliba, M.; Matsui, T.; Domanski, K.; Seo, J.-Y.; Ummadisingu, A.; Zakeeruddin, S. M.; Baena, J. C.; Tress, W.; Abate, A.; Hagfeldt, A.; Gratzel, M. Incorporation of Rubidium Cations into Perovskite Solar Cells Improves Photovoltaic Performance. *Science (80-.).* **2016**, *354* (6309), 206–209.

[178] Saliba, M.; Matsui, T.; Seo, J.-Y.; Domanski, K.; Baena, J. C.; Nazeeruddin, M. K.; Zakeeruddin, S. M.; Tress, W.; Abate, A.; Hagfeldt, A.; Gratzel, M. Cesium-Containing Triple Cation Perovskite Solar Cells: Improved Stability, Reproducibility and High Efficiency. *Energy Environ. Sci.* **2016**, *9* (6), 1989.

[179] Lee, J.; Park, N. Chemical Approaches for Stabilizing Perovskite Solar Cells. *Adv. Energy Mater.* **2020**, *10*, 1–21.

[180] Li, N.; Niu, X.; Chen, Q.; Zhou, H. Towards Commercialization: The Operational Stability of Perovskite Solar Cells. *Chem. Soc. Rev.* **2020**, *49* (22), 8235–8286.

[181] Li, D.; Zhang, D.; Lim, K.; Hu, Y.; Rong, Y.; Mei, A.; Park, N.; Han, H. A Review on Scaling Up Perovskite Solar Cells. *Adv. Funct. Mater.* **2021**, *31*, 2008621.

[182] Galagan, Y. Perovskite Solar Cells from Lab to Fab : The Main Challenges to Access the Market. *Oxford Open Mater. Sci.* **2021**, *0*, 1–9.

[183] Rong, Y.; Hu, Y.; Mei, A.; Tan, H.; Saidaminov, M. I.; Seok, S. Il; McGehee, M. D.; Sargent, E. H.; Han, H. Challenges for Commercializing Perovskite Solar Cells. *Science (80-.).* **2018**, *361* (6408).

[184] Tu, Y.; Wu, J.; Xu, G.; Yang, X.; Cai, R.; Gong, Q.; Zhu, R.; Huang, W. Perovskite Solar Cells for Space Applications: Progress and Challenges. *Adv. Mater.* **2021**, *33* (21), 2006545.

[185] Wu, T.; Qin, Z.; Wang, Y.; Wu, Y.; Chen, W.; Zhang, S.; Cai, M.; Dai, S.; Zhang, J.; Liu, J.; Zhou, Z.; Liu, X.; Segawa, H.; Tan, H.; Tang, Q.; Fang, J.; Li, Y.; Ding, L.; Ning, Z.; Qi, Y.; Zhang, Y.; Han, L. The Main Progress of Perovskite Solar Cells in 2020–2021. *Nano-Micro Lett.* **2021**, *13* (1), 152.

[186] J B Mooney, and; Radding, S. B. Spray Pyrolysis Processing. *http://dx.doi.org/10.1146/annurev.ms.12.080182.000501* **2003**, *12*, 81–101.

[187] Spincoater.com - What is Spin Coating? http://www.spincoater.com/what-is-spin-coating.php (accessed 2021 -09 -16).

[188] Alharbi, E. A.; Krishna, A.; Baumeler, T. P.; Dankl, M.; Fish, G. C.; Eickemeyer, F.; Ouellette, O.; Ahlawat, P.; Viktor, S.; John, E.; Yang, B.; Pfeifer, L.; Avalos, C. E.; Pan, L.; Mensi, M.; Schouwink, P. A.; Moser, J.; Hagfeldt, A.; Rothlisberger, U.; Zakeeruddin, S. M.; Graetzel, M. Methylammonium Triiodide for Defect Engineering of High-Efficiency Perovskite Solar Cells. *ACS Energy Lett.* **2021**, *6*, 3650–3660.

[189] Katan, C.; Mercier, N.; Even, J. Quantum and Dielectric Con Fi Nement E Ff Ects in Lower-Dimensional Hybrid Perovskite Semiconductors. *Chem. Rev.* **2019**, *119*, 3140–3192.

[190] Vasileiadou, E. S.; Wang, B.; Spanopoulos, I.; Hadar, I.; Navrotsky, A.; Kanatzidis, M. G. Insight on the Stability of Thick Layers in 2D Ruddlesden − Popper and Dion − Jacobson Lead Iodide Perovskites. *J. AM. CHEM. SOC* **2021**, *143*, 2523–2536.

[191] Ma, C.; Shen, D.; Ng, T.; Lo, M.; Lee, C. 2D Perovskites with Short Interlayer Distance for High-Performance Solar Cell Application. *Adv. Mater.* **2018**, *30*.

[192] Fidelli, A. M.; Karadeniz, B.; Howarth, A. J.; Huskic, D. I.; Dinnebier, R. E.;

Stilinovic, V.; Farha, O. K. ChemComm Metal – Organic Frameworks †. **2018**, 6999–7002.

[193] Chen, Y.; Sun, Y.; Peng, J.; Tang, J.; Zheng, K.; Liang, Z. 2D Ruddlesden – Popper Perovskites for Optoelectronics. **2018**, *1703487*, 1–15.

[194] Muljarov, E. A.; Tikhodeev, S. G.; Gippius, N. A. Excitons in Self-Organized Semiconductor/Insulator Superlattices: PbI-Based Perovskite Compounds. *Phys. Rev. B* **1995**, *51* (20).

[195] Gan, X.; Wang, O.; Liu, K.; Du, X.; Guo, L.; Liu, H. 2D Homologous Organic-Inorganic Hybrids as Light-Absorbers for Planer and Nanorod-Based Perovskite Solar Cells. *Sol. Energy Mater. Sol. Cells* **2017**, *162* (September 2016), 93–102.

[196] Babu, R.; Giribabu, L.; Singh, S. P. Recent Advances in Halide-Based Perovskite Crystals and Their Optoelectronic Applications. *Cryst. Growth Des.* **2018**, *18* (4), 2645–2664.

[197] Senocrate, A.; Moudrakovski, I.; Kim, G. Y.; Yang, T.; Gregori, G.; Graetzel, M.; Maier, J. The Nature of Ion Conduction in Methylammonium Lead Iodide : A Multimethod Approach. *Angew.Chem.Int. Ed* **2017**, *56*, 7755–7759.

[198] Dong, Q.; Fang, Y.; Shao, Y.; Mulligan, P.; Qiu, J.; Cao, L.; Huang, J. Electron-Hole Diffusion Lengths > 175 Micrometer in Solution-Grown $CH_3NH_3PbI_3$ Single Crystals. *Science (80-.).* **2015**, *347* (6225).

[199] Saidaminov, M. I.; Abdelhady, A. L.; Murali, B.; Alarousu, E.; Burlakov, V. M.; Peng, W.; Dursun, I.; Wang, L.; He, Y.; MacUlan, G.; Goriely, A.; Wu, T.; Mohammed, O. F.; Bakr, O. M. High-Quality Bulk Hybrid Perovskite Single Crystals within Minutes by Inverse Temperature Crystallization. *Nat. Commun.* **2015**, *6* (May), 1–6.

[200] Yuan, Y.; Huang, J. Ion Migration in Organometal Trihalide Perovskite and Its Impact on Photovoltaic Efficiency and Stability. *Acc. Chem. Res.* **2016**, *49* (2), 286–293.

[201] Frost, J. M.; Walsh, A. What Is Moving in Hybrid Halide Perovskite Solar Cells? *Acc. Chem. Res.* **2016**, *49* (3), 528–535.

[202] Egger, D. A.; Kronik, L.; Rappe, A. M. Theory of Hydrogen Migration in Organic–Inorganic Halide Perovskites. *Angew. Chemie Int. Ed.* **2015**, *54* (42), 12437–12441.

[203] Azpiroz, J. M.; Mosconi, E.; Bisquert, J.; De Angelis, F. Defect Migration in Methylammonium Lead Iodide and Its Role in Perovskite Solar Cell Operation. *Energy Environ. Sci.* **2015**, *8* (7), 2118–2127.

[204] Eames, C.; Frost, J. M.; Barnes, P. R. F.; O'Regan, B. C.; Walsh, A.; Islam, M. S. Ionic Transport in Hybrid Lead Iodide Perovskite Solar Cells. *Nat. Commun.* **2015**, *6*

(1), 7497.

[205] Levine, I.; Nayak, P. K.; Wang, J. T.-W.; Sakai, N.; Van Reenen, S.; Brenner, T. M.; Mukhopadhyay, S.; Snaith, H. J.; Hodes, G.; Cahen, D. Interface-Dependent Ion Migration/Accumulation Controls Hysteresis in $MAPbI_3$ Solar Cells. *J. Phys. Chem. C* **2016**, *120* (30), 16399–16411.

[206] Noh, J. H.; Im, S. H.; Heo, J. H.; Mandal, T. N.; Seok, S. Il. Chemical Management for Colorful, Efficient, and Stable Inorganic–Organic Hybrid Nanostructured Solar Cells. *Nano Lett.* **2013**, *13* (4), 1764–1769.

[207] Ruess, R.; Benfer, F.; Böcher, F.; Stumpp, M.; Schlettwein, D. Stabilization of Organic–Inorganic Perovskite Layers by Partial Substitution of Iodide by Bromide in Methylammonium Lead Iodide. *ChemPhysChem* **2016**, *17* (10), 1505–1511.

[208] Giorgi, G.; Yamashita, K. Zero-Dipole Molecular Organic Cations in Mixed Organic–Inorganic Halide Perovskites: Possible Chemical Solution for the Reported Anomalous Hysteresis in the Current–Voltage Curve Measurements. *Nanotechnology* **2015**, *26* (44), 442001.

[209] Giorgi, G.; Fujisawa, J.-I.; Segawa, H.; Yamashita, K. Organic–Inorganic Hybrid Lead Iodide Perovskite Featuring Zero Dipole Moment Guanidinium Cations: A Theoretical Analysis. *J. Phys. Chem. C* **2015**, *119* (9), 4694–4701.

[210] Halder, A.; Rakita, Y.; Cahen, D.; Sarkar, S. K. Effect of Low Pressure on Tetragonal to Cubic Phase Transition of Methylammonium Lead Iodide Perovskite. *J. Phys. Chem. Lett.* **2020**, *11* (4), 1473–1476.

[211] Mahapatra, A.; Runjhun, R.; Nawrocki, J.; Lewin, J.; Kalam, A.; Kumar, P.; Trivedi, S.; Tavakoli, M. M.; Prochowicz, D.; Yadav, P. Elucidation of the Role of Guanidinium Incorporation in Single-Crystalline MAPbI3 Perovskite on Ion Migration and Activation Energy. *Phys. Chem. Chem. Phys.* **2020**, *22*, 11467–11473.

[212] Prochowicz, D.; Runjhun, R.; Tavakoli, M. M.; Yadav, P.; Saski, M.; Alanazi, A. Q.; Kubicki, D. J.; Kaszkur, Z.; Zakeeruddin, S. M.; Graetzel, M. Engineering of Perovskite Materials Based on Formamidinium and Cesium Hybridization for High-Effi Ciency Solar Cells. *Chem. Mater* **2019**, *31* (5), 1620–1627.

[213] Huang, J.; Xu, P.; Liu, J.; You, X. Sequential Introduction of Cations Deriving Large-Grain $Cs_xFA_{1-x}PbI_3$ Thin Film for Planar Hybrid Solar Cells : Insight into Phase-Segregation and Thermal-Healing Behavior. *Small* **2017**, *13*, 1–9.

[214] Fan, L.; Ding, Y.; Luo, J.; Shi, B.; Yao, X.; Wei, C.; Zhang, D.; Wang, G.; Sheng, Y.; Chen, Y.; Hagfeldt, A.; Zhao, Y.; Zhang, X. Elucidating the Role of Chlorine in

Perovskite Solar Cells. *J. Mater. Chem. A* **2017**, *5* (16), 7423–7432.

[215] Pool, V. L.; Dou, B.; Campen, D. G. Van; Klein-stockert, T. R.; Barnes, F. S.; Shaheen, S. E.; Ahmad, I.; Hest, M. F. A. M. Van; Toney, M. F. Thermal Engineering of $FAPbI_3$ Perovskite Material via Radiative Thermal Annealing and in Situ XRD. *Nat. Commun.* **2017**, 1–8.

[216] Zuo, L.; Gu, Z.; Ye, T.; Fu, W.; Wu, G.; Li, H.; Chen, H. Enhanced Photovoltaic Performance of $CH_3NH_3PbI_3$ Perovskite Solar Cells through Interfacial Engineering Using Self-Assembling Monolayer. *J. AM. CHEM. SOC* **2015**, *137*, 2674–2679.

[217] Jiang, Q.; Zhao, Y.; Zhang, X.; Yang, X.; Chen, Y.; Chu, Z.; Ye, Q.; Li, X.; Yin, Z.; You, J. Surface Passivation of Perovskite Film for Efficient Solar Cells. *Nat. Photonics* **2019**, *13* (July), 460–466.

[218] Nie, W.; Tsai, H.; Asadpour, R.; Neukirch, A. J.; Gupta, G.; Crochet, J. J.; Chhowalla, M.; Tretiak, S.; Alam, M. A.; Wang, H.; Mohite, A. High-Efficiency Solution-Processed Perovskite Solar Cells with Millimeter-Scale Grains. *Science (80-.).* **2015**, *347* (6221), 522–526.

[219] Wu, Y.; Wang, D.; Liu, J.; Cai, H. Review of Interface Passivation of Perovskite Layer. *Nanomaterials* . 2021.

[220] Schulz, P.; Cahen, D.; Kahn, A. Halide Perovskites: Is It All about the Interfaces? *Chem. Rev.* **2019**, *119* (5), 3349–3417.

[221] Popoola, I. K.; Gondal, M. A.; Qahtan, T. F. Recent Progress in Flexible Perovskite Solar Cells: Materials, Mechanical Tolerance and Stability. *Renew. Sustain. Energy Rev.* **2018**, *82*, 3127–3151.

[222] Zhang, P.; Wu, J.; Zhang, T.; Wang, Y.; Liu, D.; Chen, H.; Ji, L.; Liu, C.; Ahmad, W.; Chen, Z. D.; Li, S. Perovskite Solar Cells with ZnO Electron-Transporting Materials. **2018**, *1703737*, 1–20.

[223] Wibowo, A.; Marsudi, M. A.; Amal, M. I.; Ananda, M. B.; Stephanie, R.; Ardy, H.; Diguna, L. J. ZnO Nanostructured Materials for Emerging Solar Cell Applications. *RSC Adv.* **2020**, *10* (70), 42838–42859.

[224] Zheng, X.; Chen, B.; Dai, J.; Fang, Y.; Bai, Y.; Lin, Y.; Wei, H.; Zeng, X. C.; Huang, J. Defect Passivation in Hybrid Perovskite Solar Cells Using Quaternary Ammonium Halide Anions and Cations. *Nat. Energy* **2017**, *2*, 1–9.

[225] Tsarev, S.; Olthof, S.; Boldyreva, A. G.; Aldoshin, S. M.; Stevenson, K. J.; Troshin, P. A. Reactive Modification of Zinc Oxide with Methylammonium Iodide Boosts the Operational Stability of Perovskite Solar Cells. *Nano Energy* **2021**, *83*, 105774.

[226] Liu, C.; Wu, W.; Zhang, D.; Li, Z.; Ren, G.; Han, W.; Guo, W. Effective Stability Enhancement in ZnO-Based Perovskite Solar Cells by MACl Modification. *J. Mater. Chem. A* **2021**, *9* (20), 12161–12168.

[227] Jung, E. H.; Chen, B.; Bertens, K.; Vafaie, M.; Teale, S.; Proppe, A.; Hou, Y.; Zhu, T.; Zheng, C.; Sargent, E. H. Bifunctional Surface Engineering on SnO_2 Reduces Energy Loss in Perovskite Solar Cells. *ACS Energy Lett.* **2020**, *5* (9), 2796–2801.

[228] Li, N.; Tao, S.; Chen, Y.; Niu, X.; Onwudinanti, C. K.; Hu, C.; Qiu, Z.; Xu, Z.; Zheng, G.; Wang, L.; Zhang, Y.; Li, L.; Liu, H.; Lun, Y.; Hong, J.; Wang, X.; Liu, Y.; Xie, H.; Gao, Y. Cation and Anion Immobilization through Chemical Bonding Enhancement with Fluorides for Stable Halide Perovskite Solar Cells. *Nat. Energy* **2019**, *4* (May), 408–415.